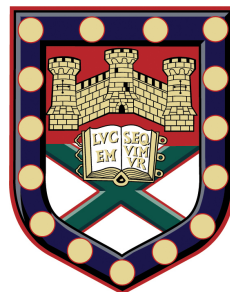


Optical Excitation of Surface Plasmon Polaritons on Novel Bigratings



Thomas James Constant

School of Physics

University of Exeter

A thesis submitted for the degree of

Doctor of Philosophy

March 2013

Optical Excitation of Surface Plasmon Polaritons on Novel Bigratings

Submitted by Thomas James Constant to the University of Exeter as a thesis for
the degree of Doctor of Philosophy in Physics
2013

This thesis is available for Library use on the understanding that it is copyright material and that no quotation from the thesis may be published without proper acknowledgement.

I certify that all material in this thesis which is not my own work has been identified and that no material has previously been submitted and approved for the award of a degree by this or any other University.

Thomas James Constant
2013

For my mum, Lel, and my sister, Emma.

Acknowledgements

First and foremost, I would like to thank my supervisors, Professor Roy Sambles and Professor Alastair Hibbins. Roy has been a constant inspiration to me throughout my research, and has kept me motivated and excited in all that I have done. The level of care and diligence he affords his students is second to none. Thank you Roy. In Alastair, I have gained not just a respected colleague, but also a close friend. In the early days of my supervisory meetings, Al was always there to step in and say “Hang on, Roy, this *isn’t* trivial.”, for which I will be forever grateful. I’ve also enjoyed many fruitful hours with Al at conferences, and many less fruitful hours down the pub. Thank you Al.

Many, many members of the Electromagnetic Materials Group at Exeter have helped me throughout my Ph. D. None more so than Matt Lockyear, without whose advice and support I most certainly wouldn’t have made it this far. Matt and I was fortunate enough to be part of RAD crew during it’s golden age, a rag-tag bunch of physicist-surfers who had some rather fantastic adventures.

Ian Hooper is Exeter’s resident grating expert, and I am indebted to him for countless discussions, arguments and comments on the physics of the diffraction grating. Currently, our running pool score stands at 97-65 to Hoops, and by the time anyone reads this I am certain he will have reached 100 and I will have had to buy us a holiday.

In the first few years of my work, I was lucky enough to have Professor Alex Savchenko as my academic mentor. Alex helped me a great deal when I was struggling, and was one of the most down to earth, empathic people I’ve ever met. Even after his untimely death in 2011, Alex’s legacy continues to have an important effect on my research. Alex’s winning of the funding for Exeter’s graphene center brought reliable nano-fabrication technology and immeasurably skilled physicists to Exeter, and in doing so allowed me to create the samples presented in this thesis.

I must thank Dave Anderson for his supreme skill at electron beam lithography and his remarkably patient and helpful attitude in dealing with me. A lot of the samples used in this work simply could not have been made without Dave’s help.

Plenty of the other academics have been great fun to work with at Exeter. Pete Vukusic has been a great help to me, providing me in the final months with some funding to develop the scatterometry kit further. Bill Barnes has always provided thought provoking questions, and the back-to-basics sessions he has run helped me lots with, well, the not-so-basics of our field. Euan Hendry has also provided useful

discussions, and has also wiped me out many times in poker. A four hour chat we had about Fourier series in optics, whilst sharing some beers in the baggage compartment of a train from London to Exeter, still helps me heavily in the physical reasoning in this thesis.

The technical workshop have been fantastic in my time at Exeter, making some remarkable devices and some less remarkable Bar stands. Originally my go-to man was Pete Cann, and after he left us to go enjoy Australia and then later family, the burden then fell to Nick Cole. They are both fantastic technicians and have made many of the results in the thesis possible by providing, or sometimes just fixing, vital kit. The other workshop boys have also been great. John, Kev and Adam have all helped me greatly, be it helping with orders (John), making things Nick can't (Kev), or just yelling instructions at me as our star defender on the post-grad football team (Adam!). In the technical areas, I can't forget Chris Forrest, who is often a lifesaver with all things IT.

Team Basement, as the dwellers of our darkest subterranean lab named ourselves, were constant fun. Ed Stone, for sharing and increasing my love for R, introducing me to Linux and providing some of the most memorable moments of these past years, I thank you! Earthquake testing Ed, though ill-advised, is possibly one of the funniest things you'll ever see. Caroline Pouya has managed to put up with me now for close to nine years. How she's managed that is completely beyond me, and despite such prolonged exposure to me, she has become one of my closest friends. Later, we were joined by Alfie, Nixon and in the final days Luke and Tim, who all took the challenge of living without daylight and the constant fear of asphyxiation, electrocution or asbestos poisoning with the good humour we've come to expect from Team Basement. I'd also like to thank Ed and Alfie particularly for listening to my ideas about using scatterometry to map iso-frequency contours, and helping me develop the experiential technique which is used heavily in this thesis. Chris Holmes was also there, but we shall get to him later.

The microwave kids in G31 have also been wonderful friends. Celia Butler has always been there for a chat, and I certainly now know more about Brownies and Gambia than I ever intended to. Mel Taylor and I did some summer project work together just prior to the Ph. D., and we had some great fun. Later Al, Simon, Panda, Liz, Laura, Ben and Ruth joined us, and they're all been fantastic friends. Another microwave bunny, Helen Rance is (quite by accident) my oldest friend at Exeter. We've known each other for so long, and through so many different experiences, that to attempt a decent acknowledgement is an exercise in futility.

For the majority of my Ph. D., I lived in Horseguards parade with Steve Hubbard, Matt Biginton, Ciarán Stewart, Chris Holmes and Pete Hale. Stormguards, as we affectionately named it, was not just a house. It was an exclusive gentleman's club, a brewery, a philosophical forum, a base of operations, a darts club, a support group, a

fraternity and a state of mind. The golden age of the Stormers saw us invent the amateur beer festival, the glove game, tea-darts, Nakatomi Plaza, develop an appreciation of fine whisky and much much more. I think it's fair to say that the two key players (other than myself) in the development of Storm-Culture was Pete and Chris; so Stormers, I thank you especially.

Plenty of other physicists have been important to me throughout this work. To list a few, I must mention Nat, Babs, Laureline, Tom D, and not forgetting the Russian contingent in Tim, Ivan, and the rest of the quantum group.

I have been fortunate to have many great friends outside of the department over the past 8 years. Holly Keatings and I met on the second day of uni, and have together sampled almost every restaurant in Exeter. My other house-mates of that era were Ashley, Rob and Jon. It was my great privilege to see Lash marry a fellow Stormer, Steve, after introducing them at our house while making name badges.

For many years I competed for the university as part of the fencing club. On the Men's 1st team I met Graham Heydon and James Parker, who are now two of my best friends. The adventures and trouble we got ourselves in make any attempt to play 'I have never' with these guys total suicide. I should also mention Pippa, otherwise she'll get in a huff.

My Aunt, Terri and my Uncle, Joe have let me live with them for the past 5 months, and have let me escape the city to be able to write this thesis. They have made me feel exceptionally welcome and tremendously loved during my stay. I'm lucky enough to say that this affection and kindness isn't unique to this period of writing, but is the norm for my entire life. Thank you, Terri and Joe.

Finally I must thank Emma and Mum. My little sister Em has always been encouraging and interested in what I've been doing, and as she's grown up has become one of my best friends. My mum, Lel, apparently used to flash brightly coloured cards at me while I was a baby in my cot, hoping to somehow induce intelligence. I'm not sure that worked, but her wish, motivation and encouragement for me to succeed at anything I put my mind to is pretty much a running theme of my entire life. It is certainly why I get to be writing this today. I love them both very much.

Abstract

This thesis details original experimental investigations into the interaction of light with the mobile electrons at the surface of metallic diffraction gratings. The gratings used in this work to support the resultant trapped surface waves (*surface plasmon polaritons*), may be divided into two classes: ‘crossed’ bigratings and ‘zigzag’ gratings.

Crossed bigratings are composed of two diffraction gratings formed of periodic grooves in a metal surface, which are crossed at an angle relative to one another. While crossed bigratings have been studied previously, this work focuses on symmetries which have received comparatively little attention in the literature. The gratings explored in this work possesses two different underlying Bravais lattices: *rectangular* and *oblique*.

Control over the surface plasmon polariton (SPP) dispersion on a rectangular bigrating is demonstrated by the deepening of one of the two constituent gratings. The resulting change in the diffraction efficiency of the surface waves leads to large SPP band-gaps in one direction across the grating, leaving the SPP propagation in the orthogonal direction largely unperturbed. This provides a mechanism to design surfaces that support highly anisotropic propagation of SPPs.

SPPs on the oblique grating are found to mediate polarisation conversion of the incident light field. Additionally, the SPP band-gaps that form on such a surface are shown to not necessarily occur at the Brillouin Zone boundaries of this lattice, as the BZ boundary for an oblique lattice is not a continuous contour of high-symmetry points.

The second class of diffraction grating investigated in this thesis is the new *zigzag* grating geometry. This grating is formed of sub-wavelength (non-diffracting) grooves that are ‘zigzagged’ along their length to provide a diffractive periodicity for visible frequency radiation. The excitation and propagation of SPPs on such gratings is investigated and found to be highly polarisation selective.

The first type of zigzag grating investigated possesses a single mirror plane. SPP excitation is found to be dependant on which diffracted order of SPP is under polarised illumination. The formation of SPP band-gaps is also investigated, finding that the band-gap at the first Brillouin Zone boundary is forbidden by the grating’s symmetry.

The final grating considered is a zigzag grating which possesses no mirror symmetry. Using this grating, it is demonstrated that any polarisation of incident light may resonantly drive the same SPP modes. SPP propagation on this grating is found to be forbidden in all directions for a range of frequencies, forming a full SPP band-gap.

Contents

Contents	vi
List of Figures	ix
List of Symbols	xx
1 Introduction	1
1.1 History	1
1.2 Scope and Outline of This Work	4
2 Background Theory	7
2.1 Introduction	7
2.2 Surface Polaritons on Planar Surfaces	7
2.3 Dispersion of SPPs on planar surfaces	11
2.3.1 Penetration Depth	12
2.3.2 Propagation Length	15
2.4 Surface Plasmon Polaritons on Diffraction Gratings	16
2.4.1 Diffraction Gratings	16
2.4.2 Coupling Surface Plasmons to Light by Coherent Scattering . . .	18
2.4.3 Surface Plasmon Polaritons on Bigratings	23
2.4.4 Coupling Strength of Light to SPPs on Gratings	25
2.4.5 Plasmonic Band Gaps	26
2.4.5.1 Coupling Light to Band Edges	29
2.4.6 Polarisation Conversion	31
3 Theoretical Methods	33
3.1 Introduction	33
3.2 The Differential Method of Chandezon et al.	34
3.3 The Finite Element Method	35
3.3.1 Solving Maxwell's Equations in the Mesh	36

3.3.2	Adaptive Meshing	36
3.3.3	Solution Evaluation and Convergence	37
3.3.4	Model Boundary Conditions	37
3.3.5	Floquet Type Excitation	39
4	Experimental Methodology	41
4.1	Sample Fabrication	41
4.1.1	Electron Beam Lithography	41
4.1.2	Thermal Evaporation	45
4.1.3	Template Stripping	45
4.1.4	Polymer Replication	46
4.2	Angle Scans	47
4.2.1	Monochromator	47
4.2.2	Fixed Wavelength Scans	48
4.2.3	Embedded Samples	49
4.3	Iso-Frequency Contour Measurement Using Scatterometry	49
4.3.1	Scatterometry	52
4.3.2	Principle of Operation	52
4.3.3	Sample Preparation	53
4.3.4	The Role of Polarisation	54
4.3.5	Corrections and Momentum-Space Deformation	55
4.3.6	Example Dataset	55
5	Optical Response of Metallic Rectangular Bigratings	58
5.1	Introduction	58
5.2	The Rectangular Bigrating	59
5.3	Dispersion of SPPs on Rectangular Bigratings	60
5.3.1	Scattering Components on Lamellar Gratings	60
5.3.2	Experimental Mapping of SPP Dispersion	62
5.3.3	Band Gap Observation Using Scatterometry	66
5.4	Polarisation Conversion on Rectangular Symmetry	68
5.5	Controlling SPP Anisotropy Using Rectangular Bigratings	71
5.6	Conclusions	76
6	Optical Response of Metallic Oblique Bigratings	77
6.1	Introduction	77
6.2	The Oblique Grating	78
6.3	Coupling of Light and SPP Mode Interaction on Oblique Gratings	80
6.4	Polarisation Conversion	84

CONTENTS

6.5	SPPs at the BZ Boundary of Oblique Bigratings	85
6.6	Conclusions	91
7	Optical Response of Metallic Zigzag Bigratings	92
7.1	Background	92
7.2	The Zigzag Grating	93
7.3	The Coupling of Plane Polarised Light to SPPs on Zigzag Gratings	94
7.3.1	Theory	94
7.3.2	Samples	97
7.3.3	Transverse Electric Coupling	100
7.3.4	Transverse Magnetic Coupling	104
7.4	Band Structure of SPPs on a Zigzag Grating	107
7.4.1	Band-Gaps at $k_x = 0$	108
7.4.2	Band-Gaps at the First Brillouin Zone Boundary	112
7.5	Anisotropic Propagation of SPP Modes for Self Collimation	115
7.6	Conclusions	120
8	Optical Response of Asymmetric Zigzag Bigratings	122
8.1	Introduction	122
8.2	The Asymmetric Zigzag Grating	123
8.3	The Coupling of Polarised Light to SPPs on an Asymmetric Zigzag Grating	126
8.3.1	Theory	126
8.3.2	Results	131
8.4	Band Structure of SPPs on an Asymmetric Zigzag Grating	134
8.4.1	Band Gaps at $k_x = 0$	135
8.4.2	Band Gaps at the 1 st BZ Boundary	136
8.4.2.1	Coupling of Light to the Band Edges	138
8.4.2.2	A Full Surface Plasmon Band Gap	141
8.5	Conclusions	144
9	Conclusions	145
9.1	Summary of Thesis	145
9.2	Future Work	147
Publications		150
References		152

List of Figures

1.1	The four types of grating geometry that are investigated in this thesis: (a) The rectangular bigrating in chapter 5, (b) the oblique bigrating in chapter 6, (c) the zigzag grating in chapter 7 and (d) the asymmetric zigzag grating in chapter 8.	4
2.1	A schematic representation of propagating electromagnetic fields at an interface between two materials.	9
2.2	The Drude model calculated with $\omega_p = 1.32 \times 10^{16}\text{Hz}$, $\gamma = 1.4 \times 10^{14}\text{Hz}$. As an example, the wavelength for a HeNe laser (632.8 nm) is highlighted, showing the permittivity of silver at this wavelength to be $\epsilon(632.8\text{ nm}) \approx -18.6 + 0.92i$	13
2.3	The dispersion of a surface plasmon polariton on a planar film approximated with the Drude model with $\omega_p = 1.32 \times 10^{16}\text{Hz}$, $\gamma = 1.4 \times 10^{14}\text{Hz}$	14
2.4	(a) Diagram of the electric field vectors of a SPP at the interface between a metal and a dielectric. (b) The exponential decay of the E_z component away from the surface, with a maximum amplitude at $z = 0$ and the different penetration lengths for the two materials shown.	15
2.5	The coordinate system used for a simple grating in the conical mount.	17
2.6	The allowed real momentum states for light incident on three diffraction gratings. The gratings reduce in period (increase in k_g) from (a) to (c). Points along the red circle are the possible momentum states for light in air (k_0). There is no corresponding circle in the metal halfspace as light in this medium is considered to be evanescently damped and so has no real value of momentum. The red stars show the momentum states for SPPs.	19
2.7	Two dispersion diagrams illustrating in-plane diffractive coupling to the (a) zero-order SPP in the extended zone scheme and (b) the higher-order diffracted SPPs coupling to zero-order light in the reduced zone scheme	21

LIST OF FIGURES

2.8	Intersections of the plane of incidence ($k_y = 0$) for (a) the unscattered surface plasmon polariton cone (b) a surface plasmon polariton cone diffracted in the plane of incidence and (c) a surface plasmon polariton cone diffracted perpendicular to the plane of incidence. The projected intersection screen also shows the radiative (white) and non-radiative (grey) regions of the light cone.	22
2.9	The reciprocal space map for an oblique bigrating with grating vectors \mathbf{k}_{gx} and \mathbf{k}_{gv} . The black lines represent zero-order modes, the blue lines represent diffracted modes. Lines represent grazing photon momentum states, dashed lines represent SPPs.	24
2.10	An example spectrum for a simple sinusoidal silver grating, calculated using the Chandeson method. the grating has the following parameters: $\lambda_{gx} = 750$ nm, and depth of 40 nm with a frequency dependent dielectric function for silver from literature. The spectrum is taken at normal incidence with the polarisation perpendicular to the grating grooves . . .	25
2.11	Cartoon of two possible SPP standing waves on a sinusoidal grating. The blue and red regions show accumulation of positive and negative charge density, respectively. These two standing waves, both which have a period of $2\lambda_g$, result in different field arrangements and so are associated with different energies.	27
2.12	The dispersion and band gap of (a) a SPP on a grating with one Fourier Harmonic and (b) on a grating with the first two Fourier Harmonics. The red line is the light line for free space light, the blue curves show the SPP contours. In (a) the black dotted line shown the unperturbed SPP contour, and the green dotted lines show the position of the first BZ. . .	28
2.13	Sketches of different grating profiles determined by the relative phases of the k_g and $2k_g$ components (left), and the resulting coupling of the light to the band-edges, shown as modelled reflectivity plots (right).	30
3.1	A graph showing the convergence of a typical FEM model as a function of adaptive passes. The black line shows the total number of elements introduced in the model, while the red line shows the ΔS parameter as a percentage.	38
3.2	Schematic of the different boundaries used in the FEM model. The unit cell shown is a zigzag grating (chapter 7) in red. The boundaries are highlighted and named in each case. The Perfect E boundary has been extruded from the bottom of the model for clarity.	39

LIST OF FIGURES

4.1 Illustration of the fabrication method used for the production of diffraction gratings.	42
4.2 System for the measurement of the reflectivity of a sample as a function of both wavelength, λ_0 and polar angle θ . White light is represented as blue lines, pseudo-monochromatic light is shown as green lines.	47
4.3 System for the measurement of angular dependant reflectivity at a set wavelength of $\lambda_0 = 632.8$ nm	48
4.4 Exploded view of the sample mount for use with a glass hemisphere. The hemisphere is adhered to the glass substrate using index matching fluid. The rig allows azimuthal rotation of the sample and hemisphere.	49
4.5 Three iso-frequency contours for the intersection of two SPP cones at angular frequencies ω_1, ω_2 and ω_3 . The contours show how the band-gap presents in k -space for the cases of a frequency lower than the band-gap (ω_1), inside the band-gap (ω_2) and above the band-gap (ω_3).	50
4.6 Experimental arrangement for the modified imaging scatterometry system. The angle θ of the light impinging on the grating, G, is approximately linearly proportional to the image's radial axis, r	53
4.7 Four raw images from the scatterometer for a wavelength of $\lambda_0 = 650$ nm. The sample is a rectangular bi-grating supporting SPPs, as will be explored in chapter 5. The polarisation states are (left to right) (1) polarisation a , which gives good contrast of the thin dark SPP bands, (2) crossed polarisers with the first polariser set to polarisation a and the second set at 90° to this, named polarisation b (3) the alternative crossed polarisation, with the first polariser set to b and the second polariser set to polarisation a , and (4) The final polarisation, with both polarisers set to b	54
4.8 The image correction for $R(\theta, \phi) \rightarrow R(k_0 \sin \theta, \phi)$. The black circles on both diagrams show contours of equal angle, ranging from 10° to 90° in 10° steps.	56
4.9 The processing of a raw dataset from the scatterometer at a wavelength of $\lambda_0 = 650$ nm. (a) Raw image obtained from scatterometer, (b) the image after the applied momentum-space deformation, and (c) the final image with corrected azimuthal angle and addition of calculated diffraction circles.	57
5.1 The coordinate system for a rectangular grating. Light is incident on the surface at a polar angle θ and an azimuthal angle ϕ . The plane of incidence contains the wavevector of the light, and the polarisations are defined accordingly.	60

LIST OF FIGURES

5.2	(a) Three examples of unit cells for lamellar grating profiles represented by equation 5.1. $f(A, \Gamma)$ for each case is $f(A, 0.5)$, $f(0.7A, 0.75)$ and $f(0.5A, 0.25)$. (b) Square of the Fourier coefficients, a_n defined by equation 5.2, in lamellar groove profiles as a function of Γ for $n = 1, 2, 3, 4$. The two grey vertical lines highlight the two values of Γ measured from the experimental sample used in section 5.3.2.	62
5.3	(a) A scanning electron micrograph of the template-stripped rectangular bigrating in silver. (b) A higher magnification of the surface showing small amounts of surface roughness attributed to anisotropic etching of the Si master. The parameters are $\lambda_x = 600$ nm, $\lambda_y = 400$ nm.	63
5.4	The reflectivity for different polarisations and azimuthal angles for a rectangular grating mapped as a function of (ω, k) in the case of (a) TM polarised light at $\phi = 0^\circ$, (b) TE polarised light at $\phi = 90^\circ$, (c) TE polarised light at $\phi = 0^\circ$ and (d) TM polarised light at $\phi = 90^\circ$	64
5.5	(a) A scattergram of a rectangular grating mapped to k -space for an illumination wavelength of $\lambda_0 = 550$ nm. The red square indicates the position of the BZ boundary. The white region bounded in the scattergram is replicated in (b), modelled using the FEM.	66
5.6	(a) Cartoon of the $(-1, 0)$ and $(1, 0)$ SPP iso-frequency contours at the BZ boundary, from the original continuous SPP contours (dotted lines) to the split modes (solid lines). (b) By considering the other interactions occurring at this point (or by using the mirror symmetry of the BZ boundary), the continuous SPP contours are recovered, leading to the observation of the SPP contour shape measured in figure 5.5.	67
5.7	Colour plots showing the magnitude of electric field at a set temporal phase (colour scale) and electric vector direction (arrows) for the (a) high energy and (b) low energy SPP standing waves occurring at the BZ boundary.	68
5.8	Spectra of polarisation conversion on the rectangular grating at $\phi = 45^\circ$. Top panel: The reflection of TE polarised light, $R_{TE:TE}$ (black) and polarisation conversion $R_{TE:TM}$ (red). Lower panel: The addition of these two reflectance curves gives a more precise position of the SPP modes.	70
5.9	Diagram of the effect on the surface profile by increasing the depth d_2 of the rectangular bigrating from (a) $d_2 = 40$ nm to (b) $d_2 = 80$ nm. A larger value of d_2 increases the diffraction efficiency of the constituent \mathbf{k}_{gy} grating.	72

LIST OF FIGURES

5.10 A sketch showing the expected iso-frequency contour deformation. Increased coupling efficiency in to the \mathbf{k}_{gy} direction deforms the SPP iso-frequency contours; represented as increasing in coupling efficiency from poorly coupled together (yellow lines) to strongly coupled (red). The blue circles represent the diffracted light circles, and the black circle represents the zero-order (un-scattered) light circle, which is the area mapped by imaging scatterometry.	73
5.11 Experimental iso-frequency contours for two rectangular bigratings at a wavelength of $\lambda_0 = 700$ nm with (a) shallow orthogonal grooves of $d_2 = 30$ nm and (b) deep orthogonal grooves of $d_2 = 80$ nm. The blue lines show the calculated position of the diffracted light circles, which unperturbed SPP contours will follow.	73
5.12 (a-b) Experimentally obtained dispersion diagrams mapped from the reflectance of rectangular bi-gratings with nominal depths of (a) 40 nm, (b) 80 nm. (c) The SPP mode position measured by reflection of TM polarised light at $\theta = 7^\circ$ as a function of angular frequency, ω . The curves are for the shallow (black) and deep (red) grating. The SPP mode shifts to lower frequencies as shown in (d).	75
6.1 Coordinate system for an oblique bigrating. The typical design parameters used in this chapter are $\lambda_{gx} = 600$ nm, $\lambda_{gy} = 400$ nm, $\alpha = 75^\circ$, $d_1 = d_2 = 40$ nm.	78
6.2 Example reciprocal lattices for an oblique grating. $\lambda_{gx} = 600$ nm, $\lambda_{gv} = 400$ nm and the angles between the two periodicities is $\alpha = 75^\circ$	79
6.3 SEM of an oblique grating master fabricated in a silicon wafer.	80
6.4 (a) The theoretically modelled iso-frequency surface for an oblique bigrating illuminated with TM polarisation at $\lambda_0 = 700$ nm. Mode intersections labelled A-C are discussed in section 4 (b) Experimentally obtained scattergram of the iso-frequency contour imaged through crossed polarisers. The yellow circles overlay indicates the theoretical mode position obtained from (a). Both colour bars range from low reflectivity (black) to high.	81
6.5 The dispersion of modes on an oblique grating for $\phi = \alpha = 75^\circ$, measured using the reflectivity as a function of polar angle and wavelength. The mode positions (grayscale minima) and calculated diffraction edges (lines) have been coloured to correspond to the scattered mode labels given in table 6.1.	83
6.6 (a) Polarisation conservation and (b) conversion mediated by out-of-plane scattered SPPs on an oblique grating.	85

LIST OF FIGURES

6.7	An experimentally obtained iso-frequency contour map of SPPs on an oblique bigrating with illuminated with incident light of wavelength $\lambda_0 = 650$ nm. SPP positions are mapped as regions of low reflectivity. The blue circles indicate diffracted light circles, and the green region is the typical BZ boundary drawn using the Wigner-Seitz method.	87
6.8	Regions of interest from figure 6.7. (a) The $(-1, 0)$ scattered SPP contour at the BZ boundary and (b) the $(+1, 0)$ scattered SPP contour at the BZ boundary.	87
6.9	Two possible Brillouin Zones for an oblique lattice. The Wigner-Seitz cell (red) and a simple trapezium (blue) contain on their boundaries the points of high symmetry labelled i_1, i_2, i_3	89
6.10	Applying the symmetry operations of the rectangular BZ (left), an arbitrary vector, \mathbf{r} (lying on the BZ boundary) corresponds to seven other vectors of known magnitude and direction. The summation of these vectors leads to no perpendicular component of the vector at the BZ boundary. In the oblique case (right), there is no such condition, the C_2 rotation operation only placing constraints on three additional vectors. . .	90
6.11	Dispersion plots mapped using the reflectivity of an oblique grating, showing the occurrence of band-gaps at the Brillouin Zones along the special cases of (a) $\phi = 0^\circ$ and (b) $\phi = 75^\circ$	91
7.1	The coordinate system of a zigzag grating. The experimental sample parameters were $\lambda_{gx} = 600$ nm, $\lambda_{gy} = 150$ nm, $d = 29.9$ nm with the plane of incidence defined at an angle ϕ and the polar angle of incidence as θ . The two polarisation orientations for the electric field vector are also shown for TM and TE polarisations.	94
7.2	The surface normal components of electric field vector for (a) TM and (b) TE polarised light (arrows) projected on a contour of the zigzag surface profile. The contour plot amplitude ranges from 1 (white) to -1 (blue). . .	95
7.3	The magnitude of the surface normal electric field in the x-direction for TM and TE polarisations.	96

7.4 Schematic cartoon of light coupling to SPPs on a zigzag grating. The top cartoons depict a zigzag cavity bounded by two metal zigzag ‘peaks’ (hashed areas) for a typical zigzag grating as investigated in this chapter. The left images show the case of TE polarised light, with the TM case on the right. The field applied for both polarisation cases lead to positive (+) and negative (–) charge distributions along the grooves. The component of electric field in the x -direction originating due to these charge arrangements is shown in red.	98
7.5 Scanning electron micrographs of: (a) an example template-strip master in Si, used for production of zigzag gratings; (b) a polymer replica of a Si master prior to metallisation, for zigzag gratings embedded in glass; (c) a template stripped sample in silver.	99
7.6 Experimental data (a) and FEM model prediction (b) of TE polarised reflectivity as a function of in-plane wavevector and angular frequency, mapping SPP dispersion on a zigzag grating. Blue lines show the positions of diffracted light lines scattered by $m\mathbf{k}_{gx}$, where $m = \pm 1, +2, 0$	100
7.7 Specular reflectivity of TE (black) and TM (red) polarised light as a function of polar angle, θ , for a wavelength of 632.8 nm, $\phi = 0^\circ$. Circles: recorded data with error bars of 1%, line: fitted FEM model prediction.	101
7.8 The \mathbf{E} field plot of a SPP excited by TE radiation found in figure 7.7, obtained by FEM. The colour scale shows the magnitude of the electric vector, \mathbf{E} , for a cross section of the zigzag grating, in the plane of SPP propagation (\parallel to $\hat{\mathbf{x}}$). The arrows show the direction of the electric vector over space. The electric field phase chosen for this travelling wave is arbitrary.	102
7.9 (a) Experimental data and (b) numerically modelled results of the TE polarised reflectivity as a function of in-plane wavevector and angular frequency, mapping the SPP dispersion on a zigzag grating in glass. Blue lines show the positions of diffracted light lines scattered by $m\mathbf{k}_{gx}$, where $m = 1, +2, 0, +3$	103
7.10 An example experimental reflectivity plot for TE and TM polarised light in the visible range at a fixed polar angle of $\theta = 53^\circ$. The broad absorption in the TM case is attributed to the weak excitation of a $+2\mathbf{k}_{gx}$ scattered SPP.	105
7.11 (a) An example spectral plot and fit at $\theta = 53^\circ$ for the TM reflectivity normalised to the TE reflectivity. (b) comparison between theory (greyscale) and experiment (black points) for a range of angles ($39^\circ < \theta < 55^\circ$). . .	106

LIST OF FIGURES

- 7.12 Experimental data of TM polarised reflectivity as a function of in-plane wavevector and angular frequency, mapping the SPP dispersion on a zigzag grating in glass. Blue lines show the positions of diffracted light lines scattered by $m\mathbf{k}_{gx}$, where $m = 1, +2, 0, +3$ 106
- 7.13 An iso-frequency scattergram mapping k-space contours for a 600 nm zigzag grating for an energy of 2.14 eV ($\lambda_0 = 580$ nm). The blue circles indicate the $\pm k_{gx}$ scattered light circles. 108
- 7.14 Cartoon of the two standing wave solutions for SPPs at $k_x = 0$, projected onto the zigzag surface. Since the anti-nodes of the SPP standing waves lie on the zigzag midsections in one case (a) and at the apexes in the other case (b), the standing waves exist in different electromagnetic environments and a band-gap may form. 109
- 7.15 The magnitude of electric field for the SPP standing waves at $k_x = 0$. (a-b) The high-energy solution for (a) the xy plane at $z = 41$ nm and (b) the xz plane, for $y = 75$ nm. (c-d) The low-energy solution for (c) the xy plane at $z = 41$ nm and (d) the xz plane, for $y = 75$ nm. 110
- 7.16 Manipulation of the band-gap observed at $k_x = 0$ through the increasing of zigzag amplitude. The unit cell and corresponding SPP dispersion around the intersection of the $+1\mathbf{k}_{gx}$ and $-1\mathbf{k}_{gx}$ scattered SPPs are shown for (a) The zigzag grating presented in this chapter and (b) a theoretical zigzag with a larger zigzag amplitude. 111
- 7.17 Modelled SPP dispersion around the intersection point of the $-1\mathbf{k}_{gx}$ and $+2\mathbf{k}_{gx}$ scattered SPPs meeting at the first BZ boundary (red dashed line). 112
- 7.18 Cartoon of the two standing wave solutions for SPPs at the 1st BZ. Since the peaks and troughs of the zigzag exist in equivalent electromagnetic environments, the solutions are degenerate in energy, and no band-gap forms. 113
- 7.19 The magnitude of electric field, $|\mathbf{E}|$ for the degenerate SPP standing waves at the first BZ. (a) One solution for the xy plane at $z = 41$ nm and (b) The second solution for the xy plane at $z = 41$ nm. 114
- 7.20 The magnitude of electric field for the degenerate SPP standing waves at the first BZ. (a-b) One solution for the (a) xy plane at $z = 20$ nm and (b) the xz plane, for $y = 75$ nm. (c-d) The second solution for the (c) xy plane at $z = 20$ nm and (d) the xz plane, for $y = 75$ nm. 115
- 7.21 Experimentally obtained dispersion plots for a zigzag grating at $\phi = 0^\circ$ and $\phi = 90^\circ$ 117
- 7.22 Measured iso-frequency contours of a zigzag grating for a range of wavelengths. The blue circles indicate calculated diffraction edges. 118

LIST OF FIGURES

- 7.23 The SPP iso-frequency contours mapped using imaging scatterometry at $\lambda_0 = 450$ nm. The green arrows show the direction of the SPP group velocity along the contour, indicating that for this wavelength the SPP waves only travel in the $\pm \mathbf{k}_{gx}$ direction. The red dotted lines show the position of the BZ boundary. 119
- 8.1 Coordinate system for the asymmetric zigzag grating. The experimental parameters were $\lambda_{gx} = 600$ nm, $\lambda_{gy} = 150$ nm, $d \approx 40$ nm, and $\delta = 150$ nm . 124
- 8.2 Two possible unit cells for a zigzag grating. (a) The grating unit cell explored previously in chapter 7. (b) An asymmetrical zigzag grating, with the central apex of the zigzag shifted by 150 nm. This shift removes the mirror-symmetry of the zigzag. 125
- 8.3 Scanning electron micrographs of (a) The asymmetric zigzag silicon master and (b) the template stripped sample in silver. 125
- 8.4 (above) A schematic of the electric field lines in the grooves (black arrows) of an asymmetric zigzag grating for two polarisation cases, and the resulting E_x component (red arrows). The points connecting the apexes lead to fixed points of zero E_x , leading to an asymmetric field distribution along the plane of propagation (bottom). 127
- 8.5 (a) The piecewise function representing E_x for TE (E_x^{TE}) polarisation (black line) and TM (E_x^{TM}) polarisation (red dotted line). Blue background shows the zigzag grating in the xy plane, with the x -coordinates aligned with the plot. $E_0 = 1$ in this diagram. 129
- 8.6 Magnitude of the electric field in region 1 (dashed) and region 2 (dotted) for the two polarisation cases of TM (black) and TE (red) polarised light, as a function of offset, δ 130
- 8.7 The square magnitude of the Fourier coefficients for $n = 0 \dots \pm 4$ with an offset of $\delta = 0.42L$, which corresponds to the experimentally measured offset of 126 ± 5 nm for the (a) TE case and (b) TM case. 131
- 8.8 The TE (black) and TM (red) reflectivity of an asymmetric zigzag grating at a wavelength of $\lambda_0 = 500$ nm. The blue dotted lines show the calculated position of the -1 and $+2$ diffraction edges. The grey bars are a width equal to the minimum step-size of the experiment, centred at the average mode minima. 132
- 8.9 The dispersion of the SPP modes mapped as a function of (a) TE and (b) TM reflectivity on an asymmetric zigzag grating. The blue lines are the calculated positions of the diffracted light lines. The colour scale indicates the absolute reflectivity. 133

LIST OF FIGURES

- 8.10 The dispersion of the SPP modes mapped as a function of unpolarised light reflectivity on an asymmetric zigzag grating. The blue lines are the calculated positions of the diffracted light lines. The colour scale indicates the absolute reflectivity. 134
- 8.11 The iso-frequency contours at $\lambda_0 = 550$ nm measured on: (a) a symmetric zigzag from chapter 7; (b) An asymmetric zigzag grating. Along $k_x = 0$ two SPP bands cross in both cases, one scattered from $-\mathbf{k}_{gx}$, and one from $+\mathbf{k}_{gx}$. The red square inset in (b) shows the magnified region of the band gap, with the red arrows showing that the direction of the group velocity contains no k_x component. 135
- 8.12 The calculated eigenmodes for the crossing of the $-1\mathbf{k}_{gx}$ and $+2\mathbf{k}_{gx}$ scattered SPPs at the first BZ for the cases of: (a) a symmetric zigzag; (b) a symmetric, high-amplitude zigzag and; (c) an asymmetric zigzag. The unit cell for each is shown above the modelled dispersion plots. 137
- 8.13 Field plots of $|\mathbf{E}|$ (colourplot) a for the (a) low energy and (b) high energy standing waves at the first BZ. The cross section is taken at $y = 75$ nm. 138
- 8.14 Field plots of $|\mathbf{E}|$ (colourplot) and $\hat{\mathbf{E}}$ (arrows) for: (a) the low energy and; (b) high energy standing waves at the first BZ. The cross sectional height is 1 nm above the grooves at 41 nm. 139
- 8.15 Experimental reflectivity colour plots mapping the dispersion of the band gap around the 1st BZ, for incident (a) TE polarised light, (b) TM polarised light and (c) average polarisation. The red dotted line indicates the position of the BZ boundary. 139
- 8.16 The (a) low energy and (b) high energy x -component of the SPP standing wave electric field (black, E_{SPP}) and incident field (red, E_x) varying across two unit cells of the asymmetric zigzag grating (light grey shapes indicate the zigzag in the xy plane). 141
- 8.17 Iso-frequency contours of an asymmetric zigzag grating for a range of wavelengths, measured using the reflectivity of unpolarised light in the imaging scatterometer. The blue circles indicate calculated diffraction edges. 142
- 8.18 (a) The dispersion of the SPP modes on an asymmetric zigzag grating for $\phi = 0^\circ$ mapped using the reflectivity of unpolarised light. Included are the wavelength slices corresponding to the iso-frequency scattergrams in figure 8.17, ranging from low frequency (red, 650 nm) to high (blue, 450 nm), (b) The scattergram for $\lambda_0 = 450$ nm, corresponding to the highest frequency slice in (a). 143

LIST OF FIGURES

9.1 A possible experimental arrangement for the observation of collimated surface waves using zigzag gratings.	148
--	-----

List of Symbols

Γ	Duty cycle / Fill-fraction of a Binary / Lamellar diffraction grating.
λ_{gx}	The period of a grating along the x -axis.
E	The electric field vector.
H	The magnetic field vector.
k	The wavevector.
\mathbf{k}_{gx}	The grating wavevector for the diffraction grating varying along the x axis.
ω	The angular frequency.
ϕ	The azimuthal angle of incidence, defining the orientation of the plane of incidence with respect to the x -axis.
θ	The polar angle of incidence, the angle between the surface normal and the incident light.
ε_m	The relative permittivity of medium m .
BZ	The Brillouin Zone
EBL	Electron Beam Lithography
FEM	The Finite Element Method for calculating the optical response of a system.
RIE	Reactive Ion Etching
SPP	Surface Plasmon Polariton

Chapter 1

Introduction

This thesis details original experimental investigations into the interaction of light with the mobile electrons at the surface of metallic diffraction gratings. The resulting quantised surface waves, *surface plasmon polaritons*, have been investigated by optical scientists for over a century, yet interest in the field has never been higher, and progress has never been faster [1, 2]. This is due in large part to the relatively recent advances in nano-fabrication techniques, which have allowed greater control over the surface wave propagation and dispersion characteristic on metallic surfaces. This work endeavours to extend the understanding of surface plasmon polaritons on diffraction gratings by exploring their propagation along symmetries and structures that have not been reported previously, and whose fabrication has only recently become achievable.

1.1 History

The phenomenon of diffraction from gratings has been reported by scientists since Francis Hopkinson peered at a street lamp through a silk handkerchief in 1785 [3, 4]. The rainbow that is seen due to the dispersion of light through such fine structure was recognised immediately as an incredibly useful optical property by Fraunhofer, and it was not long before early diffraction gratings were being manufactured by scratching fine grooves into the surfaces of glasses and metals.

In 1902, it was these early forays into the structuring of metals that led to the first recorded observations of surface plasmon polaritons' interaction with light. Wood [5] reported a bright band of enhanced reflection and a dark band of low reflection found in the projected spectrum of a ruled speculum diffraction grating produced at John Hopkins University [6]. Diffraction gratings produced by these early ruling engines were finding a multitude of uses in physics at the time, particularly in the young field of spectroscopy, and an explanation of Wood's spectral anomalies was vigorously sought.

Lord Rayleigh explained the observed dark band in his theory of diffraction gratings in 1907 [7] as the wavelength of incident light at which a diffracted light ray will start, or cease, to propagate. The redistribution of available propagating energy at this point created a reflectivity feature corresponding to one of the two Wood's anomalies. Thereafter this was referred to as the ‘Rayleigh anomaly’ and today this is also called the ‘diffraction edge’ or ‘pseudo-critical edge’.

Wood’s bright band was left unexplained for nearly thirty years until Strong [8], attempting to improve the reflective efficiency of a set of gratings by coating them with different types of metals, noticed the band shifted in energy depending on the metal coating used. This dependence on the metal’s optical characteristics led Ugo Fano [9–11], to the conclusion that this reflectivity anomaly was a signature of interactions of light with a trapped surface wave, comprised in part by the metal’s conduction electrons at the surface. He took the view that this represented a ‘zero-order’ waveguide mode: a guided mode that could still exist localised to the surface when a hypothetical supporting waveguide over-layer was decreased to zero thickness. Maxwell’s equations provided Fano with a solution for such a wave, on the condition that one material was a conductor and the other a dielectric*. Today we call this interface mode a surface plasmon polariton (SPP) and it is defined as an electromagnetic surface wave bound to the interface between a conductor and a dielectric.

While the first recorded observation of SPPs was on a diffraction grating, SPPs are not unique to these devices alone, and are generally found in systems where a conducting/dielectric interface exists. Once Fano had underpinned the physical origin of this surface wave, and in particular the momentum requirements to resonantly drive it, other methods by which to excite SPP on metal surfaces began to emerge. In the late 1950s, Ritchie [14] and Ferrell [15] both predicted the excitation of SPPs on thin, flat, metal films with accelerated electrons, with Ferrell also predicting the SPPs could decay back into light. This prediction was confirmed experimentally by Steinmann [16] two years later. Today, the use of electrons to excite SPPs has found application as a very precise method of plasmonic investigation: electron energy loss spectroscopy [17].

In 1968, Otto [18] and simultaneously Kretschman & Raether [19] excited SPPs using a prism geometry[†]. This technique used the evanescent ‘tail’ of light undergoing total internal reflection in the prism to couple to SPPs on a metal/air interface, matching the momentum of the SPP field through the classical tunnelling of the evanescent wave originating from inside the high-index material. Their techniques for prism coupling are

*Unbeknownst to Fano, similar work had been pursued by Zenneck [12] and also Sommerfeld [13] in their research on the transmission of radio-waves across large distances using trapped surface waves between seawater and air.

[†]Turbadar [20] was the first to excite this wave using a prism geometry, but unfortunately failed to connect his work to that of Fano or his observed phenomena to SPPs.

still used today, particularly in SPP based sensors which can investigate a diverse range of analytes, including the detection of fake tequila [21] and other spirits [22].

Research into SPPs on diffraction gratings continued in parallel with the development of these other excitation methods, with their observation and dispersion being investigated in the 1960s [23–25]. Research in the 1970s and 1980s focussed on the effect of deep grooves [26–29] and over-layer coatings [30, 31], driven in part by the development of holographic methods for diffraction grating manufacture [32]. This was followed by work in the 1990s that explained the influence of the grating shape on the resonances [33], SPP’s role in polarisation conversion [34] and the physical origin of observed SPP band interactions [35].

With the advances in nano-fabrication techniques, the development of detailed theoretical treatments for diffraction problems [36] and the increasing affordability and power of computers, increasingly complex diffraction grating geometries could be explored. The combinations of all these factors also helped spawn the active research field of ‘plasmonics’, and further improvements in all these areas continue to be a driving force behind the latest SPP research.

SPPs on gratings have already found many applications, and in some cases are already integral to commercial products. With the energy of a SPP resonance being highly sensitive to the local environment at the surface, SPPs have been used very successfully in sensing applications [37–39]; these have included the in-situ monitoring of chemical reactions such as catalytic conversion [40, 41], non-contact determination of surface structure [42, 43], and the measurement of optical constants of metals [44].

Coupled SPPs on gratings have also been used to enhance various optoelectronic devices; improvements to photo-detectors [45], the enhancement of laser beams [46–49] and the ability to improve the efficiency of solar cells [50–54] have all been reported in the literature. Generation of radiation has also been achieved on metallic or semiconducting gratings through SPP mediated second harmonic generation [55] or by SPPs stimulating electron photo-emission leading to the production of terahertz scale radiation [56, 57].

Additionally, SPPs on gratings have been employed as optical elements including colour filters [58], polarisation converters [59], and various surface optics for collimation or achieving negative refraction [60, 61]. They have also been used for the novel demonstration of enhanced transmission through hole arrays [62–65] and the manipulation of Magneto-optical effects such as Faraday and Kerr rotations [66]. The use of SPPs will no doubt continue to find applications in the most recent of technologies, particularly with very recent demonstration of their excitation on graphene [67].

This brief review of the investigations and applications of SPPs on gratings leads us to the present day and the theme of this thesis. In this work, unconventional gratings are used to couple to SPPs, and the propagation and dispersion of SPPs on such gratings

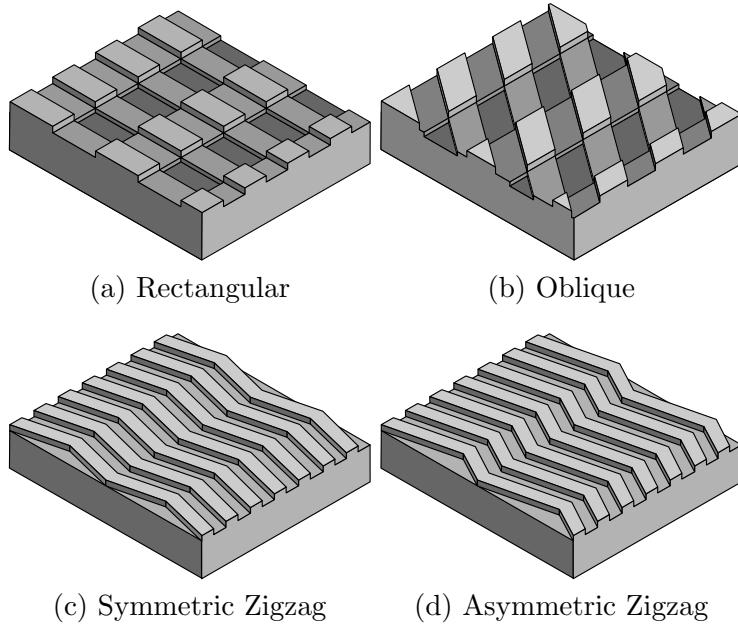


Figure 1.1: The four types of grating geometry that are investigated in this thesis: (a) The rectangular bigrating in chapter 5, (b) the oblique bigrating in chapter 6, (c) the zigzag grating in chapter 7 and (d) the asymmetric zigzag grating in chapter 8.

is investigated. The experiments presented here are done to explore the properties of SPPs on novel types of grating, and do not attempt to fit any particular application. However, many possibilities for extensions or applications are possible, and these are suggested in each chapter and summarised in the conclusions.

1.2 Scope and Outline of This Work

This thesis details experimental investigations into the propagation of SPPs on diffraction gratings that possess novel structure or symmetries. Broadly it may be divided up in to investigations of two types of diffraction grating; ‘crossed’ bigratings and a new type of diffractive optical element: the ‘zigzag grating’. Since both these types of grating possess two different diffractive periods in their surface geometry, they may both be considered a type of the larger family of metallic ‘bigratings’. There are four diffraction grating geometries investigated in this work, and these are summarised in figure 1.1. They are; the rectangular bigrating, the oblique bigrating, the ‘zigzag grating’ and the ‘asymmetric zigzag grating’.

The background theory of SPPs on both planar films and on metallic diffraction gratings is presented in chapter 2. This chapter covers the origin, coupling conditions

and band-structure of SPPs on both planar and periodic surfaces. The methods by which the optical response of the gratings under consideration have been calculated theoretically are then explained in chapter 3.

Chapter 4 details the experimental methods used for the production and measurements of gratings in this thesis. In addition to the standard experimental techniques used, a new method by which to map the plasmonic analogue to the iso-frequency ‘Fermi-contours’ of the SPP band structure is presented. These iso-frequency contours have been recorded using imaging scatterometry and this new technique, developed as part of this body of work, is used extensively throughout this thesis.

Chapter 5 presents some experimental observations on the excited SPPs supported by rectangular bigratings. These are gratings formed of two diffraction gratings of different pitch, crossed relative to each other at an angle of 90°. The dispersion of these modes on the surface and the formation of standing surface-wave states are experimentally recorded and matched to a theoretical model. It is found that by deepening the grooves of one of the constituent diffraction gratings, the propagation of SPPs along the surface becomes highly anisotropic. Control over this effective mode index in different directions along the surface could find application in surface-wave optics devices.

The work on ‘crossed’ bigratings continues in chapter 6, with the experimental investigation of SPPs on a bigrating with the reduced symmetry of an oblique lattice. The dispersion and scattering mechanisms on a fabricated oblique grating are recorded experimentally and explained. SPP mediated polarisation conversion is also observed on these gratings, as the scattered surface fields propagate along a surface of no mirror symmetry. The lack of symmetry on such a grating leads to the observation of SPP band gaps not forming at the Brillouin Zone (BZ) boundaries, and a general discussion of the oblique symmetry constraints on SPPs is offered to explain why this is so.

Chapter 7 introduces a new type of diffraction grating, the ‘zigzag grating’. This grating uses sub-wavelength structure in one direction to introduce an diffractive periodicity in the orthogonal direction. It is found, experientially and theoretically, that even-order diffracted fields only couple to SPPs for one linear polarisation of light, while odd-order diffracted fields only couple to the other, orthogonally polarised light. Further, it is shown that SPP band gaps are forbidden at the first BZ boundary by the symmetry of the zigzag surface. Finally in this chapter, it is shown that the sub-wavelength grooves on such a grating can lead to highly anisotropic SPP propagation. This anisotropy leads to SPP propagation at certain frequencies in only one single direction, irrespective of excitation angle. When combined with the lack of band gaps on such a symmetry, this makes these gratings excellent candidates for surface wave collimation devices.

The final experimental results of the thesis are presented in chapter 8, which extends the zigzag grating geometry to one with reduced symmetry. This relaxes the polarisation

conditions of the previous zigzag grating, leading to *any* SPP being coupled to with *any* incident polarisation of light, a result which could prove relevant to improving the efficiency of many plasmonic devices. The band structure of the SPPs supported by this grating is also experimentally investigated and the coupling to the different standing wave states by light which occur at the first BZ boundary is explored. The SPP anisotropy previously found for a zigzag grating is also found in this new asymmetric zigzag grating case, and combined with the large band gaps which form at the first BZ boundary, the grating is shown to support a full plasmonic band gap, for which SPP propagation is forbidden in all directions.

The thesis is concluded in chapter 9 with a summary of the findings and suggested future research which could extend the findings and applications of this work.

Chapter 2

Background Theory

2.1 Introduction

The interaction of light with metals has long proven to be a reliable path to striking optical effects. The Lycurgus cup is an example of a 4th century plasmonic device; a glass Roman goblet which uses colloidal gold and silver nano-particles to achieve a dull green surface reflection, but glows blood red when illuminated from the inside [68]. Resonant interaction between light and the electrons in these suspended metallic nano-particles provide the mechanism for this vivid effect, the same effect found in the majority of stained glass windows.

The topic of this thesis also concerns the coupling of light to electrons, specifically the mobile electrons found at the interface between dielectric and a conductor. Surface plasmon polaritons are electromagnetic surface waves coupled strongly to the longitudinal oscillations of this free electron plasma at the interface. They are quantised surface waves that propagate along the interface, evanescently decaying in the normal direction. This chapter introduces the background electromagnetic theory of these surface waves and their interaction with light.

Sections 2.2 and 2.3 deal with the origin and characteristics of surface plasmon polaritons propagating along a flat interface. Metallic diffraction gratings provide a mechanism by which to couple light to these surface waves. This coupling, and the constraints placed upon surface waves on a such periodic surfaces, are detailed in section 2.4.

2.2 Surface Polaritons on Planar Surfaces

Surface plasmon polaritons (SPPs) can be categorized as a member of a larger family of surface waves, broadly named ‘surface polaritons’. Surface polaritons are electromagnetic

surface waves coupled strongly to an elementary excitation and bound evanescently to the interface between two media. When a photon couples to the longitudinal oscillations of the free-electron plasma on metal surfaces, the resulting surface polariton is called a *surface plasmon polariton*. Surface polaritons also couple with surface lattice vibrations (*surface phonon polaritons*) [69], surface electron-hole pairs in semiconductors (*surface exciton polaritons*) [70] and collective excitations of surface electron spin (*surface magnon polaritons*) [71]. More recently, the manufacture of resonant sub-wavelength structures, or ‘metamaterials’, has allowed the design of surfaces with tailored resonances other than such elementary excitations, which may couple strongly to photons and produce surface polaritons [72, 73]. The resulting surface polaritons are often referred to as a ‘spoof’ surface plasmon polaritons.*

Solving Maxwell’s equations for an evanescently bound electromagnetic wave at an interface leads to a similar relationship between energy and momentum for all surface polaritons. The physical origin of the different types of surface excitations and their coupling to light is expressed in terms of the dielectric and magnetic functions which are frequency dependent and complex in general.

Fano [10] derived the dispersion relation for a trapped surface wave by first considering light propagating in a glass plate of finite thickness, bounded by semi-infinite vacuum and metal half-spaces. In a simple waveguide such as this, total internal reflections prevent the propagating light from escaping into the bounding medium. The necessary continuity of electric field across a boundary for light undergoing total internal reflection also requires non-propagating ‘evanescent’ waves extending into the bounding media, which do not transfer any power. The question as posed by Fano [10] was then: ‘Is there left any proper value when the thickness vanishes?’. As the thickness of the glass plate tends to zero, there is indeed still a valid solution to Maxwell’s equations for a wave travelling along the surface, evanescently bound in the normal direction; a surface polariton. In these terms, a surface polariton can be thought of as the lowest-order waveguide mode.

The dispersion of the surface polariton considered in this thesis, the surface plasmon polariton on a metal/dielectric interface, allows us to simplify the problem to that of isotropic, non-magnetic media. The derivation of this relationship [74] is presented below, and is also valid for other surface polaritons in isotropic non-magnetic media, such as surface phonon polaritons.

A schematic diagram of the system is shown in figure 2.1. Light illuminates a planar surface between two media of permittivities ε_1 and ε_2 in the xz plane, which we define to be the plane of incidence. The wavevector of the light in the m^{th} medium is

*although the inclusion of ‘plasmon’ is not strictly correct as the photon is not coupled to the free electron plasma oscillations but more usually a sub-wavelength cavity resonance.

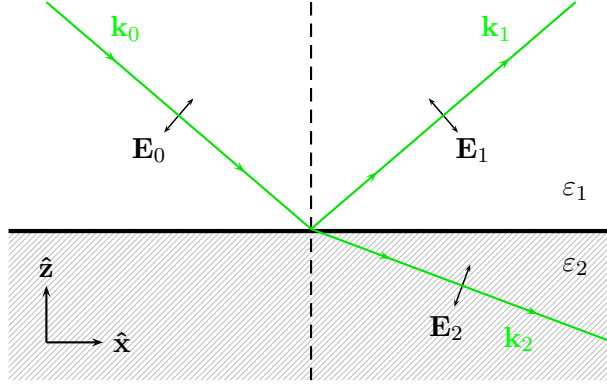


Figure 2.1: A schematic representation of propagating electromagnetic fields at an interface between two materials. The green rays illustrate the direction of the waves, which are coincident with the wavevectors, \mathbf{k} . The electric field is polarised in the xz plane, represented by black arrows. The optical response of the two media are characterised by their permittivities, ϵ_1 and ϵ_2 . The \hat{y} -direction is out of the page and the position $z = 0$ is at the interface.

$\mathbf{k}_m = k_{x_m} \hat{\mathbf{x}} + k_{z_m} \hat{\mathbf{z}} \equiv [k_{x_m}, 0, k_{z_m}]$, with no component in the $\hat{\mathbf{y}}$ -direction (out of the page). The light is then reflected back into medium 1 and refracted into medium 2. For light polarised with the electric field parallel to the plane of incidence (Transverse Magnetic, or TM polarised) the plane waves can be described as,

$$\begin{aligned}\mathbf{E}_m &= [E_{x_m}, 0, E_{z_m}] e^{i(\mathbf{k}_m \cdot \mathbf{x} + \mathbf{k}_m \cdot \mathbf{z})} e^{-i\omega t} \\ \mathbf{H}_m &= [0, H_{y_m}, 0] e^{i(\mathbf{k}_m \cdot \mathbf{x} + \mathbf{k}_m \cdot \mathbf{z})} e^{-i\omega t}\end{aligned}$$

where ω is the angular frequency of the light, t is time and m is a subscript indicating in which medium the field is propagating. H_y is the component of magnetic field in the $\hat{\mathbf{y}}$ -direction and $E_{x,z}$ is the component of electric field in the $\hat{\mathbf{x}}$ and $\hat{\mathbf{z}}$ directions, respectively. Since the surface polariton is a trapped surface wave, we set the incident wave to zero. Setting \mathbf{E}_0 to zero, we are left with two sets of fields (electric and magnetic) for the half-spaces above and below the interface,

$$z > 0 \quad \begin{cases} \mathbf{E}_1 = [E_{x_1}, 0, E_{z_1}] e^{i(k_{x_1}x + k_{z_1}z)} e^{-i\omega t} \\ \mathbf{H}_1 = [0, H_{y_1}, 0] e^{i(k_{x_1}x + k_{z_1}z)} e^{-i\omega t} \end{cases} \quad (2.1)$$

$$z < 0 \quad \begin{cases} \mathbf{E}_2 = [E_{x_2}, 0, E_{z_2}] e^{i(k_{x_2}x - k_{z_2}z)} e^{-i\omega t} \\ \mathbf{H}_2 = [0, H_{y_2}, 0] e^{i(k_{x_2}x - k_{z_2}z)} e^{-i\omega t} \end{cases} \quad (2.2)$$

We may combine the equations for electric and magnetic field in the two half-spaces

2. Background Theory

using Ampère's law,

$$\nabla \times \mathbf{H}_m = \varepsilon_m \frac{\partial \mathbf{E}_m}{\partial t}$$

where ε_m is the permittivity in medium m . The relationships between the tangential electric and transverse magnetic fields in each material are then,

$$k_{z_1} H_{y_1} = +\omega \varepsilon_1 E_{x_1} \quad (2.3)$$

$$k_{z_2} H_{y_2} = -\omega \varepsilon_2 E_{x_2} \quad (2.4)$$

Having obtained expressions for the electromagnetic fields in both media, we must now consider the continuity of these fields over the boundary. At the interface the boundary conditions for the electromagnetic waves are expressed as,

$$E_{x_1} = E_{x_2} \quad (2.5)$$

$$H_{y_1} = H_{y_2} \quad (2.6)$$

$$\varepsilon_1 E_{z_1} = \varepsilon_2 E_{z_2} \quad (2.7)$$

These are the conditions that tangential electric fields, transverse magnetic fields and the normal component of the electric displacement vector ($D_{z_m} = \varepsilon_m E_{z_m}$) must be continuous across the boundary at $z = 0$. The continuity of the tangential electric field (equation 2.5) allows us to combine equations 2.3 and 2.4,

$$\frac{k_{z_1}}{\varepsilon_1} H_{y_1} + \frac{k_{z_2}}{\varepsilon_2} H_{y_2} = 0$$

and continuity of transverse magnetic field (equation 2.6) then yields*

$$\frac{k_{z_1}}{\varepsilon_1} + \frac{k_{z_2}}{\varepsilon_2} = 0 \quad (2.8)$$

Finally, to obtain a relationship in terms of the momentum of the surface wave in the \hat{x} -direction (k_x), we consider the conservation of momentum in both regions. Conservation of tangential momentum requires that $k_{x_1} = k_{x_2} = k_x$ and so the expression for total conserved momentum is,

$$k_x^2 + k_{z_m}^2 = \varepsilon_m \left(\frac{\omega}{c} \right)^2 \quad (2.9)$$

Obtaining expressions for k_{z_1} and k_{z_2} using this conservation of momentum expression and combining them with equation 2.8, we find the dispersion relation for the surface

*At this point, we also employ some mathematical sleight of hand to substitute the permittivity, ε_m , for the relative permittivity ($\varepsilon_m/\varepsilon_0$) by cancelling the common factor of ε_0 in ε_1 and ε_2 . For clarity we redefine ε_m as the *relative* permittivity for the remainder of this thesis.

polariton,

$$k_x = \frac{\omega}{c} \sqrt{\frac{\varepsilon_1 \varepsilon_2}{\varepsilon_1 + \varepsilon_2}} \quad (2.10)$$

This equation relates the angular frequency of the field, ω to the wavevector along the surface, k_x . The energy and momentum of the surface mode is related to these quantities respectively by a factor of the reduced Planck's constant, \hbar . Because of this, it is also often referred to as the energy-momentum relation.

The final observation to be made in regards to the surface polariton dispersion is the set of ε_1 and ε_2 values which can support a bound surface wave. The continuity of normal electric displacement was mentioned briefly in equation 2.7, and we shall re-print it here.

$$\varepsilon_1 E_{z_1} = \varepsilon_2 E_{z_2}$$

This boundary condition states that the normal electric displacement must remain continuous across the interface. However, from the plane wave equation sets (equations 2.1–2.2) it is apparent that E_{z_1} is always 180° out-of-phase with E_{z_2} . E_{z_1} will always be of opposite sign to E_{z_2} . This is intuitive, as induced surface charge at the interface will naturally cause the electric field to extend into each surrounding media in opposite directions. To satisfy the boundary condition, and so support surface polaritons on such a surface, one material must be capable of ‘inverting’ the electric displacement resulting in the condition that the permittivities ε_1 and ε_2 must also be of opposite signs.

2.3 Dispersion of SPPs on planar surfaces

The optical response of a metal is characterized by the metal's frequency dependent permittivity, also called the ‘dielectric function’ of the material. This optical response function is dominated by two characteristics of metals; the fact that conduction electrons are free to move within the bulk of the material, and the presence of inter-band transitions of the valence electrons in the atomic orbitals. In the visible region, conduction electron behaviour is ballistic, oscillating and interacting with light many times before scattering from the crystal or other electrons. The inter-band transitions for a noble metal such as silver occur at the edges of the visible spectrum and so the dominant effect in the appearance of silver is due mostly to the strong interaction of the free conduction electrons with optical fields. At the surface of the metal, electromagnetic fields coupled to longitudinal oscillations of this free-electron plasma form together a surface polariton: the surface plasmon polariton.

The dispersion of a surface plasmon polariton takes the same mathematical form as equation 2.10 with one dielectric function representing the frequency dependent metal,

$\varepsilon_2(\omega)$, and the other representing a bounding non-conducting crystal with a dielectric constant, ε_1 ,

$$k_x = \frac{\omega}{c} \sqrt{\frac{\varepsilon_1 \varepsilon_2(\omega)}{\varepsilon_1 + \varepsilon_2(\omega)}} \quad (2.11)$$

A useful approximation for the metal dielectric function was presented by Drude [75]. Drude considered free electrons travelling in a classical manner, scattering from the ionic lattice with a characteristic average scattering rate. Electron-electron scattering is disregarded and the permittivity is expressed as,

$$\varepsilon_2(\omega) = \varepsilon_\infty - \frac{\omega_p^2}{\omega^2 + i\omega\gamma} \quad (2.12)$$

where ω is the angular frequency of the light, γ is the average rate of collision of the free conduction electrons with the lattice, and ε_∞ is the response of the ionic lattice, which is frequency independent and for metals in the visible domain equals 1. The ‘plasma frequency’ of the metal, ω_p , is the natural frequency of oscillation of the bulk conduction electrons.

An example of the permittivity of silver using the Drude model is shown in figure 2.2. It shows, for all visible regime wavelengths, that the real part of the silver permittivity is negative and there is a non-zero imaginary component. This is generally true for a wide range of metals at visible wavelengths. This negative permittivity of metals in the visible domain, when bounded by a dielectric with a positive real permittivity, satisfies the boundary conditions (equation 2.7) for a surface plasmon polariton. Substituting 2.12 into the dispersion relation for a surface plasmon polariton (equation 2.11), we obtain a fair approximation of the dispersion relation for a surface plasmon polariton on a planar metal film. This is plotted in figure 2.3. Figure 2.3 shows the dispersion of a surface plasmon polariton on a flat interface between silver and air. Plotted on the same scale is a line representing a grazing photon along the surface, the ‘light-line’. Notice that the light line and the surface plasmon polariton dispersion line do not cross. There is no solution at which the energy and momentum of free-space light is equal to that of the surface plasmon polariton. Since for a given energy of light, the light possesses insufficient momentum to match that of an SPP, the conclusion is that free-space light incident on a flat metallic surface cannot resonantly drive a surface plasmon polariton.

2.3.1 Penetration Depth

An excited SPP at the interface between a conductor and dielectric will possess electromagnetic fields which decay exponentially into both bounding media. A useful measure of this decay is the penetration depth, L_z , which is the distance at which the

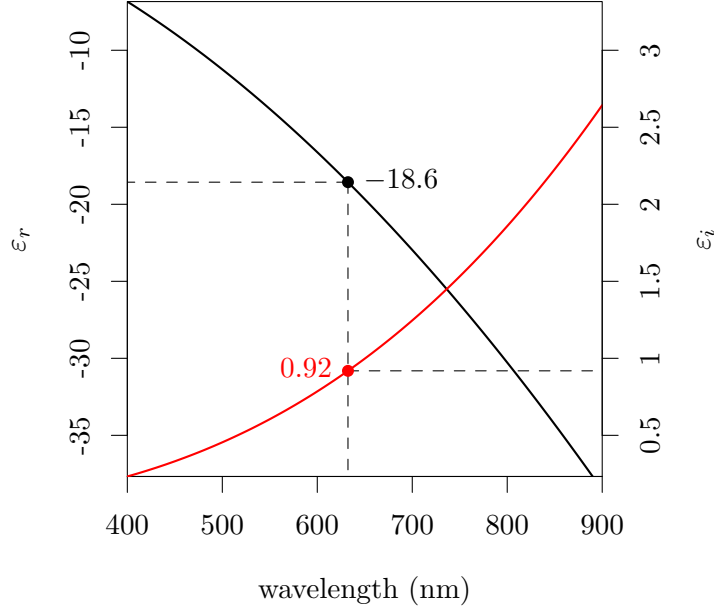


Figure 2.2: The Drude model calculated with $\omega_p = 1.32 \times 10^{16}\text{Hz}$, $\gamma = 1.4 \times 10^{14}\text{Hz}$. As an example, the wavelength for a HeNe laser (632.8 nm) is highlighted, showing the permittivity of silver at this wavelength to be $\epsilon(632.8 \text{ nm}) \approx -18.6 + 0.92i$

field amplitude has decreased to $1/e$ of its maximum value. Momentum conservation for a SPP (where $k_x > \epsilon_m k_0$) gives an expression $k_{z_m} = \sqrt{\epsilon_m k_0^2 - k_x^2}$ (equation 2.9 simplified.), which leads to the conclusion that k_{z_m} for SPPs must be purely imaginary. Substituting an imaginary k_{z_m} into an expression for the electric field at the surface gives*,

$$\mathbf{E}_m = [E_{x_m}, 0, E_{z_m}] e^{ik_x x} e^{-k_{z_m} z} \quad (2.13)$$

which is an expression for an electric field which does indeed decay exponentially into the two bounding media, and travels along the surface in the x direction. The value of z for which E_{z_m} falls to e^{-1} of the maximum value is then $1/k_{z_m}$. Substituting equation 2.10 into equation 2.9 we find that the expression for k_{z_m} is given by,

$$k_{z_m} = \pm k_0 \sqrt{\epsilon_m - \left(\frac{\epsilon_1 \epsilon_2}{\epsilon_1 + \epsilon_2} \right)} = \pm k_0 \sqrt{\frac{\epsilon_m^2}{\epsilon_1 + \epsilon_2}} \quad (2.14)$$

*the time dependent term, $e^{-i\omega t}$ has been omitted for clarity.

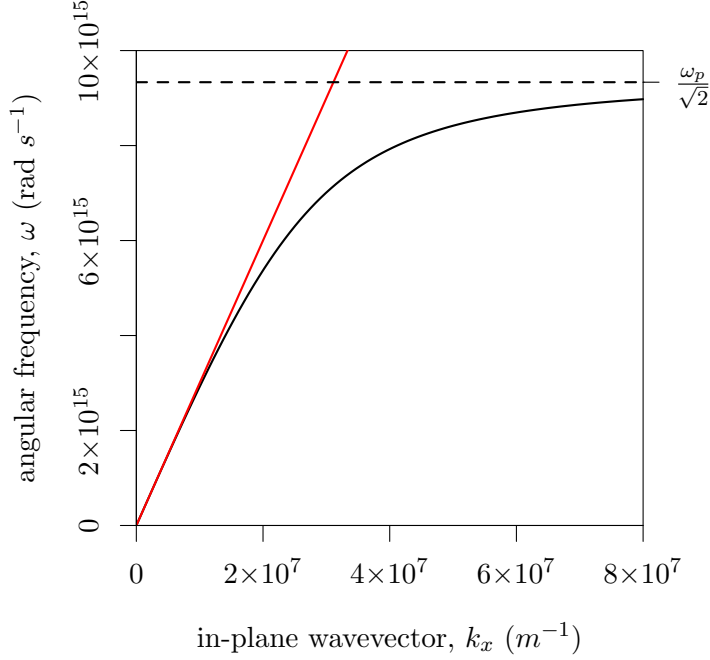


Figure 2.3: The dispersion of a surface plasmon polariton on a planar film approximated with the Drude model with $\omega_p = 1.32 \times 10^{16}$ Hz, $\gamma = 1.4 \times 10^{14}$ Hz.

We may simplify this expression for the case under consideration with medium $m = 1$ being a non-absorbing dielectric, $\text{Re}(\varepsilon_1) > 0$ and $\text{Im}(\varepsilon_1) = 0$, and medium $m = 2$ a lossy metal, $\text{Re}(\varepsilon_2) < 0$ and $\text{Im}(\varepsilon_2) > 0$. In the case where the metal is highly conducting we also have the considerations $|\text{Re}(\varepsilon_2)| \gg 1$ and $|\text{Re}(\varepsilon_2)| \gg \text{Im}(\varepsilon_2)$. Under these conditions, equation 2.14 simplifies to,

$$k_{z_m} = \pm k_0 \sqrt{\frac{\text{Re}(\varepsilon_m)^2}{\text{Re}(\varepsilon_2)}} \quad (2.15)$$

The penetration depth is then,

$$L_{z_m} = \frac{1}{k_{z_m}} = \lambda_0 \frac{1}{2\pi} \sqrt{\frac{|\text{Re}(\varepsilon_2)|}{|\text{Re}(\varepsilon_m)^2|}} \quad (2.16)$$

For a typical planar silver surface in air with $k_0 = 2\pi/\lambda_0 = 2\pi/632.8\text{nm}$, the penetration depth for the SPP into the air is calculated, using equation 2.16, to be $L_{z_1} \approx 415\text{nm}$ and in to the metal $L_{z_2} \approx 24\text{ nm}$. The field at the surface and this associated exponential

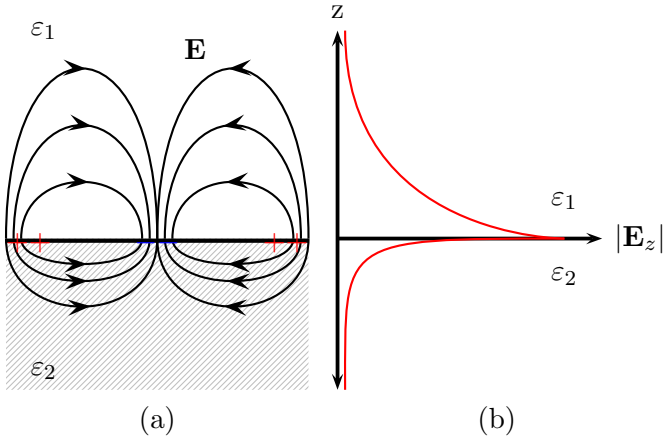


Figure 2.4: (a) Diagram of the electric field vectors of a SPP at the interface between a metal and a dielectric. (b) The exponential decay of the E_z component away from the surface, with a maximum amplitude at $z = 0$ and the different penetration lengths for the two materials shown.

decay of the SPP fields in the z direction is shown diagrammatically in figure 2.4 for an SPP in the visible regime.

In the limit of a perfect conductor, where $\epsilon_2 \rightarrow -\infty$, equation 2.16 shows that the penetration depth into the metal $L_{z_1} \rightarrow 0$ and the penetration depth into the dielectric tends to $L_{z_2} \rightarrow \infty$. With no field in the metal and the ‘decay length’ in z never actually decaying in the dielectric medium, the result is a grazing plane wave and no localisation of the field to the surface can be said to exist. This is why the excitation of SPP waves in the microwave regime is not observed on unaltered planar surfaces, as at these frequencies the metals approximate a perfect conductor and so the vanishingly-small localisation of the bound surface modes leads to the SPP resembling a grazing photon.

2.3.2 Propagation Length

By similar considerations of the surface electric field, we define the propagation length of the SPP along the surface as the length at which the field intensity has fallen to e^{-1} of its maximum value. While the SPP propagates in the x direction, it will be damped by Joule losses to the metal. This leads to the expression for k_x to be generally complex, and the imaginary component of k_x again provides the exponential decay of the SPP as it travels along the interface. The imaginary part of k_x is given by,

$$\text{Im}(k_x) = \frac{k_0 \text{Im}(\epsilon_2)}{2 \text{Re}(\epsilon_2)^2} \left(\frac{\epsilon_1 \text{Re}(\epsilon_2)}{\epsilon_1 + \text{Re}(\epsilon_2)} \right)^{\frac{3}{2}} \quad (2.17)$$

This gives the propagation length, L_x as,

$$L_x = \lambda_0 \frac{\text{Re}(\varepsilon_2)^2}{2\pi \text{Im}(\varepsilon_2)} \left(\frac{\varepsilon_1 + \text{Re}(\varepsilon_2)}{\varepsilon_1 \text{Re}(\varepsilon_2)} \right)^{\frac{3}{2}} \quad (2.18)$$

For a typical planar silver surface in air with $k_0 = 2\pi/\lambda_0 = 2\pi/632.8\text{nm}$, the propagation length is $L_x = 42.6\text{ }\mu\text{m}$. This propagation length is large enough so the SPP intensity is sufficient to interact strongly and Bragg scatter on diffraction gratings with sub-micron periodicity, a topic we shall cover in the next section.

2.4 Surface Plasmon Polaritons on Diffraction Gratings

2.4.1 Diffraction Gratings

A diffraction grating is an optical device in which the dielectric constant varies periodically across the surface, and whose period is of the order of the wavelength of light. This periodic variation leads to the diffraction of light by way of localised phase changes in the impinging field, resulting in either the coherent constructive or destructive interference of the waves in the far-field.

The first recorded observation of diffraction by fine structure was by Francis Hopkinson in the late 1700s. Peering at a street lamp through a silk handkerchief, Hopkinson observed rainbows and enquired with his friend, Rittenhouse as to the cause. Rittenhouse then went on to manufacture and study the first reported ‘diffraction grating’ made of parallel hairs, set between two brass wires cut with a fine screw head [3]. This was the first example of a transmission grating and the device’s dispersive nature.

In this thesis, a periodic modulation across a reflecting surface is achieved by surface-relief. Shallow grooves are cut into a metal surface with a defined period, on the order of the wavelength of visible light, causing diffraction in the reflected light from the surface. Other methods by which diffraction gratings may be produced exist, such as phase-modulated diffraction gratings [32] or periodic hole arrays, but these will not be dealt with here.

The coordinate system for a simple reflection grating of this type is shown in figure 2.5. The grating consists of a set of periodic grooves in a metal surface, with the amplitude varying along the x -axis, with a periodicity of λ_{gx} . Light impinges on the grating surface at a polar angle θ , in a plane of incidence defined at an azimuthal angle ϕ , where $\phi = 0^\circ$ corresponds to when the plane of incidence is perpendicular to the grating grooves. The grooves are a depth d . The polarisation of the incident light is defined with respect to the plane of incidence, such that Transverse Electric (TE) polarised light is when the electric field, \mathbf{E}_{TE} is oriented perpendicular (transverse) to

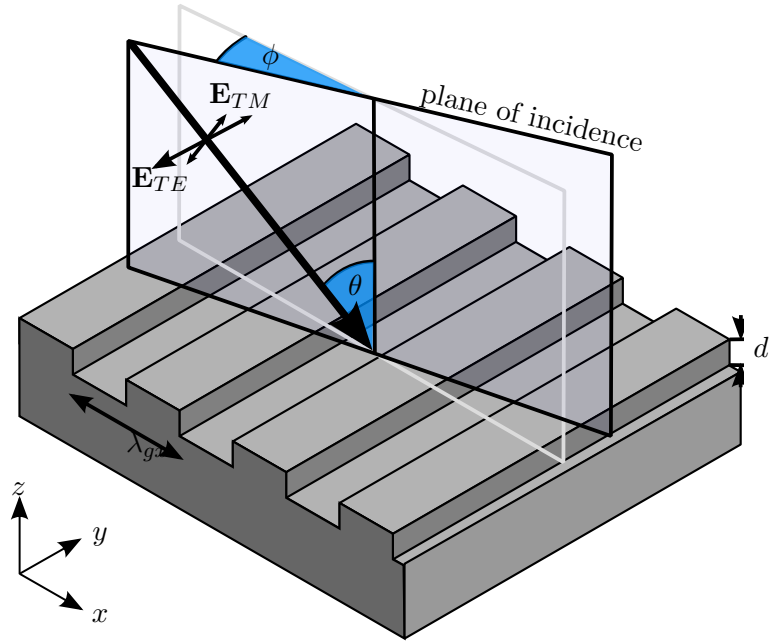


Figure 2.5: The coordinate system used for a simple grating in the conical mount.

the plane of incidence, and Transverse Magnetic polarised light is defined as the electric vector \mathbf{E}_{TM} lying within the plane of incidence.

In this orientation, where ϕ is allowed to vary and is not necessarily equal to 0° , the diffracted beams form in general a ‘cone’ of diffraction, and so it is named the ‘conical’ mounting/arrangement.

The relationship between incident and diffracted light in the conical mount is given by the equation,

$$n \frac{\lambda_0}{\lambda_{gx}} = (\sin \theta \cos \phi + \sin \theta_n \cos \phi_n) \quad (2.19)$$

where n is an integer denoting the spectral order of diffraction, λ_0 is the incident wavelength and θ_n, ϕ_n is the polar and azimuthal angle of the n^{th} diffracted order, respectively.

The wavevector of light is defined as $\mathbf{k}_0 = 2\pi\hat{\mathbf{r}}/\lambda_0$, where $\hat{\mathbf{r}}$ is the unit vector denoting the direction of the wave. This wavevector is associated with the light’s momentum by a factor of the reduced Planck’s constant, such that $\mathbf{p} = \hbar \mathbf{k}_0$, and its scalar equivalent is the wavenumber (k_0). Similarly, the grating wavevector is defined, in this case, as $\mathbf{k}_{gx} = 2\pi\hat{\mathbf{x}}/\lambda_{gx}$ (its wavenumber is k_{gx}). We may re-write equation 2.19 in terms of

these quantities,

$$-k_0 \sin \theta_n \cos \phi_n = k_0 \sin \theta \cos \phi - nk_{gx} \quad (2.20)$$

$$\mathbf{k}_n^{\parallel} = \mathbf{k}_0^{\parallel} - nk_{gx} \quad (2.21)$$

where \mathbf{k}_n^{\parallel} is the wavevector component of the diffracted light parallel to the surface and \mathbf{k}_0^{\parallel} is the incident light's wavevector parallel to the surface. So a diffraction grating modifies the surface wavevector of the incident light by the addition or subtraction (since n may be positive or negative) of an integer number of grating wavevectors.

Recall from section 2.3 that the coupling of free-space light to surface plasmon polaritons is not possible on flat surfaces due to the mismatch between the SPP and light's wavevectors (or, equivalently, the momentum mismatch). Since the diffraction grating allows us to modify the wavevector of incident light, the diffraction grating may be used to couple to these previously unmatchable modes. This will be explored in the next subsection.

2.4.2 Coupling Surface Plasmons to Light by Coherent Scattering

The three illustrations in figure 2.6 show the momentum-space diagrams for monochromatic light of frequency $\omega_0 (= ck_0)$ incident on three gratings of different pitch, at a fixed polar angle in the classical mount of $\phi = 0^\circ$ ^{*}. The allowed real momentum states of propagating light are represented as a red circle of radius k_0 . Conservation of energy requires that any vectors representing propagating light have a magnitude of k_0 , and as such are represented as radial arrows of this circle. Points that lie outside of the red light circle possess greater momentum than the incident light circle and represent non-propagating (evanescent) light with imaginary momenta. The red stars on the diagram are the allowed momentum states of a surface plasmon polariton. The surface plasmon polariton momentum state lies at a finite real value of k_x , with no real value of k_z , indicating the surface mode has a purely imaginary value of k_z and so evanescently decays normal to the surface while propagating along it. Notice the surface plasmon polariton state lies outside the light circle, illustrating that even grazing light possesses insufficient momentum to match that of the surface mode.

The in-plane (k_x) component of light momentum on a grating surface is altered by the addition of an integer number of grating vectors (equation 2.21). In figure 2.6(a), three possible scattering events of incident light are shown, a $+1k_g$, a $1k_g$ and no scattering ($0k_g$). The allowed momentum states of light with these new values of k_x show that

*For the conical mount, these allowed momentum states would form instead a hemisphere in three-dimensional k -space.

2. Background Theory

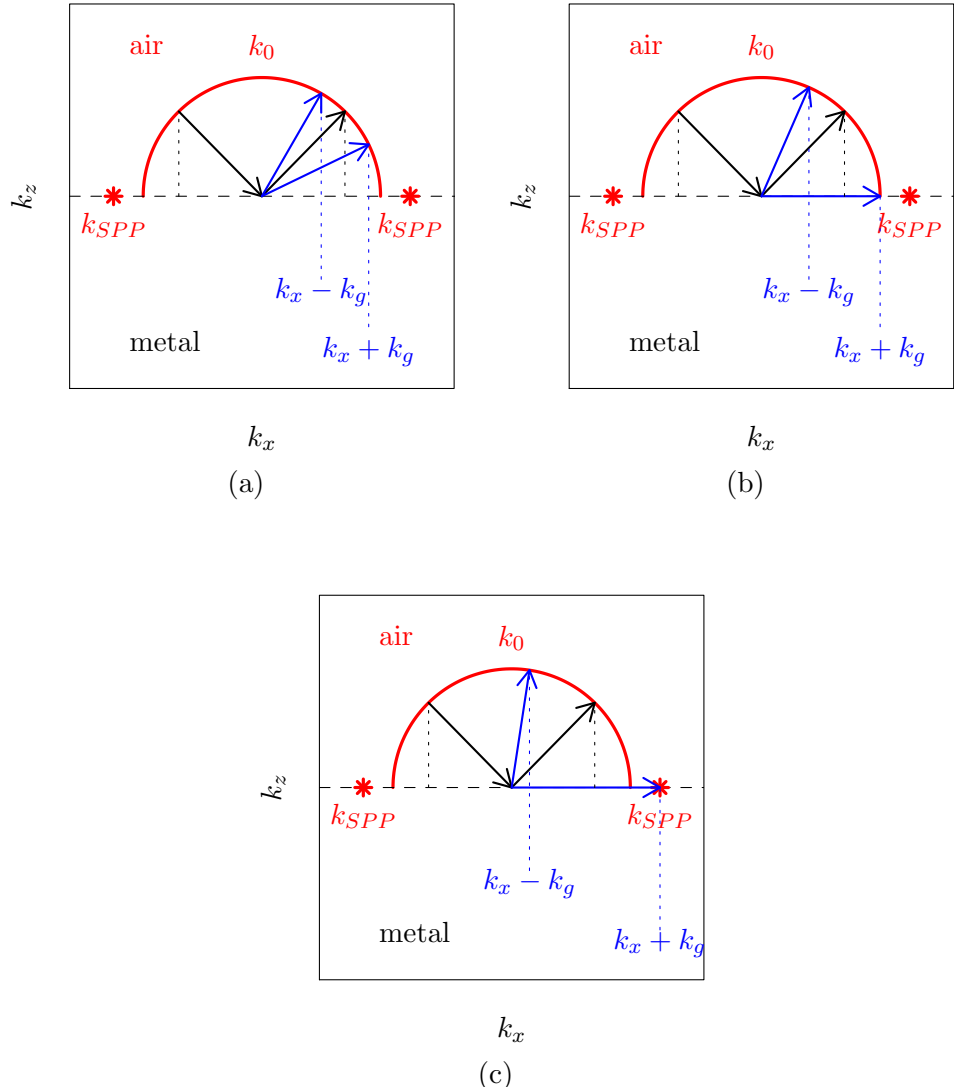


Figure 2.6: The allowed real momentum states for light incident on three diffraction gratings. The gratings reduce in period (increase in k_g) from (a) to (c). Points along the red circle are the possible momentum states for light in air (k_0). There is no corresponding circle in the metal halfspace as light in this medium is considered to be evanescently damped and so has no real value of momentum. The red stars show the momentum states for SPPs.

diffracted light must leave the surface at a different polar angle to the specular reflection ($0k_g$) to conserve total momentum, k_0 (and so still lie on the radial line of constant total momentum). This angle of diffraction is dependent on the size of the light circle, determined by the frequency of the radiation, which illustrates the dispersive properties of a diffraction grating. The grating represented in figure 2.6(b) has a periodicity less than that of grating 2.6(a). The period has been chosen to illustrate the case where the $+1k_g$ diffracted order is grazing the surface. An increase in the polar angle, or a decrease in the incident light wavelength would leave no available propagating light momentum states for the $+1k_g$ order. The order would become evanescent. To satisfy energy conservation, this transition from propagating diffracted order to evanescent light requires the power of that order to be re-distributed to the remaining propagating orders. In spectra or angular data this is shown as a step in the intensity of reflected light. First observed by Wood [5] and explained by Rayleigh [7], this feature is referred to in literature as a diffraction edge, a critical edge or a Rayleigh anomaly. In this thesis we will adopt the convention of calling this feature a diffraction edge.

Finally, figure 2.6(c) shows a grating of sufficient pitch where a $+k_g$ scattering photon has sufficient momentum to match the momentum state of a surface plasmon polariton. This light's value of in-plane momentum is $k_x + k_g$. The grating has coupled free space light to the surface mode by enhancing the in-plane wavevector of the light to match to that of the surface plasmon polariton. Momentum conservation is still maintained as, while the real part of $k_z = 0$, the imaginary part is not. Using equation 2.19 this condition is expressed in this case as,

$$\mathbf{k}_{SPP} = \mathbf{k}_1 = \mathbf{k}_x + \mathbf{k}_{gx} \quad (2.22)$$

Notice that this scattered light vector is now greater than the radial k_0 circle, showing it may no longer match a momentum state of propagating light and so does not propagate away from the surface. The light is an evanescent diffracted order which resonantly drives the surface plasmon polariton. This case may be represented on the dispersion diagram for a SPP as shown in figure 2.7(a), where the zero-order SPP dispersion now passes through the diffracted light cones (in blue). For all the points along the SPP dispersion which lie inside the diffracted light cones (represented as blue circles along the SPP dispersion (black line)), coupling can occur between the evanescent light and the SPPs. Since all of this occurs in the non-radiative region, no optical effect related to the SPP excitation is observed in this case. However, this surface plasmon polariton may also decay back into the zero-order reflectivity by itself diffracting by $-1k_g$. The light returning to the specular order, having undergone two scattering events (and an excitation and decay event), will be out of phase with the incident light leading to a

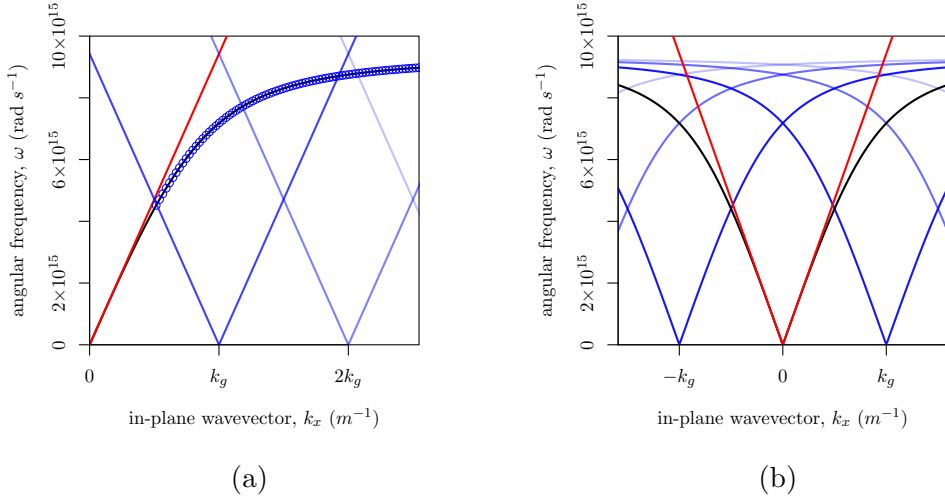


Figure 2.7: Two dispersion diagrams illustrating in-plane diffractive coupling to the (a) zero-order SPP in the extended zone scheme and (b) the higher-order diffracted SPPs coupling to zero-order light in the reduced zone scheme

sharp drop in the reflectivity observed. The observation of this interaction on the SPP dispersion is shown in figure 2.7(b). Light diffracts and couples to the zero-order SPP, then diffracts and decays back into propagating light inside the zero-order light cone. For the SPP dispersion points lying inside the (red) light cone, we expect there to be an effect on light matching these momentum and energy values. It is exactly equivalent to interpret figure 2.7(b) as the zero-order SPP curve (black) itself diffracting into the light cone, as the surface waves themselves Bragg scatter to interact with zero-order light. Typically this interpretation will be favoured in this thesis, as it allows a simplified discussion for mode interaction without sacrificing any scientific rigour.

This coherent scattering of SPPs will produce extrema in the specular reflectivity of the grating indicative of the light having interacted with a SPP. By mapping the zero-order reflectivity of a diffraction grating as a function of ω and k , we may reproduce the dispersion curves of the SPPs, with the reflectivity extrema occurring at the diffracted SPP mode positions.

The shape of these dispersive bands is dependent on the plane of incidence, the orientation of the grating and, in the case of bigratings, covered later, the additional available scattering grating vectors. Figure 2.8 shows three possible intersections of a plane of incidence with scattered SPP cones in (ω, k_x, k_y) space and their possible coupling. Since the SPP dispersion is approximated to be isotropic in all directions*,

*This is not generally true on grating surfaces, as the grooves have destroyed the isotropy of the

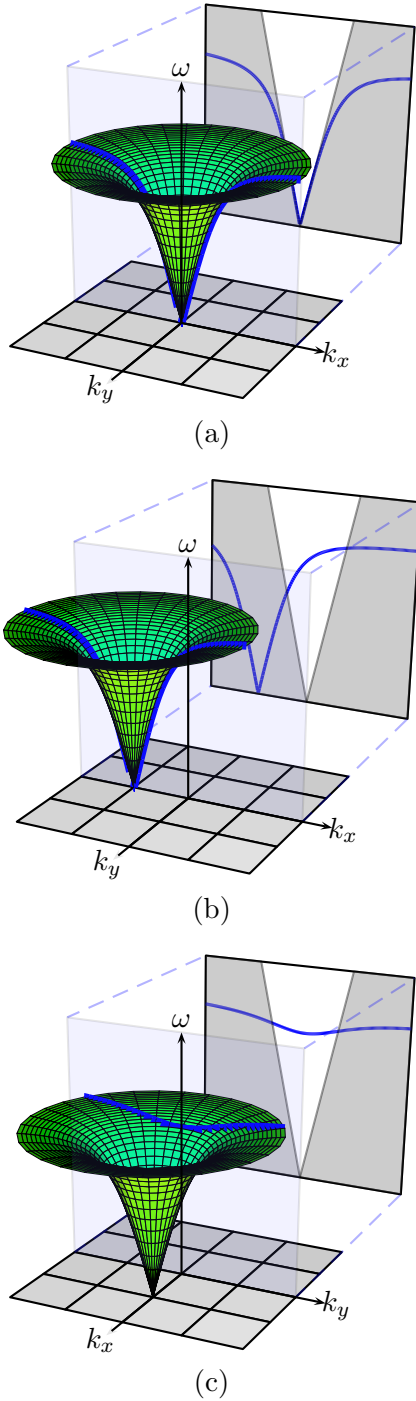


Figure 2.8: Intersections of the plane of incidence ($k_y = 0$) for (a) the unscattered surface plasmon polariton cone (b) a surface plasmon polariton cone diffracted in the plane of incidence and (c) a surface plasmon polariton cone diffracted perpendicular to the plane of incidence. The projected intersection screen also shows the radiative (white) and non-radiative (grey) regions of the light cone.

the SPP dispersion can be shown as a cone formed by sweeping the dispersion line around the ω axis. Figure 2.8(a) is the non-scattered zero-order SPP cone. The plane of incidence and the conic-like intersection(along k_x in all cases here), is projected in a back plane, with the region of propagating light shown in white, and the evanescent light in grey. In this case, the experiment would yield the same dispersion as shown in figure 2.3, with none of the available (blue) SPP momentum states passing through the region of free-space light. In figure 2.8(b), a SPP cone has been scattered in the plane of incidence by $1k_g$. The projected intersection in the plane-of incidence shows that now a portion of the SPP momentum states lies within the white region of free-space light, and so observable coupling can occur. The shape of the SPP band is the same as the in-plane scattered SPPs shown in figure 2.3.

Finally, figure 2.8(c) shows the results of a SPP cones having scattered in a direction 90° to the plane of incidence. This can occur for a monograting oriented so that $\phi = 90^\circ$, or this could be the result of the SPP undergoing a different possible scattering event on a square bigrating. The SPP momentum of this scattered mode does cross the region of free space light (white area on the projected screen), and forms a flatter band shaped as shown which may couple to the free-space light. These figures 2.8(b) and 2.8(c) show two possible functional forms of coupled SPPs in the plane of incidence. Real diffraction gratings will contain many of these scattering mechanisms, and the mapped dispersion will consequently be formed of multiple versions of these SPP bands.

2.4.3 Surface Plasmon Polaritons on Bigratings

Bigratings are defined as diffraction gratings which possess two grating vectors which do not lie collinear to each other. The grating equation from equation 2.21 then becomes,

$$\mathbf{k}_{(n_x, n_v)}^{\parallel} = \mathbf{k}_0^{\parallel} \pm n_x \mathbf{k}_{gx} \pm n_v \mathbf{k}_{gv} \quad (2.23)$$

where the variables are defined as they were for equation 2.21, with \mathbf{k}_{gv} the grating vector of the second pitch which is oriented at an angle α to the x -direction. n_x is the integer number representing the spectral order in the x direction and n_v is the spectral order in the v direction. In this thesis we shall occasionally use the notation (n_x, n_v) to refer to different diffracted orders, for example a $(+1, +1)$ scattered SPP would be represented as $\mathbf{k}_{SPP} = \mathbf{k}_0^{\parallel} + 1\mathbf{k}_{gx} + 1\mathbf{k}_{gv}$.

With this simple definition, all the possible 2D Bravais lattices for a diffraction grating can be realised. With the angle α equal to the angle between the gratings in real space (the corresponding angle in reciprocal space is $\alpha^* = 180^\circ - \alpha$), we have the following definitions listed in table 2.1.

surface on which the SPPs propagate.

Bravais Lattice	α	$\mathbf{k}_{gx}, \mathbf{k}_{gv}$	References
Square	$\alpha = 90^\circ$	$ \mathbf{k}_{gx} = \mathbf{k}_{gv} $	[44, 52, 53, 76–78]
Rectangular	$\alpha = 90^\circ$	$ \mathbf{k}_{gx} \neq \mathbf{k}_{gv} $	[79–81][This Work]
Hexagonal	$\alpha = 60^\circ$	$ \mathbf{k}_{gx} = \mathbf{k}_{gv} $	[44, 58, 76, 82]
Oblique	$\alpha \neq 90^\circ$	$ \mathbf{k}_{gx} \neq \mathbf{k}_{gv} $	[This Work]
Rhombic	$\alpha \neq 90^\circ$	$ \mathbf{k}_{gx} \neq \mathbf{k}_{gv} $	[83]

Table 2.1: The Bravais lattice types and associated work on SPPs on such symmetries. Rhombic is also called centred-rectangular, see Kittel [75] for an example.

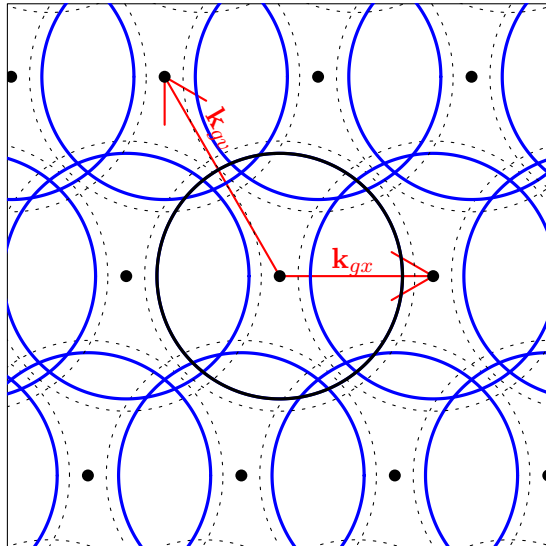


Figure 2.9: The reciprocal space map for an oblique bigrating with grating vectors \mathbf{k}_{gx} and \mathbf{k}_{gv} . The black lines represent zero-order modes, the blue lines represent diffracted modes. Lines represent grazing photon momentum states, dashed lines represent SPPs.

The coupling of light to SPPs on such a bigrating is best visualised in the k -space diagrams for SPPs on such lattices. Figure 2.9 shows an oblique lattice in k -space with $\alpha = 60^\circ$. The two grating vectors, \mathbf{k}_{gx} and \mathbf{k}_{gv} are illustrated as red arrows. The black solid circle represents the momentum of a grazing zero-order photon and so the inside of this circle contains all the possible momentum states of propagating free-space light. The momentum states of this diffracted light are shown as blue circles, centred around

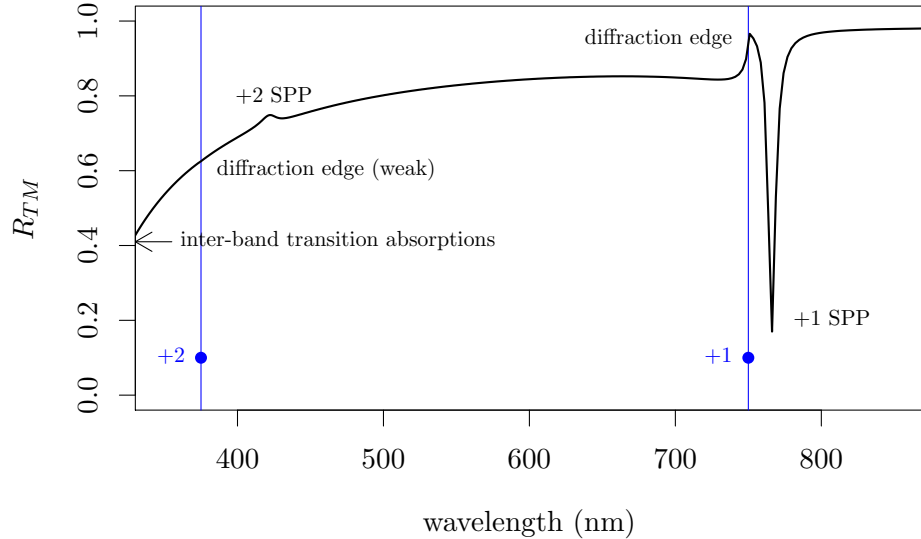


Figure 2.10: An example spectrum for a simple sinusoidal silver grating, calculated using the Chandeson method. The grating has the following parameters: $\lambda_{gx} = 750$ nm, and depth of 40 nm with a frequency dependent dielectric function for silver from literature [84]. The spectra is taken at normal incidence with the polarisation perpendicular to the grating grooves.

their respective lattice points and of equal size. The portions of blue circle which lie within the zero-order black circle represent diffracted orders which may couple out and travel away from the surface, the diffracted light. The dashed lines represent the SPP momentum states. The black dashed SPP cone cannot be coupled to by free-space light, while the diffracted SPPs (blue dashed) which lie inside the zero-order light circle may be coupled with free-space radiation. These k -space diagrams also indicate the direction of the group velocity of the surface modes, which travel away from their respective lattice points and always lie perpendicular to the SPP contour.

2.4.4 Coupling Strength of Light to SPPs on Gratings

A typical specular reflection spectrum for a metal diffraction grating is shown in figure 2.10 and demonstrates some typical features observed in the reflectivity of a grating supporting SPPs. This spectrum, produced using the Chandeson theoretical modelling method outlined in chapter 3, is for a sinusoidal grating with a pitch of $\lambda_{gx} = 750$ nm, and depth of 40 nm with a frequency dependent dielectric function for silver determined from literature [84]. The spectrum is calculated at normal incidence with the polarisation perpendicular to the grating grooves.

Features of interest in this figure are labelled on the graph. The diffraction edge, the wavelength at which the first diffracting order begins to (or ceases to) propagate is clearly shown at 750 nm as a sharp critical edge. Slightly higher in wavelength, at $\lambda_0 \approx 765$ nm, there is a sharp resonance in the reflectivity presenting as a minimum in the reflected light. This minimum is a result of the reflected light being out-of-phase with the light which is re-radiated from decaying SPPs. The incident light is scattered by the grating and, when the coupling conditions are met, resonantly excites a SPP which travels along the surface. This SPP may then decay and scatter back into reflected light. A total of two scattering processes, an excitation and subsequent decay of a SPP, give the total phase change of the re-radiated light of $90^\circ + 90^\circ + 90^\circ + 90^\circ = 360^\circ$ relative to the incident light, while the reflected light which did not interact with the SPP has accumulated a total phase change of 180° by the simple reflection from a metal surface. This results in the re-radiated light being out-of-phase with the reflected light by 180° , causing the observation of a minimum in reflection. Since no light is reflected, the energy is lost to Joule heating.

The position of the second order diffraction edge is marked on the spectrum, but is very weak. Beyond this diffraction edge, at $\lambda_0 \approx 420$ nm there is a small resonance exhibited as a region of enhanced reflectivity, a ‘bright spot’. This is the result of reflected light being in-phase with the light re-radiated from the coupling of a 2nd order SPP. The presentation of an optical interaction with a SPP as a maximum in the reflectivity is again a result of the phase difference accumulated from the scattering, coupling, and decay of light and the SPP. On a purely sinusoidal grating such as the one modelled here, multiple scattering processes are required to couple to this SPP, leading to the re-radiated light being in-phase with the non-interacting reflection. The waves constructively interfere, resulting in a maximum in the reflectivity coefficient.

The drop in the reflectivity at lower wavelengths is due to the metal’s natural absorptions due to inter-band transitions and bulk plasmon excitations. The imaginary component of the metal’s dielectric function at these wavelengths reflect these absorptions by becoming much larger. This ‘background’ absorption can be seen in all the silver grating results in this thesis.

2.4.5 Plasmonic Band Gaps

When a propagating SPP encounters a counter-propagating SPP with equal energy and equal and opposite momentum, they will constructively interfere producing SPP standing waves [35, 85]. Typically, two possible SPP standing waves can occur, with the nodes and anti-nodes of one SPP standing wave shifted $\lambda/4$ in space with respect to the other, a typical result of any quantised standing waves confined to a single value of

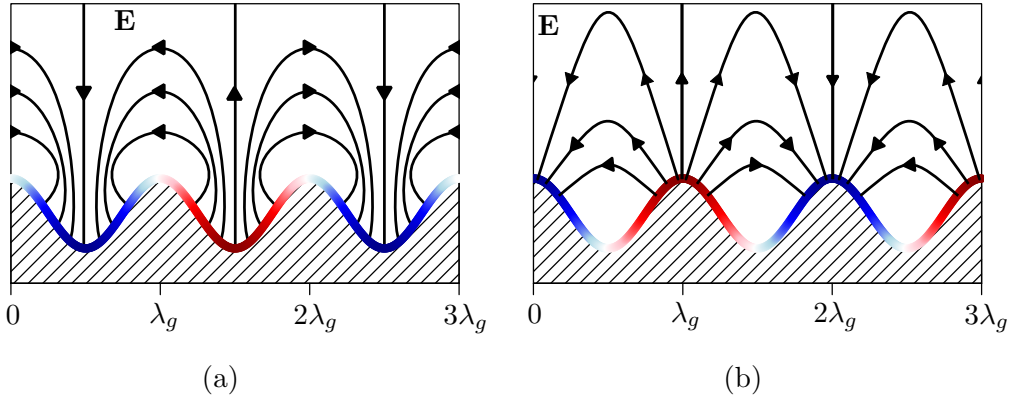


Figure 2.11: Cartoon of two possible SPP standing waves on a sinusoidal grating. The blue and red regions show accumulation of positive and negative charge density, respectively. These two standing waves, both which have a period of $2\lambda_g$, result in different field arrangements and so are associated with different energies.

momentum. This is analogous to the well known physical examples of electron standing waves formed at Brillouin Zone (BZ) boundaries, or the vibrational modes of a solid rod.

On a flat surface, these two surface standing waves of electron density and coupled electromagnetic field are indistinguishable, save for the phase difference between them. They occur at the same energy and momentum as one another. On a diffraction grating the situation is quite different. The arrangements of charge along the shaped surface can result in the electron surface charge density sitting in very different electromagnetic potentials, for example at the bottom of a grating groove or at the top, which is depicted in figure 2.11. In this case, the two possible standing waves have the same period (enforced by the periodic lattice) and so the same momentum, but will be associated with a different electromagnetic energy. Between these two energy values, SPP propagation is forbidden, due to destructive interference of the surface waves. An energy region of forbidden SPP propagation has been opened up, a plasmonic band-gap. This is shown in the extended zone scheme dispersion plot in figure 2.12(a) which shows the Bragg scattering of SPPs at the first BZ boundary (at $k_g/2$) causing the formation of a band gap.

The band gap shown in figure 2.12(a) will not be observed, as no available scattering event can diffract this region into the zero-order light cone. However, the band gap which occurs at the 2nd BZ boundary may be, as shown in the repeated zone scheme dispersion in figure 2.12(b)*. In this case, while a single $1k_g$ scattering event may bring

*In this figure, the previous band gap at $k_x = k_g/2$ has been omitted for clarity.

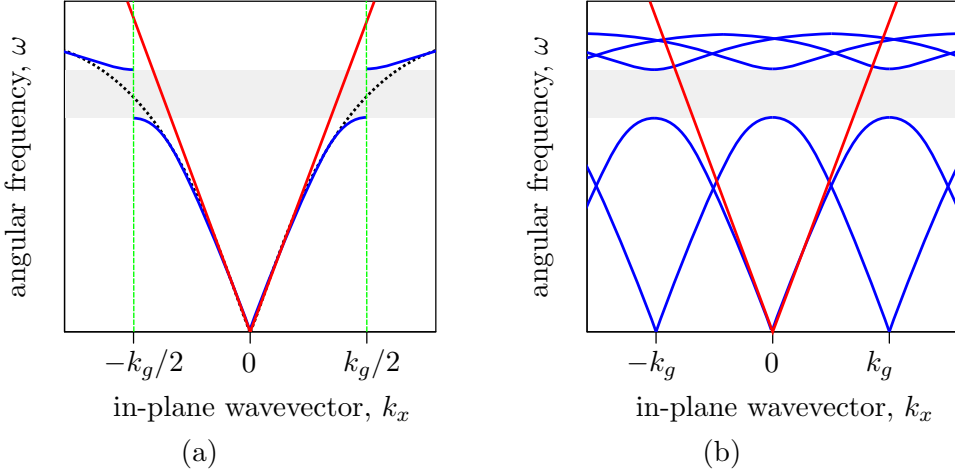


Figure 2.12: The dispersion and band gap of (a) a SPP on a grating with one Fourier Harmonic and (b) on a grating with the first two Fourier Harmonics. The red line is the light line for free space light, the blue curves show the SPP contours. In (a) the black dotted line shown the unperturbed SPP contour, and the green dotted lines show the position of the first BZ.

the band gap region into the radiative zone, the interaction which leads to band gap formation is between a zero-order and the 2^{nd} order SPP at the 2^{nd} BZ boundary ($k_x = k_g$). This means that the required scattering of the SPPs must be a $2k_g$ event for band gap formation. On purely sinusoidal gratings, which possess no $2k_g$ component in their grating profile, this scattering process is mediated by multiple scattering events, which are very weak. Since this scattering amplitude for the SPP is so weak, the interference between counter-propagating modes will also be weak, and band gaps are unlikely to be large enough to be observed. If, however, the grating profile contains a $2k_g$ component (by, for example, the addition of a secondary pitch of the grating equal to half the period of the fundamental period), the SPPs may couple together to form a standing wave via a single strong scattering event. It is the $2k_g$ component that couples the SPPs together to form the band-gap, and the $1k_g$ component that scatters this into the radiative region and so may be observed, as shown in figure 2.12(b).

Again, this is analogous to the formation of the electron band-structure of crystals, formed when considering nearly-free electrons in a periodic potential [75], or photonic band-gaps in dielectric stacks/photonic crystals [86].

A subtle difference in the definition used in this thesis, and common in the research on surface plasmons, is that a ‘plasmonic band-gap’ might only occur over a limited

range of angles, whereas for electron band structure or photonic crystals a ‘band-gap’ occurs in all possible propagation directions, and the term ‘stop-band’ is used for single-direction gaps. Here, we adopt the convention of a band-gap occurring if an energy gap exists for which SPP propagation is forbidden over a given angle range, and reserve the term ‘full plasmonic band-gap’ for forbidden SPP propagation for a range of frequencies in all directions.

2.4.5.1 Coupling Light to Band Edges

To scatter SPPs into the radiative region and also couple the two SPP modes together to form standing waves requires suitable grating harmonics in the grating profile. While the magnitude and position of the band gap is determined solely by the presence and size of these grating harmonics, the coupling of light to the SPP standing waves depends strongly on the relative phase between the grating components. We can demonstrate this simply by considering the band gap which will open at normal incidence ($\theta = 0^\circ$) for a grating described by the simple Fourier sum,

$$f(x) = A_1 \sin(k_g x) + A_2 \sin(2k_g x + \psi_2)$$

where, in our case, $A_1 = 5$ nm, $A_2 = 2$ nm, $k_g = 2\pi/\lambda_g$ where $\lambda_g = 605$ nm. $\varepsilon = -17.5 + 0.7i$. ψ_2 is the relative phase of the $2k_g$ component relative to the k_g component. Three reflectivity plots as a function of angular frequency and in-plane momentum around the band gap region are shown on the right side of figure 2.13, with each plot showing the numerically calculated reflectivity for different values of ψ_2 . The method used for calculation is the Chandezon method [87, 88], detailed later in chapter 3. For the first case, $\psi = 0^\circ$, both band edges couple strongly to light, and are shown as a minimum in the reflectivity, forming two symmetric blue bands. For $\psi = +90^\circ$, only the upper frequency (higher energy) is coupled, while for $\psi = -90^\circ$, only the lower frequency band edge is coupled.

The explanation for this phase dependent coupling is demonstrated in the figures of the grating profiles and components, also shown in figure 2.13. The lower half space of each of these sketches shows the relative phase between the two grating components, and the upper half-space shows the resultant surface profile by addition of the k_g and $2k_g$ components. Firstly, by symmetry, the nodes and anti-nodes of a SPP standing wave on such a grating will occur at *either* the peaks *or* the troughs of the $2k_g$ component. Alternating nodes and anti-nodes at these points provide a SPP standing wave which satisfies the symmetry of the grating, and also has a wave vector equal to $(k_g - (-k_g))/2 = k_g$ at normal incidence (which is half way between the $+k_g$ and $-k_g$ scattered SPPs). One SPP standing wave charge arrangement will require

2. Background Theory

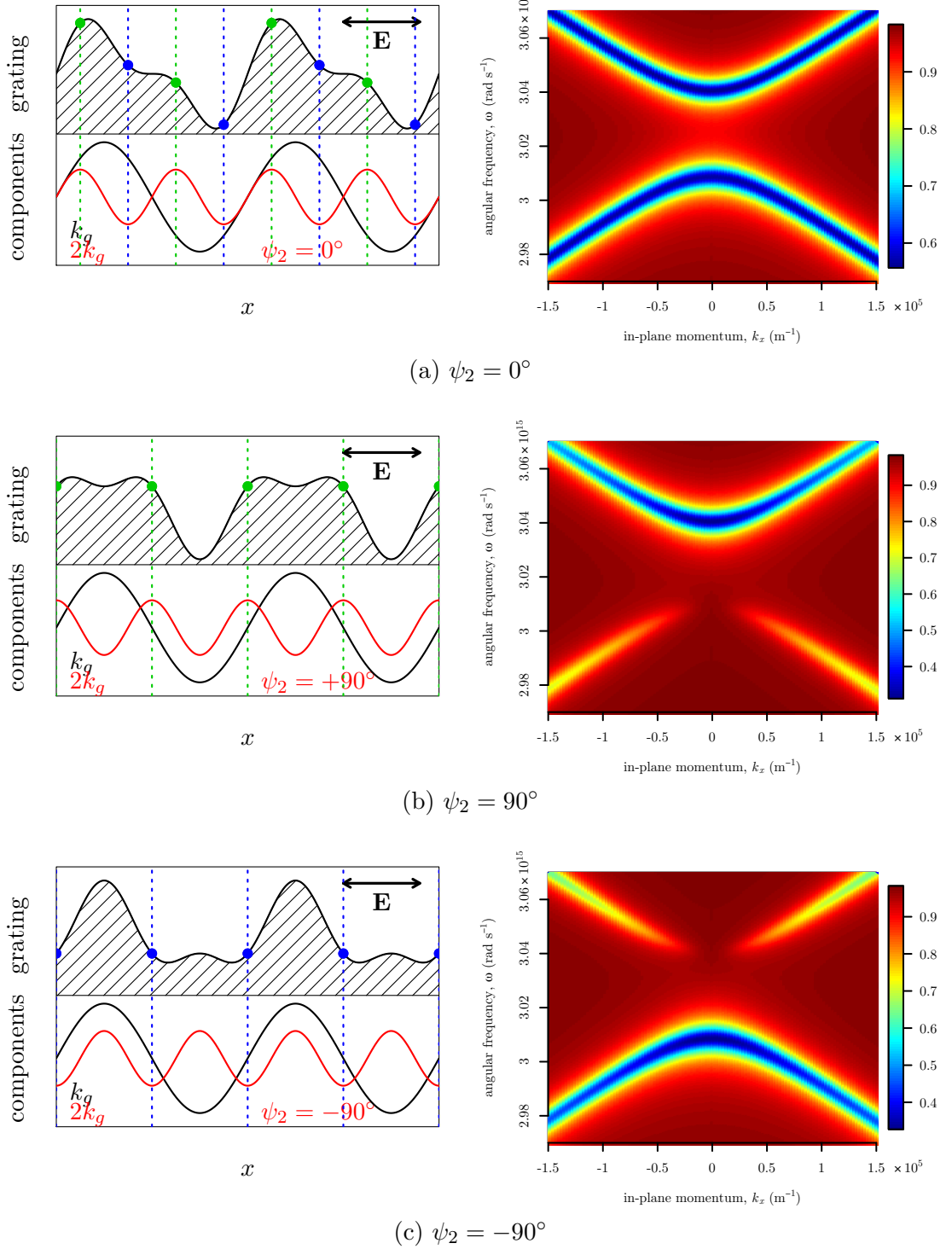


Figure 2.13: Sketches of different grating profiles determined by the relative phases of the k_g and $2k_g$ components (left), and the resulting coupling of the light to the band-edges, shown as modelled reflectivity plots (right).

induced charge at the peaks of the $2k_g$ component, while the other solution will require the charge to accumulate at the troughs.

In order for light to couple to the SPP standing waves, the electric field vector must have a component normal to the surface by which the impinging field may induce surface charge and hence couple to the surface electron density oscillations. In figure 2.13(a), the addition of the in-phase ($\psi = 0^\circ$) $2k_g$ component leads to points for both the high energy (green dots) and low energy (blue dots) nodes and anti-nodes which lie on the grating profile where the gradient of the profile is not zero. Because the grating profile at these points is not flat, there is indeed a surface normal component which can match to the impinging electric field, and the result is that both the high energy and low energy solutions may couple to incident light. In the second case in figure 2.13(b), where $\psi_2 = +90^\circ$, the resulting surface profile only has a non-zero gradient for the high energy solution (green dots), while the position of the low-energy ‘hot-spots’ (the $2k_g$ minima) occur at a flat region of the grating. Consequently, no coupling occurs for the lower-energy mode, and only the upper band is coupled, as seen in the reflectivity plot. Finally, for the $\psi_2 = -90^\circ$ case in figure 2.13(c), the resulting geometry provides a normal component of the surface to the electric field only at the blue dot locations, corresponding to an induced charge arrangement for the low-energy band. The high-energy arrangement points are located at the $2k_g$ component’s maxima, and exist on flat regions of the grating geometry. The coupling of light in this case is then only to the lower-energy mode.

2.4.6 Polarisation Conversion

Linearly polarised light incident on a grating may be converted to the orthogonal linear polarisation state in a process named ‘polarisation conversion’. Two mechanisms have been identified for this conversion using diffraction gratings; one is mediated by SPPs, and the other is due to the phase lag of the different reflected polarisation state reflections on deep gratings.

SPPs may mediate the polarisation conversion of incident light when the excited SPPs travel along the grating surface in a direction of broken symmetry [26, 34, 89, 90]. For the monograting case, this is any azimuthal angle other than $\phi = 0^\circ$ or 90° . In such an orientation, both TM and TE polarised light provide a normal component of electric field to the grating surface and so may induce surface charge and resonantly drive SPPs. Since this is the case, it is clear that SPPs decaying back into propagating light may couple back out into either the TM or TE polarisation state, and so polarisation conversion is possible. For shallow gratings, the maximum polarisation conversion occurs at an azimuthal angle of $\phi = 45^\circ$, where the coupling to SPPs with TM and TE polarised

2. Background Theory

light is equal. For shallow gratings, the polarisation converted signal is proportional to $\sin^2(2\phi)$, which is shown simply by the consideration of the electric field components relative to the grating surface [34]. For bigratings, the same considerations hold true. A SPP can mediate polarisation conversion when travelling along an axis with no mirror symmetry, and cannot otherwise. For example, at $\phi = 45^\circ$ on a square bigrating, no polarisation conversion is expected.

The second method by which diffraction gratings may exhibit polarisation conversion is again due to broken symmetry between the two orthogonal polarisation states [59]. This process is not mediated by SPPs and may occur on sub-wavelength, non-diffracting gratings providing the grooves are sufficiently deep. Consider the simple case of a non-diffracting monograting, the electric field incident on the grating surface may be considered to decompose in two directions, one parallel to the grating grooves (E_{\parallel}) and one perpendicular (E_{\perp}) to the grooves. Since E_{\parallel} does not cut across the grating grooves, this field will reflect as if it were reflected from a planar surface at a position equal to the average plane of the grating. However, since E_{\perp} cuts across the grating grooves, circulating fields may be produced in these grooves which alter the effective average plane of reflection for this field component. The difference in position of these ‘effective mirrors’ produces a phase difference between the two components which serves to rotate the plane of polarisation, leading to polarisation conversion. The maximum polarisation conversion on such gratings occurs when the phase difference between the reflected E_{\parallel} and E_{\perp} is 180° , and so is a cyclic function with respect to the depth of the grating. This necessity for the field components to be 180° out of phase requires the gratings to be reasonably deep. For a gold sinusoidal grating illuminated with $\lambda_0 = 632.8$ nm with a pitch of 300 nm the maximum polarisation converted signal occurs at a groove depth of ≈ 180 nm [59].

Chapter 3

Theoretical Methods

3.1 Introduction

The calculation of the optical response of diffraction gratings has been an active pursuit of electromagnetic research for over a century. In 1907, Lord Rayleigh proposed a treatment for the reflected light from periodic surfaces by considering them a perturbation of the case of a flat surface [7]. This theory calculated that there must be a sharp discontinuity in the reflectivity from the grating when a diffracted order of light emerges from, or disappears beneath, the grating surface. This discontinuity, first observed experimentally as a dark band by Wood [5], corresponds to the instances at which power must be redistributed to the propagating orders of light as a diffracted order either starts, or ceases, to propagate at the grating surface. However, Rayleigh's theory was inadequate for all but the shallowest gratings, as it lacked a full consideration for the fields that could occur in the grating grooves. Furthermore, Rayleigh's treatment left the bright band observed by Wood, characteristic of a SPP excitation, unexplained.

Since 1907, many methods by which to model the optical response of gratings have been developed and have been verified experimentally. Methods such as Finite Difference Time domain methods and Fourier modal-matching methods have all been tested. A review of the these, and other, numerical methods of grating analysis can be found in reference [36].

The purpose of this chapter is to provide a background to the methods used in this thesis, namely the Finite Element Method (FEM) method and the coordinate transformation method of Chandezon et al. [87].

3.2 The Differential Method of Chandezon et al.

The method of Chandezon et al. [31, 87] solves Maxwell's equations by utilising a coordinate transformation which maps the grating interfaces on to flat, parallel, planes. This avoids the Rayleigh theory's failure to account fully for field inside the grooves, as the grating is effectively flattened by the coordinate transformation and the boundary conditions are then matched across this flat interface. For a monograting the transformed coordinates are,

$$u = x \quad (3.1)$$

$$w = y \quad (3.2)$$

$$v = z - S(x) \quad (3.3)$$

Where $S(x)$ is the interface profile of the grating. The ease of matching the boundary conditions in this modified frame is achieved at a cost of the need for more complex expressions for Maxwell's equations in a non-orthogonal coordinate system of (u, v, w) . In this method, the derivation of the incident and scattered fields from Maxwell's equations are expressed as an infinite series of plane waves, a Fourier expansion.

In order to solve this problem numerically, the infinite Fourier series must be truncated, placing a limit on the number of scattered field components in the model. The order of truncation is chosen from a compromise between obtaining suitable convergence of the solution and minimising computation time. In this thesis, we primarily use Chandezon method modelling to provide illustrative examples of reflectivity by which we may explain certain observed optical features. For this purpose, we find that limiting the number of scattered fields in the system to 6 is sufficient.

The one-dimensional case was presented by Chandezon in 1980 [87]. Since then, it has been extended to multi-layered gratings [91, 92] and to bigratings [93]. The method used in the thesis is the multi-layer bigrating method reported by Harris et al.[93]. This allows for two crossed gratings of different pitches to be considered, and the coordinate transformation is altered from the equations 3.1, 3.2 and 3.3 to,

$$u = x \quad (3.4)$$

$$w = y' = x \cos \alpha + y \sin \alpha \quad (3.5)$$

$$v = z - S(x, y') \quad (3.6)$$

Where α is the angle between the two crossed gratings. This interface profile $S(x, y')$ is represented by a Fourier sum. Because the technique is a differential method, sharp discontinuities in the surface profile gradient are difficult to model. The number of

Fourier components required to correctly simulate a step-like grating profile can become prohibitively large, although extensions to the method have shown than the method can be applied well to trapezium shaped grooves [94]. For a precise description of a lamellar grating as produced by our fabrication techniques a large number of Fourier harmonics are required to represent $S(x, y')$, which can make computation times prohibitively long. However for the grating periodicities used in this thesis only the dominant scattering associated with low order Fourier components need be considered to gain sufficient insight into the underlying physical processes.

The Chandezon method has been used successfully to probe the electromagnetic response of hexagonal bigratings [44], the effect of groove shape on reflectivity resonances due to SPP excitations [33, 42], to examine asymmetric excitation of SPPs on blazed gratings [95] and to determine the surface profile of gratings from experimentally acquired reflectivity measurements [43].

3.3 The Finite Element Method

The finite element method (FEM) for predicting the electromagnetic response of systems is a numerical modelling process that subdivides a system into discrete elements, solving Maxwell's equations for each element and ensuring the solutions are consistent across each elementary boundary [36, 96]. Broadly, the process iteratively applies three steps until a solution is found:

1. Determining the distribution and size of elements across the model. The continuous array of elements is referred to as the ‘mesh’ of the model.
2. Numerically solving Maxwell's equations for each element and for the mesh as a whole.
3. The evaluation of the quality of the solution, to see if the model converges to a consistent and physically accurate solution. If not, the process repeats from (1), further refining the mesh.

The software package used for FEM modelling in this thesis is the HFSS package from Ansys, Inc. [97]. The software includes a computer aided design component, which allows the building of three-dimensional models to represent the sample under consideration. These 3D models may be assigned different optical parameters, such as frequency-dependent permittivities and permeabilities, and may be parametrised for automated parametric alterations. The software’s default element shape is a tetrahedron, with many tetrahedra forming a conformal mesh in the problem domain. In the case of 3D models which contain curved surfaces, the software may also use curvilinear

tetrahedral elements, greatly reducing the number of elements required to approximate a curved surface.

3.3.1 Solving Maxwell's Equations in the Mesh

The FEM package attempts to solve for the electric field [98], \mathbf{E} , for each element using the wave equation,

$$\nabla \times \left(\frac{1}{\mu} \nabla \times \mathbf{E} \right) - k_0^2 \varepsilon \mathbf{E} = 0 \quad (3.7)$$

where k_0 is the free space wavenumber and ε and μ are the relative permittivity and relative permeability, respectively. As a numerical simulation, the software attempts to minimise the left hand side of equation 3.7 to be as close to zero as possible for each element, it will not in general, equal exactly zero. The magnetic field, \mathbf{H} is then calculated using,

$$\mathbf{H} = \frac{1}{\omega \mu} \nabla \times \mathbf{E} \quad (3.8)$$

where ω is the angular frequency of the wave. The values for \mathbf{E} and \mathbf{H} must be found for all the elements forming the conformal mesh in the problem space, and must be consistent across each tetrahedron boundary. This leads to thousands of simultaneous equations in the form of equation 3.7 for each finite element in the model, which are combined into a matrix and solved for \mathbf{E} numerically.

Once the fields have been determined, a generalised scattering matrix (S-Matrix) is derived for the system, from which initial and final optical properties such as reflectivity or transmission can be extracted. The software may also attempt to find the frequencies at which the poles of the S-Matrix occur, and so calculate the eigenmodes of the system and their associated fields.

3.3.2 Adaptive Meshing

The structure of the mesh used in the FEM model is critical to obtaining an accurate simulation. In general, a higher resolution of mesh is required in areas where the electric (and magnetic) field vary rapidly. To achieve a suitable mesh, the FEM package uses a process of adaptive meshing, refining the mesh in areas where the error in the electric field calculation are high.

In the process, the software generates an initial, geometrically conformal mesh, and solves equation 3.7 for the electric field for each of the tetrahedra. Based on this initial solution, the area of the problem domain where the exact solution has a large amount of error is determined [98]. This is done by examining the residuals of equation 3.7,

such that the approximate solution, \mathbf{E}_{approx} gives,

$$\nabla \times \left(\frac{1}{\mu} \nabla \times \mathbf{E}_{approx} \right) - k_0^2 \varepsilon \mathbf{E}_{approx} = residual \quad (3.9)$$

for each tetrahedron. A set percentage of tetrahedra with the largest residuals are then refined by sub-dividing the element into even smaller tetrahedra. Another solution is then found with this new mesh, and the process is repeated until the convergence criteria has been met, or the total number of adaptive passes, set by the user to prevent overly complex and memory intensive meshes, has been met.

It is important to note that the simple addition of elements to the problem is inefficient, and that the software's determination of the refinement areas by consideration of highest tetrahedral residuals is not foolproof. Occasionally, the software may attempt to refine the mesh in locations that are not critical, but do lie in the upper percentile of tetrahedral locations with high residuals. Users can make the simulation more efficient by defining the initial mesh conditions using mesh operations in the software. For example, someone setting up a simulation for plasmonic resonances in thin cavities may start the initial mesh with a greater density of elements in the grooves (where they expect rapidly varying fields) than the software alone might allocate.

3.3.3 Solution Evaluation and Convergence

The accuracy of the solution is determined by the model's 'convergence'. Because of the direct relationship between the electric fields for a solution and the corresponding S-Matrix, the convergence is measured by the change in the magnitude of two successive solutions and is called the ΔS value. It is a measure of the change in electric field distribution between solutions. When the ΔS values becomes less than a user-specified amount, the model is deemed to be 'converged' and the final solution is obtained. An example of mesh refinement is shown in figure 3.1. Here, we find that the refinement algorithm adds more elements to the mesh, to a total of over 40,000 in the final case, in order to reduce the ΔS value (red line) and achieve convergence. This particular example is the convergence for a zigzag grating model, the results of which are detailed in chapter 7. For the results in this thesis, the maximum ΔS value used was 2%.

3.3.4 Model Boundary Conditions

In the FEM package, the modelled system must be surrounded by appropriate boundary conditions so a solution can be determined. Diffraction gratings in this thesis are approximated to infinite periodic structures, as the propagation lengths of SPPs is far smaller than the sample size. Thus, a unit cell of the structure with appropriate

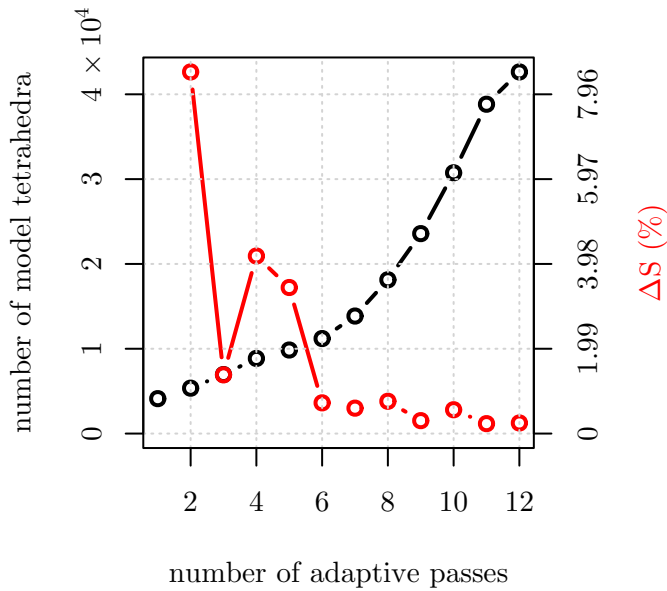


Figure 3.1: A graph showing the convergence of a typical FEM model as a function of adaptive passes. The black line shows the total number of elements introduced in the model, while the red line shows the ΔS parameter as a percentage.

boundary conditions is suitable for a full solution to the problem, an example being shown in figure 3.2. This unit cell is surrounded by 4 types of boundary, labelled in the figure. The first type is called a master-slave boundary. This boundary pair constrains the electric and magnetic field so that fields at the master boundary must match exactly the field at the slave boundary. The periodic boundary conditions imposed by the master-slave pair ensure that the solution is exactly equivalent to an infinite array of unit cells. The slave boundary may also replicate the fields at the master with an additional relative phase delay. This phase delay is how the software calculates the fields for an angle of incidence other than normal with the phase delay calculated internally from the provided polar and azimuthal angles. The next type of boundary is the ‘Perfect E’ boundary. This boundary acts as a perfect lossless conductor. It is placed on the bottom of the metal film, and acts as an easy way to double the thickness of the metal film by reflecting perfectly any impinging radiation. Since the field penetration for visible radiation in to a metal such as silver is very small (on the order of 20 nm), a metal film thickness of 50 nm, used together with the Perfect E boundary, provides a suitable approximation to a semi-infinite metal substrate without the additional cost of increasing the number of tetrahedra. The final boundary is a Floquet port. This acts

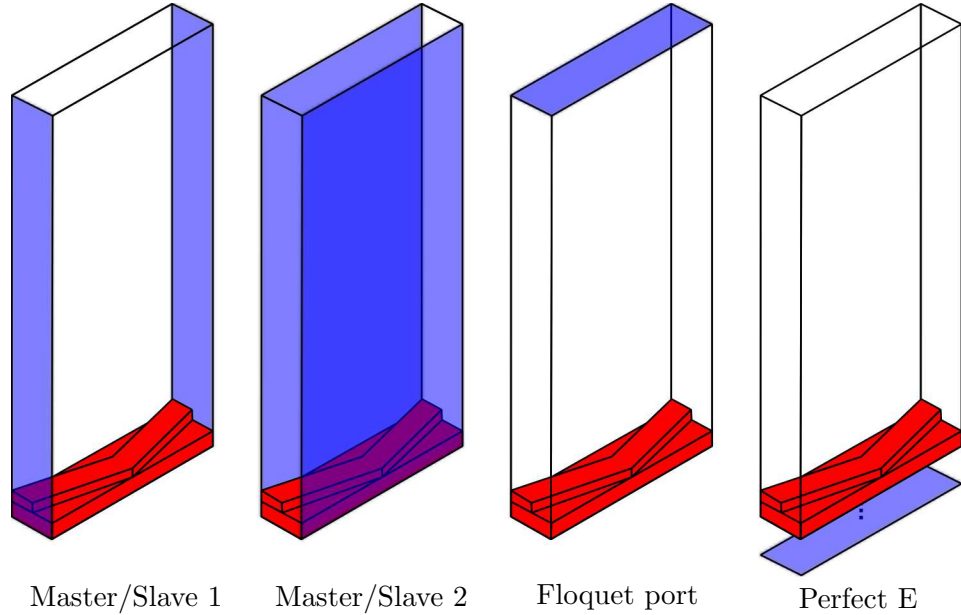


Figure 3.2: Schematic of the different boundaries used in the FEM model. The unit cell shown is a zigzag grating (chapter 7) in red. The boundaries are highlighted and named in each case. The Perfect E boundary has been extruded from the bottom of the model for clarity.

as a radiation boundary that is open to free-space. The FEM package actually absorbs any radiation that hits this boundary, without reflection, mimicking the character of radiation escaping to free-space. This Floquet port also acts as an excitation source and a way by which certain orders of diffracted field are extracted, which is covered in the next subsection.

3.3.5 Floquet Type Excitation

When extracting the reflectivity of a diffracting sample from the S-Matrix, it becomes clear that simply examining the total field arriving above the sample does not correspond meaningfully to the types of experiments typically conducted in this thesis. This is because the modelled fields would contain the zero-order reflection and all the diffracted orders simultaneously, while experimentally we would only usually collect light from the zero-order reflected beam. Floquet analysis allows us to extract the appropriate order of diffracted light by recognising that the reflected light will be a superposition of all these possible fields, whose in-plane momentum will be totally defined by the polar angle of incidence and the diffracting periodicities. The wavevectors of waves arriving

3. Theoretical Methods

above and at a plane parallel to the sample surface will be of the form,

$$\mathbf{k}_{\parallel} = \mathbf{k}_0 \sin \theta + n\mathbf{k}_{gx} + m\mathbf{k}_{gv} \quad (3.10)$$

Where \mathbf{k}_{\parallel} is the parallel wavevector, \mathbf{k}_0 is the free-space wavevector. \mathbf{k}_{gx} and \mathbf{k}_{gv} are the grating wavevectors in the x and v directions, defined as $\mathbf{k}_{gx} = 2\pi\hat{\mathbf{x}}/\lambda_x$ and $\mathbf{k}_{gv} = 2\pi\hat{\mathbf{v}}/\lambda_x$. Depending on the diffracted order, they have the integer multiples n and m , so, for example, the first-order diffracted field in the x direction would be $n = 1$ and $m = 0$.

Diffracted waves reflected from, or transmitted through, a sample must have well defined periods parallel to the surface and are determined by the diffracted orders, such that,

$$\mathbf{E}_{n,m}(\mathbf{k}_0) = \mathbf{E}_{n,m}(\mathbf{k}_0 + n\mathbf{k}_{gx} + m\mathbf{k}_{gv}) \quad (3.11)$$

Where $\mathbf{E}_{n,m}$ is the $(n,m)^{th}$ electric field diffracted order.

The FEM package calculates all the possible propagating orders, based simply on the periodicity of the surface and the wavelength of the incident field, and is then able to extract from the S-Matrix each field solution corresponding to each order. Because the periods of the fields in the simulation are now restricted, if there are strong effects from evanescent, non-propagating orders, (such as trapped SPPs) these must be included as well. The calculation of which ‘Floquet modes’ to include is undertaken at a single frequency, so it is important to calculate these using the highest frequency that is to be simulated, to include all possible diffracted orders. The choice of the number of Floquet modes to include is the equivalent of determining how many Fourier components of light or of a surface to include for an accurate result, much like in the Chandezon case.

Chapter 4

Experimental Methodology

This chapter details the experimental methods used in this work for the fabrication and measurement of metallic diffraction gratings supporting SPPs. Section 4.1 describes the fabrication method for the gratings, a combination of electron beam lithography (EBL) and template stripping. The second section explains the established methods by which the reflectivity of gratings was measured as functions of both wavelength and angle. Finally, section 4.3 introduces a new experimental method for the mapping of SPP iso-frequency contours in momentum space, which was developed as part of this work and has not been reported previously in the literature.

4.1 Sample Fabrication

The production of diffraction gratings used in this thesis has been achieved using a combination of electron beam lithography and template stripping. Briefly, this process involves the exposure of resist to a diffraction grating pattern using a focussed electron beam. This resist, when developed, is used as an etching mask for the silicon substrate, producing a master template in a silicon ‘chip’. This chip is then metallised and the pattern is transferred to a glass substrate by gluing the metal surface to the glass substrate and removing the master with a razor blade. This leaves an inverse copy of the master grating on the glass substrate, and the silicon master may be reused to produce further copies.

An outline of the process is shown in figure 4.1. The details of the process are explained in depth in the following sections.

4.1.1 Electron Beam Lithography

All electron beam lithography steps are performed in an ISO class 6 cleanroom. This minimises the risk of small particle contamination and unwanted organic residues being

4. Experimental Methodology

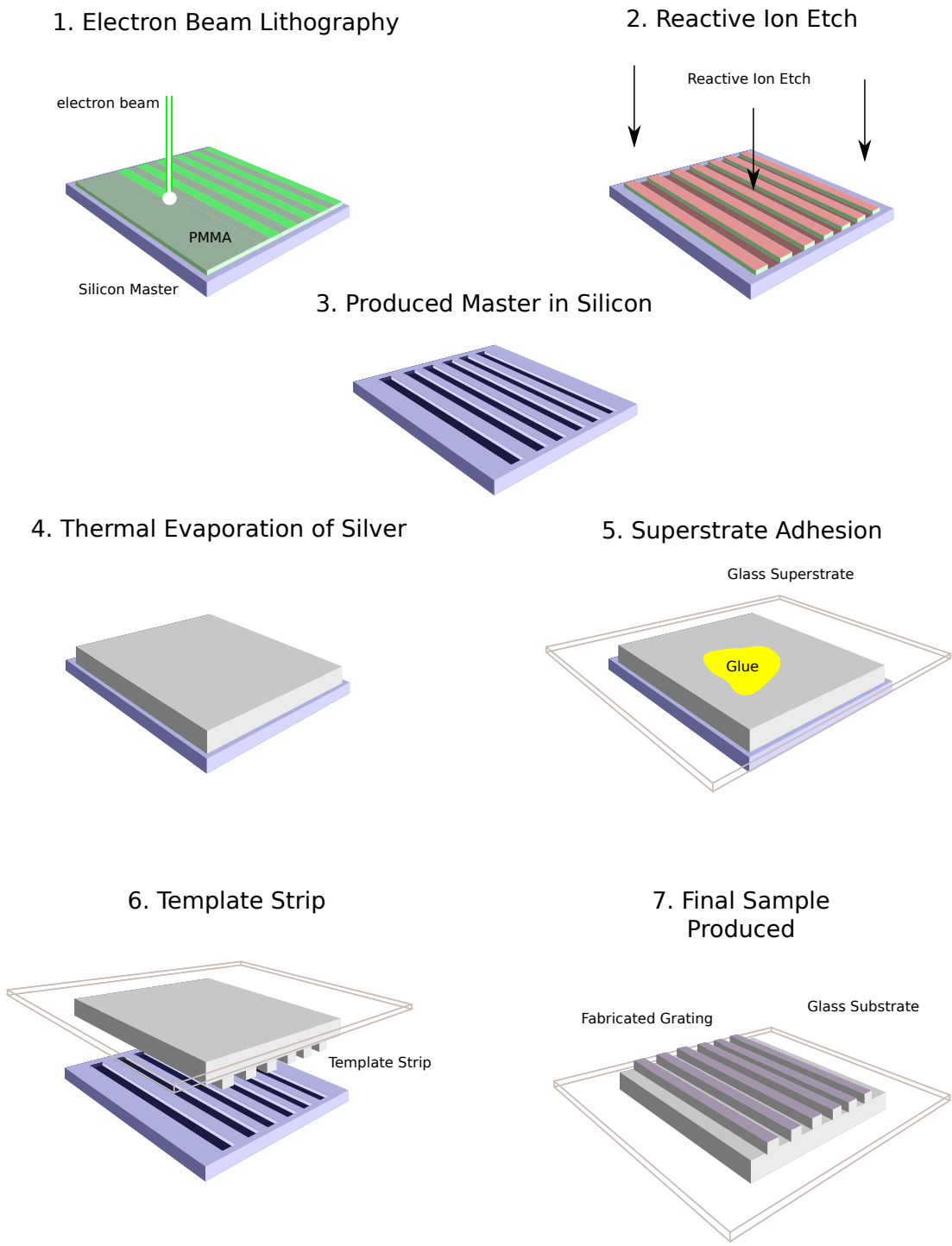


Figure 4.1: Illustration of the fabrication method used for the production of diffraction gratings.

4. Experimental Methodology

introduced to the samples.

A silicon wafer is prepared as a master substrate. Any large-particle dust is removed from the wafer surface using pressurised nitrogen gas. The wafer surface is then spin-coated in a $\approx 600\text{ nm}$ thick protective layer of Poly(methyl methacrylate) (PMMA). The typical protective polymer used was PMMA 950K A6, spun at 2000 RPM for 40 seconds to produce the 600 nm layer. The wafer was then diced into 1 mm^2 chips which would be used as the grating master substrates. The resist layer protects the chip surface from the silicon dust that the dicing process produces. This layer, and the accompanying contamination, is removed by inverting the chips in 100 ml of warm acetone for 10 minutes. After removing the protective resist, the chips are placed into a fresh solution of boiling acetone (80°C) for 1 hour, and then sonicated in 100 ml of isopropanol for 1 hour. The substrates may occasionally splinter during sonication, (introducing unwanted Si dust to the solution), these chips are discarded. After 1 hour of sonication the chips are removed from the isopropanol and dried using pressurised nitrogen gas. The clean wafer chips are then inspected under dark-field optical microscopy to ensure the surface is optically clean. If not, the cleaning process is repeated.

The electron resist is then added to the surface. The resist used in all grating fabrications included here is PMMA 950K A4. This is a positive electron-resist, whereby exposure of the resist to the electron beam causes de-cross-linking of the polymer chain, allowing the removal of the exposed resist with developer. The chip is placed in a motorised spincoater, and 3-4 drops of PMMA are introduced to the surface using a new, clean glass pipette. The chip plus resist is then spun at 4500 RPM for 40 seconds to leave a 180 nm thick layer of resist on the surface [99]. The substrate is then baked at 165°C for 10 minutes on a hot-plate. This baking raises the resist temperature above the glass transition temperature, and also causes the evaporation of any remaining solvent (Anisole), improving substrate adhesion.

The substrate is then loaded into the electron beam lithography system and the grating pattern is exposed. The system used is a nB4 Electron Beam Lithography system (NanoBeam Limited [100]) and exposures are performed with a beam current of 2 nA and a beam accelerating voltage of 80 keV. The exposure dose ranged between $400 - 600\text{ }\mu\text{C cm}^{-2}$, depending on the grating. Initially, the grating pattern was exposed four times at different locations on one substrate, each grating using a different test dose. The final samples produced from these test areas are examined using scanning electron microscopy and the grating's electromagnetic response is measured using the optical techniques listed in section 4.2, in order to determine the most suitable electron dose to use for each particular grating. Once a suitable dose has been determined, future gratings are produced with one grating per chip.

The electron beam write field size, (the region exposed before the substrate needs to

4. Experimental Methodology

be moved) was 100 μm , to minimise the effect of height variation across the substrate. This is the maximum write field available in the system used. The nB4 electron beam system has a theoretical beam diameter of 2.3 nm at 100 keV, and the stitching error between write-fields is on the order of 20 nm. This stitching error introduces an extremely weak long-pitch periodicity to the samples, on the order of the write field size. The weak diffractive properties from these stitching errors are not found to inhibit the optical efficiencies of the gratings significantly, and are not observed experimentally.

The exposed sample then requires development to remove the de-cross-linked polymer and provide a polymer etching mask for the Si. The developer used is a 15:5:1 solution of IPA:Methyl isobutyl ketone:Methyl ethyl ketone (IPA:MIBK:MEK) [101]. An endothermic reaction occurs when this solution is first mixed, so to ensure development times remain consistent between processes the developer must be allowed to return to room temperature before use. The exposed chip is submerged in the solution for 1 minute, followed immediately by a further 1 minute in a beaker of IPA. When transferring the sample between the developer and the IPA, it is advisable to maintain a small amount of the developer in a droplet on the sample surface, to prevent premature exposure to the air. After the 1 minute in IPA, the sample is removed and blow-dried with nitrogen gas. At this point the diffraction properties of the sample will be apparent, and illumination with an appropriate wavelength laser allows an estimation/check of the grating's periodicity and orientation.

At this stage, the grating pattern has been transferred to the resist and successfully developed. The sample consists of a coating of un-exposed PMMA layer, in which a 180 nm deep pattern has been developed. This polymer grating sits on a Si substrate. The pattern is now transferred to the Si chip by means of reactive ion etching (RIE), using the PMMA as a polymer mask. The reactive ion etching gas used is an oxygen, CHF₃ mix, with the following parameters: 100 sccm* CHF₃, 3 sccm O₂, at 38 mTorr of pressure and 100 W power. This gives an etch rate into the Si of approximately 29 nm min⁻¹. The selectivity of Si to PMMA etching is sufficient for a 180 nm thick layer of PMMA to be a suitable etching mask for depths of up to 80 nm etched into the Si substrate. After RIE, any excess resist is removed by boiling the sample in acetone and sonication in IPA. This leaves a master grating pattern in a Si substrate.

For ‘crossed’ bigratings, where a second periodicity runs along the grating surface at an angle to the first periodicity, this process is repeated with a previously fabricated Si master grating used in place of the flat Si substrate. This double exposure method was preferred as the result is a grating where the two amplitudes have been summed, which is consistent with the theoretical modelling undertaken with the method of Chandezon

*standard cubic centimetre per minute

introduced in chapter 3.

4.1.2 Thermal Evaporation

To produce metallic diffraction gratings from the Si master, the master substrate is first metallised using thermally evaporated silver under high vacuum.

The clean template is placed in a vacuum chamber facing a molybdenum boat containing 99.999% pure silver. The pressure in the vacuum chamber is reduced to 5×10^{-6} mbar by use of both a rotary pump (down to 1×10^{-2} mbar) and a water-cooled turbo pump. At this low pressure, current is passed through the boat, which heats, via Joule heating, to a temperature sufficient for the silver to evaporate, with the silver vapour then condensing on to the structure. The rate at which the silver evaporates is controlled by the current passing through the molybdenum boat. A typical driving voltage of 70 V produces a deposition rate of approximately 3 \AA s^{-1} . The rate of deposition and the nominal thickness is measured using a quartz crystal thickness monitor.

The depth of the features for a grating produced by template stripping (described in the next section) is pre-determined by the silicon master's depth that was etched via RIE. The amount of silver deposited on the master must then be greater than the depth of the structures to ensure the sample is optically thick. It is found that for the nominal depths of grating produced (ranging from 30 nm to 80 nm), a 300 nm thick layer of silver was sufficient to ensure good pattern transfer and optically thick samples, without producing unwanted silver film tension that may cause the silver to flake as the layer relaxes during cooling.

4.1.3 Template Stripping

The method for transferring the master pattern to a glass substrate is based on the method of Nagpal et al [102, 103]. A glass substrate is prepared by first swabbing the surface with an acetone soaked cotton bud to remove any organic residue. The surface is then drag-cleaned using lens tissue and IPA, removing any larger dust/cotton particles before being examined under an optical microscope.

The metallised Si template is then positioned on a flat, clean surface and a small amount of UV optical adhesive (Norland 60 or 65) is introduced to the metallised patterned area using a micro-pipette tip. Great care must be taken to ensure no air-bubbles are present in this adhesive polymer, so it is advisable to de-gas the glue first by agitation in a UV free environment. The clean glass substrate is then placed gently on the master and the glue is allowed to spread across the interface*. Without

*If too much adhesive has been added, the glue may reach areas of the Si chip which are not

4. Experimental Methodology

moving the sample, the adhesive is cured under incoherent UV light provided by a mercury lamp. The polymer is cured for a total of 20 minutes under this light*.

After curing, the sample is turned over and a clean, sharp razor blade is inserted between the glass (now the substrate) and Si chip (now the superstrate). With a small amount of force, the master Si chip will be pried free and removed from the glass, leaving behind the silver metal and, in it, the inverse metallic pattern. Once the Si chip is freed from the glass/silver surface, the razor blade should be supplanted with soft-tipped tweezers and the chip removed carefully, so as not to scratch or damage the fragile silver surface.

Since silver degrades in the laboratory environment due to sulphur present in air, this last step can be delayed until the sample is to be used. Until this point, the grating pattern remains embedded in the Si/Silver interface, protected from the air and any other possible contaminants.

Comparison between the master and sample SEMs shows less than 2% difference between their mark-to-space ratios, indicating the high precision of copies taken from the silicon master. The small difference may be attributed to the thermal relaxation of the silver.

4.1.4 Polymer Replication

The embedding of gratings in a glass-like material can be desirable if the experimenter wishes to access modes that may be lowered in energy in to the visible regime by use of a higher refractive index. This is the case for a sample in chapter 7, and so the details of embedding the grating in a high index material is covered briefly here. The Si master of the grating, prepared via EBL, and RIE, is coated with a UV curable polymer and a thin, flexible polymer sheet (acetate sheet). This combined polymer sheet and glue is placed under pressure and cured rapidly using a high intensity UV source. The polymer replica is then peeled off the master, and coated with a second UV curable polymer (Norland 63). A clean glass slide is placed on top of this arrangement, and the glue is cured, again by a UV light source. The polymer-master is peeled off the glass substrate, leaving a polymer-replica on the glass substrate. This is then metallised via thermal evaporation with a thickness of 300 nm of silver, and the bare side of the glass substrate is adhered to a hemi-spherical prism using index matching fluid. The resulting sample is illuminated through the prism/index matching fluid/glass/grating side, allowing for metallised. In this case the template strip will be unsuccessful, and the process must be abandoned at this point. The glass substrate is removed with great care and the master cleaned carefully by submerging it in Acetone and then IPA.

*It is useful to include the pipette under the UV light also, as the residual glue present provides a secondary check that the polymer is fully cured before attempting the template strip.

the investigation of a grating sample embedded in a high index of $n = 1.52$.

4.2 Angle Scans

4.2.1 Monochromator

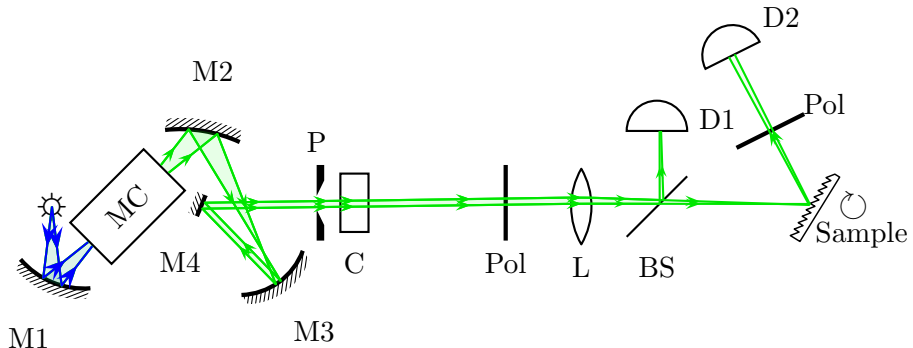


Figure 4.2: System for the measurement of the reflectivity of a sample as a function of both wavelength, λ_0 and polar angle θ . White light is represented as blue lines, pseudo-monochromatic light is shown as green lines.

To record the optical response of the diffraction gratings as a function of both incident wavelength, λ_0 , and polar angle, θ , a conventional rotational stage/monochromator system is used. A schematic of the equipment is shown in figure 4.2. The incident wavelength is selected by directing a white light source through the monochromator via the focussing mirror, M1. Using an internal metallic diffraction grating and an output slit, the monochromator outputs a beam of almost monochromatic light with a spectral width of $\lambda_0 \pm 0.25$ nm, with a selectable wavelength range between $400 \text{ nm} < \lambda_0 < 850 \text{ nm}$. This light is then collimated by a pair of mirrors, labelled M2 and M3 in figure 4.2, and directed down the primary optical axis by a plane mirror located at M4. The light is then spatially filtered by a 0.5 mm pinhole (P) and passed through an optical chopper (C) operating at approximately 1.3 kHz. The chopper's operating frequency is passed to a pair of phase-sensitive detectors and is used as the triggering frequency for the signals obtained from the detectors (D1 and D2) that are photomultiplier tubes. The beam is then passed through a linear polariser (Pol) with which the polarisation dependence of the optical response may be investigated.

For small-area samples, such as diffraction gratings fabricated using EBL, the grating area may be as small as 2 mm^2 . In order to ensure the entire optical field impinges the grating, and not the surrounding material, the beam is focussed with a lens, L, with a focal length of 0.5 m. The distance between the pinhole, P, and the lens, L, is approximately 1 m, approximating to a collimated far-field image with a radius of

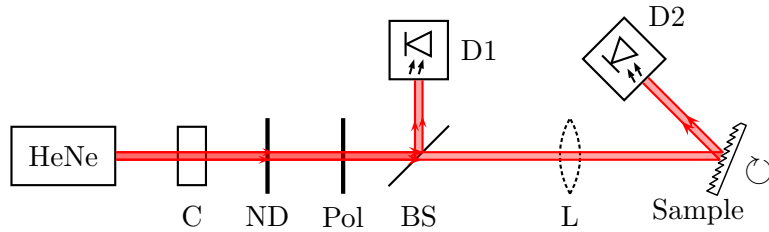


Figure 4.3: System for the measurement of angular dependant reflectivity at a set wavelength of $\lambda_0 = 632.8 \text{ nm}$

0.5 mm, which is reproduced at the lens's focal point. For smaller beam-spot areas, a smaller pinhole may be used, at the cost of light intensity.

A small fraction of the light is directed to a reference detector, D1 via a plane-glass beam splitter, BS. This reference signal allows for the normalization of the time-dependence of the white-light source intensity. The transmitted beam continues along the primary optical axis and hits the sample positioned precisely on a robotic rotational stage, such that the sample position is central to the rotational axis and also at the focal position of lens L. The robotic table, controlled via computer, sets the polar angle, θ of the sample, with the spectral reflectivity detector, D2, mounted so that it moves a corresponding angle of 2θ .

The spectrally reflected light is collected by the detector D2 after passing through a second linear polariser. Both detectors, D1 and D2, are photomultipler tubes whose output current varies linearly with incident light intensity. The signals from the detectors are passed to a set of phase sensitive detectors which, together with the chopper triggering signal, extract the reference and reflectivity measurement and pass the information to the computerised recording software via an analogue interface card.

To obtain a reflectivity spectrum of a sample, the output voltages from both the reference and reflection PSDs are recorded as a function of both angle and wavelength. To normalise the resulting dataset, the sample is removed and the light directed into the reflectivity detector at $\theta = 0^\circ$. The spectra of this 'straight-through' reference signal is recorded, and then the original dataset is divided by the reference spectra, obtaining the normalised reflection spectrum of the sample as a function of both wavelength and polar angle.

4.2.2 Fixed Wavelength Scans

A similar set-up is used for acquiring angle dependent reflectivity of samples at a single wavelength. In this set-up, shown in figure 4.3, a HeNe laser ($\lambda_0 = 632.8 \text{ nm}$) is passed through an optical chopper, C, a neutral density filter, ND, and a polariser before a

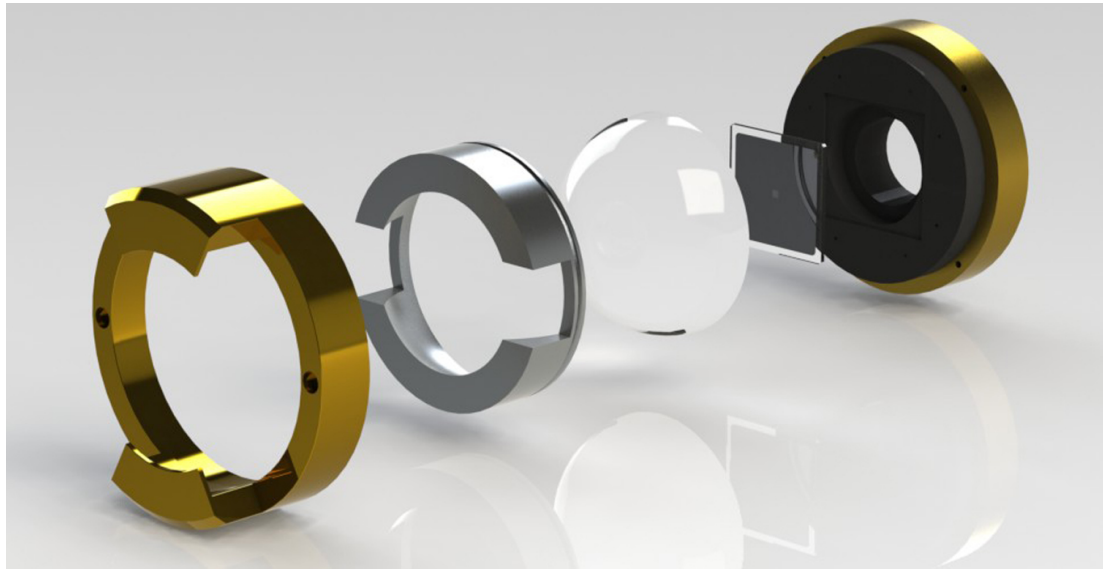


Figure 4.4: Exploded view of the sample mount for use with a glass hemisphere. The hemisphere is adhered to the glass substrate using index matching fluid. The rig allows azimuthal rotation of the sample and hemisphere.

beamsplitter (BS) directs a small fraction of the beam to a reference detector. The beam transmitted through the beam splitter continues along the optical axis and is passed through an optional lens before impinging on the sample placed, again, at the center of rotation of a robotic table. The detectors used are photo-diodes, whose voltage output is linearly dependent on the incident intensity. The signal from the detectors are passed to a set of phase sensitive detectors, and the signal extracted, as before, using the mechanical chopper as a triggering reference.

4.2.3 Embedded Samples

Some samples presented in this thesis are investigated with the grating embedded in a high-index substrate. For such samples, a glass hemisphere arrangement is used (Figure 4.4). This allows illumination of the sample without the need for any corrections to the polar angle which might otherwise be necessary because of refraction. The sample is affixed to the hemisphere using index-matching fluid.

4.3 Iso-Frequency Contour Measurement Using Scatterometry

A desirable measurement of the dispersion of SPPs on diffraction gratings is to record the mode's iso-frequency contours in reciprocal space. By mapping the position of

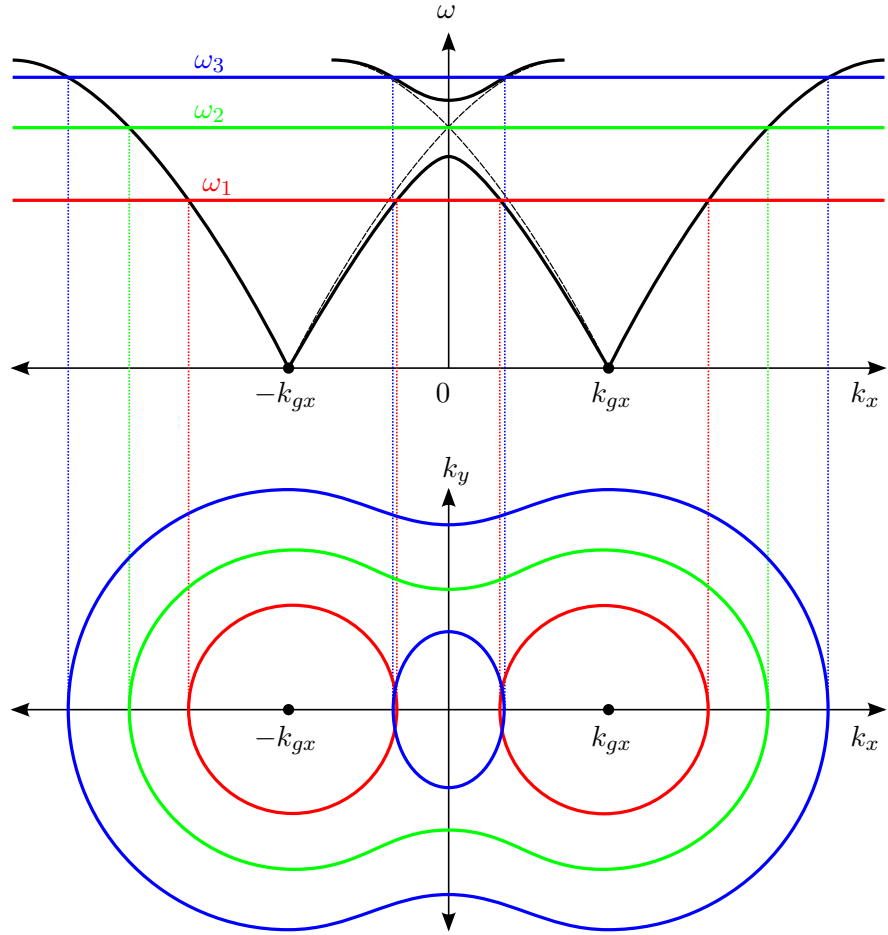


Figure 4.5: Three iso-frequency contours for the intersection of two SPP cones at angular frequencies ω_1, ω_2 and ω_3 . The contours show how the band-gap presents in k -space for the cases of a frequency lower than the band-gap (ω_1), inside the band-gap (ω_2) and above the band-gap (ω_3).

the SPP contours in k -space, information is obtained about the 2D plasmonic crystal lattice and the interaction of scattered SPP modes on the surface. These iso-frequency contours are obtained as ‘slices’ through the 3D dispersion plot (ω, \mathbf{k}) of the SPPs on a grating for a constant frequency, and so are often referred to as equi-energy contours. Examples of such iso-frequency contours are shown in figure 4.5. The upper figure shows the intersection of two SPP dispersion cones (black lines), one scattered by $+k_{gx}$ and the other by $-k_{gx}$, plotted in the $\omega - k_x$ plane. At $k_x = 0$ these two SPP dispersion curves meet and form a band gap, as shown in the figure. The dotted black line shows how the SPP dispersion would have continued with no interaction. Three slices of iso-frequency are shown, ω_1, ω_2 and ω_3 , each chosen to illustrate a different SPP contour

4. Experimental Methodology

type. The corresponding SPP contours in k -space are shown in the lower figure. The frequency ω_1 is below the plasmonic band-gap in the dispersion, and the SPP cones trace two distinct, approximately circular, contours in k -space. For ω_2 , the energy slice is taken in the band-gap and the resulting SPP contours have ‘merged’, with no SPP solution along the $k_y = 0$ line around the intersection. Finally, ω_3 shows an intersection of the dispersion cones above the band-gap. This results in two contours, one a larger merged ‘peanut’-shaped contour and a smaller SPP contour based around $k_x = k_y = 0$. These SPP contours are analogous to iso-frequency Fermi-surfaces found in solid state physics. This simplified figure is not periodic as it only includes two scattered SPP cones for clarity, but the features observed for each energy slice will be similar in all cases of SPP contour measurement. These contours show the presence of band-gaps, the direction of SPP propagation (since the group velocity lies normal to the contour) and gives information about the underlying scattering lattice. The complete three-dimensional band structure of SPPs on periodic systems may be mapped by collating the iso-frequency contours for a range of frequencies. The ability to map these iso-frequency slices in momentum space is hence a powerful tool in the understanding of a plasmonic system.

The most common method to map these iso-frequency contours is the use of reflectivity plots for a range of azimuthal angle, ϕ . By collecting reflectivity as a function of polar angle θ for a range of ϕ , the position of the SPP mode in reciprocal space may be mapped by the transformation $R(\theta, \phi) \rightarrow R(k_0 \sin \theta, \phi) \equiv R(k_x, k_y)$. This method has several drawbacks. The accuracy of determining a SPP mode position in θ can be limited if the plane of incidence lies parallel to a SPP contour, as the reflectivity minima associated with the SPP will be broad. The resolution of this method is also limited by the step size in ϕ , which, for experimental purposes, may have to be limited to prevent the experiment taking a prohibitively long time (particularly with silver samples, which degrade over time).

Several methods to measure the reciprocal space map for plasmonic systems directly have been previously published. Reports of using crystal defects [104] to couple to the SPP modes have revealed the general shape of the underlying lattice of photonic crystals. Direct recording of the ‘photonic Fermi surfaces’ using a plasmon topography technique [105], which images a sample in the Fourier plane of an optical microscope have been reported, as well as direct imaging of the contours using scattering through transmission gratings [106]. Direct observation of dispersion in a single plane of incidence using multiple wavelengths simultaneously is also found in the literature [107–109], but these methods are not related to mapping the full SPP contours in k -space but rather obtaining the in-plane dispersion curve directly.

In this thesis, we present a new method for directly obtaining the k -space contours

of SPP at single frequencies by adapting an imaging scatterometer used commonly in Natural Photonics investigations. This new method records the SPP contours of a reflection grating across the entire light cone to a high degree of accuracy, and the results can be numerically compared to theoretical predictions. By collating the contours from a range of frequencies, the entire 3D band structure of the SPPs may be experimentally determined.

4.3.1 Scatterometry

Scatterometry has been used previously to record the scattering patterns from samples found in Natural Photonics, such as the naturally diffuse scattering of the *Chrysochroa fulgidissima* beetle [110] or the *Morpho aega* butterfly [111]. It has also been used to show the hexagonal shaped Brillouin zone of a pseudo-hexagonal lattice found in the *E. imperialis* moth[112].

In this work, the previously reported experimental arrangement [111] has been modified by the addition of spectral filters to limit the image acquired to a single wavelength. Using a plasmonic grating sample, the scatterometer directly images the iso-frequency surface of the plasmonic dispersion. By applying a simple deformation to the image (also an adaptation new in this thesis) the scatterometer provides a map of the coupled SPP iso-frequency contours in momentum-space over the entire incident light cone.

4.3.2 Principle of Operation

A schematic of the scatterometry arrangement is shown in figure 4.6. White light is directed through a collimating lens, L1 and an optional linear polariser allows the investigation of the polarisation sensitivity of the acquired image. The white light is then focussed through an alignment pinhole and the beam is reflected via the beam-splitter, BS, on to an ellipsoidal mirror with an eccentricity of 0.833. The mirror, M1, focusses the light onto the sample, positioned at G.

If aligned precisely, the cone of light focussed by the mirror will include light from all directions (all azimuthal, ϕ , angles) and a range of polar angle ranging from $\theta \approx 2^\circ$ to $\theta \approx 90^\circ$. The lower limit of θ is determined by the shadow cast by the sample itself.

The reflected light from the sample is then collected by the same ellipsoidal mirror, M1 and is focussed through a second alignment pinhole, P2, positioned at the mirror's secondary focal point. This light is then collimated which causes the polar angle θ to be approximately linearly proportional to the obtained image's radial axis*. The beam is

*The small correction applied to the image that is required to obtain the true $R(\theta, \phi)$ image is detailed later in section 4.3.5

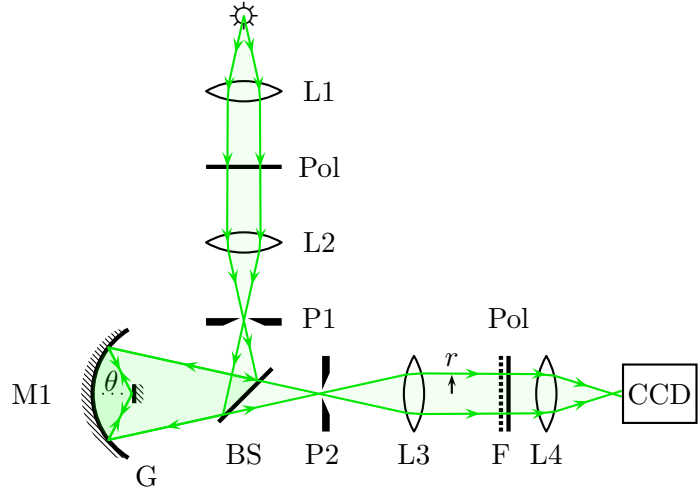


Figure 4.6: Experimental arrangement for the modified imaging scatterometry system. The angle θ of the light impinging on the grating, G, is approximately linearly proportional to the image's radial axis, r .

finally passed through a spectral filter and imaged using a CCD camera. The acquired image is a directly mapped reflectivity plot of all polar and azimuthal angles, $R(\theta, \phi)$, with a high resolution determined by the pixel size and density of the CCD. Using a range of spectral filters, the wavelength, and hence energy, of the map can be selected. The filters used are: 450 ± 5 nm, 500 ± 5 nm, 550 ± 5 nm, 580 ± 5 nm, 600 ± 5 nm, 650 ± 5 nm, 700 ± 5 nm and 750 ± 5 nm. The reflectivity of the sample for a single wavelength over the range $0 < \phi < 90^\circ$ and $2 < \theta < 90^\circ$ is thus recorded in a single image by the CCD.

Light of appropriate in-plane momentum may couple to diffracted SPP contours that exist within the recorded zero-order light circle. At the values of θ and ϕ which match the momentum of such a SPP, a reflectivity anomaly will be found in the acquired image. These reflectivity extrema, to a first approximation, map the position of the SPP iso-frequency contours over the large range of θ and ϕ available to this experiment.

4.3.3 Sample Preparation

Since the lower limit of polar angle, θ is determined by the size of the sample area, a small sample area is desirable to maximise the polar angle range. The grating samples are prepared by template stripping from a Si master, (a process detailed in section 4.1) to the centre of a large plate of glass, which acts as the substrate. The grating is then further reduced in size by using a clean razor blade to remove excess sample area.

Most previously reported work using scatterometry use a glass pipette to place the sample at the focal point of the ellipsoidal mirror. The pipette casts a characteristic

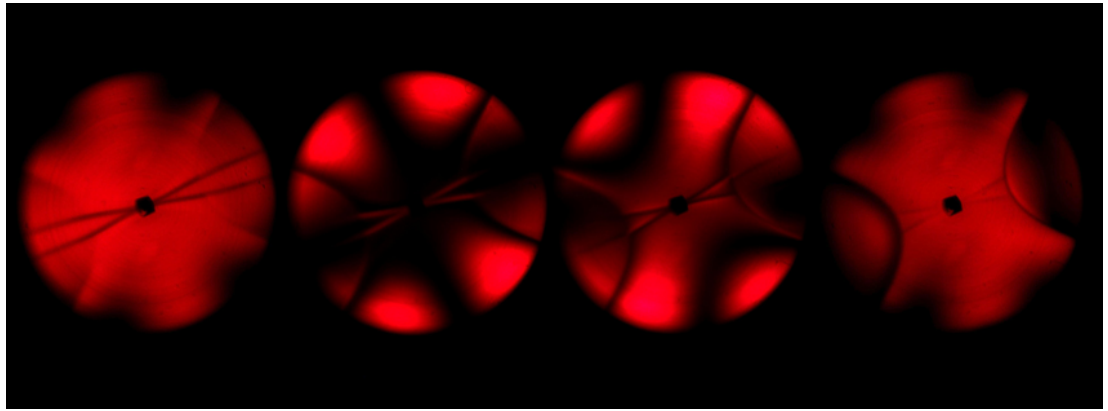


Figure 4.7: Four raw images from the scatterometer for a wavelength of $\lambda_0 = 650$ nm. The sample is a rectangular bi-grating supporting SPPs, as will be explored in chapter 5. The polarisation states are (left to right) (1) polarisation a , which gives good contrast of the thin dark SPP bands, (2) crossed polarisers with the first polariser set to polarisation a and the second set at 90° to this, named polarisation b (3) the alternative crossed polarisation, with the first polariser set to b and the second polariser set to polarisation a , and (4) The final polarisation, with both polarisers set to b .

shadow that may hide important spatial features. By using a large glass plate substrate that covers the entirety of the the mirror face, shadows from alternative positioning devices are avoided. It is found, by comparison of our final images with calculated diffraction edges and theoretical predictions, that any distortion effects due to refraction through the substrate are negligible.

4.3.4 The Role of Polarisation

The use of unpolarised light in this experiment is often adequate for the complete mapping of SPP modes diffracted into the zero-order light circle. Greater contrast of particular modes may be achieved by the use of two linear polarisers placed in the set-up at the positions marked. The complicated polarisation arrangement, due to the focussing from the ellipsoidal mirror, can cause ‘lobes’ of high and low reflectivity to appear, as the multiple reflections on the mirror lead to polarisation conversion for all but two radial axes. Still, if a single contour is of particular interest, the experimenter may adjust the polarisers to obtain the greatest contrast between the reflectivity extrema and the background. Depending on the polarisation states of the two polarisers, SPPs interacting with light may present as a maximum, minimum or inflection of the reflectivity. This is shown in an example dataset in figure 4.7.

These scattergrams are for a rectangular bigrating which will be discussed in chapter

5. Notice that in the first polarisation case (left most), rather flat SPP contours are seen clearly as dark contours crossing at the center ($\theta = 0^\circ$), while for the second case when the polarisers are crossed, the same SPPs exhibit as bright bands. This is a demonstration of SPP mediated polarisation conversion[34]. Diffracted SPP contours due to a second orthogonal pitch are best seen in the last polarisation case, and in this case have a far smaller radius of curvature. Discussion of these particular experimental results will continue in chapter 5.

The polarisation is chosen in each scattergram case depending on which SPP modes are to be best observed, and this choice will be stated along with the results.

Notice in these scattergrams how 4 distinct dark lobes in the first polarisation case change to bright lobes in the second and third cases, and return to dark in the last case. These are regions of polarisation conversion due to the mirror, and not due to the sample.

4.3.5 Corrections and Momentum-Space Deformation

To obtain a map of momentum-space from the scattergrams, two image corrections are required. The first corrects the aberration of the ellipsoidal mirror to obtain an image whose radial axis is linearly scaled with respect to the polar angle, θ . This correction is detailed in previous work [111].

The second deformation, scales the radial axis of the image to be proportional to the in-plane momentum, such that the reflectivity plot, $R(\theta, \phi)$ becomes,

$$R(\theta, \phi) \rightarrow R(k_0 \sin \theta, \phi) \equiv R(k_x, k_y)$$

Where $k_0 \sin \theta$ is the in-plane momentum for a specular reflected photon in the plane of incidence, at an azimuthal angle ϕ . The effect of this deformation is illustrated in figure 4.8. This figure illustrates an important experimental consideration for the use of scatterometry for the direct imaging of momentum space. Due to the $\sin \theta$ radial dependence of the final k -space diagram, higher values of θ provide less information than the angles close to normal incidence. It is then possible to map a very large area of momentum space, while only illuminating up to $\theta = 70^\circ - 80^\circ$ degrees.

4.3.6 Example Dataset

The processing of a raw dataset is shown in figure 4.9. The example shows a diffraction grating with a period of 600 nm illuminated at a wavelength of $\lambda_0 = 650 \pm 5$ nm. In figure 4.9(a), the raw image taken from the scatterometer is shown, with two dark contours of reflectivity minima showing the position of the $\pm \mathbf{k}_{gx}$ scattered SPP contours

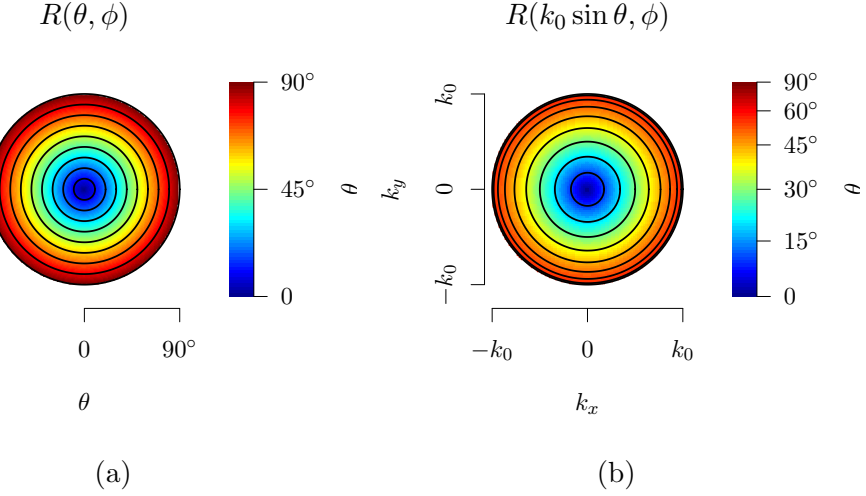


Figure 4.8: The image correction for $R(\theta, \phi) \rightarrow R(k_0 \sin \theta, \phi)$. The black circles on both diagrams show contours of equal angle, ranging from 10° to 90° in 10° steps.

in $\theta - \phi$ space. The image correction is then applied and the result is shown in figure 4.9(b), producing a momentum-space picture. Notice how the SPP contours have become broader and towards the radial edge curve inwards to form a more circle-like dispersion than they do in the raw image. Figure 4.9(c) shows the data adjusted for an azimuthal angle of rotation so that the SPP contours lie in the (arbitrarily chosen) k_x direction. This is to ensure our definitions between k_x and k_{gx} remain consistent. Two blue lines are added to figure 4.9(c), which are the calculated positions of the $\pm \mathbf{k}_{gx}$ diffracted light cones. The SPP contours, as expected, lie just outside these cones (see background theory chapter 2). The contours sit closer to the diffraction lines along $k_x = 0$ than they do at the extremes of the radius of the dataset, due to a small anisotropic dispersion of the SPPs. This anisotropic dispersion is because this example diffraction grating is, in fact, a complex grating type called a zigzag grating, which will be explained in detail in chapters 7 and 8.

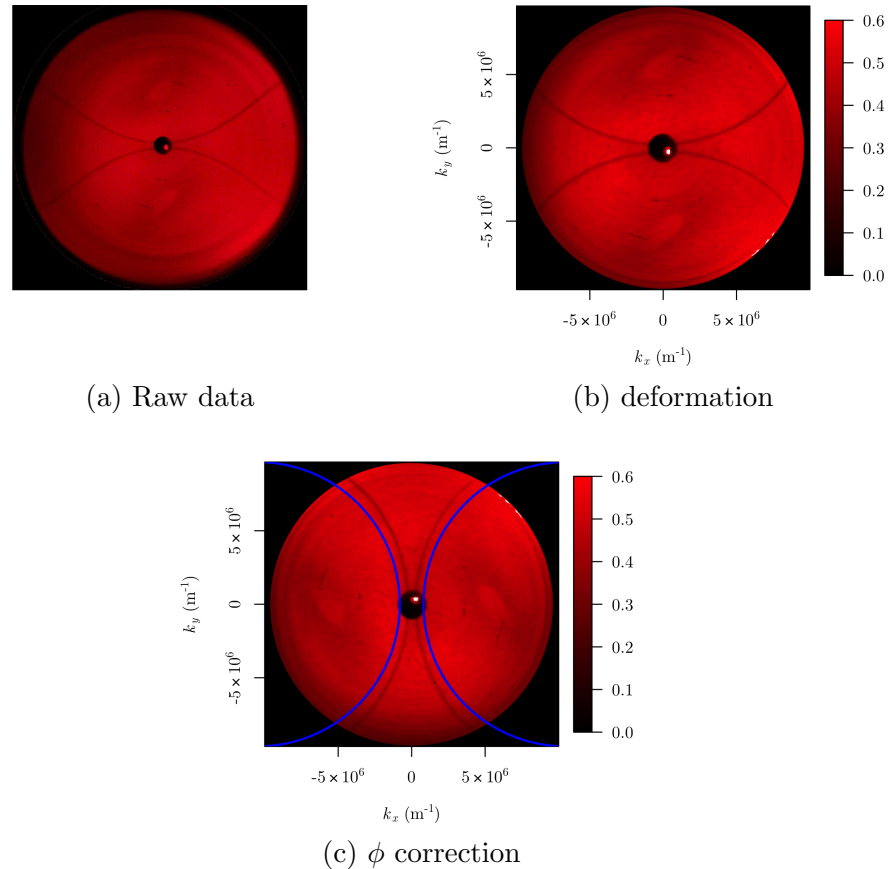


Figure 4.9: The processing of a raw dataset from the scatterometer at a wavelength of $\lambda_0 = 650$ nm. (a) Raw image obtained from scatterometer, (b) the image after the applied momentum-space deformation, and (c) the final image with corrected azimuthal angle and addition of calculated diffraction circles.

Chapter 5

Optical Response of Metallic Rectangular Bigratings

5.1 Introduction

Bigratings consist of two monogratings ‘crossed’ at some angle relative to each other [93]. The study of SPPs on such gratings has covered various symmetries, and various novel optical effects have been observed. Hole arrays that exhibit extraordinary enhanced transmission that is mediated by SPPs travelling along the surface [62, 79, 113] are types of bigrating, often with square symmetry. Full photonic band gaps for surface waves has been demonstrated on hexagonal symmetry gratings [114], as has total absorption of unpolarised light [77], and absorption of light across a broad angle range [115].

This chapter details the optical response of metal bigratings with rectangular lattice symmetry. This symmetry of gratings has received comparatively less attention in the published literature and serves as a good introduction to the methods and physics of SPP on bigratings observed throughout this thesis. This chapter also shows experimentally how anisotropic propagation of SPPs may be designed by controlling the scattering amplitude in one direction and leaving the orthogonal direction unaltered.

The gratings used for this investigation, and all subsequent investigations in this thesis, have straight-walled grooves and are commonly referred to as lamellar gratings. It is instructive, then, to review the scattering properties of such lamellar type gratings, and so a simple Fourier analysis giving the scattering amplitudes of a lamellar grating is presented in section 5.3.1.

A fabricated rectangular bigrating is used to demonstrate the coupling to, and observation of SPPs supported by such a structure. The reflectivity of a silver rectangular bigrating is then used to experimentally map the SPP dispersion in section 5.3.2. The observed coupling of light and the interaction of the SPP modes is explained with

respect to the available scattering harmonics present in the constituent gratings. These scattering harmonics are inferred from the Fourier expansion found in section 5.3.1 and SEMs of the sample. These results serve to demonstrate the experimental techniques used to map the SPP dispersion and also how the mark-to-space ratio is a key parameter in the understanding of the scattering on such lamellar gratings.

The observation of polarisation conversion is also experimentally studied in section 5.4, showing that the reflected polarisation may be rotated when the plane of incidence is not along an axis of high symmetry.

The new technique of imaging scatterometry is used in section 5.3.3 to map the iso-frequency SPP contours in reciprocal space for the grating. The obtained iso-frequency maps show the formation of a band-gap at the first BZ boundary, a result that is reproduced using a FEM model and shows good agreement. This model is used to calculate the electric field of the two different SPP standing waves that occur at the BZ boundary.

Finally, section 5.5 of this chapter shows how the deepening of one of the constituent gratings provides a mechanism to control the anisotropic SPP propagation along the surface. The deformation of the SPP iso-frequency contours is experimentally recorded using imaging scatterometry.

5.2 The Rectangular Bigrating

A rectangular bigrating consists of two monogratings of different pitches ‘crossed’ at an angle $\alpha = 90^\circ$. The coordinate system for this type of grating is shown in figure 5.1. The plane of incidence is defined at an azimuthal angle of $\phi = 0^\circ$ when the wavevector of incidence light, impinging at some polar angle, θ , lies in the xz plane. When the electric field vector of the impinging radiation is contained within the plane of incidence, the light is said to be TM polarised, and when the electric vector lies orthogonal to the plane, it is TE polarised. The x -direction is in the plane of diffraction for the longer-pitch grating, which possesses a periodicity of λ_{gx} , and for all the gratings presented in this chapter is equal to 600 nm. The grating vector for this grating is defined as $\mathbf{k}_{gx} = 2\pi\hat{\mathbf{x}}/\lambda_{gx}$. The second, shorter-pitch grating lies at an angle of $\alpha = 90^\circ$ to the x -direction, and has $\lambda_{gy} = 400$ nm in this chapter. As before, the grating vector of this short-pitch grating is defined as $\mathbf{k}_{gy} = 2\pi\hat{\mathbf{y}}/\lambda_{gy}$. The depths of the gratings are d_1 and d_2 , and are chosen in this chapter so that $d_1 = d_2 \approx 40$ nm.

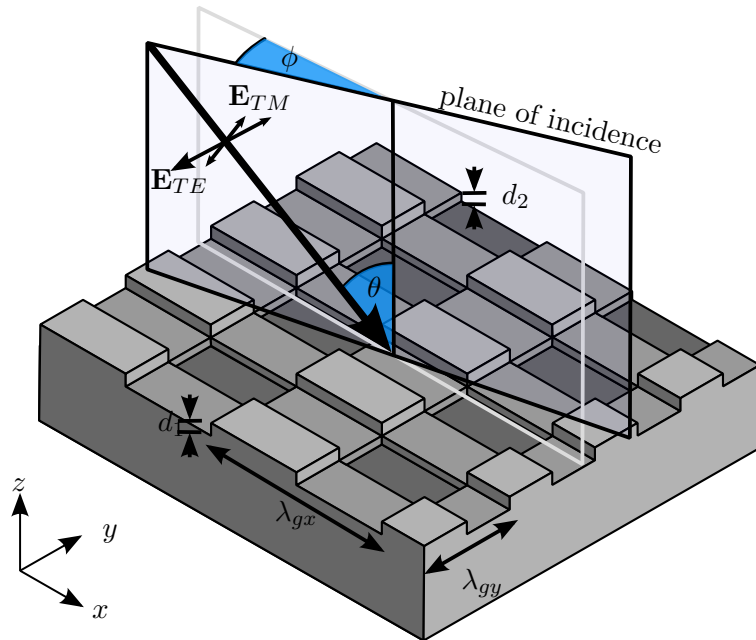


Figure 5.1: The coordinate system for a rectangular grating. Light is incident on the surface at a polar angle θ and an azimuthal angle ϕ . The plane of incidence contains the wavevector of the light, and the polarisations are defined accordingly.

5.3 Dispersion of SPPs on Rectangular Bigratings

5.3.1 Scattering Components on Lamellar Gratings

In this chapter we use rectangular bigratings that have been fabricated using the electron beam lithography and template stripping method outline in chapter 4. These have surface relief grooves whose groove profiles are to a good approximation represented by a rectangular step function. Gratings such as this are often referred to as ‘lamellar’ gratings, ‘binary’ gratings, or occasionally ‘rectangular gratings’. To avoid confusion in this chapter, we shall reserve the label ‘rectangular’ for discussion of the bigrating lattice, and refer to the groove profile shape as simply ‘lamellar’.

To explain the SPP coupling and dispersion on rectangular bigratings we must gain a qualitative understanding of the scattering strength from lamellar profile gratings. The strength of scattering for fields at the grating surface is determined by the Fourier components of the surface profile. This is because the incident field’s wavevector will be modified by the addition or subtraction of an integer number of surface profile wavevectors, and the diffraction efficiency into each order is proportional to the Fourier coefficients of these harmonics squared [116, 117]. To fully understand the excitation and interaction of SPPs on rectangular bigratings, we must first obtain expressions for

5. Optical Response of Metallic Rectangular Bigratings

these Fourier harmonics present for lamellar gratings.

A step function representing a monograting surface profile can be expressed by the piecewise linear function,

$$f(x) = \begin{cases} -A, & -L < x < -\frac{mL}{2} \\ A, & -\frac{mL}{2} < x < \frac{mL}{2} \\ -A, & \frac{mL}{2} < x < L \end{cases} \quad (5.1)$$

Where A is the amplitude of the grating, $\lambda_g = 2L$ is the period of the periodic function, and m is a variable that affects the groove widths. Two common ways of defining the relative size of the region of grooves to the peaks for such functions are the '*mark-to-space ratio*' (MSR) and the '*duty cycle*' or '*fill-fraction*' (Γ) of the function. The MSR is defined as the ratio between the peak length and the trough length, while the duty cycle is defined as the fraction of the period which the peak occupies. The variable m in the piecewise linear function was used for the convenience of calculation for the Fourier series. MSR and Γ are defined in terms of m as,

$$\begin{aligned} MSR &= \frac{m}{2-m} \\ \Gamma &= \frac{m}{2} \end{aligned}$$

MSR varies between $0 < MSR < \infty$ while Γ varies between $0 < \Gamma < 1$.

Several examples of the grating function (equation 5.1) are shown in figure 5.2(a). This function is an even function and so may be expressed as a Fourier sum containing only cosine terms, with coefficients a_n given by,

$$a_n = \frac{4A}{n\pi} \sin \frac{n\pi m}{2} \quad (5.2)$$

The Fourier sum is then,

$$F(x) = \sum_{n=1}^{\infty} \frac{4A}{n\pi} \sin \frac{n\pi m}{2} \cos \frac{n\pi x}{L}$$

The amplitudes of the first four Fourier coefficients as a function of the duty cycle of the grating is shown in figure 5.2(b). The gratings fabricated in this chapter were designed for a $\Gamma = 0.5$, which gives peaks equal in length to the troughs. For $\Gamma = 0.5$, ($MSR = 1$), there are no even Fourier components present in the surface expansion ($a_{2,4,\dots} = 0$). This means that, for a lamellar grating with $\Gamma = 0.5$, there is no direct scattering of light by even scattering vectors, and the even-ordered diffraction is

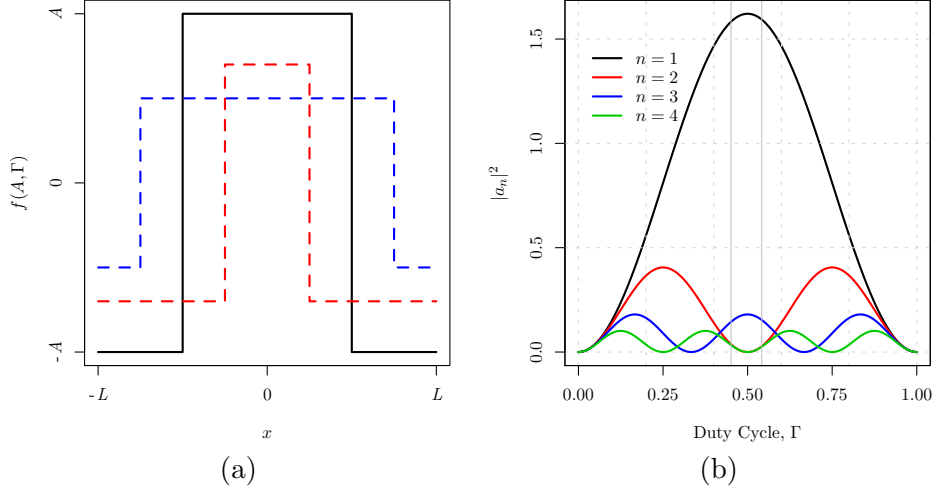


Figure 5.2: (a) Three examples of unit cells for lamellar grating profiles represented by equation 5.1. $f(A, \Gamma)$ for each case is $f(A, 0.5)$, $f(0.7A, 0.75)$ and $f(0.5A, 0.25)$. (b) Square of the Fourier coefficients, a_n defined by equation 5.2, in lamellar groove profiles as a function of Γ for $n = 1, 2, 3, 4$. The two grey vertical lines highlight the two values of Γ measured from the experimental sample used in section 5.3.2.

consequently very weak. Even-ordered diffraction in this case is not forbidden, however, as light may scatter multiple times via odd-ordered scattering events (clearly present for $\Gamma = 0.5$ in figure 5.2(b)), but the strength of this multiple scattering process is normally quite weak. Small fabrication errors in Γ will lead to non-zero values of even Fourier harmonics, and in this case direct scattering events will occur.

The expression of the Fourier components as a function of Γ is relevant to all the gratings produced and measured in this thesis.

5.3.2 Experimental Mapping of SPP Dispersion

This section demonstrates the experimental mapping of SPP dispersion on rectangular gratings using reflectivity measurements. An electron micrograph of the fabricated grating is shown in figure 5.3. This sample is a silver grating fabricated using electron beam lithography to produce a silicon master, followed by the coating of the master with silver and then template stripped on to a clean glass substrate. This process is detailed in depth in chapter 4. The measured parameters from the SEM were $\lambda_{gx} = 592 \pm 10$ nm and $\lambda_{gy} = 395 \pm 9$ nm with the duty cycle of the grating in the x direction measured as $\Gamma_x = 0.45$ and in the y direction as $\Gamma_y = 0.54$. The variation of Γ from the designed duty cycle of $\Gamma = 0.5$ will lead to possible direct scattering events for both odd and even grating harmonics, as can be seen by referring back to figure 5.2(b), in which these two

5. Optical Response of Metallic Rectangular Bigratings

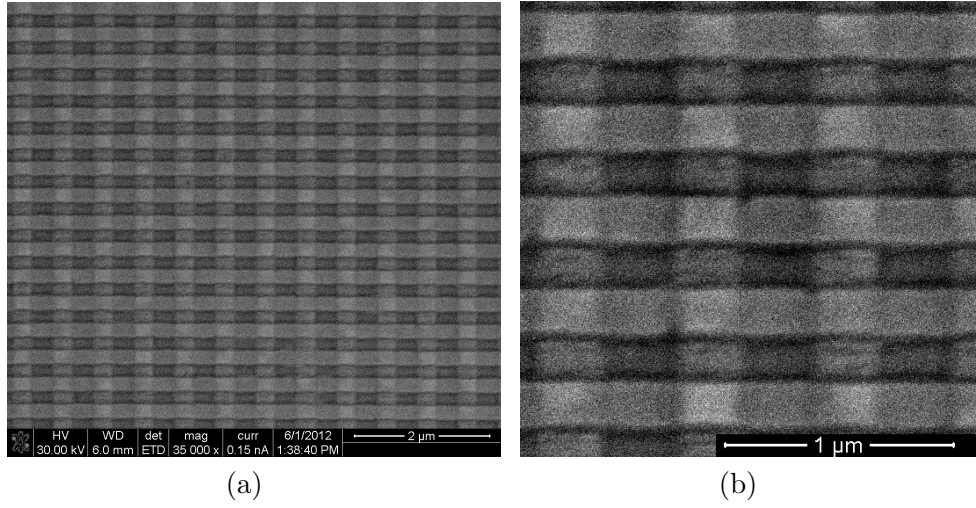


Figure 5.3: (a) A scanning electron micrograph of the template-stripped rectangular bigrating in silver. (b) A higher magnification of the surface showing small amounts of surface roughness attributed to anisotropic etching of the Si master. The parameters are $\lambda_x = 600$ nm, $\lambda_y = 400$ nm.

values of Γ are marked with grey lines.

The dispersion of SPPs on such a grating was experimentally mapped from the sample's zero-order reflectivity using the technique outlined in chapter 4. Using this method, the re-radiated light from SPPs will in general differ in phase to the zero-order reflection and so produce reflectivity features that map the SPP dispersion. The polar angle range used was $7^\circ < \theta < 60^\circ$ in steps of 0.5° , and the wavelength range used was 400 nm $< \lambda_0 < 800$ nm in steps of 2 nm. The resultant reflectivity plots for different polarisations and azimuthal angles are shown in figure 5.4. Since both periodicities on this bigrating will provide observable scattering at some point in our discussions, we adopt the notation of using two integers (m, n) to represent the $m\mathbf{k}_{xg} + n\mathbf{k}_{yg}$ scattering events.

Figure 5.4(a) shows the measured reflectivity of TM polarised light for a rectangular grating at $\phi = 0^\circ$. The blue lines show the momentum states of grazing photons for various diffracted orders and in this figure include the $\pm 1\mathbf{k}_{gx}$, $+2\mathbf{k}_{gx}$ scattered and the zero-order light line. No diffraction lines associated for the λ_{gy} period are present, as the pitch of λ_{gy} was chosen to ensure, for the orientation of the grating at $\phi = 0^\circ$, there was no diffraction present from the shorter period in this frequency range.

The figure shows dark bands of low reflectivity that map the positions of the $\pm 1\mathbf{k}_{gx}$ and $+2\mathbf{k}_{gx}$ scattered SPP modes. These modes lie beyond their respective diffracted light lines, as the momentum of SPPs is greater than that of corresponding scattered

5. Optical Response of Metallic Rectangular Bigratings

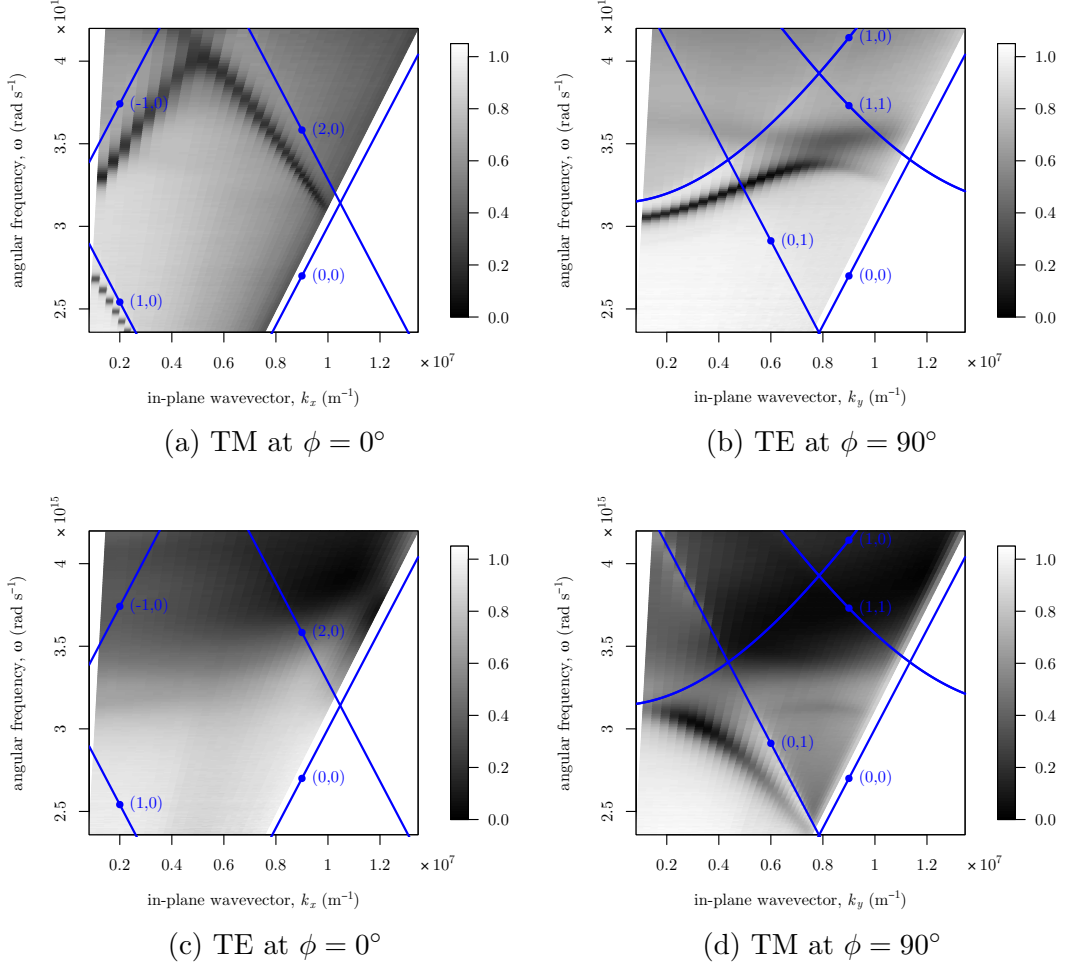


Figure 5.4: The reflectivity for different polarisations and azimuthal angles for a rectangular grating mapped as a function of (ω, k) in the case of (a) TM polarised light at $\phi = 0^\circ$, (b) TE polarised light at $\phi = 90^\circ$, (c) TE polarised light at $\phi = 0^\circ$ and (d) TM polarised light at $\phi = 90^\circ$.

light. Several conclusions can be made about this grating from the observation of the SPPs. Firstly, the $\pm 1\mathbf{k}_{gx}$ scattered SPP is coupled strongly to light, presenting as a reflectivity minimum with only $\approx 20\%$ of the light being reflected. This is due to the phase of the re-radiated light from the SPPs being out-of-phase with the direct (non-interacting) reflected light from the surface. The $+2\mathbf{k}_{gx}$ SPP is also coupled well and is observed as a dark band. This suggests that there is a $2\mathbf{k}_{gx}$ component in the grating surface profile, as for light to interact with a $+2\mathbf{k}_{gx}$ scattered SPP and present as a dark band the light has undergone a single scattering process equal to $+2\mathbf{k}_{gx}$, which is only strongly observed if the profile itself contains a $2\mathbf{k}_{gx}$ component. This is

expected for $\Gamma_x = 0.45$, as measured from the SEM in figure 5.3. If $\Gamma_x = 0.5$, there would be no $2k_{gx}$ component in the grating surface and the $+2\mathbf{k}_{gx}$ could only present in the reflectivity data via weak multiple scattering processes.

At the first BZ boundary these two counter-propagating modes meet and form a small band-gap, which is not fully mapped as it occurs at the upper limit of the experiment's frequency range. The observable part of this band-gap is the lower band edge occurring at $k_x = \pi/\lambda_{gx} = 0.52 \times 10^7 \text{ m}^{-1}$. These SPPs coupling together to form a band-gap means that the grating profile also contains a $3k_{gx}$ component which couples these two modes together (see chapter 2). A $3k_{gx}$ component in the surface profile is fully expected for lamellar gratings with $\Gamma_x = 0.45$.

Figure 5.4(c) shows the same reflectivity map, this time for TE polarised light. TE polarised light provides no normal component of electric field to the surface of the long pitch grating, and so no SPPs are excited. In the top corner of the dispersion, at larger values of k_x and at high frequencies, there is a broad dark region that is attributed to a largely over-coupled mode associated with the $n\mathbf{k}_{gy}$ scattered SPPs, for which the TE polarisation is suitable for SPP excitation.

Rotating the grating by $\phi = 90^\circ$, so that the plane of incidence now lies along the k_y direction allows the observation of the $\pm 1\mathbf{k}_{gx}$ and $\pm 2\mathbf{k}_{gx}$ SPPs that present now as out-of-plane modes when the light is TE polarised (Figure 5.4(b)). These mapped SPP bands follow curved diffraction lines formed by the conic intersection of an out-of-plane diffracted light cone (see the discussion in chapter 2).

A band-gap is observed in this direction between the $(\pm 1, 0)$ and the $(\pm 1, 1)$ scattered SPPs, with the centre of the band-gap at $\omega = 3.45 \times 10^{15} \text{ rad s}^{-1}$. This corresponds to an illumination wavelength of $\lambda_0 = 546 \text{ nm}$, and we shall use a wavelength close to this to observe this band-gap using scatterometry later in section 5.3.3.

These bands are coupled to well beneath these diffraction lines, and appear weakly coupled once the band passes above the diffraction lines. This is due to the re-radiated light from SPPs now being able to couple not just to the zero-order light, but also to the allowed modes of diffracted light scattering along the k_x axis. This additional loss mechanism of the light leaves less of the out-of-phase re-radiated light in the measured specular reflection.

The straight lines in figure 5.4(b) show the diffraction lines associated with the $+1\mathbf{k}_{gy}$ light and the zero-order light line. No SPP is observed that is associated with the $+1\mathbf{k}_{gy}$ light line, as the polarisation conditions are not met for the excitation of this mode.

The final dispersion map is shown in 5.4(d) for $\phi = 90^\circ$ and TM polarised light. In this case the SPPs associated with the $n\mathbf{k}_{gy}$ scattering events should be observed. Following the $+1\mathbf{k}_{gy}$ light line, a dispersive mode, broader than the SPP bands seen previously,

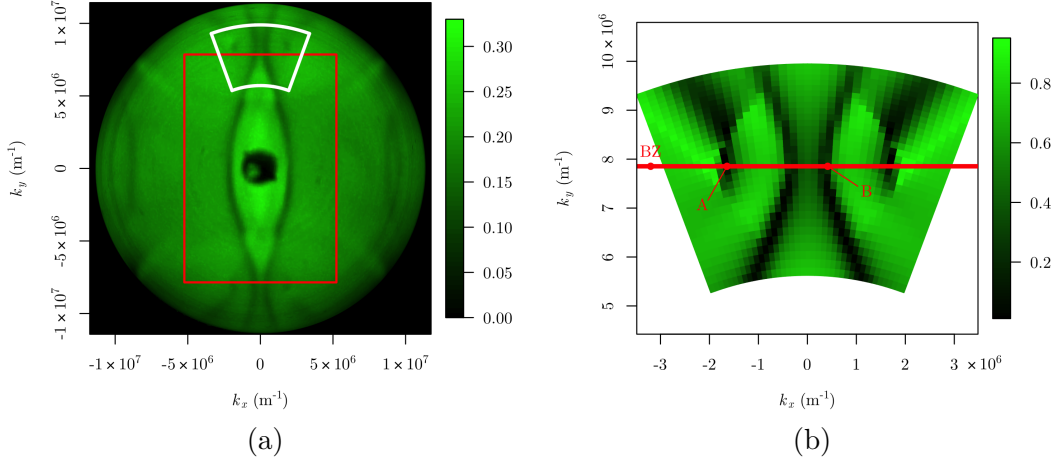


Figure 5.5: (a) A scattergram of a rectangular grating mapped to k -space for an illumination wavelength of $\lambda_0 = 550\text{ nm}$. The red square indicates the position of the BZ boundary. The white region bounded in the scattergram is replicated in (b), modelled using the FEM.

is observed. This mode forms a large band-gap at $k_y = 0$, with a forbidden frequency range observed between $3.2 \times 10^{15} \text{ rad s}^{-1} < \omega < 3.5 \times 10^{15} \text{ rad s}^{-1}$, suggesting a large $2k_{gy}$ component in the grating which may directly couple the counter-propagating SPPs together. Above this band-gap, a very large broad absorption band is seen, with the reflectivity being reduced further inside the $+1k_{gy}$ diffraction cone. This is attributed to largely over-coupled SPP modes, and the extra available loss channels inside the diffraction cone. The small dark band observed at $\omega \approx 3.1 \times 10^{15} \text{ rad s}^{-1}$ is the lower band edge of a band gap formed at the 1st BZ boundary in the k_y direction.

5.3.3 Band Gap Observation Using Scatterometry

Scatterometry has been used in this section to observe the band-gaps that form at the first BZ in the k_y direction due to the interaction of a $+1\mathbf{k}_{gx}$ and a $-1\mathbf{k}_{gx}$ scattered SPP. This is a new technique presented in this thesis, and the methodology is covered in chapter 4. Figure 5.5(a) shows the results for a rectangular grating for an illuminating wavelength of $\lambda_0 = 550\text{ nm}$.

In this figure, the BZ boundary is shown as a red rectangle and the $\pm 1\mathbf{k}_{gx}$ scattered SPPs present as dark bands in the reflectivity. The $\pm 1\mathbf{k}_{gy}$ scattered SPPs are also observed as extremely weak bright bands, due to the selected polarisation for this scattergram, which was chosen to provide greatest contrast for the $\pm 1\mathbf{k}_{gx}$ scattered SPPs. The $\pm 2\mathbf{k}_{gx}$ scattered SPPs are also observed as dark bands near the edges of

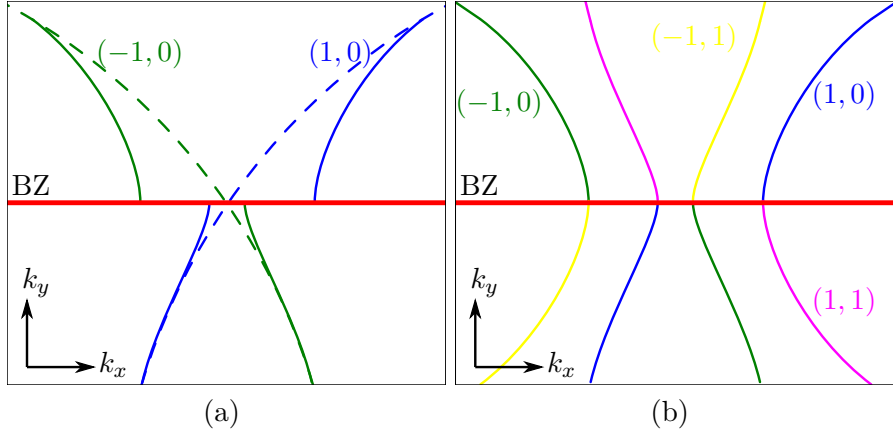


Figure 5.6: (a) Cartoon of the $(-1, 0)$ and $(1, 0)$ SPP iso-frequency contours at the BZ boundary, from the original continuous SPP contours (dotted lines) to the split modes (solid lines). (b) By considering the other interactions occurring at this point (or by using the mirror symmetry of the BZ boundary), the continuous SPP contours are recovered, leading to the observation of the SPP contour shape measured in figure 5.5.

the plot at $|k_x| = 0.9 \times 10^7 \text{ m}^{-1}$. This sample was produced from the same master as the grating presented in section 5.3.2, so a $2k_{gx}$ component in the surface profile is not unexpected.

As the scattered SPP contours cross at the BZ boundary, they are seen to split. The contours intersect the BZ boundary perpendicularly, indicating that there is zero group velocity in the k_y direction, as one would expect for a set of standing waves. The shape of these contours is explained in figure 5.6 as the splitting of the modes due to a band-gap.

The region of the band-gap is highlighted in white in figure 5.5(a), and in figure 5.5(b) the data in the area shown has been reproduced using a FEM model. The SPP contour at point A appears discontinuous at this boundary, but this cannot be true. The SPP contours are never discontinuous due to the translational symmetry of reciprocal space as illustrated in figure 5.6, and this apparent discontinuity in the contour is in fact the SPP simply being poorly coupled beyond the point of the BZ boundary. The SPP contour at A will connect with the SPP eigenmode associated with the $(-1, 1)$ scattered SPP contour, and the coupling of light to this eigenmode is sufficiently weak as to cause this apparent discontinuity.

The model shows good agreement to the obtained scattergram with the parameters as follows: $d_1 = d_2 = 35 \text{ nm}$, $\lambda_{gx} = 600 \text{ nm}$, $\lambda_{gy} = 400 \text{ nm}$ with $\Gamma_x = 0.45$, $\Gamma_y = 0.54$ and silver parameters from literature [118]. From this model, the electric field profiles in the yz plane were extracted and plotted in figure 5.7. These band gap solutions

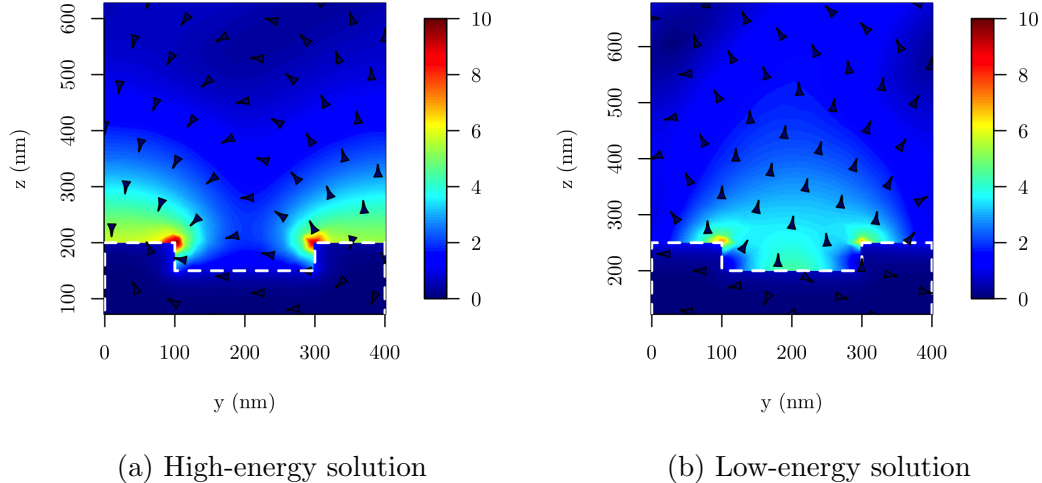


Figure 5.7: Colour plots showing the magnitude of electric field at a set temporal phase (colour scale) and electric vector direction (arrows) for the (a) high energy and (b) low energy SPP standing waves occurring at the BZ boundary.

correspond to the points A and B in figure 5.5(b), where the SPP contour intersects the BZ boundary perpendicularly, indicating the SPP mode possesses zero group velocity in the k_y direction, indicative of a standing wave.

The electric field plots show that both standing waves have a wavevector such that $k_y = k_{gy}/2$, as is expected at the first BZ boundary. One mode extends further into the air, and is the ‘photon-like’, high energy solution (figure 5.7(a)). This shows that charge accumulates mostly on the grating peaks, while the charge is localised to the grating grooves in the lower energy case of figure 5.7(b), in agreement with the analogous case of simple sinusoidal gratings discussed in chapter 2.

5.4 Polarisation Conversion on Rectangular Symmetry

The conversion of the polarisation of light is of some importance in many plasmonic applications. The two mechanisms of polarisation conversion outlined in chapter 2 detail how the geometry of a diffraction grating and the presence of SPPs on a surface may mediate significant changes in the polarisation state of the reflected light. Both these mediating processes are possible when the light impinging on a grating surface does so along an axis of reduced symmetry. The basic principle of this is quite intuitive; one does not expect any physical response of the system to possess a different symmetry

5. Optical Response of Metallic Rectangular Bigratings

to that with which it started. So, when the electric field of an incident light beam lies in a plane of mirror symmetry shared by both the light and a surface, it is correctly expected that the reflected light's electric field will occupy the same plane. This offers us an intuitive understanding for a typical diffraction grating with a single periodicity reflecting polarised light. We do not expect the polarisation of the TE or TM polarised light to change upon reflection when the electric field lies either parallel or perpendicular to the grating's grooves as this is when the polarised electric (and magnetic) field vectors lie in the grating's mirror symmetry planes (when $\phi = 0^\circ$ or $\phi = 90^\circ$). However, if the light field vectors do not lie in the mirror symmetry planes of the diffraction grating, say by rotating the grating azimuthally by an angle which is not $\phi = 0^\circ$ or $\phi = 90^\circ$, the mirror symmetry considerations place no constraints on the rotation of polarisation, and polarisation conversion may be observed. In fact, maximum polarisation conversion of the incident light (for a monograting) occurs half way between these two angles, at $\phi = 45^\circ$.

This is a general symmetry description of polarisation conversion, which gives us an intuitive insight as to when we might expect the rotation of light's polarisation to change, or when it will not. On a square bigrating, with $\lambda_{gx} = \lambda_{gy}$, there is an additional plane of mirror symmetry, at $\phi = 45^\circ$. At this angle, again, no polarisation conversion is observed and the polarisation state of reflected light is unchanged [119].

In the rectangular bigrating case, the plane of incidence will only be collinear with planes of mirror symmetry when $\phi = 0^\circ, 90^\circ, 180^\circ, 270^\circ$. We expect to observe rotation of the polarisation state of incident light for any azimuthal angle which is not $\phi = 0^\circ$ or $\phi = 90^\circ$. To highlight the differences in the rectangular grating to the square grating, we choose here an angle of $\phi = 45^\circ$ to investigate the grating's ability to rotate the polarisation.

To record the polarisation conversion of light from TE to TM (and from TM to TE), spectra were recorded in the range $450 \text{ nm} < \lambda_0 < 800 \text{ nm}$ in steps of 2 nm. The incident light was passed first through a linear polariser set to either TE or TM, and then directed on to the grating surface, which was oriented at $\phi = 45^\circ$. The zero-order reflected light was then passed through a second linear polariser, which for the purposes of detecting polarisation conversion was crossed at 90° with respect to the first polariser. Normalisation of the polarisation converted signal was performed by dividing the reflectivity spectra with a straight-through spectra of linearly polarised light (both polarisers set to the same polarisation).

Figure 5.8 shows the results of this experiment. The upper half of the figure shows the reflectivity for uncrossed (black) polarisers both set to the TE polarisation, and the crossed (red) polarisers set to TE and TM respectively. Resonant features exist in both spectra characteristic of SPP interaction with the light. For the polarisation

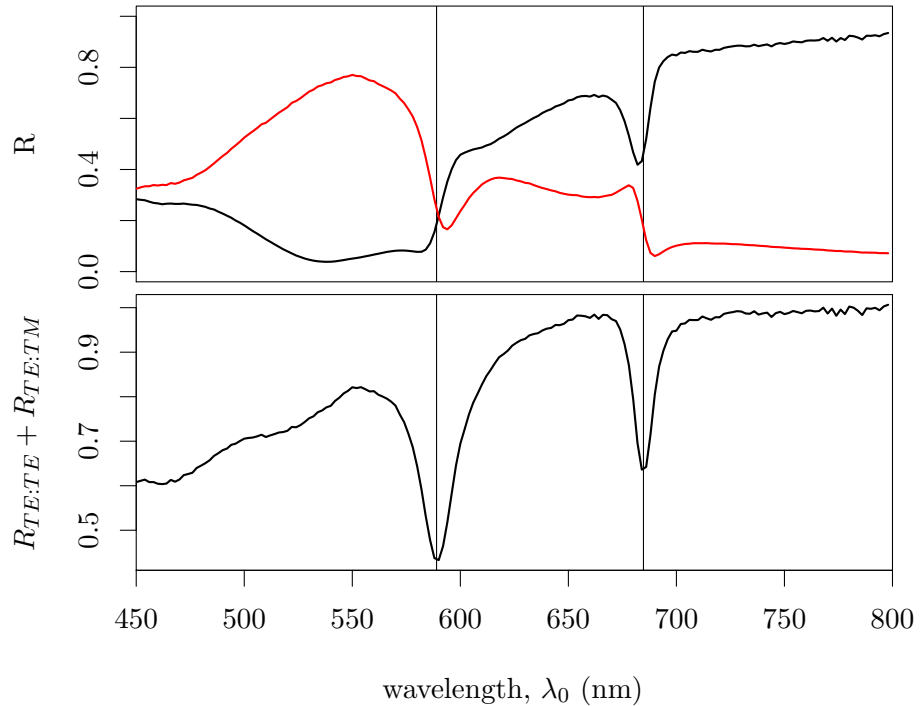


Figure 5.8: Spectra of polarisation conversion on the rectangular grating at $\phi = 45^\circ$. Top panel: The reflection of TE polarised light, $R_{TE:TE}$ (black) and polarisation conversion $R_{TE:TM}$ (red). Lower panel: The addition of these two reflectance curves gives a more precise position of the SPP modes.

conversion signal (red line) we see a large broad region of polarisation conversion between $500 \text{ nm} < \lambda_0 < 600 \text{ nm}$, which we attribute to polarisation conversion mediated by largely over-coupled modes at high frequencies, evidence for which we observed previously in section 5.3.2. The second resonant feature at $\lambda_0 \approx 690 \text{ nm}$ presents as an inflection of the polarisation converted signal and is in the same region as the reflectivity minimum in the R_{TE} case (black line).

This highlights an important point when dealing with the mapping of SPP position in systems of low symmetry. Normally, the measurement of the SPP energy or momentum is accomplished by measuring the resonant minima (or maxima) position in energy or momentum space. However, when SPPs propagate along axes of broken symmetry, the phase of the re-radiated light into a single polarisation state is insufficient to determine the exact SPP location, as additional loss channels are available (The SPP may couple out to a different polarisation state, and the phase of this light with respect to the incident field may be different). This is highlighted in the lower portion of figure 5.8,

where the two obtained reflectivities have been summed to obtain the reflectivity of both TE:TE and TE:TM polarised reflections. The result shows reflectivity resonance minima which better position the SPP in wavelength, as some of the additional phases have been accounted for through interference by the summation of the two reflectivities. The grey lines across both figures show that in the original upper spectra, the mode positions do not correspond to this corrected (bottom) spectra.

5.5 Controlling SPP Anisotropy Using Rectangular Bi-gratings

It was demonstrated in section 5.3.2 that SPP band-gaps form in both the \mathbf{k}_{gx} and \mathbf{k}_{gy} directions on a rectangular bigrating. The size of these band-gaps is proportional to the diffraction efficiency required to couple two counter-propagating SPPs together to form the required SPP standing waves. This diffraction efficiency into a particular diffracted order is also proportional to the Fourier components squared, and an expression for these was derived in section 5.3.1.

Examining equation 5.2, it is possible to increase the diffraction efficiencies of a constituent grating by simply increasing the grating's amplitude. Since on a lamellar type grating, each Fourier component is proportional to this grating amplitude, the size of all the possible SPP band-gaps may be controlled by simply deepening the grating.

On a rectangular bigrating there are two constituent lamellar gratings oriented orthogonal to one another. SPP band-gaps in one direction may be controlled by deepening the appropriate grating, leaving the band-gaps that form in the orthogonal direction along the other constituent grating largely unaffected. This should allow the design of SPP anisotropy, where the SPP dispersion varies largely depending on the direction in which the SPP travels along the grating.

In this section, we deepen the short-pitch grating and observe the effect of increased SPP anisotropy using imaging scatterometry. The variable we adjust is d_2 , and the effect on the surface profile of increasing this is shown in figure 5.9.

Two bigratings were produced for this experiment, with the aim that they be identical save for the depth of the shorter-pitch grating, d_2 . The two gratings are manufactured at the same time via electron beam lithography, using the same electron dose to expose the pattern. The long pitch is $\lambda_{gx} = 600$ nm and for the short pitch $\lambda_{gy} = 400$ nm. The target depth of the long pitch for both gratings was $d = 40$ nm, which is achieved by reactive ion etching the masters in the same etching exposure run. The second short-pitch grating was then added to the master and the depth varied between samples. For the 'shallow' bigrating, the target depth of 40 nm was used, for

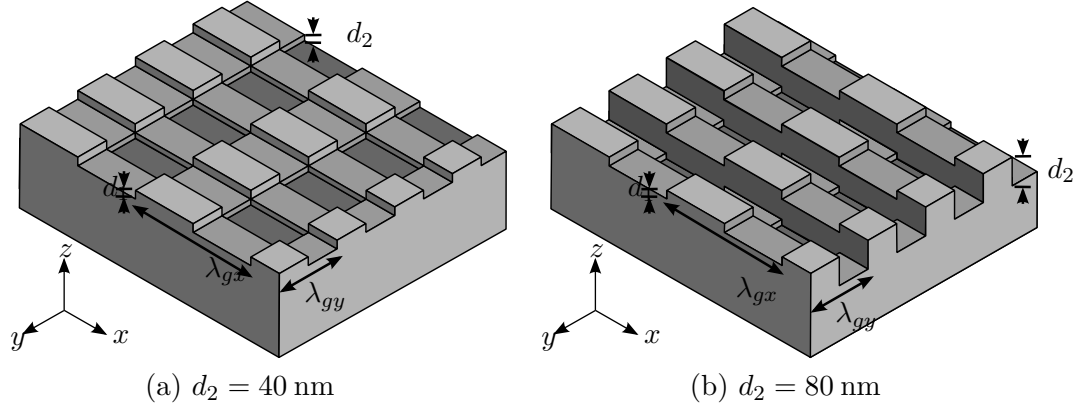


Figure 5.9: Diagram of the effect on the surface profile by increasing the depth d_2 of the rectangular bigrating from (a) $d_2 = 40$ nm to (b) $d_2 = 80$ nm. A larger value of d_2 increases the diffraction efficiency of the constituent \mathbf{k}_{gy} grating.

the ‘deep’ bigrating the target depth was $d_2 = 80$ nm

The expected effect on the SPP iso-frequency contours is shown in figure 5.10. The increase in the diffraction efficiency of the $\pm\mathbf{k}_{gy}$ scattering events will be the dominant effect observed for the chosen grating’s parameters. By increasing the diffractive coupling between SPPs, the $(\pm 1, 0)$ SPPs will interact and form larger band-gaps at the 1^{st} BZ boundary in the k_y direction. This is shown in the figure as a relatively weakly coupled SPP contour (yellow line) evolving into the stronger coupled SPP contour (red line). The effect of this is to ‘flatten’ the band along the k_y axis. The interactions between these contours and the $(\pm 1, 0)$ are not included in this picture as they will require a multiple scattering process by which to interact, and consequently are very weak. A more detailed description as to the presentation of these bands in k -space is discussed in chapter 4, under the experimental methodology for imaging scatterometry.

Figure 5.11 shows the experimentally mapped iso-frequency contours for the two rectangular bigratings at a wavelength of $\lambda_0 = 700$ nm. Figure 5.11(a) shows two SPP contours as dark bands of reflectivity closely following the $\pm 1\mathbf{k}_{gx}$ scattered diffraction cones (blue lines). The SPP contours in figure 5.11(a) exhibit a small degree of anisotropy with respect to their dispersion, with the SPP contour closer to the diffracted light lines at $k_y = 0$ than elsewhere along the contour. This is due to the $(\pm 1, 0)$ scattered SPPs interacting and forming band gaps with the $(\pm 1, \pm 1)$ or $(\mp 1, \pm 1)$ SPPs. This interaction is strong as it only requires a single scattering event of $\pm 1\mathbf{k}_{gy}$ to couple the SPPs together, which is a harmonic that is present in the grating’s surface

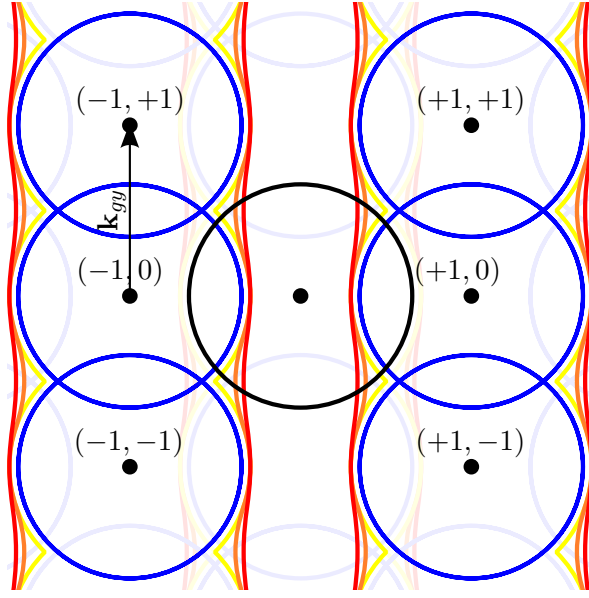


Figure 5.10: A sketch showing the expected iso-frequency contour deformation. Increased coupling efficiency in to the k_{gy} direction deforms the SPP iso-frequency contours; represented as increasing in coupling efficiency from poorly coupled together (yellow lines) to strongly coupled (red). The blue circles represent the diffracted light circles, and the black circle represents the zero-order (un-scattered) light circle, which is the area mapped by imaging scatterometry.

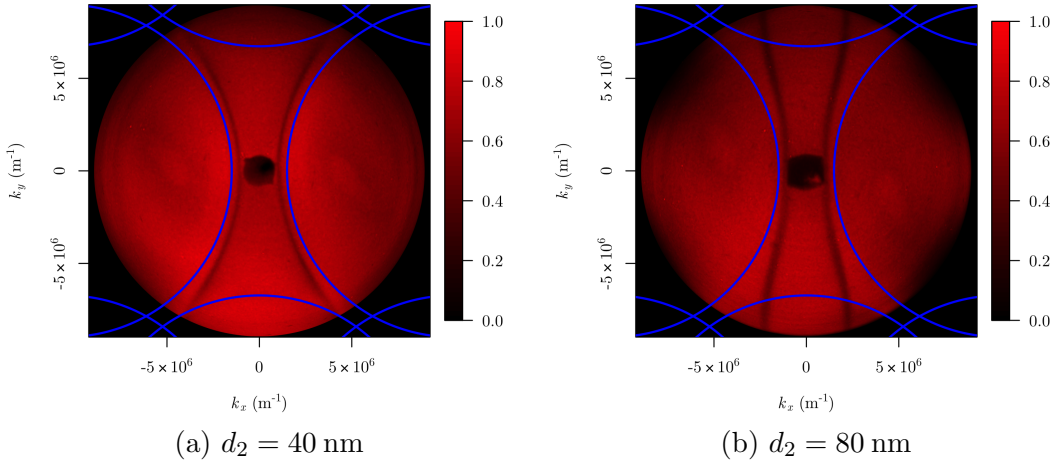


Figure 5.11: Experimental iso-frequency contours for two rectangular bigratings at a wavelength of $\lambda_0 = 700 \text{ nm}$ with (a) shallow orthogonal grooves of $d_2 = 30 \text{ nm}$ and (b) deep orthogonal grooves of $d_2 = 80 \text{ nm}$. The blue lines show the calculated position of the diffracted light circles, which unperturbed SPP contours will follow.

profile. The strength of this interaction causes the deformation in the value for k_{SPP} for different azimuthal angles. This interaction corresponds to the yellow SPP example contour drawn in figure 5.10, as the $(\pm 1, 0)$ modes which weakly interact with the $(\pm 1, \pm 1)$ and $(\mp 1, \pm 1)$ scattered modes.

By deepening the short-pitch grating to 80 nm this anisotropy is increased. This is seen clearly in the experimental results in figure 5.11(b) where the $(\pm 1, 0)$ scattered SPPs interact with the $(\pm 1, \pm 1)$ and $(\mp 1, \pm 1)$ scattered SPPs have served to flatten the SPP contours, pulling them away from their associated diffraction circles.

In both cases the interaction between the $(\pm 1, 0)$ and the $(0, \pm 1)$ scattered SPPs is not observed as the weak multiple scattering processes do not strongly couple the modes together. Further, the $(0, \pm 1)$ scattered SPPs are not seen in these scattergrams, as the polarisation has been selected to highlight only the $(\pm 1, 0)$ scattered modes for clarity.

Of interest is the effect of this increasing band gap on the SPPs travelling solely along the \mathbf{k}_x direction. Since the deepening of the short-pitch grating affects only the diffraction efficiency in the y -direction, it is not expected that the SPP travelling solely in the x -direction should be affected. Experiments show, however, that this is not the case. For the scattergrams in figure 5.11, along $k_y = 0$ we see that the SPP contour lies further from the diffraction circles in the deep grating case when compared to the shallow grating. Mapping the dispersion for these two gratings using the zero-order reflectivity maps as a function of (ω, k_x) we obtain the dispersion of the SPP modes in the plane of incidence containing k_x , and these are shown in figure 5.12.

The SPP bands in the deep grating case are suppressed in frequency compared to those obtained from the shallow grating. This frequency shift is seen more clearly in the spectral plots and overlay of the dispersions shown in figures 5.12(c) and 5.12(d). For the overlays of dispersion the reflectivity minima were taken as the SPP mode positions (as it will be travelling along an axis of mirror symmetry, polarisation conversion does not occur). These were extracted from the spectra of each plot for a given incidence angle and collated together.

The results show that the effective mode index of the SPP can be altered both in the k_x and k_y direction by increasing the depth of the short-pitch grating. This is analogous to the work of Pendry [72] and the subsequent work on ‘spoof’ surface plasmons [73], where surface structure is used to manipulate the asymptotic limit of surface wave dispersion, introducing the concept of an ‘effective surface plasma frequency’. We shall return to this conclusion in chapter 7, where we demonstrate that the short-pitch can be extremely sub-wavelength ($\lambda_{gy} = 150$ nm) and still affect the propagation of SPPs along grating surfaces.

5. Optical Response of Metallic Rectangular Bigratings

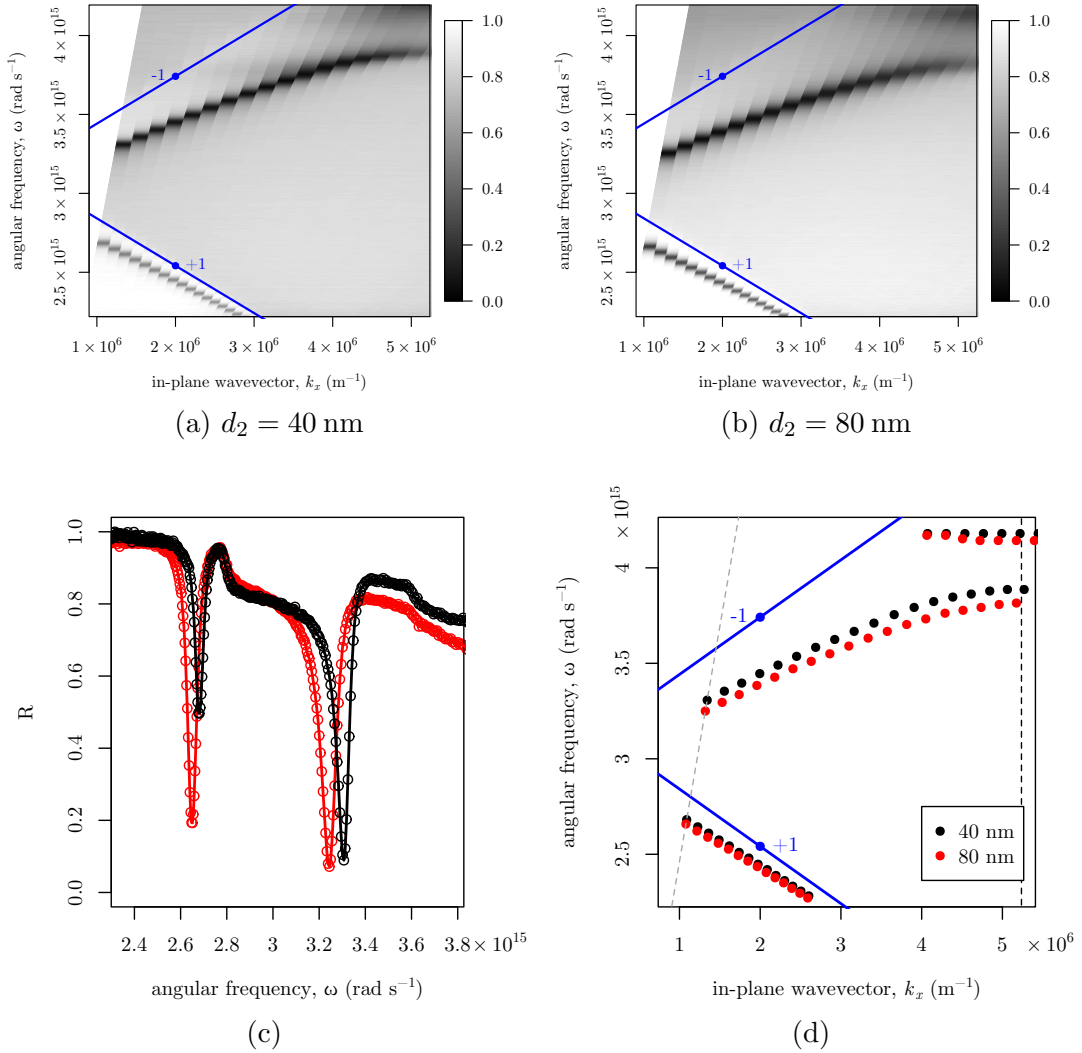


Figure 5.12: (a-b) Experimentally obtained dispersion diagrams mapped from the reflectance of rectangular bi-gratings with nominal depths of (a) 40 nm, (b) 80 nm. (c) The SPP mode position measured by reflection of TM polarised light at $\theta = 7^\circ$ as a function of angular frequency, ω . The curves are for the shallow (black) and deep (red) grating. The SPP mode shifts to lower frequencies as shown in (d).

5.6 Conclusions

In this chapter we have introduced the concept of a bigrating as a grating with two grating vectors which are not collinear. The example used in the chapter was the rectangular bigrating, which possesses two grating vectors of different magnitude, oriented at $\alpha = 90^\circ$.

The dispersion of these rectangular gratings was mapped from the reflectivity of the samples in section 5.3.2. It was found that small errors in mark-to-space ratio of such gratings lead to the strong coupling of even-ordered modes, which would not be expected to couple strongly on such a surface if the mark-to-space ratio was 1. A discussion as to the features associated with SPPs on such a surface has been presented. This will be a background to future discussions on dispersion mapping throughout this thesis.

Band gaps forming between the $+1\mathbf{k}_{gx}$ and $-1\mathbf{k}_{gx}$ scattered SPPs were experimentally observed using imaging scatterometry, as presented in section 5.3.3, demonstrating this technique for the first time. FEM modelling of the gratings show the field orientation for these SPP standing waves which occur at the BZ boundary.

In section 5.4 it was found that such rectangular bigratings exhibit polarisation conversion at $\phi = 45^\circ$, which is different from conventional square bigratings. This is attributed to the fact that SPPs propagating out of the plane of incidence inhabit an axis of broken mirror symmetry, and so may decay into either polarisation state.

Finally section 5.5 investigates the effect on SPP dispersion by deepening the short-pitch of the rectangular bigrating. It is found that the anisotropy of the SPP mode can be controlled by changing this depth, which controls the strength of coupling between counter-propagating SPP modes. Finally, the mode index of the in-plane SPP (travelling along the k_x direction) is also found to be affected slightly by the deepening of the orthogonal pitch.

Chapter 6

Optical Response of Metallic Oblique Bigratings

6.1 Introduction

In this chapter, we examine the propagation of SPPs on periodic surfaces with the lowest possible order of symmetry. The underlying Bravais lattice for these grating is oblique, containing no reflection or rotational symmetry operations, save for the one inversion operation shared by every possible Bravais lattice.

Section 6.2 discusses the oblique grating samples, their fabrication, the coordinate system used and the reciprocal space lattice for an oblique grating. A comparison between experiment and a theoretical model for a typical SPP iso-frequency contour in k -space on such a grating is presented in section 6.3. The mapped dispersion of SPPs on this geometry are recorded, with which their band-structure on the fabricated oblique gratings are explained. Polarisation conversion mediated by SPPs is also found on the oblique grating, with SPPs travelling in directions which are not in the plane of incidence rotating the reflected light's polarisation.

The most striking result in this chapter is that this low-symmetry class of grating is shown to be the only exception for the formation of band-gaps at Brillouin Zone (BZ) boundaries of all the 2D Bravais lattices. We show experimentally in section 6.5 that an SPP propagating across a BZ boundary does not split to form a band-gap, and offer a generalised symmetry discussion as to why this is so. The dispersion of SPPs along axes containing the unique points of high-symmetry on an oblique grating are obtained experimentally, and it is shown that for these discrete planes of incidence, SPP band-gaps at BZ boundaries are still formed due to the symmetry of these axes.

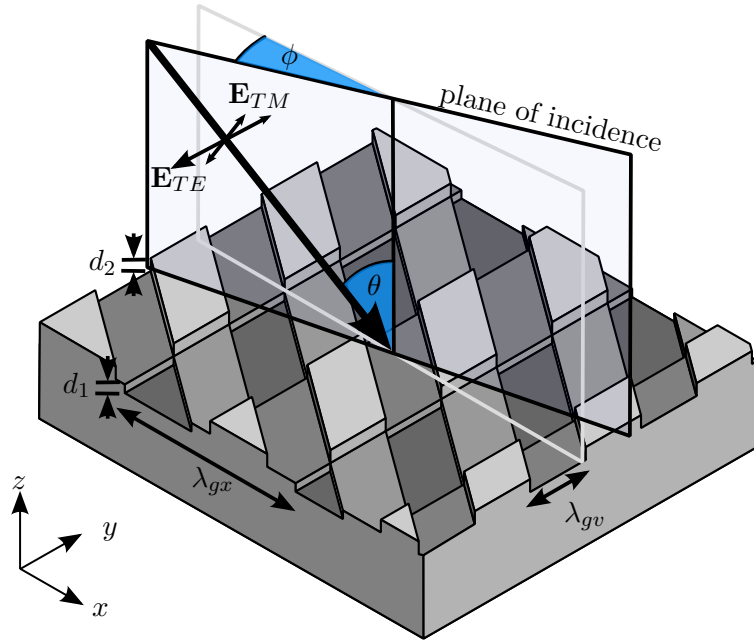


Figure 6.1: Coordinate system for an oblique bigrating. The typical design parameters used in this chapter are $\lambda_{gx} = 600 \text{ nm}$, $\lambda_{gy} = 400 \text{ nm}$, $\alpha = 75^\circ$, $d_1 = d_2 = 40 \text{ nm}$.

6.2 The Oblique Grating

An oblique lattice is formed of an infinite array of lattice points separated by two lattice vectors of different magnitudes, oriented at an angle with respect to each other α , such that $\alpha \neq 90^\circ$. To realise this symmetry using surface-relief gratings, two diffraction gratings of different pitches are ‘crossed’ at an angle α such that $\alpha \neq 90^\circ$, forming an oblique bigrating.

The coordinate system for this type of grating is shown in figure 6.1. The plane of incidence is defined at an azimuthal angle of ϕ so that when $\phi = 0^\circ$ the wavevector of incidence light lies along the x -direction. When the electric field vector of the impinging radiation is contained within the plane of incidence, the light is said to be TM polarised, and when the electric vector lies orthogonal to the plane, it is TE polarised. The x -direction is collinear with the grating vector $\mathbf{k}_{gx} = 2\pi\hat{\mathbf{x}}/\lambda_{gx}$ for the longer-pitch monograting, which possesses a periodicity of λ_{gx} . This period, for all the gratings presented in this chapter, is $\lambda_{gx} = 600 \text{ nm}$. The second, shorter-pitch grating lies at an angle of $\alpha = 75^\circ$ along the v axis (defined in the plane of the xy plane at an angle α to $\hat{\mathbf{x}}$) and for the grating presented in this chapter has a period $\lambda_{gv} = 400 \text{ nm}$. As before, the grating vector of this short-pitch grating is defined as $\mathbf{k}_{gv} = 2\pi\hat{\mathbf{v}}/\lambda_{gv}$. An angle of $\alpha = 75^\circ$ was chosen to lie midway between the high symmetry cases of $\alpha = 60^\circ$

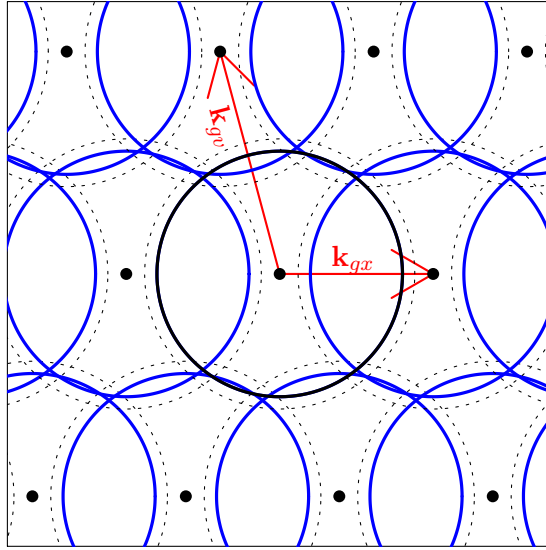


Figure 6.2: Example reciprocal lattices for an oblique grating. $\lambda_{gx} = 600$ nm, $\lambda_{gv} = 400$ nm and the angles between the two periodicities is $\alpha = 75^\circ$

(hexagonal-like) and $\alpha = 90^\circ$ (square/rectangular). The fill fraction of the gratings is designed as $\Gamma_x = \Gamma_v = 0.5$. The depths of the gratings are d_1 and d_2 , and are chosen in this chapter so that $d_1 = d_2 \approx 40$ nm.

The reciprocal space map of the corresponding lattice is shown in figure 6.2 and constitutes the lowest symmetry lattice set of all the two-dimensional Bravais lattices. The reciprocal lattice of the oblique grating is itself oblique, with the reciprocal lattice vectors defined as \mathbf{k}_{gx} and \mathbf{k}_{gv} , oriented at an angle $\alpha^* = 180^\circ - 75^\circ = 105^\circ$ with respect to each other. The only symmetry operation possible for this oblique lattice is a rotation around a lattice point of 180° , which for 2D lattices is the equivalent of a inversion operation. Centred about each lattice point are circles representing various scattered iso-frequency contours. The circles formed with solid lines show the contours for a grazing photon, and the dashed lines represent the iso-frequency contours for scattered SPPs which lie outside their respective grazing-photon lines (diffraction lines) due to the greater momentum of SPPs compared to light. In this simple cartoon, the SPPs do not interact and cross through each other unperturbed. However, if the SPPs interact to form band-gaps these iso-frequency contours will deform as detailed in chapter 4. The black circle is the case of the un-scattered zero-order light, which is the region of k -space accessible for mapping using the experimental method of imaging scatterometry.

The gratings for this chapter were fabricated using electron beam lithography (EBL)

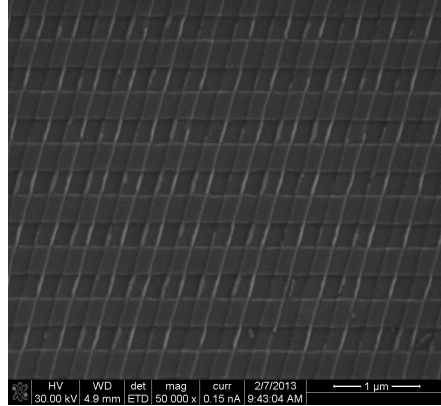


Figure 6.3: SEM of an oblique grating master fabricated in a silicon wafer.

and the template stripping method outlined in chapter 4. A scanning electron mircograph of a fabricated oblique grating master in silicon is shown in figure 6.3. The target parameters of this grating were $\lambda_{gx} = 600$ nm, $\lambda_{gv} = 400$ nm, $\Gamma_x = \Gamma_v = 0.5$, $d_1 = d_2 = 40$ nm.

6.3 Coupling of Light and SPP Mode Interaction on Oblique Gratings

A square profile grating such as those fabricated using EBL contain little or no even-Fourier components in their surface profile (see chapter 5). Consequently, the momentum of a plane wave incident on such a grating may be modified with direct scattering events with values of $\pm m\mathbf{k}_g$, where m is odd. A direct scattering event, where the plane wave is modified by $\pm n\mathbf{k}_g$, where n is even, is not possible on a grating where $\Gamma = 0.5$. There does exist, however, the opportunity for the plane wave to be modified by a total value of $\pm n\mathbf{k}_g$ through multiple-scattering processes, summing the contributions from $\pm m\mathbf{k}_g$ scattering events. These multiple scattering events are found in experiment to be so weak that they are rarely experimentally observed.

These scattering efficiencies also dictate the strength of interaction between counter-propagating SPP modes. Modes that are separated by a direct scattering event will interact strongly. Little, if any, interaction is observed for modes separated by the weaker multiple-scattering process.

Figure 6.4 shows the theoretical and experimentally measured iso-frequency contours for an oblique bigrating at $\lambda_0 = 700$ nm. Figure 6.4(a) shows the numerical prediction using the Chandeson method, approximating the square groove profiles with the Fourier

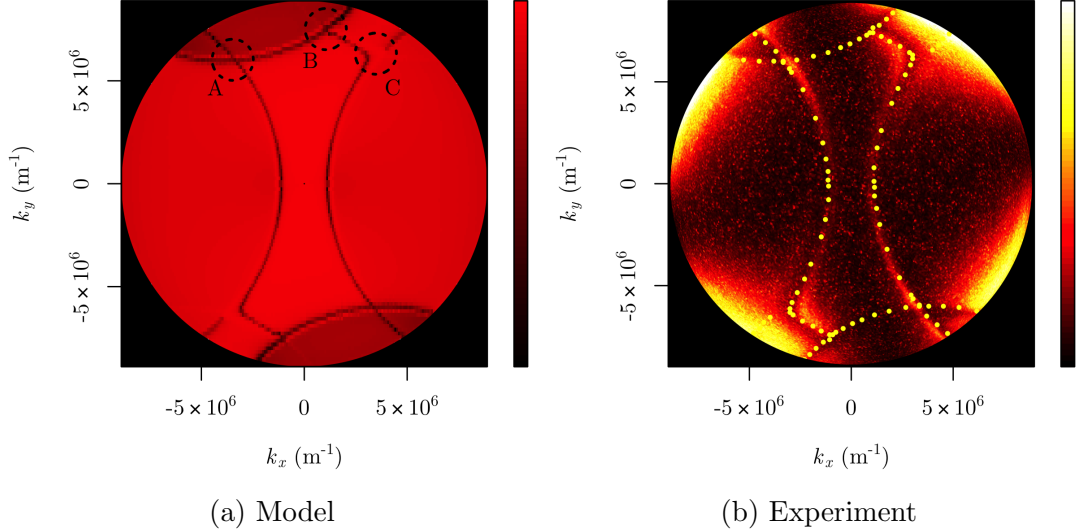


Figure 6.4: (a) The theoretically modelled iso-frequency surface for an oblique bigrating illuminated with TM polarisation at $\lambda_0 = 700$ nm. Mode intersections labelled A-C are discussed in section 4 (b) Experimentally obtained scattergram of the iso-frequency contour imaged through crossed polarisers. The yellow circles overlay indicates the theoretical mode position obtained from (a). Both colour bars range from low reflectivity (black) to high.

sums,

$$F(x) = \sum_{n=1}^3 \frac{4A}{n\pi} \cos \frac{2n\pi x}{\lambda_{gx}} \quad (6.1)$$

$$F(y) = \sum_{n=1}^3 \frac{4A}{n\pi} \cos \frac{2n\pi v}{\lambda_{gv}} \quad (6.2)$$

Providing a suitable approximation to a lamella bi-grating with a depth of $2A = 40$ nm, $\lambda_{gx} = 600$ nm, $\lambda_{gv} = 400$ nm, $\alpha = 75^\circ$ and $\Gamma = 0.5$. The dielectric function of silver is taken from literature [84], and for the illuminating wavelength of 700 nm is equal to $\epsilon = -23.13 + 0.59i$. The light in the theoretical plot is TM polarised for every azimuthal angle. Only the $n = 1, 3$ components are included in the calculation, as the even components are considered to be absent for a grating with $\Gamma = 0.5$.

The corresponding experimentally obtained iso-frequency surface is shown in figure 6.4(b). The contour is obtained using imaging scatterometry detailed in chapter 4. For the illuminating wavelength of 700 nm, the contrast of the entire SPP contour to the background is weak, making the determination of the mode position in k -space difficult.

6. Optical Response of Metallic Oblique Bigratings

To improve the contrast, the polarisers of the scatterometer are crossed, producing a dark background reflectivity against which the polarisation conversion mediated by the SPPs [34] provides greater contrast for the mode positions. The four bright lobes of high reflectivity is polarisation conversion mediated by the ellipsoidal mirror in the apparatus (see chapter 4).

The modelled values for the mode position (taken from the theoretical plot at the position of reflectivity minima) found in figure 6.4(a) are plotted on the experimental results in figure 6.4(b) as yellow circles, and show good agreement, especially considering the simplicity of the model. This shows that the dominant scattering amplitudes in the observable SPP band structure are only the $n = 1, 3$ components.

In the upper half-space of figure 6.4(a), three SPP contour crossings are labelled A-C*. Crossing point A is the meeting of a $(-1, 0)$ and a $(0, 1)$ Bragg scattered SPP contour. These two SPP curves are separated in k -space by a minimum of two scattering vectors, and so require a multiple scattering process to interact with each other. With no 2nd order harmonics in the grating profile, the interaction is weak and no band-gap is observed. The crossing point B is the intersection of the $(0, 1)$ and $(1, 1)$ SPPs. This is a process by which the SPPs must scatter a total of $1\mathbf{k}_{gx}$ to interact, and so a small band-gap forms. At point C, the $(1, 0)$ and $(1, 1)$ SPP cross. These are separated by a single scattering vector $1\mathbf{k}_{gv}$, and so interact, forming a large band-gap.

The coupling efficiencies of plane-polarised light to all these SPP modes is strong as the majority of the contours present are Bragg scattered back into the light circle by a single scattering vector, which is inherent in the grating profile. The exception is the $(1, 1)$ SPP, (the contour between points B and C), which is scattered back in to the light circle by a multiple scattering process. It is, however, observed quite strongly between points B and C, though not strongly (and observed as a weak bright band) outside of these points.

This coupling between points B and C is an example of SPPs ‘self-coupling’, the $(0, 1)$ and $(1, 0)$ SPPs coupling to the SPP contour close to the crossing points where there is a component of the SPPs that fulfil the required energy and momentum matching conditions for the $(1, 1)$ mode. These well coupled $(0, 1)$ and $(1, 0)$ SPPs resonantly drive the $(1, 1)$ SPP, resulting in its observation as a dark band.

These interactions can also be observed by mapping the dispersion relation of the SPPs by recording the zero-order reflectivity from the sample as a function of polar angle and wavelength. TE polarised light is incident on the sample and the reflectivity measured for the wavelength range $400 \text{ nm} < \lambda_0 < 850 \text{ nm}$ and the angle range $7^\circ < \theta < 75^\circ$ (see chapter 4). These experimental results are shown in figure

*These mode crossings are equivalent through an inversion symmetry operation to the crossings in the lower half-space

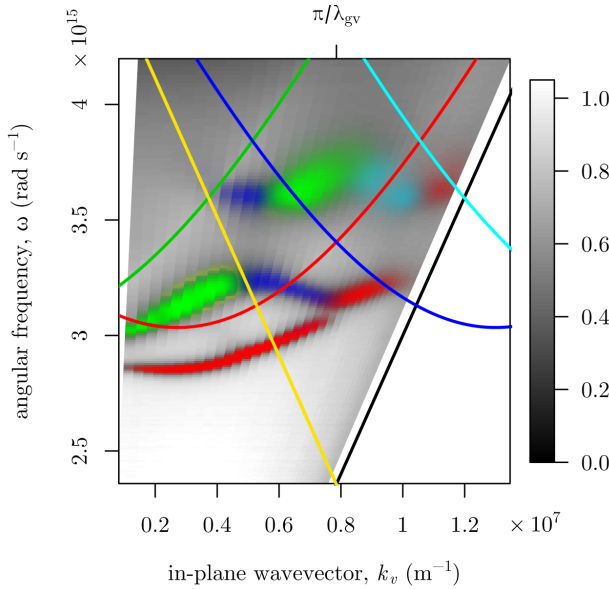


Figure 6.5: The dispersion of modes on an oblique grating for $\phi = \alpha = 75^\circ$, measured using the reflectivity as a function of polar angle and wavelength. The mode positions (grayscale minima) and calculated diffraction edges (lines) have been coloured to correspond to the scattered mode labels given in table 6.1.

(n, m)	(-1,0)	(1,0)	(1,1)	(-1,1)	(0,1)
(-1,0)				✓	
(1,0)			✓		
(1,1)		✓			✓
(-1,1)	✓				
(0,1)			✓		
Light	✓	✓			✓*

Table 6.1: The expected strong coupling (✓) between SPP modes. The colour of the (n, m) mode labels correspond to the highlighted modes in figure 6.5 scattered by $(n\mathbf{k}_{gx}, m\mathbf{k}_{gv})$. ✓* indicates coupling, but only for the orthogonal polarisation (TM) and so is not observed in figure 6.5.

[6.5](#) for an azimuthal angle of $\phi = 75^\circ$, with the plane of incidence containing \mathbf{k}_{gv} . To facilitate the discussion of mode interactions, the dark-bands of low reflectivity which map the SPP dispersion have been colour coded depending upon which dominant scattering event the SPP contour is associated with. The associated diffraction lines have also been coloured accordingly. These scattering interactions between the present modes are summarised in the companion table [6.1](#).

The band gaps are clearly observed for the interactions between the $(1, 0)$ scattered SPP band (green) and the $(1, 1)$ scattered SPP band (blue). Another large band-gap is observed for the interaction of the $(-1, 1)$ scattered SPP (cyan) and the $(-1, 0)$ scattered SPP (red), which again are SPPs separated in k -space by a single grating vector of $1\mathbf{k}_{gv}$.

A smaller band-gap is also observed for the $(-1, 0)$ and $(1, 1)$ SPP crossing (red and blue bands, respectively). This coupling is mediated either by multiple scattering events or a weak direct-scatter due to a small deviation in Γ away from the designed value of 0.5, and consequently the frequency gap formed is small in comparison to the other observed band-gaps.

The presence of a dark band associated with the $(1, 1)$ scattered SPP is clearly observed in the mapped dispersion and coloured as a blue band of low reflectivity, despite the $(1, 1)$ scattering event requiring multiple scattering with which to interact with zero-order light. This region of the dispersion is observed for the same reason the iso-frequency contour between points B and C in figure [6.4](#) is observed, a component of the $(-1, 0)$ and $(1, 0)$ SPP fields present on the surface resonantly drive this mode. The SPPs have ‘self-coupled’. A very small reflectivity minimum (not coloured) lies between the red $(-1, 0)$ and the green $(1, 0)$ scattered SPP bands. There is also weak self-coupling of these modes to the in-plane $(0, 1)$ SPP (its presence cannot be attributed to the incident light field, as the incident light’s polarisation state is incorrect for its excitation for this orientation).

6.4 Polarisation Conversion

In this section we discuss how SPPs on an oblique bigrating mediate the rotation of the incident field’s polarisation. An example is experimentally demonstrated in figure [6.6](#).

This figure shows the reflectivity of an oblique grating as a function of (ω, k_v) , mapping the SPP dispersion by the characteristic minima in reflected intensity. For subfigure [6.6\(a\)](#), the incident polarisation is set to be TE polarised, and the detector’s polariser is also set to TE. The corresponding polarisation conversion signal is recorded by rotating the detector’s polariser by 90° to TM, and is shown in figure [6.6\(b\)](#). The bright bands of polarisation converted signal lie along the same SPP contours, showing

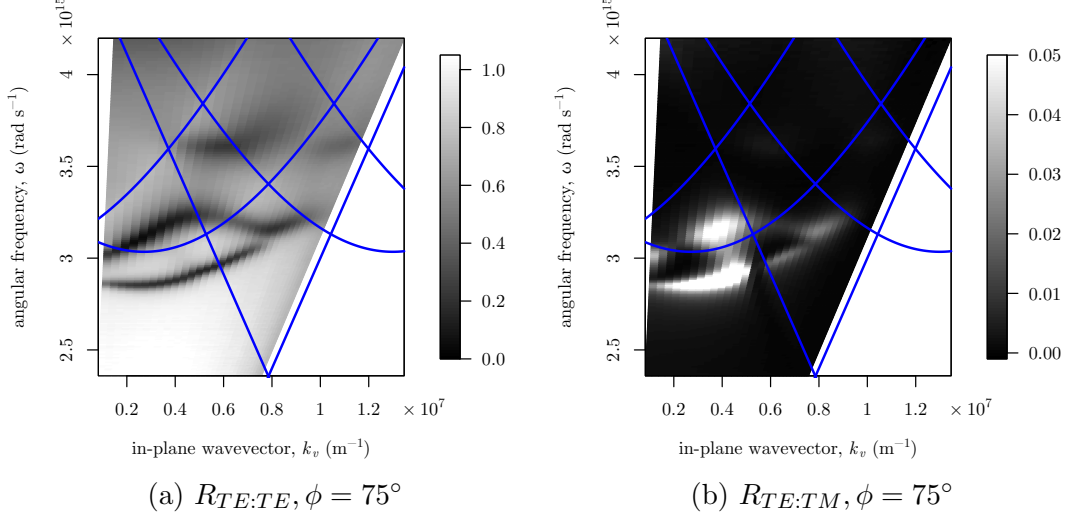


Figure 6.6: (a) Polarisation conservation and (b) conversion mediated by out-of-plane scattered SPPs on an oblique grating.

that it is the surface waves which mediate this polarisation conversion.

The polarisation converted signal is normalised to the reference spectrum with both polarisers set to TE polarised, and with this definition, only a maximum of $\approx 5\%$ of the light coupled into the SPPs is re-radiated in to the orthogonal polarisation state. Additionally, the SPP modes in the plane (which travel collinear to the wavevector \mathbf{k}_{gv}), do not participate in this polarisation conversion as the SPPs are travelling along a mirror-plane of the grating associated with the \mathbf{k}_{gv} direction (although there are no mirror planes associated with the overall bigrating structure). This is an important point: SPP mediated polarisation conversion occurs only when the SPPs are travelling along the surface in a direction out of the plane of incidence and along a direction of broken mirror symmetry. An oblique bigrating always provides out-of-plane scattering mechanisms and so polarisation conversion will always be observed for out-of-plane scattered SPPs. If, however, the plane of incidence contains a grating vector, conservation of momentum dictates that the SPP associated with this grating vector will travel along in the plane of incidence and polarisation conversion does not occur, even though the SPP is traversing a surface of broken symmetry.

6.5 SPPs at the BZ Boundary of Oblique Bigratings

The formation of photonic band-gaps on an oblique bigrating is of interest, as in this section we present results that show that on a surface with such broken symmetry

6. Optical Response of Metallic Oblique Bigratings

the locations in k -space of SPP standing waves do not necessarily occur at the BZ boundary. This concept is known for the band-gaps that occur for electron propagation in semiconductor crystals [120], but has not previously been demonstrated for SPPs on gratings. To show this clearly, we must identify how photonic band-gaps are illustrated in the iso-frequency contours recorded with imaging scatterometry. The iso-frequency image obtained using scatterometry maps k -space at a single frequency, with SPP bands seen as an anomaly in the reflected light. The group velocity of a general propagating wave is defined as,

$$\mathbf{v}_g = \nabla_k \omega(\mathbf{k}) \quad (6.3)$$

where \mathbf{v}_g is the group velocity, $\omega(\mathbf{k})$ is the angular frequency of the wave as a function of wavevector, \mathbf{k} , and ∇_k is the gradient operator with respect to k . For a small change in frequency $d\omega$, the corresponding small movement in k -space, $d\mathbf{k}$, is related to this group velocity simply by,

$$d\omega = \nabla_k \omega(\mathbf{k}) \cdot d\mathbf{k} \quad (6.4)$$

For an iso-frequency contour, there must be no change in frequency along the contour ($d\omega = 0$). Setting $d\omega = 0$ restricts the values of $d\mathbf{k}$ to those values that move along a contour of equal frequency. It is then apparent that in the resultant expression,

$$\mathbf{v}_g \cdot d\mathbf{k} = 0 \quad (6.5)$$

that \mathbf{v}_g lies perpendicular to $d\mathbf{k}$. This is true for any general contour of constant frequency. If the group velocity in one direction falls to zero at a boundary, such as at the BZ boundary, the iso-frequency SPP contour will intersect that boundary perpendicularly.

Plasmonic band-gaps on surface relief gratings are covered in chapter 2. To briefly recap, when a SPP meets an equivalent, counter-propagating SPP a standing wave forms. There are generally two possible arrangements of the electric field for a SPP standing wave on a grating, which will generally differ in energy. This leads to an upper and lower energy band, with an energy range between where SPP propagation is forbidden. The energy gap size is dependent on the energy of the two possible field distributions, and so is linked intimately to the surface geometry. The surface profile also provides the scattering mechanism by which SPPs Bragg scatter to meet counter-propagating SPPs and form these standing waves. The strength of this scattering, and so the amplitude of the Bragg scattered SPP, was discussed earlier in chapter 5 and affects the magnitude in energy of the band-gap.

Figure 6.7 shows the mapped iso-frequency contours of SPPs for the oblique grating at a wavelength of $\lambda_0 = 650$ nm. The position of the SPP contours are found to present

6. Optical Response of Metallic Oblique Bigratings

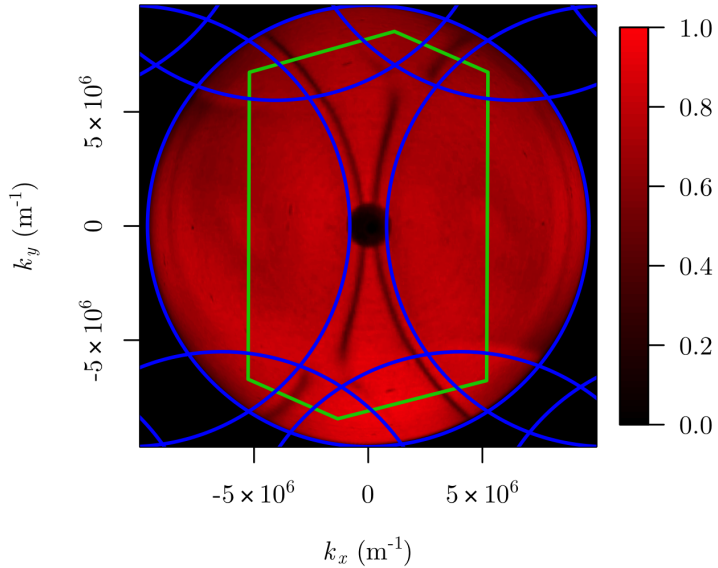


Figure 6.7: An experimentally obtained iso-frequency contour map of SPPs on an oblique bigrating with illuminated with incident light of wavelength $\lambda_0 = 650 \text{ nm}$. SPP positions are mapped as regions of low reflectivity. The blue circles indicate diffracted light circles, and the green region is the typical BZ boundary drawn using the Wigner-Seitz method.

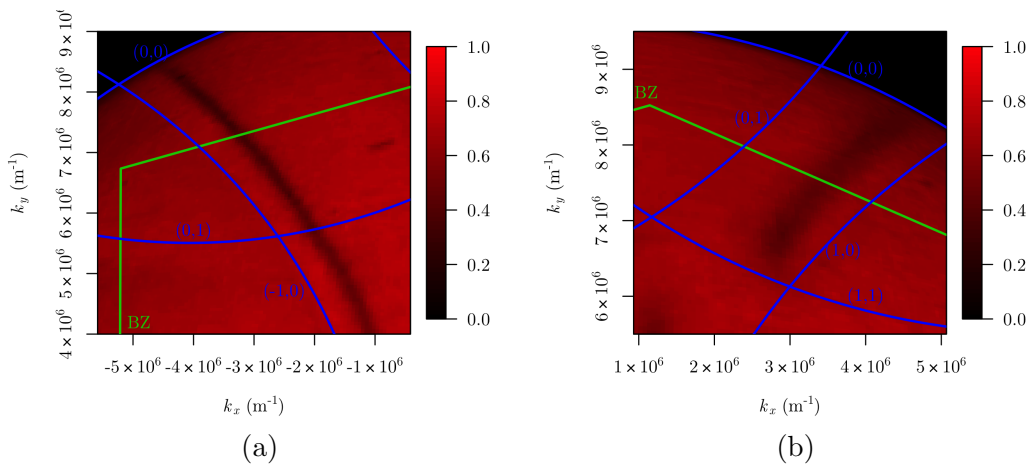


Figure 6.8: Regions of interest from figure 6.7. (a) The $(-1, 0)$ scattered SPP contour at the BZ boundary and (b) the $(+1, 0)$ scattered SPP contour at the BZ boundary.

6. Optical Response of Metallic Oblique Bigratings

as bands of low reflectivity, with the polariser of the experiment chosen in this case to best couple light to the $(\pm 1, 0)$ modes. Also annotated on the figure are the diffracted light circles (blue lines) and the BZ boundary formed using the Wigner-Seitz method [75] (green line).

It is observed that the SPP contour passes through the BZ boundary seemingly unperturbed. Figure 6.8 shows the two regions in which this occurs in greater detail. In figure 6.8(a) the SPP contour following the $(-1, 0)$ diffracted light circle is shown to pass through the BZ at an angle which is not perpendicular to the boundary. This means that at the boundary, the SPP's group velocity in the $(0, 1)$ direction is not zero, and no standing-wave states in this direction have formed. The $(0, 1)$ scattered SPP is not observed in this figure as the polarisation of the illuminating light has been chosen to only couple strongly to the $(1, 0)$ SPP. Additionally the $(-1, 0)$ and (uncoupled) $(0, 1)$ SPPs are not seen to interact, separated as they are by a weak multiple scattering process.

The same behaviour is observed in the second region in figure 6.8(b). Here, a band-gap has formed inside the BZ*, but the group velocity at the BZ boundary is still finite. This highlights the fact that the mode crossing positions on an oblique grating do not coincide with BZ boundary constructed using the Wigner-Seitz method.

A Brillioun Zone boundary in reciprocal space outlines a unit cell in the reciprocal lattice and contains on the boundary points of high-symmetry. One way to determine a boundary that contains the maximum amount of high-symmetry points is to connect the perpendicular bisectors of the vectors connecting the nearest neighbours to one lattice point, a method known as the Wigner-Seitz method. The area mapped out by this method, for the highly-symmetric cases of square, rectangular or hexagonal lattices, is exactly equivalent to the area we call the Brillioun Zone, and no other choice of unit cell contains as many points of high-symmetry in the boundary.

In the oblique case, we may again use the Wigner-Seitz method to construct a perfectly valid BZ, shown in figure 6.9 as the area bounded by a red line. In this figure, it is seen that the only points of high symmetry on the oblique lattice are the singular points lying midway along the perpendicular bisectors, and are labelled i_1, i_2 and i_3 . These points are equivalent to the points i_1^*, i_2^* and i_2^* by a rotation operation of 180° , and are isolated points of symmetry. However, this unit cell is not a unique choice, we can easily contain these points of high-symmetry lying on the boundary of a unit cell by using instead a trapezoidal unit cell, as shown by a blue line. In conclusion: The most primitive unit cell of an oblique lattice is not unique.

The arbitrary choice of the unit cell which contains the high symmetry points, and

*Recall that the SPP eigenmodes are unaffected by the coupling of the light, and so although some branches of the SPP contours are uncoupled to light in this scattergram, the band-gap still exists.

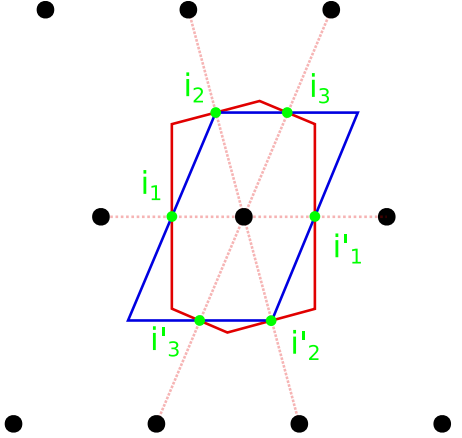


Figure 6.9: Two possible Brillouin Zones for an oblique lattice. The Wigner-Seitz cell (red) and a simple trapezium (blue) contain on their boundaries the points of high symmetry labelled i_1, i_2, i_3 .

that both choices is as useful as the conventional BZ in the oblique case, highlights that the properties of physical phenomena on the lattice are determined, not by the BZ boundary, but by the symmetry operations of the lattice.

Neumanns principle with respect to our system requires that the physical properties of phenomena associated with the grating possess the same symmetry as the point symmetry group of the grating [121]. While we could discuss specific propagation properties of the surface modes with respect to its lattice, let us instead generalize these concepts to some arbitrary vector field and see what restrictions the symmetry of the grating places upon it. Figure 6.10 shows an arbitrary vector, \mathbf{r} lying on the boundary of a rectangular or oblique unit cell. In the case of a rectangular grating, the mirror and translational symmetry allows the deduction of the other shown vectors through various reflections in the σ_v and σ_h planes or rotations about the C point. These vectors sum to give a magnitude of zero in the direction perpendicular to the zone boundary. Whether this vector field represents the SPPs momentum, group velocity or Poynting vector, the conclusion is the same: a standing wave forms perpendicular to the BZ boundary. In the plasmonic case, a SPP has Bragg-scattered and interfered with a counter-propagating SPP. The interference between these two SPPs, which by symmetry can be equal in magnitude and opposite in direction, forms a standing wave. The symmetry considerations we have outlined show us that this is possible, with no restrictions on a mirrored SPP occupying the same position and, importantly, that their vector properties will have equal magnitudes and so interfere completely. The two possible field arrangements for SPP standing waves on gratings lead to two solutions of different energies with a forbidden band of no propagating waves between the two: a

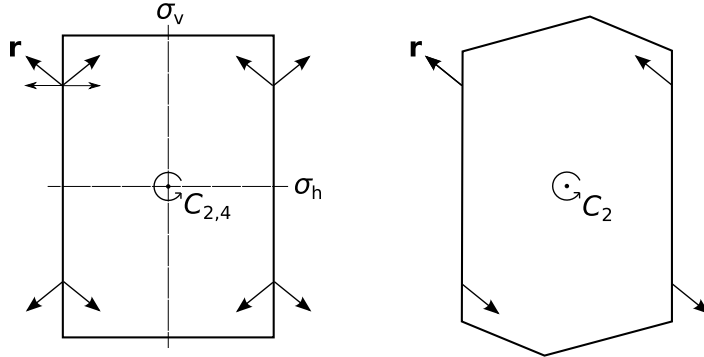


Figure 6.10: Applying the symmetry operations of the rectangular BZ (left), an arbitrary vector, \mathbf{r} (lying on the BZ boundary) corresponds to seven other vectors of known magnitude and direction. The summation of these vectors leads to no perpendicular component of the vector at the BZ boundary. In the oblique case (right), there is no such condition, the C_2 rotation operation only placing constraints on three additional vectors.

plasmonic band gap. These are observed experimentally as discontinuities of the SPP curves at the BZ boundary, as was seen in chapter 5.

Using the same approach, we apply the symmetry operations of the oblique lattice to an arbitrary vector field in figure 6.10. With no mirror symmetry, the oblique lattice possesses only translational and a two-fold rotation symmetry operations (a two fold rotation operation is equivalent in two dimensions to an inversion operation). As shown in the figure, there are no special conditions on the vectors lying along the BZ boundary formed using the Weigner-Seitz method, and no condition for the vectors to cancel perfectly. Standing waves do not necessarily occur at the BZ boundary.

This leads to the observation that the band-gaps observed do not form at the BZ boundaries, but simply where the SPP meets a Bragg scattered counter-propagating SPP. The mid-points of BZ boundaries are of high symmetry in both rectangular and oblique cases (points i_1, i_2, i_3 in figure 6.9), and do allow the total cancellation of our vector field. We can observe the points of zero group velocity at these BZ boundaries by mapping the dispersion of the SPP mode in the special cases of $\phi = 0^\circ$ and $\phi = 75^\circ$, which place the plane of incidence intersecting points i_1 and i_2 in figure 6.9. In these cases, we fully expect a band-gap to be present at the BZ boundary. These plots are shown in figure 6.11. In the case of a dispersion diagram such as this, zero group velocity is shown as $\partial\omega/\partial k_{||} = 0$.

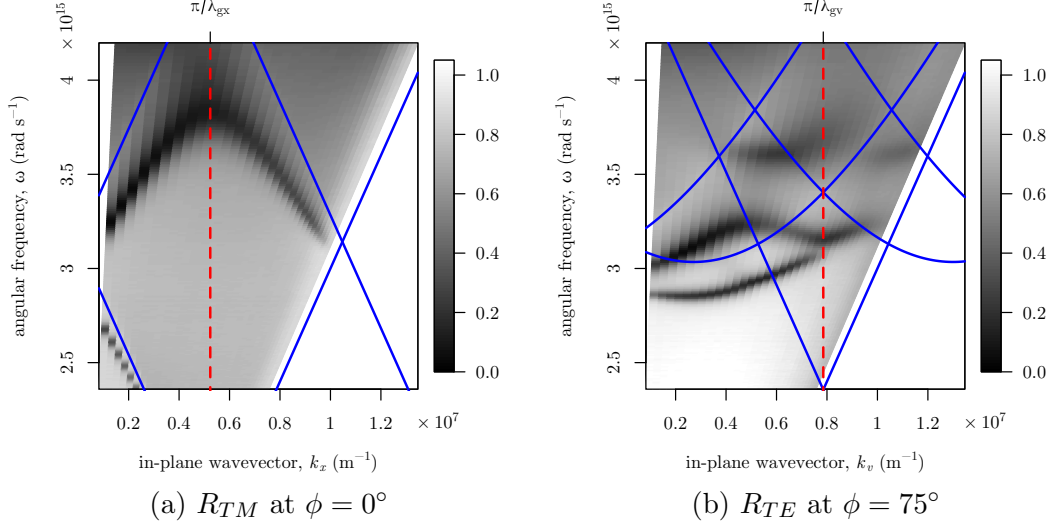


Figure 6.11: Dispersion plots mapped using the reflectivity of an oblique grating, showing the occurrence of band-gaps at the Brillouin Zones along the special cases of (a) $\phi = 0^\circ$ and (b) $\phi = 75^\circ$.

6.6 Conclusions

In this chapter, SPPs propagating on an oblique bigrating have been investigated. The dispersion of these surface modes has been mapped and the SPP interactions discussed in terms of the available scattering amplitudes of the grating. Polarisation conversion is observed on this grating, as SPPs travelling in a direction other than the plane of incidence mediate the rotation of the light's polarisation state.

Using imaging scatterometry, it is observed that the SPP contours are not perturbed as they pass through the conventional BZ boundary. A generalized discussion on the symmetry of the BZ is presented, concluding that this is because the BZ boundary on an oblique grating is not a contour of high symmetry, and only contain isolated points around which the symmetry conditions may be met for the formation of SPP standing waves. Finally, when the plane of incidence intersects these unique points, SPP band gaps may still be observed.

Chapter 7

Optical Response of Metallic Zigzag Bigratings

7.1 Background

This chapter introduces a novel type of diffraction grating, the zigzag grating. A detailed experimental and theoretical study of the SPPs excited on such a grating is explored, with interesting results pertaining to the polarisation requirements of the coupled light, the plasmonic band-gap character of interacting SPP modes, and the highly anisotropic propagation of SPP on such a grating.

In 2005, Kleemann et al. [122] presented a new method for designing diffractive optical elements with efficiencies and properties comparable to traditional surface relief gratings. These gratings use sub-wavelength features perpendicular to the diffractive periodicity to control the Fourier components available to scattering light [123]. The symmetry and structure of these sub-wavelength features control the diffraction efficiencies on such a grating, the way traditional surface relief gratings may ‘blaze’ their groove profile to achieve the same result [32]. These diffraction gratings can be produced using well established lithography techniques to pattern the surface, a simpler task than producing complicated and precise groove shapes on traditional blazed gratings. Kleemann et al. named these gratings Area Coded Effective medium structures (ACES), and the versions exhibiting similar characteristics to blazed surface-relief gratings ‘BLACES’. Surface Plasmon Polaritons were excited on such BLACES in 2009 by Bai et al.[95] and showed that asymmetrical excitation of the SPPs could be achieved at normal incidence, typical of the grating’s blazed character. It is established by this previous work that a patterned metallic surface with sub-wavelength features perpendicular to the diffractive periodicity is capable of manipulating the strength of diffracted orders and, consequently, the coupling of SPPs to light. The use of the sub-wavelength structure to manipulate

the optical response of these surfaces qualifies them as a type of ‘metamaterial’ surface [124].

In the work to date on BLACES, the propagation of the SPPs has been along an axis of mirror symmetry. Other work has hinted at novel optical effects, such as ‘magnetic mirrors’ [125, 126] or spatial control of coherent anti-Stokes emission [127], when plasmonic resonances are coupled to by light on geometries of broken symmetry.

In this chapter, we present a new ACES grating with sub-wavelength structure with a diffracting periodicity along an axis of broken mirror-symmetry. We name this grating a ‘zigzag’ grating. Coupling of light to SPPs on this grating is highly polarisation selective and both TM and TE polarised light can excite SPPs propagating in the same plane, which is theoretically investigated in section 7.3.1 and experimentally verified in sections 7.3.3 and 7.3.4. Further, we find that the symmetry of this grating places restraints on the formation of plasmonic band-gaps at Brillouin Zone (BZ) boundaries, which is explored in section 7.4 and that the propagation of SPPs is highly anisotropic with respect to azimuthal angle (section 7.5). The degree of SPP anisotropy is so great, that the zigzag grating is suggested as an excellent candidate for single-wavelength collimation of SPP beams for use in plasmonic circuits. This highly anisotropic SPP band structure leads to the observation of out-of-plane SPPs associated with the sub-wavelength periodicity, which evolve to have cavity-resonance character for deep zigzag gratings.

7.2 The Zigzag Grating

A diagram of a zigzag grating is shown in figure 7.1, including the coordinate system used throughout this chapter. The zigzag grating is formed of a surface-relief grating of sub-wavelength, and hence non-diffracting grooves that run along a silver surface. Perpendicular to this non-diffracting grating, the grooves are perturbed in the surface plane to introduce a long-pitch variation that may diffract visible light. This zigzag perturbation introduces a diffracting pitch of λ_{gx} , which lies perpendicular to the short-pitch of the surface-relief grating, λ_{gy} . In many ways, the zigzag geometry is similar to a conventional rectangular bi-grating, however, the long-pitch is present due to a zigzag surface perturbation (not surface-relief grooves). This makes the zigzag grating’s optical response quite unlike that of a standard bigrating .

The plane of incidence is defined at an azimuthal angle, ϕ , which equals 0° when the plane is coincident with the plane of diffraction from the long pitch. The polar angle θ of impinging radiation lies in the plane of incidence, and is defined as $\theta = 0^\circ$ when the light is incident normal to the average plane of the surface. The polarisation of the light is defined as Transverse Magnetic (TM) polarised when the electric field vector

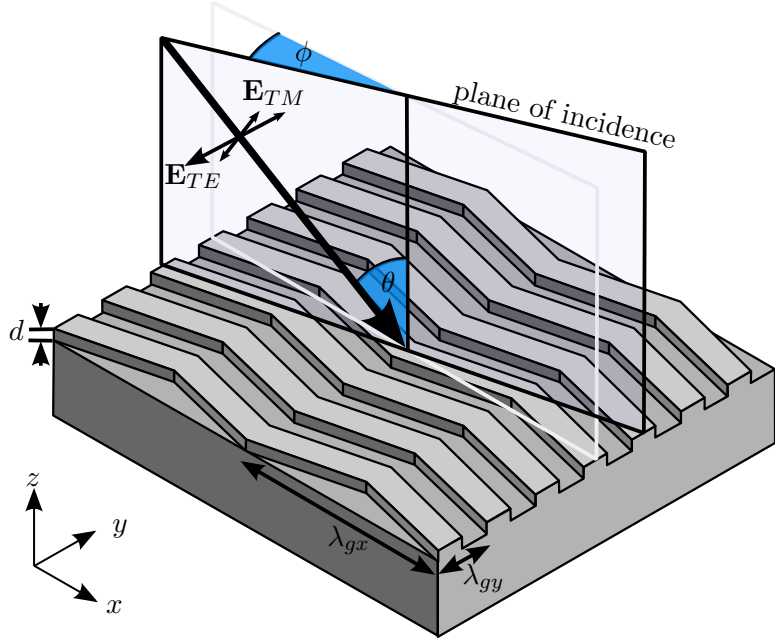


Figure 7.1: The coordinate system of a zigzag grating. The experimental sample parameters were $\lambda_{gx} = 600$ nm, $\lambda_{gy} = 150$ nm, $d = 29.9$ nm with the plane of incidence defined at an angle ϕ and the polar angle of incidence as θ . The two polarisation orientations for the electric field vector are also shown for TM and TE polarisations.

lies in this plane of incidence, and Transverse Electric (TE) polarised when the electric field vector lies orthogonal to it. The zigzag grating under consideration in this chapter possesses mirror symmetry along the yz planes defined at $x = 0, \lambda_{gx}/2, \lambda_{gx}$.

7.3 The Coupling of Plane Polarised Light to SPPs on Zigzag Gratings

7.3.1 Theory

To examine how the orientation of the electric field vector of impinging radiation may relate to the excitation of SPPs on a zigzag grating, we consider the magnitude of the electric vector that lies normal to the zigzag surface for the two polarisation cases of TM and TE polarised light. The induced local surface charge is, to a good approximation, proportional to the electric vector normal to the surface [128], so by considering how the local normal of electric field varies along the grating, we may infer what local surface charge arrangements are possible on such a grating. At normal incidence ($k_x = 0$), the wavevector of these different charge distributions are then equal to the Bragg vectors

7. Optical Response of Metallic Zigzag Bigratings

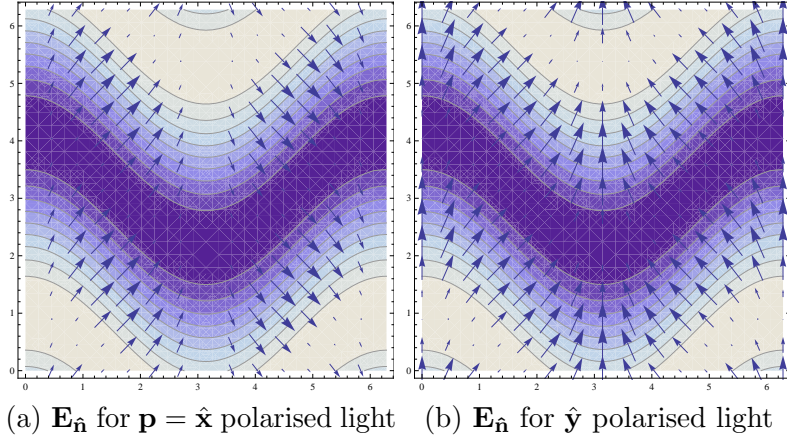


Figure 7.2: The surface normal components of electric field vector for (a) TM and (b) TE polarised light (arrows) projected on a contour of the zigzag surface profile. The contour plot amplitude ranges from 1 (white) to -1 (blue).

required of the zeroth order SPP to scatter and interact with light.

A simple expression for the local normal component of electric field can be obtained by considering an approximation to the zigzag surface given by,

$$\mathbf{r} = \mathbf{x} + \mathbf{y} + \cos(y - \cos x) \hat{\mathbf{z}} \quad (7.1)$$

representing a zigzag profile having unit amplitudes, and periodicities of 2π . At normal incidence to the xy plane, the polarisation vector of the electric field is defined as $\mathbf{p} = \hat{\mathbf{x}}$ for TM and $\mathbf{p} = \hat{\mathbf{y}}$ for TE polarisations. The normalized surface normal function is

$$\hat{\mathbf{n}} = \frac{\partial_x \mathbf{r} \times \partial_y \mathbf{r}}{|\partial_x \mathbf{r} \times \partial_y \mathbf{r}|} \quad (7.2)$$

To induce surface charge density at the interface, the electric field will require a component normal to the surface. The electric vector lying normal to the surface is then simply,

$$\mathbf{E}_{\hat{\mathbf{n}}} = (\hat{\mathbf{n}} \cdot \mathbf{p}) \hat{\mathbf{n}} \quad (7.3)$$

The normal electric field vector for each polarisation case is shown projected on to the approximated zigzag surface in figure 7.2. It is clear that *both* TM and TE polarisation vectors result in a surface normal component of electric field on the zigzag surface, and so may induce surface charge.

We can now examine the functional form of the allowed normal electric field in the propagation direction for a SPP. The components, E_{TE} and E_{TM} , of the electric field

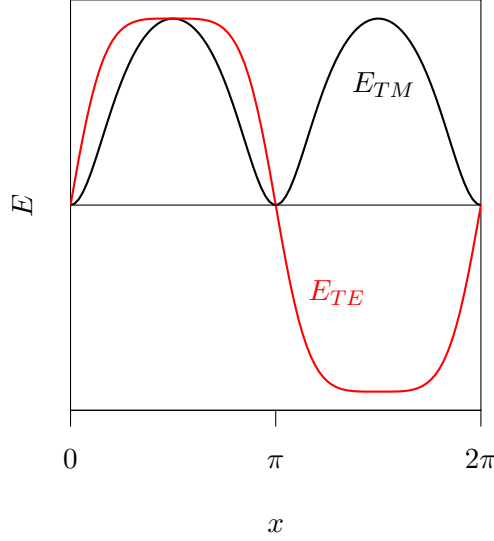


Figure 7.3: The magnitude of the surface normal electric field in the x-direction for TM and TE polarisations.

normal to the surface, lying along the direction of propagation (the \hat{x} direction) and integrated over y for the two polarisation cases are found to be,

$$E_{TM} = -\frac{4\pi \sin^2(x)}{\cos(2x) - 3} \quad (7.4)$$

$$E_{TE} = -\frac{4\pi \sin(x)}{\cos(2x) - 3} \quad (7.5)$$

Both E_{TE} and E_{TM} are non-zero, so we may conclude that either polarisation may induce surface charge and possibly excite SPPs. Plots of E_{TM} and E_{TE} in figure 7.3 show that the electric field vector normal to the surface varies spatially twice as fast for the TM case as for the TE case. This leads to the conclusion that the wavevector of a TM-coupled SPP is required to be twice that of the TE-coupled case. By expanding both these expressions as a Fourier sum in x , we may express the E_{TM} and E_{TE} as a sum of plane-waves. It is possible then to find which in-plane wavevectors of incident light are required to match these field profiles. Doing so yields,

$$E_{TE} = \sum_{n=1,3,5,\dots}^{\infty} a_n \cos(nx) \quad (7.6)$$

$$E_{TM} = a_0 + \sum_{n=2,4,6,\dots}^{\infty} b_n \sin(nx) \quad (7.7)$$

where a_n and b_n are the Fourier series coefficients. For incident light to match E_{TE} requires a series of only odd-ordered terms, while E_{TM} requires a series of only even-ordered terms. Diffracted fields at the surface will contain both odd and even wavevector components. Equations 7.6 and 7.7 predict that TE polarised light will provide a suitable electric field distribution to enable the excitation of SPPs via only odd-ordered diffracted orders, while TM polarised light will excite SPPs only via even-ordered diffracted orders. This concept will be discussed again with reference to the experimental and modelled results in sections 7.3.3 and 7.3.4.

We can visualise these coupling conditions in a simplistic diagrammatic way, shown in figure 7.4. Choosing the electric field vector to be at a single instance in time, we consider the effect on the charge carriers under the influence of this (effectively DC) field. The arrangement of these charges is illustrated in figure 7.4. These arrangements lead to an electric potential across the width of the grooves, with zero field along the lines connecting the zigzag apexes (red dots). The component of the respective electric fields along the plane of incidence (red arrows) is clearly different in both cases, with the TM field distribution varying twice as fast as the TE distribution in the plane of incidence. Crucially, neither solution for the TE or TM field arrangement along the x -axis is zero, meaning that charge density may be induced by either TE and TM polarisations. Returning to the periodicity of the fields, it is clear that the TM case has a wavelength equal to $\lambda_{gx}/2$, while the TE case has a wavelength equal to λ_{gx} . To resonantly drive these fields with incident light, the impinging field must match the wavevector of these surface plasmon field distributions ($2\mathbf{k}_{gx}$ for the TM case, \mathbf{k}_{gx} for the TE case). This is achieved via diffraction coupling, with first order diffraction $\mathbf{k}_0 \pm \mathbf{k}_{gx}$ matching the fields of the TE case, and the second order diffraction, $\mathbf{k}_0 \pm 2\mathbf{k}_{gx}$ matching the field of the TM case. As such, the polarisation selectivity of coupling diffracted light to the surface plasmons is demonstrated.

7.3.2 Samples

A schematic of the experimental sample is shown in figure 7.1, comprising of a grating with a 600 ± 5 nm zigzag pitch (λ_{gx}) to provide diffractive coupling to the SPPs. The periodicity of the non-diffracting surface-relief grooves (λ_{gy}) is 150 ± 5 nm. A master of the zigzag grating was produced in silicon using electron beam lithography, as detailed in chapter 4. The pattern was exposed in PMMA using a write field of $400 \mu\text{m}$ and a write field stitching error on the order of 20 nm. The exposed pattern was developed and reactive ion etched into a Si master. This produced a 2.5 mm^2 grating on a silicon wafer. A scanning electron micrography of one such master is shown in figure 7.5(a).

Results from two different versions of this zigzag grating sample are presented in this

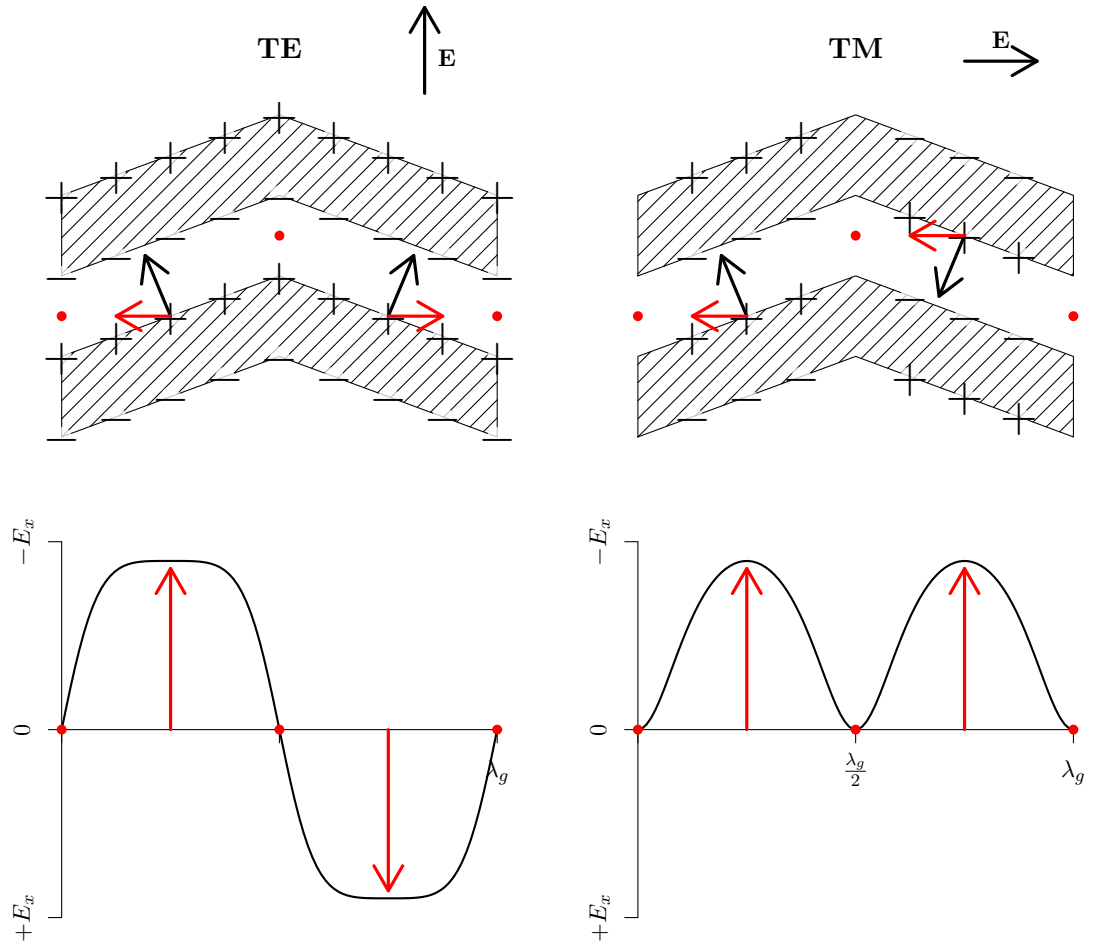


Figure 7.4: Schematic cartoon of light coupling to SPPs on a zigzag grating. The top cartoons depict a zigzag cavity bounded by two metal zigzag ‘peaks’ (hatched areas) for a typical zigzag grating as investigated in this chapter. The left images show the case of TE polarised light, with the TM case on the right. The field applied for both polarisation cases lead to positive (+) and negative (−) charge distributions along the grooves. The component of electric field in the x -direction originating due to these charge arrangements is shown in red.

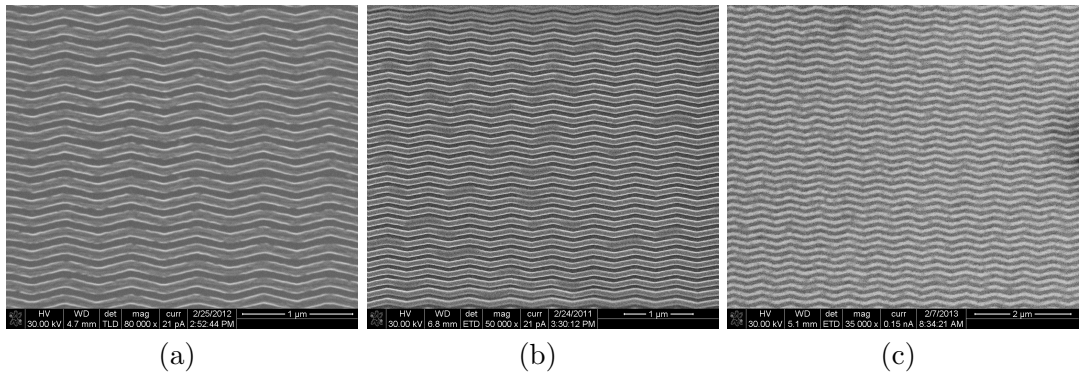


Figure 7.5: Scanning electron micrographs of: (a) an example template-strip master in Si, used for production of zigzag gratings; (b) a polymer replica of a Si master prior to metallisation, for zigzag gratings embedded in glass; (c) a template stripped sample in silver.

chapter. One is a zigzag grating produced by the template stripping method detailed in chapter 4, the SPPs propagating along the air/metal interface. The second sample is the same zigzag grating embedded in glass, so that the SPPs propagate along the glass/metal interface. The reason for the two samples is that observation of novel higher-frequency modes, such as the 3rd order diffracted SPPs, may be out of the visible domain when the SPP propagates along the air/metal interface. Using a higher index bounding material, the phase velocity of the SPPs is reduced and so for the same value of in-plane momentum, these modes may be brought down in frequency into the visible domain. The glass/grating sample was produced using a slightly different embossing method, detailed below. In each section, the grating used is clearly stated at the start.

For the glass/grating sample, the structure was duplicated in UV-cured polymer. Scanning electron microscopy was used to image the surface of this zigzag grating replica in the polymer (figure 7.5(b)), prior to metallisation. From this micrograph, the mark-to-space ratio of the final grating structure was determined to be 0.75 with $\lambda_{gx} = 600 \pm 5$ nm, and $\lambda_{gy} = 150 \pm 5$ nm. This pattern was then transferred to another UV cured polymer (Norland Optical Adhesive 73) adhered to a glass substrate ($n_{632.8\text{ nm}} = 1.518$) using an embossing method. Silver was thermally evaporated under high vacuum (5×10^{-6} mbar) with 50 nm depositions followed by 10 minutes relaxation time repeated until an optically thick layer of 200 nm was recorded on the quartz crystal thickness monitor. This stepped procedure was used to prevent the temperature rising on the substrate enough to damage the polymer. The substrate was then adhered to the back of a prepared glass hemisphere of radius 21.75 mm and refractive index $n = 1.518$ using index matching fluid, the base of the hemisphere having been modified

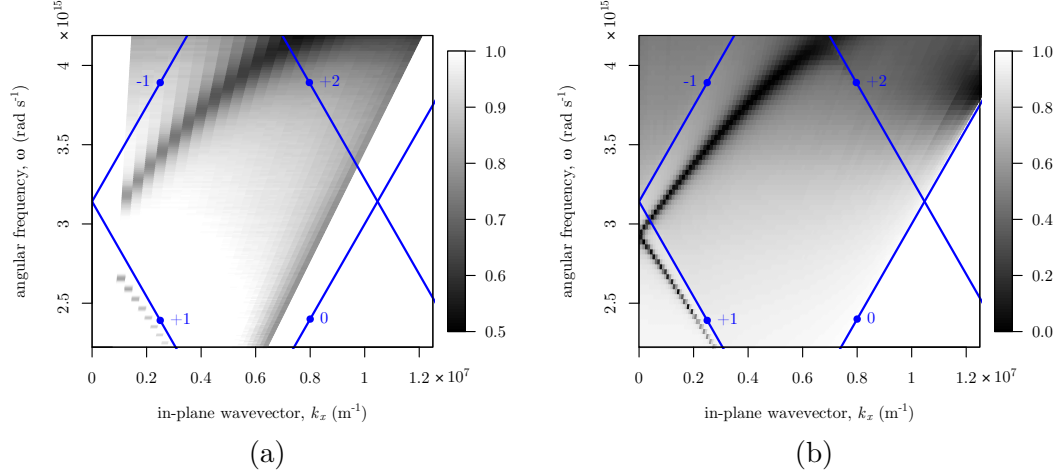


Figure 7.6: Experimental data (a) and FEM model prediction (b) of TE polarised reflectivity as a function of in-plane wavevector and angular frequency, mapping SPP dispersion on a zigzag grating. Blue lines show the positions of diffracted light lines scattered by $m\mathbf{k}_{gx}$, where $m = \pm 1, +2, 0$

by removing 1 mm to account for the affixed substrate thickness. This arrangement allows illumination of the embedded grating structure at the metal/glass interface at all angles of incidence. The mounting also protects the surface of the silver from sulphur contamination [129].

7.3.3 Transverse Electric Coupling

The dispersion of the SPPs supported on a zigzag grating is mapped as a function of in plane wavevector, \mathbf{k}_{gx} , by varying the polar angle θ and angular frequency, ω , using a polarised, collimated, monochromatic beam, produced by a white light source together with a spectrometer. The wavelength range used was $400 < \lambda_0 < 850$ nm with the angle range $7^\circ < \theta < 60^\circ$ (see chapter 4). When the energy and in-plane momentum of the light matches that of a SPP mode, the light couples to a SPP and an extremum of the reflectivity is observed. The experimental and theoretical reflectivity of incident TE polarised light at $\phi = 0^\circ$ is shown in figure 7.6, for a zigzag grating in air.

Two dark bands of low reflectivity are observed associated with the $\pm\mathbf{k}_{gx}$ light lines (blue lines). These bands map the position in $\omega - k_x$ space of SPPs scattered by grating vectors equal to $\mathbf{k}_{SPP} = \mathbf{k}_x \pm \mathbf{k}_{gx}$. As predicted by equation 7.7, this odd-scattered mode is coupled to by TE polarised light. The dispersion of the mode in the experimental data (figure 7.6(a)) and theoretical model obtained using FEM (figure 7.6(b)) show excellent agreement. The model parameters used were for a depth of 70 nm and a

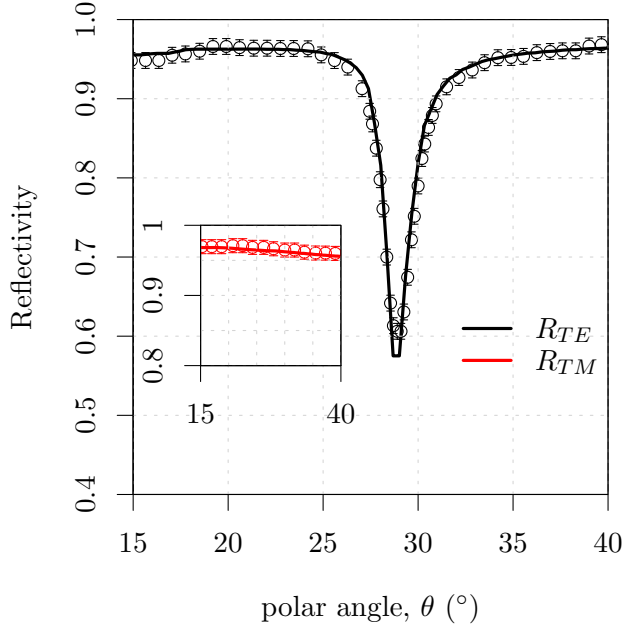


Figure 7.7: Specular reflectivity of TE (black) and TM (red) polarised light as a function of polar angle, θ , for a wavelength of 632.8 nm, $\phi = 0^\circ$. Circles: recorded data with error bars of 1%, line: fitted FEM model prediction.

mark-to-space ratio between the sub-wavelength grooves of 1, using the silver dielectric function as reported by Nash & Sambles [84]. The experimental sample is expected to be shallower than the designed 70 nm from duplication, leading to the observation that the experimental SPP is not coupled optimally to the incident light, and so the reflectivity band is not as dark as the FEM prediction.

This band of low reflectivity is investigated further in figure 7.7. The reflected intensity of light from a zigzag grating embedded in glass is illuminated with TE polarised light, at a wavelength of 632.8 nm, and recorded as a function of the polar angle of incidence, θ . At $\theta = 28^\circ$, a minimum is observed in the TE reflectivity from the grating close to the first-order diffraction edge (calculated as $\theta = 18^\circ$), indicative of the excitation of a SPP that has been scattered by one grating vector, \mathbf{k}_{gx} . Incident light resonantly couples to this diffracted SPP and is scattered back in to the specular order with π phase retardation [130]. Out of phase with the specular reflection, a dark band is observed with the missing energy being dissipated as Joule heating. For comparison, the excitation of an in-plane SPP such as this on a mono-grating or bi-grating would require

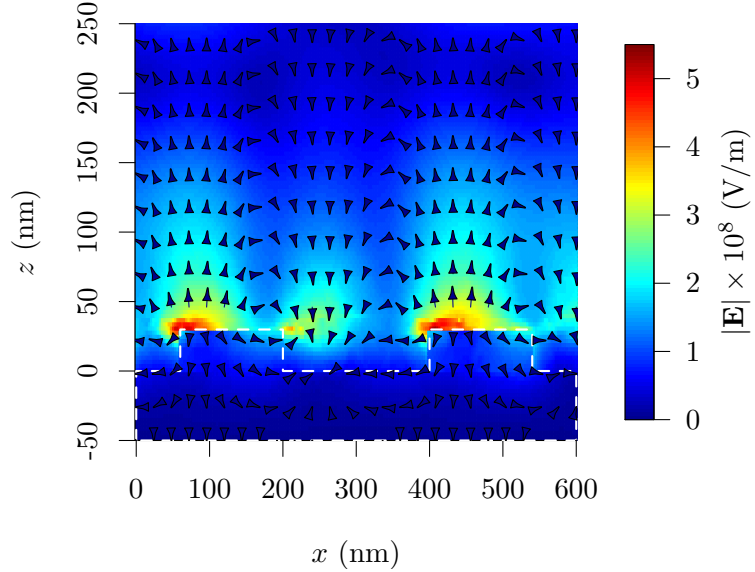


Figure 7.8: The \mathbf{E} field plot of a SPP excited by TE radiation found in figure 7.7, obtained by FEM. The colour scale shows the magnitude of the electric vector, \mathbf{E} , for a cross section of the zigzag grating, in the plane of SPP propagation (\parallel to $\hat{\mathbf{x}}$). The arrows show the direction of the electric vector over space. The electric field phase chosen for this travelling wave is arbitrary.

the light to be TM polarised. However, on this zigzag grating for a SPP Bragg scattered by \mathbf{k}_{gx} , excitation with TM polarised light is forbidden (see 7.3.1) and no minimum in the TM data is observed. The data show excellent agreement with the theoretical reflectivity obtained from finite element method (FEM) modelling, also shown in figure 7.7, with fitting parameters of $\lambda_{632.8\text{nm}} = -17.5 + 0.55i$, a groove depth of 29.9 nm. The mark-to-space ratio of 0.75 in the model was determined from the electron micrographs (figure 7.5(b)). These fitting parameters confirm that the grating was indeed shallowed in the fabrication process. Surface roughness and small groove profile changes from the embossing method are not accounted for in the modelling.

Using the fitted FEM model, the magnitude of the electric field in the xz plane is plotted for this SPP mode in figure 7.8. The electric field is evanescently confined to the surface with the field maximum occurring near the top, flat surface of the zigzags at $z = d = 29.9$ nm and exponentially decaying away into both the air and the metal. The SPP for this wavelength and angle propagates along the zigzag with a wavevector given by $k_{SPP} = nk_0 \sin \theta - k_{gx} = 1.67k_{gx}$, corresponding to a SPP wavelength of $\lambda_{SPP} = 358$ nm. The plane of intersection and temporal phase of the wave is arbitrarily and chosen for the figure as $y = 70$ nm and 0° phase, respectively. The propagation of the SPP along the zigzag, rather than over the grooves, has important consequences for

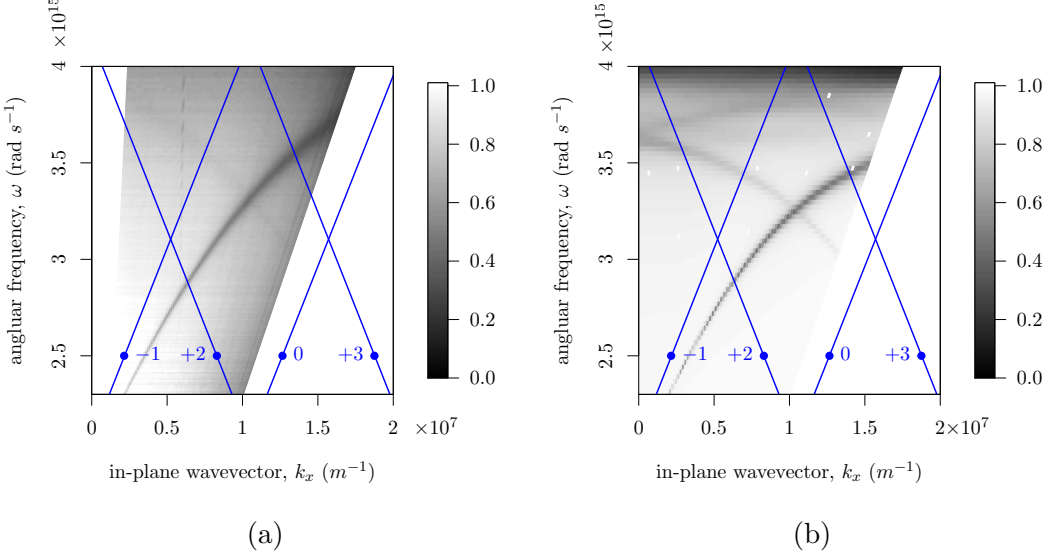


Figure 7.9: (a) Experimental data and (b) numerically modelled results of the TE polarised reflectivity as a function of in-plane wavevector and angular frequency, mapping the SPP dispersion on a zigzag grating in glass. Blue lines show the positions of diffracted light lines scattered by $m\mathbf{k}_{gx}$, where $m = 1, +2, 0, +3$.

the band structure for SPPs on this type of surface, and will be discussed in section 7.4.

It is desirable to fully confirm the coupling conditions outlined in equation 7.7 for other odd-order diffracted modes, rather than just the $\pm\mathbf{k}_{gx}$ scattered SPP. By embedding a zigzag grating in a higher refractive index, such as glass, we are able to access the $+3\mathbf{k}_{gx}$ scattered SPP using visible frequency radiation. The experimentally obtained dispersion of the SPPs on the glass/metal interface is mapped as a function of in plane wavevector, \mathbf{k}_{gx} , by varying the polar angle θ and angular frequency, ω , using a polarised, collimated, monochromatic beam, produced by a white light source together with a spectrometer, in the wavelength range $400 < \lambda_0 < 850$ nm. The reflectivity of incident TE polarised light at $\phi = 0^\circ$ is shown in figure 7.9(a).

With the grating embedded in glass two Bragg-scattered SPP dispersion curves are observed for this polarisation case. One originates at $-\mathbf{k}_{gx}$ and the other at $+3\mathbf{k}_{gx}$. These odd-order diffracted SPPs are excited by TE polarised light. There is no evidence of a SPP dispersion curve from a $+2\mathbf{k}_{gx}$ scattering event as, on a zigzag grating, it is not excited by TE polarised light as predicted by equation 7.7. Using the fitted parameters from figure 7.7, the dispersion plots were reproduced from FEM modelling and found to be in good agreement and are shown in figure 7.9(b). The small difference between the model asymptotic limits of the SPPs and experiment may be attributed to

the differences between the dielectric function of silver used for the model [84] and our experimental sample.

In summary, the SPPs are shown to be excited on the zigzag grating, with TE polarised light coupling to the odd-order Bragg scattered SPPs. The dispersion of the SPPs has been mapped for the two cases of the grating in air and in glass, and agrees well with a numerical model. No even-order modes are observed when the sample is illuminated with TE polarised light. There is no excitation of odd-order modes with TM polarised light.

7.3.4 Transverse Magnetic Coupling

The observation of even-order Bragg scattered SPP modes coupled to by TM radiation is expected from the allowed charge distributions examined in section 7.3.1. For our sample, the experimental observation of this mode is difficult, as the zigzag grating is not optimally coupled to the SPP due to shallowing of the grating during fabrication, and the even-ordered diffraction is also very weak, only mediated by multiple scattering processes of $\pm \mathbf{k}_{gx}$.

To investigate the weak coupling of TM polarised light to the $+2\mathbf{k}_{gx}$ SPP, spectral plots are analysed for a range of angles for which, theoretically, only the $2\mathbf{k}_{gx}$ SPP can be present. A zigzag grating in air was investigated over an angle range of $(39^\circ < \theta < 55^\circ)$, to remove the ambiguity of which SPP mode is under observation. Comparison to the TE reflectivity, which should not couple to the SPP, further helps identify the mode. An example spectrum for both TE and TM polarised illumination at $\theta = 53^\circ$ is shown in figure 7.10. There is a clear broad absorption of the light in the TM case which is missing from the TE case, reducing the reflectivity by approximately 7%.

Both the TE and TM reflectivity drop at higher frequencies due to the UV absorption inherent in the optical response of silver. To remove this high frequency absorption and better judge the position of the broad reflectivity discontinuity associated with a weakly coupled SPP, the TE and TM reflectivity may be normalized with respect to each other. The TE reflectivity spectra, containing no observed SPP modes but containing the higher frequency absorption of silver, may be used to normalize the TM data and remove the high frequency silver absorption. This allows a greater accuracy in the determination of the broad TM coupled SPP mode's position in frequency, which is judged by the fitting of a Gaussian curve to the local maximum of the normalized reflectivity in figure 7.11(a). To further confirm that this reflectivity anomaly is due to the weak excitation of the $+2\mathbf{k}_{gx}$ scattered SPP, the dispersion of this mode in frequency for the angle range $39^\circ < \theta < 55^\circ$ is plotted on the modelled dispersion of the 2nd order mode in figure 7.11(b), obtained from the same FEM model that showed

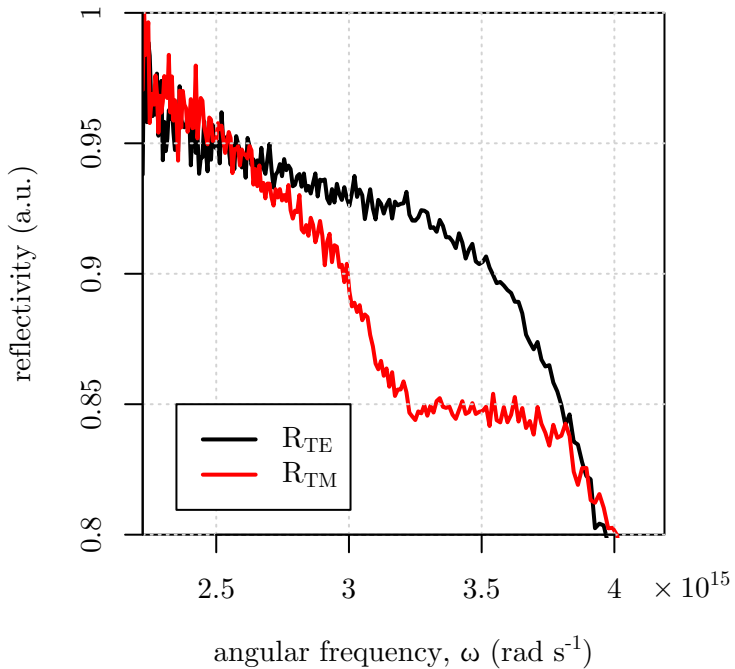


Figure 7.10: An example experimental reflectivity plot for TE and TM polarised light in the visible range at a fixed polar angle of $\theta = 53^\circ$. The broad absorption in the TM case is attributed to the weak excitation of a $+2\mathbf{k}_{gx}$ scattered SPP.

excellent agreement for the TE case in figure 7.6. The SPP mode dispersion is found to be in good agreement with the theoretical prediction for the $+2\mathbf{k}_{gx}$ scattered SPP, and we conclude that this 2^{nd} order mode is excited by TM polarised radiation, and is not excited by TE polarised light, in agreement with section 7.3.1.

Figure 7.12 shows the dispersion of the SPPs on the zigzag grating embedded in glass and mapped by using TM polarised light, obtained both experimentally and using FEM modelling. The only noticeable feature is a band of low reflectivity at high frequency, which does not appear to be associated with any of the in-plane diffracted light lines. This absorption of light is due to the excitation of a SPP that has been scattered by an out-of-plane grating vector, (\mathbf{k}_{gy}) , and is observed as a flat parabolic curve. The explanation of this SPP band's shape for out-of-plane scattered SPPs intersecting the plane of incidence can be found previously in chapter 2. Both the experimental and theoretical figures show this band, although the experimental band lies at a higher frequency compared to the theoretical curve, due to the difference in the metal's dielectric function between that of the experimental sample and the values used

7. Optical Response of Metallic Zigzag Bigratings

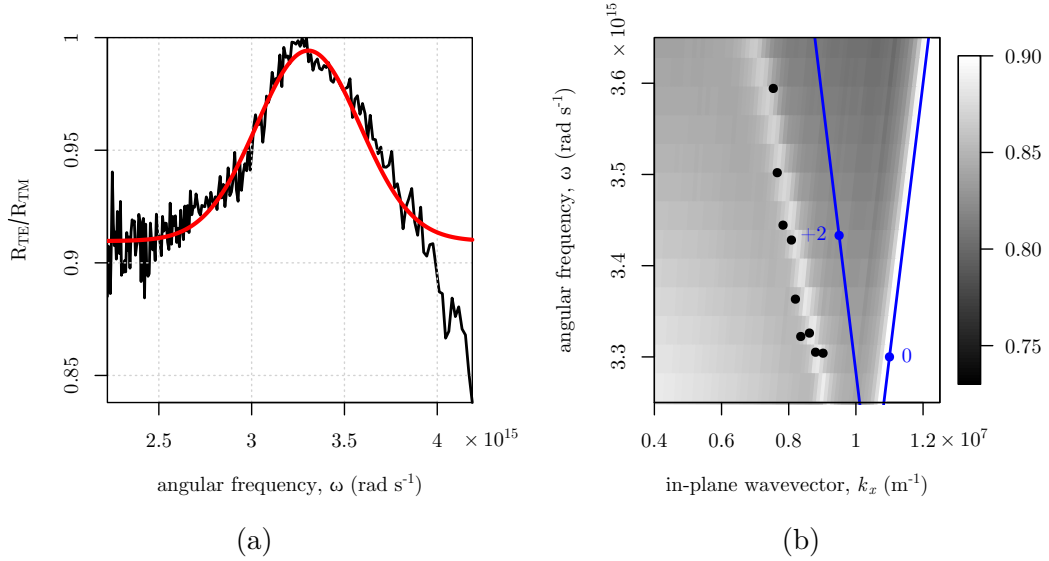


Figure 7.11: (a) An example spectral plot and fit at $\theta = 53^\circ$ for the TM reflectivity normalised to the TE reflectivity. (b) comparison between theory (greyscale) and experiment (black points) for a range of angles ($39^\circ < \theta < 55^\circ$).

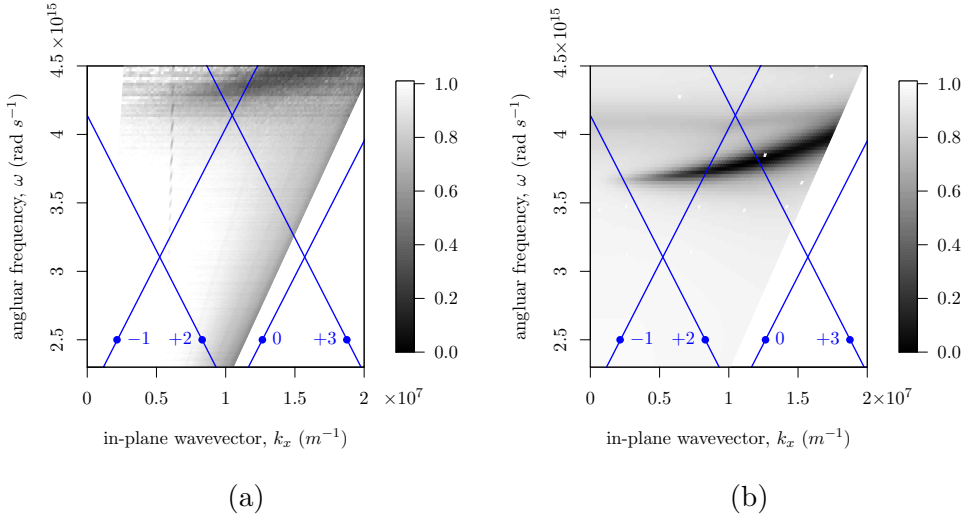


Figure 7.12: Experimental data of TM polarised reflectivity as a function of in-plane wavevector and angular frequency, mapping the SPP dispersion on a zigzag grating in glass. Blue lines show the positions of diffracted light lines scattered by $m\mathbf{k}_{gx}$, where $m = 1, +2, 0, +3$.

for FEM. In the experimental case, this frequency is at the limit of the monochromator's spectral resolution, and so the signal to noise ratio is lower than for previous plots.

This out-of-plane SPP mode lies significantly removed from the diffracted light line for the $\pm \mathbf{k}_{gy}$ light cone, which is not plotted as it occurs at a higher frequency than the displayed spectral range. Comparing this difference, Δk_x , for in-plane modes observed under TE illumination, the observation of a \mathbf{k}_{gy} scattered SPP mode with a large enough Δk_y to be observed suggests a high level of anisotropic dispersion of the SPP in the \mathbf{k}_x and \mathbf{k}_y directions. This will be discussed further in section 7.5.

In summary, the observation of weak even-scattered SPPs excited by TM polarised light has been demonstrated experimentally. To facilitate stronger coupling by even-order scattered SPPs and TM polarised light, an even \mathbf{k}_{gx} component may be added to the zigzag profile, but this would remove the mirror symmetry of the grating and the polarisation selectivity would be destroyed. This will be discussed further in chapter 8. An out-of-plane SPP associated with $\pm \mathbf{k}_{gy}$ has also been observed, indicating that the SPP dispersion in the $\hat{\mathbf{y}}$ direction is significantly perturbed from the in-plane ($\hat{\mathbf{y}}$) dispersion case. This anisotropic propagation of SPPs will be discussed further in section 7.5.

7.4 Band Structure of SPPs on a Zigzag Grating

The formation of SPP band-gaps relies on the ability for a propagating SPP mode to Bragg scatter and interfere with its counter-propagating self [35, 85]. This interference forms two possible SPP standing waves on the surface of the grating, which will typically have two possible field solutions, with the fields of one solution spatially shifted by $\lambda_{gx}/4$ with respect to the other. Since only diffracted SPPs are observed in the light-cone, the minimum momentum by which a SPP must scatter to intersect an equivalent counter-propagating mode, and still be able to couple to light and be observed, is a total of $2\mathbf{k}_{gx}$.

On traditional surface-relief gratings, the positions of the standing wave anti-nodes correspond to induced surface charge on the grating grooves. The two possible standing waves will cause the surface charge density to sit in different arrangements per solution which will, in general, sit charge in different potentials. This means that the energy of the two standing wave solutions will differ, with no propagating SPPs between the two energies due to destructive inference. This is the essence of plasmonic band-gap formation.

On a zigzag grating, the SPPs propagating along the \mathbf{k}_{gx} direction do not run over surface relief grooves, but follow the zigzag shape along the surface. The two possible standing waves which form when counter-propagating SPPs interact will differ

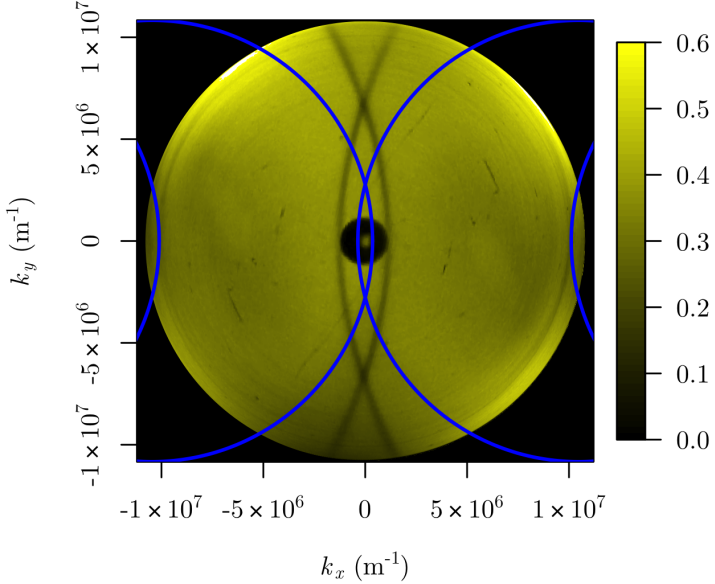


Figure 7.13: An iso-frequency scattergram mapping k-space contours for a 600 nm zigzag grating for an energy of 2.14 eV ($\lambda_0 = 580$ nm). The blue circles indicate the $\pm k_{gx}$ scattered light circles.

in energy by an amount determined by the zigzag structure of the surface and not the shape or depth of the grooves. The positions of the standing wave anti-nodes correspond to induced surface charge along the zigzag, and by consideration of these charge arrangements, the band-gap character of zigzag gratings may be inferred.

7.4.1 Band-Gaps at $k_x = 0$

For a zigzag grating with a periodicity of $\lambda_g = 600$ nm in air, the $\pm \mathbf{k}_{gx}$ scattered SPPs meet at $k_x = 0$ within the visible frequency range. An experimentally obtained iso-frequency contour for these modes is displayed in figure 7.13. The dark bands of low reflectivity map the SPP mode positions. At $k_x = 0$ the $+1\mathbf{k}_{gx}$ and $-1\mathbf{k}_{gx}$ SPP contours cross, and no significant perturbation of these contours is observed. No band-gap is detected at the mode intersections. The lack of interaction of these modes along $k_x = 0$ is consistent with the known scattering properties of a zigzag grating. The grating profile, being totally described by odd functions, contain no significant $2k_{gx}$ components. The result of which is that a SPP must undergo multiple scattering processes of $\pm n\mathbf{k}_{gx}$, where n is odd, in order to diffract and intersect other SPP modes. These multiple scattering processes are very weak, and result in such a small perturbation of the modes as they intersect in k -space that no band-gap is observed experimentally.

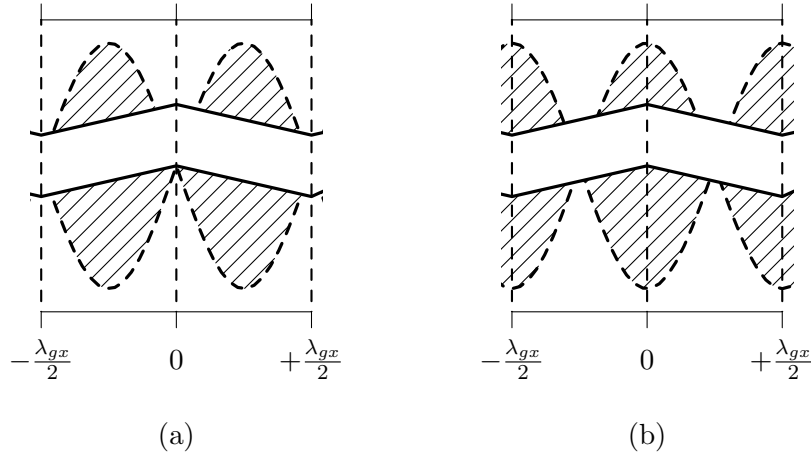


Figure 7.14: Cartoon of the two standing wave solutions for SPPs at $k_x = 0$, projected onto the zigzag surface. Since the anti-nodes of the SPP standing waves lie on the zigzag midsections in one case (a) and at the apexes in the other case (b), the standing waves exist in different electromagnetic environments and a band-gap may form.

While no band-gap is measured, the existence of a band-gap in this case is not forbidden. Figure 7.14 shows a diagrammatic representation of the expected locations of nodes and anti-nodes at $k_x = 0$ for the xy plane. As previously mentioned, the SPPs on zigzag gratings run along the zigzag, not over the grooves. For two SPP standing waves to be energetically dissimilar, the pertinent consideration is the field arrangements along the zigzag structure itself, which is why we consider the xy plane. The wavevector of this standing wave is half that of the Bragg vector by which the SPPs have scattered, in this case $2\mathbf{k}_{gx}/2$, leading to a standing wave with the periodicity of λ_{gx} . It is seen in the figure that the areas on which the surface charge is induced are at the zigzag apexes in one case (figure 7.14(a)), and at their midsection in the other case (7.14(b)). Using a FEM model, the electric field for these two possible standing waves at $k_x = 0$ are calculated plotted in figure 7.15.

The grating is modelled with the following parameters: $\lambda_{gx} = 600$ nm, $\lambda_{gy} = 150$ nm, $d = 40$ nm, with a mark-to-space ratio of 1 and a frequency-dependent silver dielectric function [84]. We may identify if these standing waves differ in energy, and which of these two is higher in energy relative to the other, by the field decay length into the two media. The higher-energy solution, having been shifted higher in frequency and therefore towards the diffracted light line, will be more photon-like than the lower energy solution, its fields extending further into the dielectric than the low-energy solution. The lower-energy solution will have been shifted lower in frequency, away from the light line

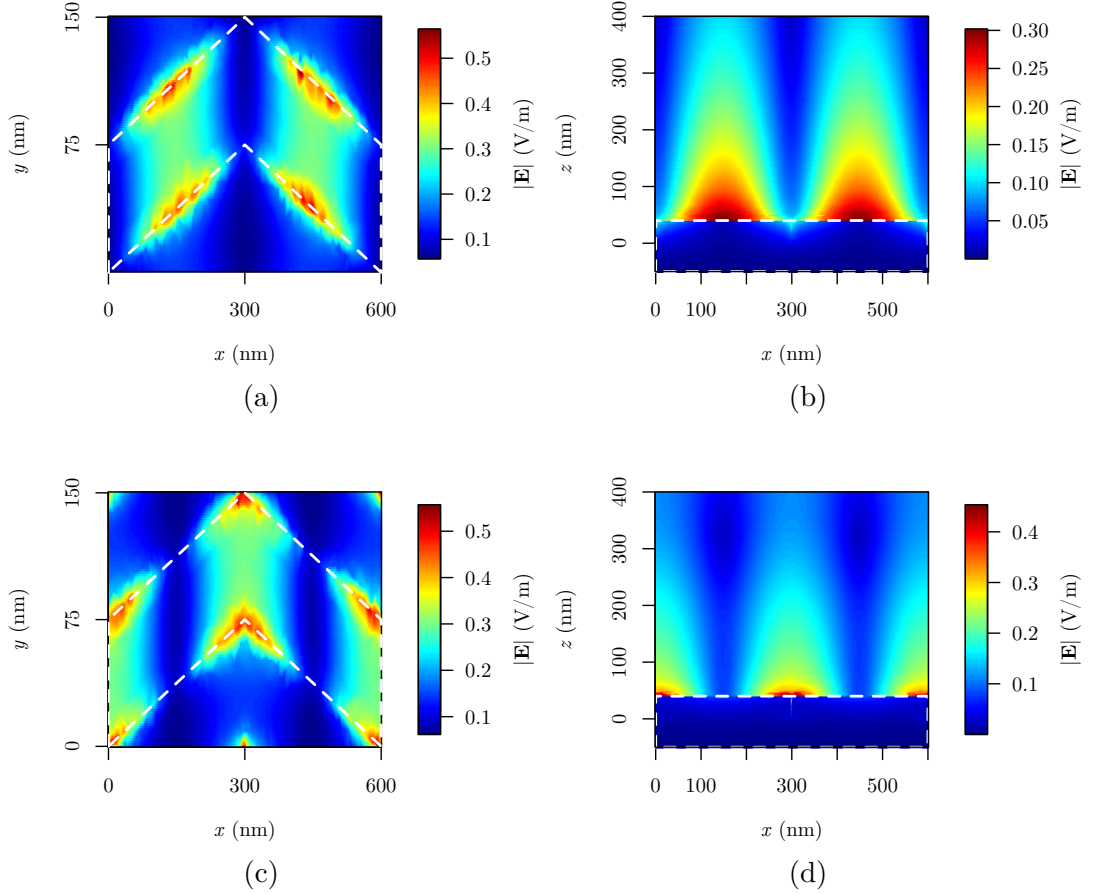


Figure 7.15: The magnitude of electric field for the SPP standing waves at $k_x = 0$. (a-b) The high-energy solution for (a) the xy plane at $z = 41$ nm and (b) the xz plane, for $y = 75$ nm. (c-d) The low-energy solution for (c) the xy plane at $z = 41$ nm and (d) the xz plane, for $y = 75$ nm.

and so will be more plasmon-like, constrained closer to the surface. These deductions can be applied in the comparison between the fields of the high energy standing wave in figure 7.15(b) and the lower energy standing wave in figure 7.15(d). Subfigures 7.15(a) and 7.15(c) show the magnitude of electric field for an arbitrary phase in a plane placed 1 nm above the zigzag surface at $z = 41$ nm. The two field distributions have the expected period of λ_{gx} . The higher-energy standing wave (figure 7.15(a)) has the field maxima along the edges of the zigzag grooves, while the lower energy standing wave has the field hotspots on the zigzag apexes. It is this energy difference between the two possible standing waves which leads to the plasmonic band-gap.

Analogous to the case of surface relief gratings, whereby the charge sits at the

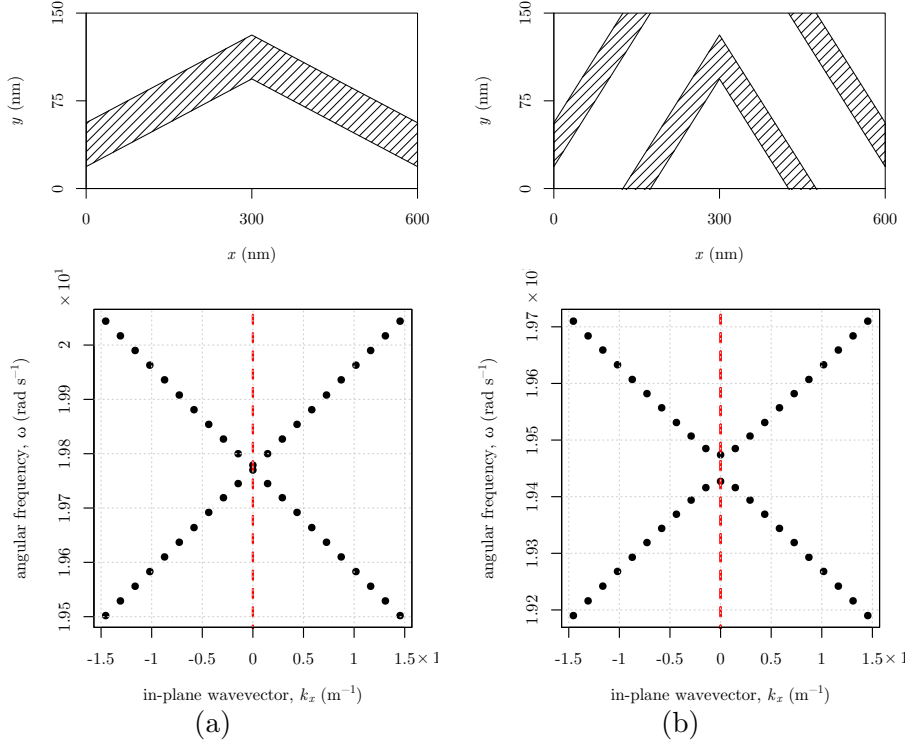


Figure 7.16: Manipulation of the band-gap observed at $k_x = 0$ through the increasing of zigzag amplitude. The unit cell and corresponding SPP dispersion around the intersection of the $+1\mathbf{k}_{gx}$ and $-1\mathbf{k}_{gx}$ scattered SPPs are shown for (a) The zigzag grating presented in this chapter and (b) a theoretical zigzag with a larger zigzag amplitude.

maxima or minima of the grooves (outlined in the background theory chapter 2), we expect the dependence of this band-gap size to vary as some function of zigzag (in the surface plane) amplitude.

An eigenmode solution is found for two possible unit-cells using FEM modelling, the results of which are shown in figure 7.16. The parameters for this model used the unit cells shown, with depths of 40 nm, silver parameters from literature [84] and with the global environment refractive index $n = 1.518$. The large-amplitude zig-zag was produced by shifting the central apex in the y direction by 150 nm. This causes multiple zigzags to overlap in a single unit cell, in order to maintain the sub-wavelength period of $\lambda_{gy} = 150$ nm. It is clearly shown that with an increase of zigzag amplitude, a band-gap is opened at $k_x = 0$. This gap is small, as the SPPs must still rely on multiple scattering processes to diffract and interact. This is the first example in this thesis of using the zigzag structure and symmetry to manipulate the band structure of the SPPs, a topic

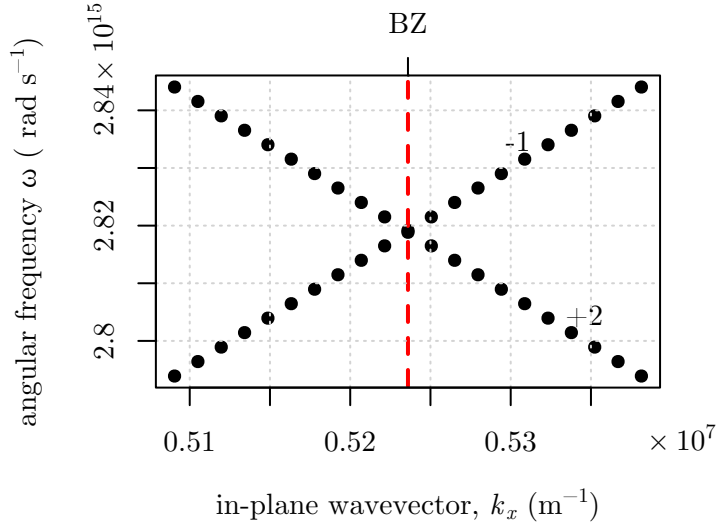


Figure 7.17: Modelled SPP dispersion around the intersection point of the $-1\mathbf{k}_{gx}$ and $+2\mathbf{k}_{gx}$ scattered SPPs meeting at the first BZ boundary (red dashed line).

which will be examined further in chapter 8.

7.4.2 Band-Gaps at the First Brillouin Zone Boundary

Normally at Brillouin zone (BZ) boundaries, diffractive coupling results in two counter propagating SPPs, which establish a standing wave [85]. The two standing wave solutions correspond to different field distributions with respect to the grating profile, and between these two energy solutions no surface modes propagate: a SPP band-gap forms. However, the experimentally mapped dispersion shown in figures 7.6 and 7.9(a), and also the predictions from FEM modelling (figures 7.6 and 7.9(b)) shows no measurable SPP band-gaps at the first BZ boundaries for this zigzag grating.

There are two considerations to be made here to determine the possibility of a band-gap between the $-\mathbf{k}_{gx}$ and $+2\mathbf{k}_{gx}$ scattered SPPs: (1) is there a sufficient scattering amplitude present for these modes to Bragg scatter and interact with one another?, and (2) how do the possible standing wave states differ in energy to produce a frequency band of disallowed SPP propagation, if at all?

Firstly, for the $-\mathbf{k}_{gx}$ and $+2\mathbf{k}_{gx}$ SPPs modes to scatter and interact strongly, they require a total momentum of $3\mathbf{k}_{gx}$. If the grating were to contain a $3\mathbf{k}_{gx}$ component in its surface profile, this would be a simple direct-scattering event and a strong interaction can occur. Since we observe the $3\mathbf{k}_{gx}$ scattered SPP in the reflectivity mapped in figure 7.9(a) (interacting with zero-order light), we can safely assume that the grating provides

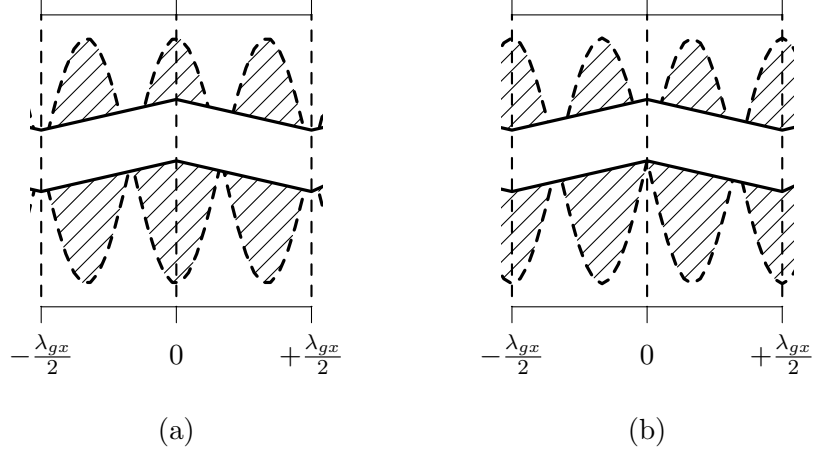


Figure 7.18: Cartoon of the two standing wave solutions for SPPs at the 1st BZ. Since the peaks and troughs of the zigzag exist in equivalent electromagnetic environments, the solutions are degenerate in energy, and no band-gap forms.

a strong $3\mathbf{k}_{gx}$ scattering mechanism. However, despite the ability for the grating to scatter SPP modes with a reasonable $3\mathbf{k}_{gx}$ component, there is still no observable band-gap between the $-\mathbf{k}_{gx}$ and $+2\mathbf{k}_{gx}$ at the first BZ boundary. A numerical model of these modes crossing at the BZ is shown in figure 7.17. The numerical model is used to extract the possible eigenmodes of the SPPs at the 1st BZ boundary, with modelling parameters of $\lambda_{gx} = 600$ nm, $\lambda_{gy} = 150$ nm, $d = 40$ nm, a mark-to-space ratio of 1 and $\varepsilon(\omega)$ from literature [84]. No band-gap is observed, to within the accuracy of the numerical model.

The lack of band-gap at the first BZ boundary is explained considering the allowed standing-wave symmetries on a zigzag grating. Generally, the in-plane wavevector of a standing SPP wave is half that of the total Bragg vector by which the two counter propagating SPPs have been scattered. For the $-\mathbf{k}_{gx}$ and $+2\mathbf{k}_{gx}$ scattered SPPs, crossing at the first BZ boundary, the SPP wavevector is $3\mathbf{k}_{gx}/2$. Through symmetry, there are two possible solutions for this standing wave on a zigzag grating, with the areas of high field of one solution shifted spatially by $\lambda_{gx}/4$ with respect to the other solution. These two solutions are drawn in figure 7.18, illustrating the node and anti-node positions of a standing wave along the zigzag. Since SPPs run along the zigzag pattern, (rather than over the grooves), the only possible manner by which to organise charge in dissimilar energetic arrangements is to consider how the charge may accumulate on the zigzag groove sides. Comparing this simple cartoon with the magnitude of electric field in the xy plane, 1 nm above the grating surface, shown in figure 7.19, we

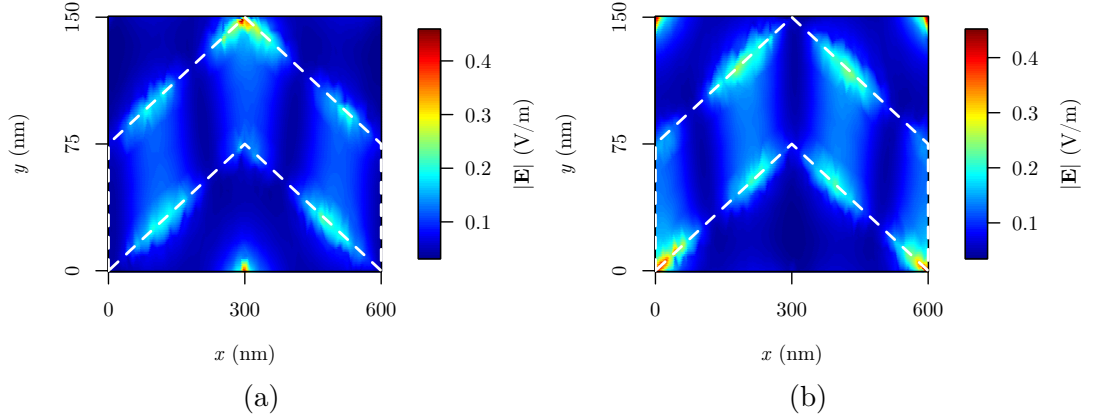


Figure 7.19: The magnitude of electric field, $|\mathbf{E}|$ for the degenerate SPP standing waves at the first BZ. (a) One solution for the xy plane at $z = 41$ nm and (b) The second solution for the xy plane at $z = 41$ nm.

see that the unit cell contains three hotspots, corresponding to the expected period of $\lambda_{SPP} = 2\pi/|\mathbf{k}_{SPP}| = 2\lambda_{gx}/3$, with the field arrangements sitting in the locations predicted by the cartoon. These field plots are extracted from the same numerical model that mapped the dispersion in figure 7.17. In both cases, one hotspot sits on a zigzag apex, and the other two sit symmetrically either side on the zigzag edges.

The electric field arrangements for the two possible standing wave modes at the BZ boundary in the grooves (in the xy plane with $z = 20$ nm) and in the xz plane (with $y = 75$ nm), are extracted from the numerical model and plotted in figure 7.20. These standing waves have three ‘hotspots’ per unit cell, corresponding to a standing wave with the expected period of $\lambda_{SPP} = 2\lambda_{gx}/3$. Comparing the magnitude of electric field in the grooves for the xz plane in figures 7.20(b) and 7.20(d), it is clear that the field arrangements are shifted spatially with respect to each other by $\lambda_{gx}/4$, as one would expect for two standing wave solutions which in general will lie $\pi/2$ degrees out-of-phase with each other. Figures 7.20(a) and 7.20(c) show the calculated field arrangements as figure 7.18 illustrated. Lying at the same potential, these field arrangements are clearly equivalent, shifted spatially by λ_{gx} with respect to each other, yet both occupying a degenerate electromagnetic environment. The magnitude of electric field in the xz plane presented in figures 7.20(b) and 7.20(d) show that the decay of the electric fields into both bounding media are the same for each case, and that neither solution can be labelled more ‘photon-like’ nor ‘plasmon-like’ than the other. This further demonstrates the equivalence in energy of these two standing waves.

The equivalence in energy of these two standing wave solutions can be broken by

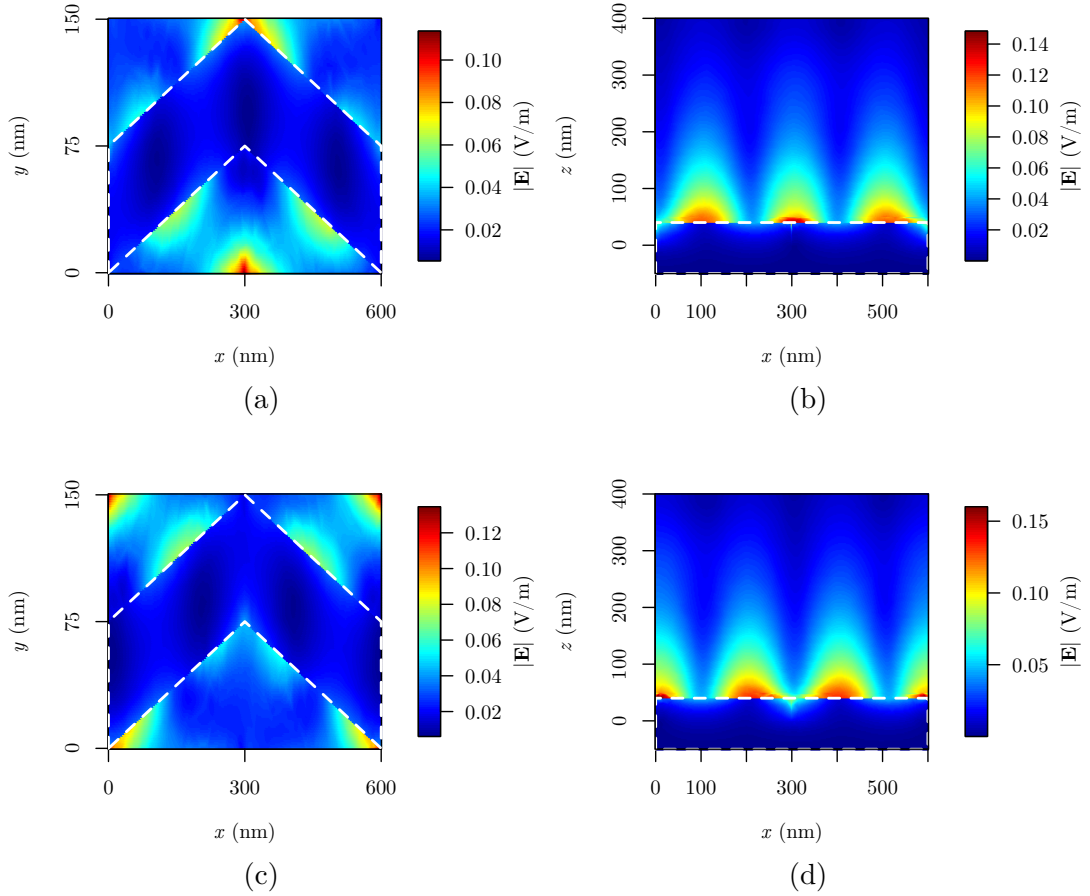


Figure 7.20: The magnitude of electric field for the degenerate SPP standing waves at the first BZ. (a-b) One solution for the (a) xy plane at $z = 20$ nm and (b) the xz plane, for $y = 75$ nm. (c-d) The second solution for the (c) xy plane at $z = 20$ nm and (d) the xz plane, for $y = 75$ nm.

the removal of the zigzag grating's mirror plane. By making the zigzag asymmetric, the electric field arrangements for both possible standing waves differ in energy and a band-gap may form. This is demonstrated in chapter 8

7.5 Anisotropic Propagation of SPP Modes for Self Collimation

Plasmonic circuits couple and direct SPPs along designed structures to provide a transfer of power and information [55, 131]. These optoelectronic devices require the development of SPP optics which behave like their classical optics counterparts.

One of the most crucial roles of these surface-optics is the ability to generate a collimated SPP beam, so that the SPPs may be directed efficiently without any detrimental loss across the device due to divergence. The ideal device should receive incident SPPs over a wide range of angles and the SPPs should then propagate through the component with a narrow angular divergence. This effect has been observed for light in photonic crystals, and was named self-collimation. [132, 133]

Recently, such components have been manufactured that use square bi-gratings to manipulate the local curvature of the SPP iso-frequency contour. These gratings have demonstrated self-collimation in the microwave regime [134] as well as in the visible [61]. They have also been designed to achieve all-angle negative refraction of surface waves [135, 136]. The work by Stein et al. [61] showed that the self-collimation effect could be achieved around the M symmetry point in k -space due to the mini-gaps formed by band-gapping SPPs over a momentum range of $1 \mu\text{m}^{-1}$. It is desirable that this momentum range is large, so as to maximise the angular divergence over which the device could collimate SPPs.

We have found that zigzag gratings possess a mechanism for the collimation of SPPs at a single wavelength. This mechanism is similar to previous work, as it relies on plasmonic band-gaps to cause anisotropic propagation of SPPs along the surface, which is observed as a deformation of the SPP iso-frequency contours to approximately flat bands with no curvature. However, the azimuthal angle range over which SPPs possess a single direction is far larger than previously reported results, extending over the entire observable region of k -space.

Up until now, we have only considered the effects of the λ_{gx} periodicity of the zigzag grating with respect to the SPP propagation. With a designed orthogonal pitch of $\lambda_{gy} = 150 \text{ nm}$, the diffracted SPPs from a \mathbf{k}_{gy} scattering mechanism have such a large momentum that for the plane of incidence $\phi = 0^\circ$, the SPP features will lie well above the visible frequency range.

However, an important point to note about SPPs travelling along the \mathbf{k}_{gy} direction is that they will be travelling over surface relief grooves and not, like the $\pm\mathbf{k}_{gx}$ surface plasmons, along the zigzag contours. This means that the charge arrangements for standing-waves at the BZ boundaries will differ in energy considerably, as for traditional surface-relief gratings. Plasmonic band-gaps in the \mathbf{k}_{gy} direction are expected, and will be similar to those on typical bigratings. Evidence for these band-gaps are seen in figure 7.21. The experimental results show the dispersion mapped using the reflectivity of the zigzag grating to indicate the SPP mode positions for a wavelength range of $450 < \lambda_0 < 800 \text{ nm}$ and an angular range $7^\circ < \theta < 65^\circ$, for two planes of incidence. One plane of incidence includes the \mathbf{k}_{gx} grating vector ($\phi = 0^\circ$) and the orthogonal plane of incidence ($\phi = 90^\circ$) contains the \mathbf{k}_{gy} vector. In both cases the $\pm 1\mathbf{k}_{gx}$ scattered SPP is

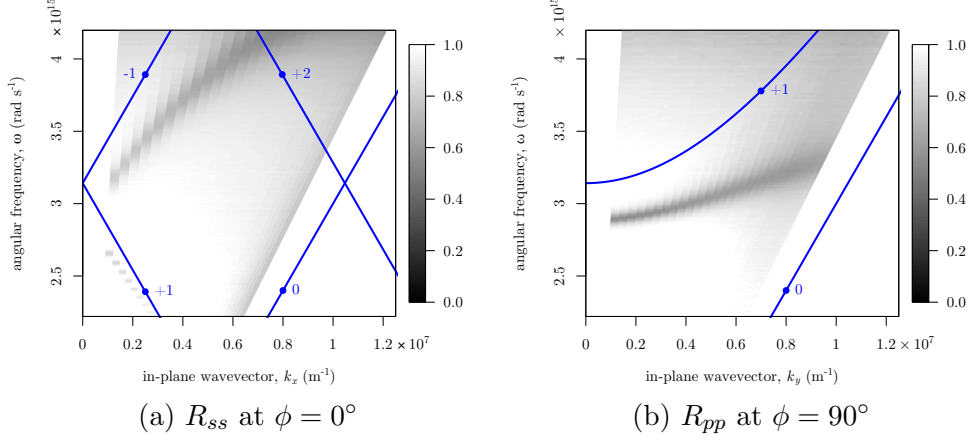


Figure 7.21: Experimentally obtained dispersion plots for a zigzag grating at $\phi = 0^\circ$ and $\phi = 90^\circ$

observed. For $\phi = 0^\circ$ the SPP dispersion is an asymptotic curve, while for $\phi = 90^\circ$ it is seen as a hyperbolic conic intersection, but both map the same SPP in momentum space. For the coupling of light to the SPP in figure 7.21, the polarisation of the incident light has been rotated 90° , and so is TM polarised.

It is found that in the $\phi = 90^\circ$ orientation, the SPP dispersion curve asymptotes far faster than the $\phi = 0^\circ$ case. This lower asymptote is evidence of a large band-gap at the first BZ in the \mathbf{k}_{gy} direction, with the mode meeting the BZ boundary with zero group velocity at $2.1 \times 10^7 \text{ m}^{-1}$. This band-gap is the result of the interaction between the $\pm \mathbf{k}_{gx}$ and $\pm \mathbf{k}_{gx} + \mathbf{k}_{gy}$ scattered SPPs which are separated by a single scattering vector that is also a harmonic of the grating surface profile, \mathbf{k}_{gy} . Strong interaction is then expected, and the freedom of the charge to organise into energetically dissimilar arrangement in the grooves leads to a large plasmonic band-gap in this direction.

The relevance of this large band-gap to the collimation of SPPs becomes apparent in the evolution in wavelength of the SPP iso-frequency contours mapped using imaging spectrometry, shown in figure 7.22.

The scattergrams map the iso-frequency contours of the $\pm 1\mathbf{k}_{gx}$ scattered SPPs in k -space, with the minimum of reflection indicating the SPP mode position as the reflection is suppressed by SPP excitation. The polarisation is set so that the electric field lies orthogonal to the \mathbf{k}_{gx} vector at $k_y = 0$, satisfying the TE excitation condition for these SPPs in this plane. As detailed in section 7.3.3, the $\pm 2\mathbf{k}_{gx}$ scattered SPPs are not excited with this polarisation, and are not observed. The grating used for these scattergrams is a silver zigzag grating in air as detailed in section 7.3.3, with a depth of $d \approx 40 \text{ nm}$.

7. Optical Response of Metallic Zigzag Bigratings

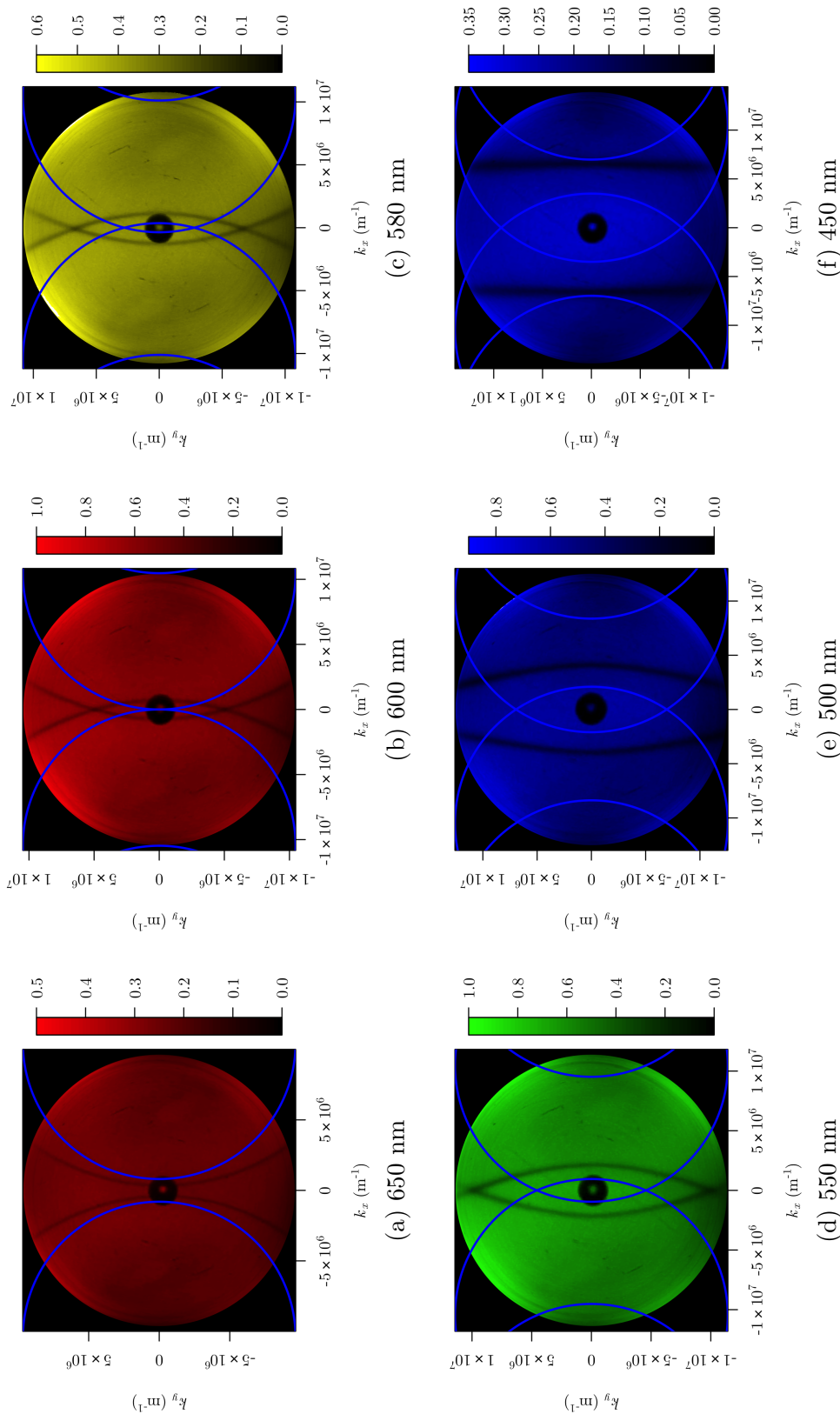


Figure 7.22: Measured iso-frequency contours of a zigzag grating for a range of wavelengths. The blue circles indicate calculated diffraction edges.

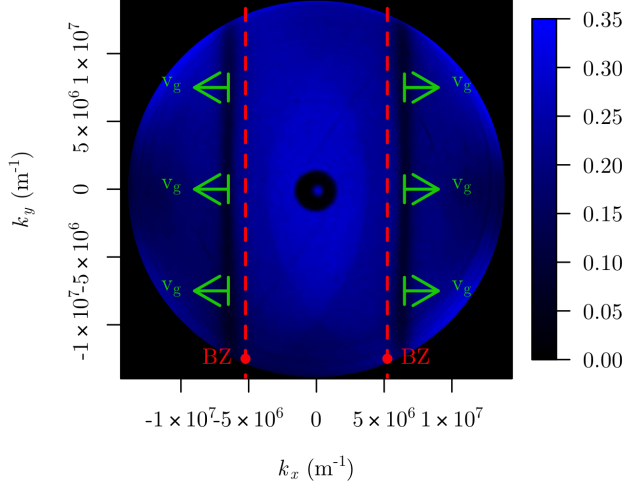


Figure 7.23: The SPP iso-frequency contours mapped using imaging scatterometry at $\lambda_0 = 450$ nm. The green arrows show the direction of the SPP group velocity along the contour, indicating that for this wavelength the SPP waves only travel in the $\pm \mathbf{k}_{gx}$ direction. The red dotted lines show the position of the BZ boundary.

As the frequency increases (the wavelength shifting from red to blue), the $\pm 1\mathbf{k}_{gx}$ scattered SPP contours grow increasingly flat-banded. This is due to the increasing overlap and interaction with the $\pm 1\mathbf{k}_{gx} \pm 1\mathbf{k}_{gy}$ scattered SPPs and the formation of a large band-gap well outside the available momentum space to the free-space light. At $\lambda_0 = 450$ nm, the SPP bands become flat, with essentially no curvature. This scattergram is repeated in figure 7.23, with some additional important annotations.

Since the group velocity of the SPP wave is determined from $\mathbf{v}_g = \nabla\omega(\mathbf{k})$, the direction of the SPP energy flow is in the direction orthogonal to the SPP contour (see chapter 6 for more details on this inference). Six example group velocity directions are shown as green arrows in figure 7.23, showing that, for a given scattered SPP, the group velocity is only in the k_x direction. This corresponds to a self-collimated SPP wave across a momentum range of at least $2.2 \times 10^7 \text{ m}^{-1}$, an order of magnitude higher than previous results [61], and successfully collimates SPPs for an incident azimuthal range of $-63.4^\circ < \phi < 63.4^\circ$ at $\lambda_0 = 450$ nm.

An Important observation is to be made of figure 7.23; that the $\pm 1\mathbf{k}_{gx}$ scattered SPP contours lie outside of the BZ boundary (red dotted lines). Two comments must be made about this: the first is that the BZ represents the smallest unit cell which, when repeated by translational symmetry operations, reproduces fully the band structure of the system. Clearly, the BZ lying between the two red lines does not replicate the band structure of the grating once translated. This is because the $\pm 2\mathbf{k}_{gx}$ scattered SPPs

are not coupled strongly to light in our experiment. The eigenstates for the SPPs are still present in the BZ, just not excited by the incident radiation, and so the validity of the BZ holds. The second point is that the $\pm 1\mathbf{k}_{gx}$ SPPs have passed through the BZ boundary unperturbed. This is important, as if the contours were perturbed at this boundary, the efficiency of the collimation of SPP waves would be impacted. Because band-gaps at the first BZ are forbidden (not just weak) in the k_x direction, unwanted perturbation of the SPP contour at this boundary will not occur. This is a condition due to the mirror symmetry of the zigzag grating surface, and an analogy cannot be found in traditional gratings.

7.6 Conclusions

This chapter has introduced a new type of diffraction grating, a zigzag grating. This grating uses sub-wavelength surface structure to provide a diffractive periodicity to wavelength-scale light. SPPs may be diffractively coupled to using a metallic zigzag grating, and their excitation and band structure are found to depend on the symmetry of the zigzag pattern.

The polarisation of light coupling to SPPs on such a grating is found to be dependent on the diffracted order used. For odd-ordered diffraction, TE polarised light couples to the SPPs, while for even-ordered diffraction, TM polarised light is required. This has been explained using a simple analytical formula which considers the available normal component of electric field to the surface of the grating, and the polarisation selectivity has been demonstrated experimentally on fabricated silver zigzag gratings.

This polarisation selectivity may be found to be of use for plasmonic devices in which polarisation separation is desirable. As an example, the incorporation of zigzag gratings in metal-insulator-metal structures designed for the generation of light could yield a polarisation dispersing light source. These SPP mediated light sources, when incorporated with a zigzag grating, would emit different polarisations of light in to different diffracted orders. Breaking the mirror symmetry of the zigzag pattern provides a route to polarisation-independent absorption of light into SPPs, a topic which is explored in greater detail in chapter 8.

The band structure of SPPs on zigzag gratings is found to be highly dependent on the surface symmetry. Most strikingly, the formation of a band-gap at the first BZ boundary is forbidden by the degeneracy of the allowed standing wave states.

Using scatterometry, the propagation of SPPs on such surface is shown to be highly anisotropic, due to the large band-gaps which occur orthogonal to the diffraction plane. These highly perturbed SPP contours, combined with the forbidden band-gaps at the first BZ boundary in the x -direction, lead to wide-angle surface wave collimation.

7. Optical Response of Metallic Zigzag Bigratings

The use of zigzag gratings to generate surface-waves with highly directional planar wave-fronts in plasmonic circuits, over a wide range of azimuthal angles, could be of great interest to optoelectronic engineers. Further investigation of this phenomenon is left for future work, with the recommendation of using near-field imaging of SPPs to characterise the surface waves and exploring also the collimating effect of the grating.

Chapter 8

Optical Response of Asymmetric Zigzag Bigratings

8.1 Introduction

This chapter demonstrates how the surface symmetry of a zigzag grating may be used to manipulate both the coupling of light to SPPs, and the band structure of SPPs on the zigzag surface. Much of the discussion in this chapter draws parallels with the zigzag grating explored in chapter 7. The zigzag grating explored in chapter 7 will be referred to as a ‘symmetric’ zigzag grating, due to the presence of mirror symmetry in the yz plane. The zigzag grating which shall be the topic of this chapter has no such symmetry, and so will be referred to as an ‘asymmetric’ zigzag grating. The asymmetric zigzag grating is formed from a set of sub-wavelength (non-diffracting) grooves that are zigzagged along their length such that the zigzag apexes do not lie at high symmetry points within the rectangular unit cell. The length scale of the zigzag pitch is on the order of the wavelength of impinging light, so that the grating may diffractively couple to SPPs.

The resulting structure is 2D chiral, much like ‘fish-scale’ nanowires reported previously, [137–141] but we restrict our investigation to the excitation and band structure of SPPs along such a surface, rather than any optical chirality exhibited by the grating.

In this chapter it is demonstrated that any polarisation of light may couple to the SPP modes on a zigzag grating which possesses no mirror symmetry. Furthermore, it is shown that light of different polarisation will couple to the exact same SPP modes, and these SPP modes propagate in the same direction, regardless of polarisation. This latter point is subtle, but important, as previous work has shown that the excitation of SPPs on crossed bigratings may also couple arbitrary polarised light into SPPs on the surface [44, 77, 142], but in this case different incident polarisations states excite

different, or multiple, SPPs. The coupling of arbitrarily polarised light to SPPs on deep lamella gratings has also been shown [143], where the SPP modes evolve to become similar in character to localised cavity modes. In the zigzag case presented here, light of any arbitrary polarisation is coupled to the same SPP modes, and the energy flow across the surface is mediated by these SPPs travelling in a single direction only. This makes these asymmetric gratings an excellent possible component for efficient plasmonic circuitry [131].

The manipulation of available Fourier components by altering the geometry of the asymmetric zigzag surface also allows the design of the SPP band structure on such gratings. We find in section 8.4, theoretically and experimentally, how the asymmetric zigzag pattern can cause band gaps to form between the $+k_{gx}$ and $-k_{gx}$ scattered SPPs, by providing a direct scattering mechanism by which they may interact. We also show in section 8.4 how the degeneracy of standing wave solutions at the first BZ boundary, described in chapter 7 for the symmetric case, is destroyed in the asymmetric zigzag case. The coupling of light to the two energetically dissimilar standing wave states is also investigated, as the high energy solution is found to be poorly coupled to light compared to the lower energy mode.

Finally, highly anisotropic propagation of SPPs along zigzag gratings, when combined with the possible large band gap at the first BZ boundary, causes the formation of a full-plasmonic band gap, for which propagation of SPP for a given frequency range is forbidden in all directions. Full plasmonic band-gaps have shown potential in surface plasmon based lasers [47–49, 144], and are usually only found in systems with hexagonal [114], not rectangular, symmetry.

8.2 The Asymmetric Zigzag Grating

The coordinate system used for the asymmetric zigzag grating is shown in figure 8.1. Light impinges on the surface at a polar angle θ in the plane of incidence that lies at an angle ϕ , with $\phi = 0^\circ$ containing the primary grating vector, $k_{gx} = 2\pi\hat{\mathbf{x}}/\lambda_{gx}$. The polarisation of the light is defined as TM polarised light when the electric vector is in the plane of incidence, and TE polarised light when the electric vector lies perpendicular to the plane of incidence. The offset of the zigzag apex, δ is the distance between the centre of the unit cell and the closest apex, as shown. It is this offset that removes the mirror symmetry of the zigzag grating. The grating grooves are of a depth d . The target parameters (for fabrication) used in this chapter are as follows: $\lambda_{gx} = 600 \text{ nm}$, $\lambda_{gy} = 150 \text{ nm}$, $d \approx 40 \text{ nm}$ and $\delta = 150 \text{ nm}$ with the grating made of silver. The zigzag amplitude is defined as the distance between a low and high apex of the zigzag divided by two.

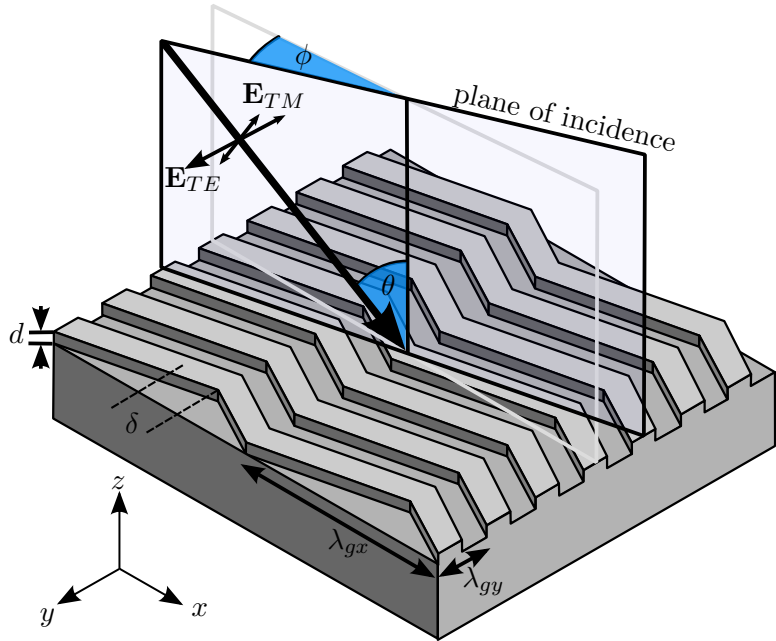


Figure 8.1: Coordinate system for the asymmetric zigzag grating. The experimental parameters were $\lambda_{gx} = 600$ nm, $\lambda_{gy} = 150$ nm, $d \approx 40$ nm, and $\delta = 150$ nm .

The zigzag grating presented in this chapter has a reduced symmetry from the zigzag grating presented in chapter 7. This is achieved by offsetting one of the zigzag apexes along \hat{x} with respect to the centre of the unit cell by a distance $\delta = 150$ nm, as shown in figure 8.2. This produces a grating structure with no mirror or rotational symmetry in real space, but still having a rectangular unit cell and a rectangular lattice in reciprocal space. For ease of description, we refer to the ‘left hand side’ of the grating, the region $0 \text{ nm} < x < 450 \text{ nm}$ (to the left of the apex), as ‘region 1’ and the right hand side of between $450 \text{ nm} < x < 600 \text{ nm}$ as ‘region 2’.

The samples are produced using electron beam lithography as detailed in chapter 4. Scanning electron micrographs of the silicon master and the template stripped sample in silver are shown in figure 8.3, with the following parameters: $\lambda_{gx} = 597 \pm 5$ nm, $\lambda_{gy} = 156 \pm 9$ nm, $d \approx 40$ nm, $\delta = 126 \pm 5$ nm with a zigzag amplitude of 121 ± 3 nm.

Due to the template stripping method of fabrication, the produced silver grating is an inverse duplicate of the grating master. The master SEM 8.3 also shows a clear stitching error on the right of the SEM, where the zigzag continuity has been broken. These stitching errors are infrequent and, over the area of the grating, do not effect the optical response greatly.

Notice that the zigzag amplitude of the sample is greater than that of the unit cell in figure 8.2. The experimental and modelled results will show that since an

8. Optical Response of Asymmetric Zigzag Bigratings

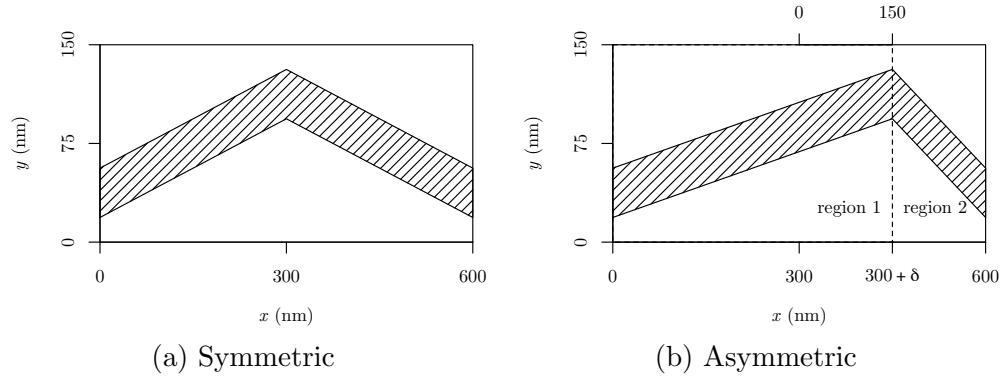


Figure 8.2: Two possible unit cells for a zigzag grating. (a) The grating unit cell explored previously in chapter 7. (b) An asymmetrical zigzag grating, with the central apex of the zigzag shifted by 150 nm. This shift removes the mirror-symmetry of the zigzag.

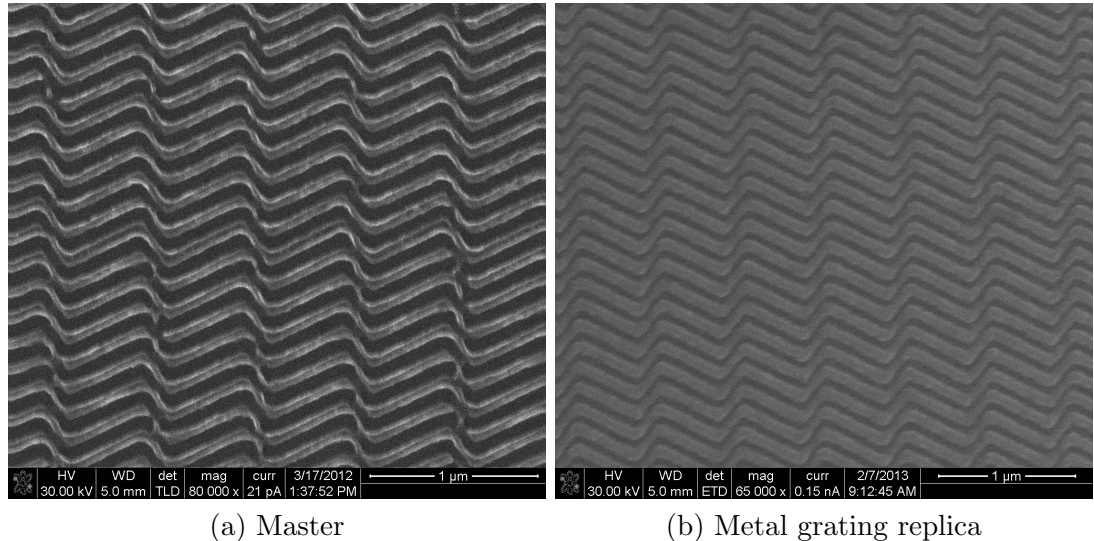


Figure 8.3: Scanning electron micrographs of (a) The asymmetric zigzag silicon master and (b) the template stripped sample in silver.

increased zigzag amplitude alone does not alter the symmetry of the zigzag surface, the fundamental optical response of the grating is unaltered. For simplicity in understanding only consideration of the unit cell in figure 8.2 is necessary to gain an insight into the optical response of our sample.

8.3 The Coupling of Polarised Light to SPPs on an Asymmetric Zigzag Grating

8.3.1 Theory

In chapter 7, it was shown that a zigzag grating possesses a surface profile that allows surface charge density oscillations to be induced by either TE or TM polarised light. This is because both TE and TM light provide a component of the incident electric field that lies normal to some part of the metal surface. For the case of the grating examined in chapter 7, the field profiles of these induced charge density oscillations were constrained by the symmetry of the surface so that the wavevector of SPPs coupling to TE polarised light are only the odd-orders of diffraction, while the TM polarised light could only match the wavevector of even-order diffracted SPPs. These coupling conditions can be deduced from the plane wave expansion equations 7.4 and 7.5. Since the functions E_{TE} and E_{TM} will possess the same mirror symmetry as the surface function, so the Fourier expansions of E_{TE} and E_{TM} only require every-other Fourier coefficient to fully describe the functions. This is what leads to the polarisation selectivity of this type of grating.

However, by removing the mirror symmetry of the zigzag surface the equivalent expressions for E_{TE} and E_{TM} in the asymmetric zigzag case will themselves not be mirror symmetric. We can demonstrate this simply by considering the E field for normal incident light, as shown diagrammatically in figure 8.4.

In this figure, the possible electric fields across the zigzag grooves are shown for two electric vectors, one in the x direction (left), and one in the y direction (right). The electric vectors pointing along a single axes like this represents two orthogonal polarisations at a single instant in time when the light is incident normal to the surface. The plane of incidence at $\theta = 0^\circ$ is not defined, as the wavevector possesses no component in the surface plane xy , but for $\phi = 0^\circ$ and for a very small polar angle θ , the polarisation is defined as TE for the vector lying along the x axis (right) and TM for the vector lying along the y axis (left), so we shall refer to the left-hand diagram as the TE polarised case, and the right-hand side as the TM polarised case.

The figure shows that for the electric vector oriented along the x or the y axis, the incident field may provide a normal component to the grating surface and so induce

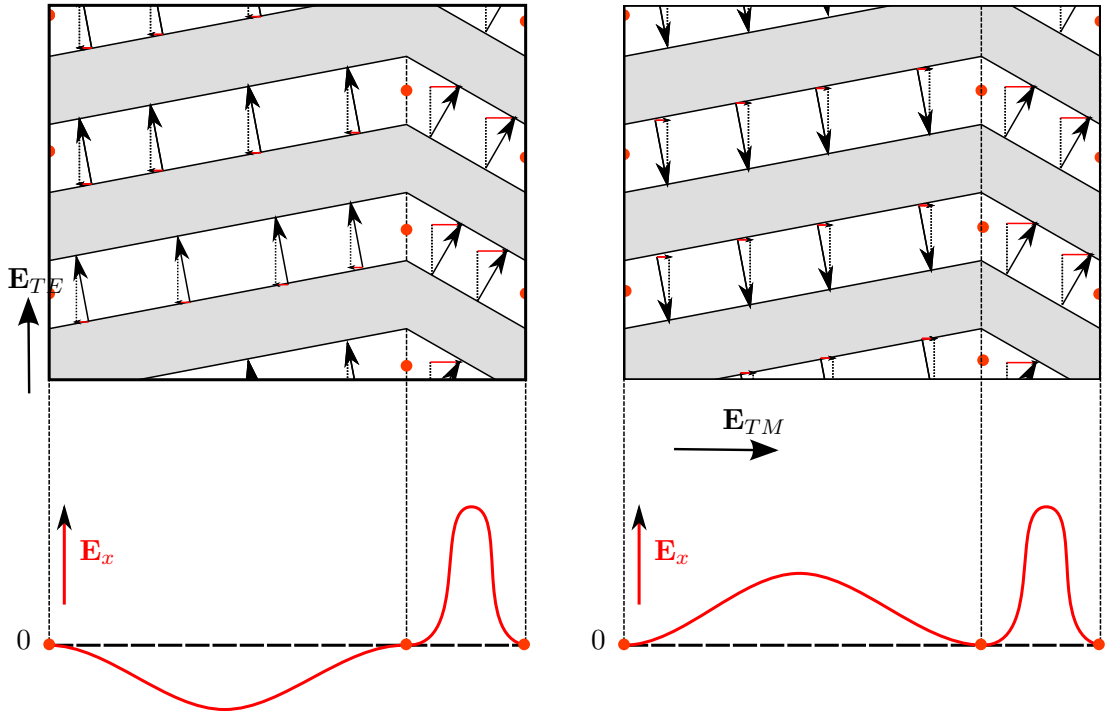


Figure 8.4: (above) A schematic of the electric field lines in the grooves (black arrows) of an asymmetric zigzag grating for two polarisation cases, and the resulting E_x component (red arrows). The points connecting the apexes lead to fixed points of zero E_x , leading to an asymmetric field distribution along the plane of propagation (bottom).

surface charge. Because of the surface geometry, charge density oscillations may be induced on the grating surface and so there exists a possibility of exciting SPPs. Since in our experiments λ_{gy} is sub-wavelength, we need only consider the electric field profile along the x axis, as this is the axis along which momentum conservation requires diffracted SPPs to propagate. The x -components of the electric fields in the grooves are shown as red arrows in the figure. Possible example functions for each polarisation which fulfil the asymmetry criteria of the grating are shown in the lower half of figure 8.4, which have been deduced from the diagrams above. These functions are neither odd nor even, both possessing only the symmetry of the grating (a rotation and translation operation or ‘glide operation’), and will in general vary in amplitude in the two regions.

The key point illustrated in this figure is that the normal component of electric field varies in the x -direction asymmetrically with respect to the unit cell. This is because the x -component of the electric field originating from charge carriers must be pinned to zero at the zigzag apexes by the geometry of the grating, and the position of these apexes do not lie at points of any high-symmetry. The plane wave expansion description of such general diffracted SPPs fields on such a surface will necessarily contain all Fourier

components including both odd and even harmonics, for both polarisation cases.

In chapter 7, we calculated the Fourier series of $E_{TE} (\equiv E_x^{TE})$ and $E_{TM} (\equiv E_x^{TM})$ by first deriving the electric field from the expected induced surface charge along x as the functions E_x^{TE} and E_x^{TM} . Examination of the plane wave expansion of these fields determines the coupling of light to different orders of diffracted SPP. In the asymmetric case, the strict derivation of E_x^{TE} and E_x^{TM} is difficult, due to the lack of symmetry in the grating's geometry. We can instead construct an example function from careful consideration of the conditions an E_x field must possess along such a grating. We place five constraints on any function we choose: (1) That the function must be continuous along x , with no sharp discontinuities or undefined points; (2) that the function is periodic, with a period equal to that of a single grating period, λ_{gx} ; (3) that the function must equal $E_x = 0$ at the x coordinates which correspond to a zigzag apex; (4) that between these zeros, the magnitude of E_x will reach a maximum value determined by the polarisation and local geometry and; (5) the resulting function must possess the same symmetry as the grating (a single C_2 rotation operation).

Such a function must be defined piecewise, with the same symmetry as the intuitive example functions drawn in figure 8.5. Choosing a simple sine wave for each region, the function we shall use is defined as,

$$E_x^{TM}(x) = \begin{cases} E_{x_1}^{TM*} \left(1 + \sin \left(-\frac{L}{2} + \frac{2\pi x}{(L+\delta)} \right) \right) & 0 < x < L + \delta \\ E_{x_2}^{TM*} \left(-1 + \sin \left(\frac{L}{2} + \frac{2\pi(x-L-\delta)}{(L-\delta)} \right) \right) & L + \delta < x < 2L \end{cases} \quad (8.1)$$

$$E_x^{TE}(x) = \begin{cases} E_{x_1}^{TE*} \left(1 + \sin \left(-\frac{L}{2} + \frac{2\pi x}{(L+\delta)} \right) \right) & 0 < x < L + \delta \\ -E_{x_2}^{TE*} \left(-1 + \sin \left(\frac{L}{2} + \frac{2\pi(x-L-\delta)}{(L-\delta)} \right) \right) & L + \delta < x < 2L \end{cases} \quad (8.2)$$

Where $2L = \lambda_{gx}$. The variable δ represents a positive offset of the central zero point from $x = L$ and the function is defined as periodic with a period $2L$. These functions are plotted in figure 8.5

The magnitude of E_x in the two regions ($E_{x_1}^{TE*}, E_{x_2}^{TE*}, E_{x_1}^{TM*}, E_{x_2}^{TM*}$) will not in general be equal and will vary as a function of the offset δ . This magnitude will be a result of the dot product between the impinging field vector and the local surface normal, which will be different for TE and TM polarised light. To a good approximation, the amount of induced surface charge density will be proportional to this dot product, and the resulting SPP electric field may be decomposed along the x axis to see which plane wave components will couple strongly to it. Using these considerations the expressions

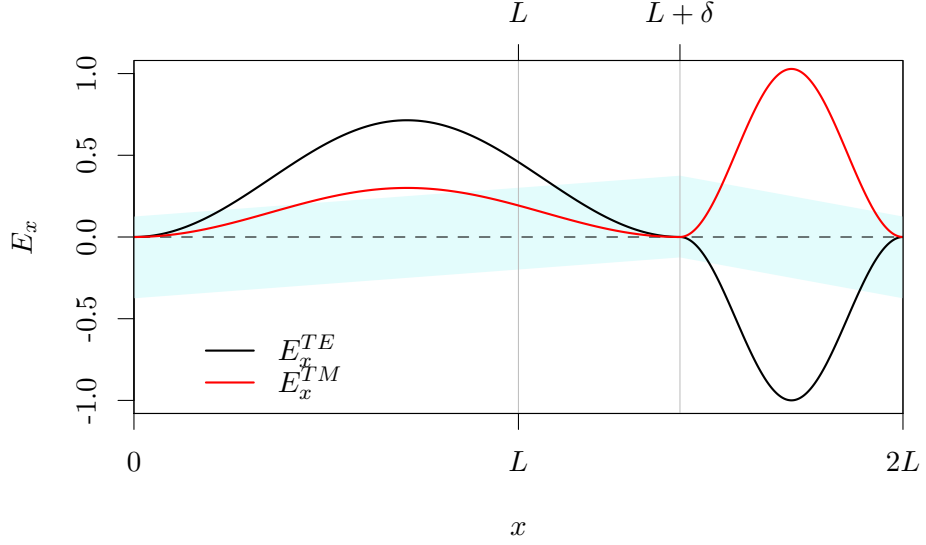


Figure 8.5: (a) The piecewise function representing E_x for TE (E_x^{TE}) polarisation (black line) and TM (E_x^{TM}) polarisation (red dotted line). Blue background shows the zigzag grating in the xy plane, with the x -coordinates aligned with the plot. $E_0 = 1$ in this diagram.

for maximum $|E_x|$ will be given by,

$$E_{x_1}^{TE*} = E_0 \cos\left(\tan^{-1}\left(\frac{h}{L-\delta}\right)\right) \sin\left(\tan^{-1}\left(\frac{h}{L-\delta}\right)\right) \quad (8.3)$$

$$E_{x_1}^{TM*} = E_0 \sin^2\left(\tan^{-1}\left(\frac{h}{L-\delta}\right)\right) \quad (8.4)$$

$$E_{x_2}^{TE*} = E_0 \cos\left(\tan^{-1}\left(\frac{h}{L+\delta}\right)\right) \sin\left(\tan^{-1}\left(\frac{h}{L+\delta}\right)\right) \quad (8.5)$$

$$E_{x_2}^{TM*} = E_0 \sin^2\left(\tan^{-1}\left(\frac{h}{L+\delta}\right)\right) \quad (8.6)$$

where h is half the zigzag amplitude and E_0 is the initial field magnitude. These functions are plotted in figure 8.6 as a function of δ , and show how the E_x component varies rapidly for region 2, as the increasing offset forces the normal component of the surface increasingly in the x direction. In the extreme case of $\delta = L$, TM polarised light will be perpendicular to the region 2 surface normal, and TE will be parallel to it, leading to $E_{x_2}^{TM*} = E_0$ and $E_{x_2}^{TE*} = 0$.

We may now expand these two functions as a Fourier sum to determine which diffracted SPP wavevectors may be matched with incident plane waves for each polarisation case. We do this for an asymmetric zigzag grating with $\delta = 0.42L = 126$ nm the

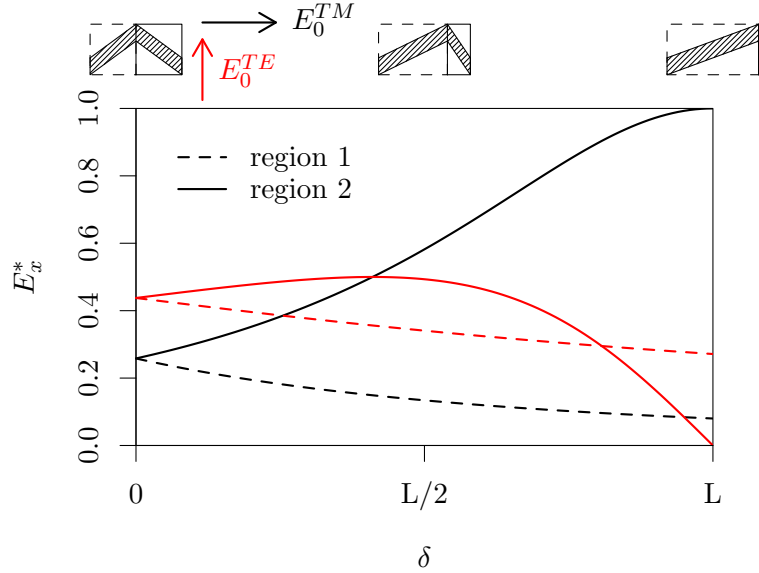


Figure 8.6: Magnitude of the electric field in region 1 (dashed) and region 2 (dotted) for the two polarisation cases of TM (black) and TE (red) polarised light, as a function of offset, δ .

offset which was measured from the SEMs of the produced sample. Since the E_x^{TE} and E_x^{TM} functions are neither odd nor even, we expand them as a complex Fourier sum, and take the magnitude of the Fourier components squared to obtain a qualitative understanding of the relative scattering efficiencies [116]. The complex Fourier series coefficients are given by,

$$C_n = \frac{1}{L} \int_{-L}^L f(x) \exp(-inx) dx \quad (8.7)$$

Where n is the order of the Fourier harmonic. The Fourier components for both E_x^{TE} and E_x^{TM} functions are plotted in figure 8.7. The efficiency with which light will couple to the SPPs on an asymmetric zigzag grating will be directly linked to the amplitudes of these Fourier coefficients, as the strength of each harmonic equates to the scattering amplitude of the SPPs. These coefficients are different for each polarisation, but they will not be zero.

This leads to the conclusion that both TE and TM polarised light will couple to all orders of SPPs on such a grating, with different (but non-zero) coupling strength depending on the diffracted order used to couple to the SPP. It is possible to excite any diffracted SPP mode with any polarisation of light on such a grating. That is to say, the same SPP mode may be driven with either polarisation.

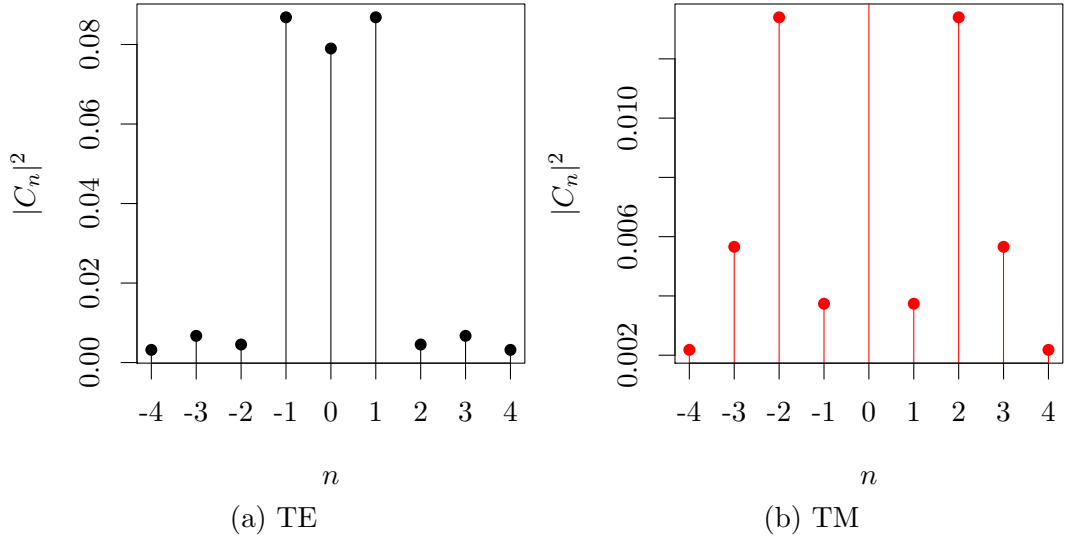


Figure 8.7: The square magnitude of the Fourier coefficients for $n = 0 \dots \pm 4$ with an offset of $\delta = 0.42L$, which corresponds to the experimentally measured offset of 126 ± 5 nm for the (a) TE case and (b) TM case.

Incidentally, examining the Fourier coefficients for no offset (setting $\delta = 0$), we recover the polarisation selectivity predicted in chapter 7 for a symmetric zigzag grating.

8.3.2 Results

The coupling of light to SPPs on an asymmetric zigzag grating is demonstrated experimentally in figure 8.8. This figure plots reflectivity for both TE and TM polarised light illuminating an asymmetric zigzag grating as a function of polar angle of incidence (θ), at $\phi = 0$ and $\lambda_0 = 500$ nm. The reflectivity was obtained using the experimental method outlined in chapter 4, with a robotic table controlling the polar angle and a spectrometer setting the incident wavelength. The polar angle range is $7^\circ < \theta < 60^\circ$. The zigzag grating sample has the following parameters: $\lambda_{gx} = 597 \pm 5$ nm, $\lambda_{gy} = 156 \pm 9$ nm, $d \approx 40$ nm, $\delta = 126 \pm 5$ nm with a zigzag amplitude of 121 ± 3 nm, measured from the sample SEMs.

Both polarisations show a reflectivity minimum at $\theta \approx 19^\circ$, characteristic of the light resonantly driving the $-1\mathbf{k}_{gx}$ scattered SPP. Both curves also show a second resonant minimum at $\theta \approx 32^\circ$, indicative of the light interacting with the $+2\mathbf{k}_{gx}$ SPP. In both the TE and TM case, these reflectivity minima lie at the same angle to within the experimental error (shown by grey bars in the figure) for each polarisation, suggesting it is indeed the same SPP mode being excited in each case.

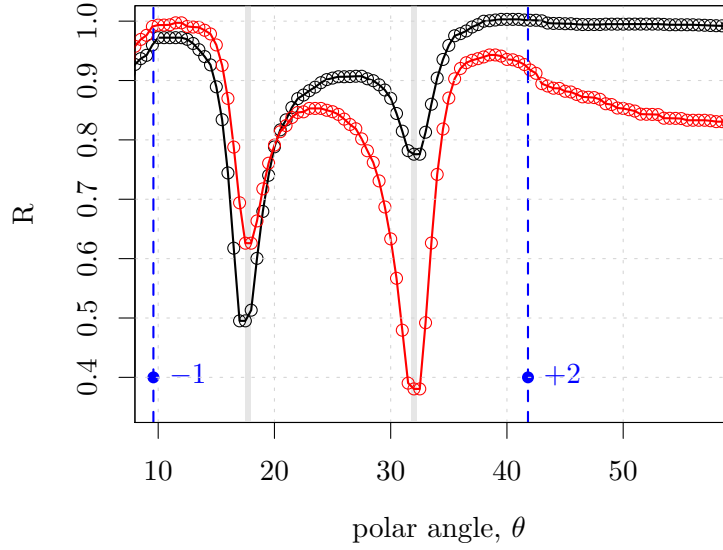


Figure 8.8: The TE (black) and TM (red) reflectivity of an asymmetric zigzag grating at a wavelength of $\lambda_0 = 500$ nm. The blue dotted lines show the calculated position of the -1 and $+2$ diffraction edges. The grey bars are a width equal to the minimum step-size of the experiment, centred at the average mode minima.

This is an example of a zigzag grating coupling either polarisation to the SPP on the zigzag surface, as the impinging electric field on the asymmetric zigzag profile provides a normal component with which to induce local surface charge regardless of polarisation. Since the electric vectors for TE and TM polarised light lie orthogonal to each other, we may generalize and state that *any* plane polarisation of light will excite SPPs on asymmetric zigzag gratings.

The reflectivity minimum associated with the $+2\mathbf{k}_{gx}$ scattered SPP at $\theta \approx 32^\circ$ is lower for the TM polarised case than the TE. While the minima associated with $-1\mathbf{k}_{gx}$ shows the opposite, with TM polarised light coupling stronger than the TE polarised light. Returning to the Fourier coefficients shown in figure 8.7, this is unsurprising. These coefficients relate to the strength by which surface fields may couple to the plane wave light. With $|C_1|^2$ larger for the TE case, and $|C_2|^2$ larger for the TM case, we expect the $\pm 1\mathbf{k}_{gx}$ scattered SPPs to be couple more strongly to the TE polarised light, and the $\pm 2\mathbf{k}_{gx}$ scattered SPPs to be couple more strongly to TM polarised light, as observed in our experimental results.

The dispersion of the in-plane SPPs ($\phi = 0^\circ$) propagating along an asymmetric zigzag grating was measured from the reflectivity of TE and TM polarised light, and these results are shown in figure 8.9. These data were obtained using the methods

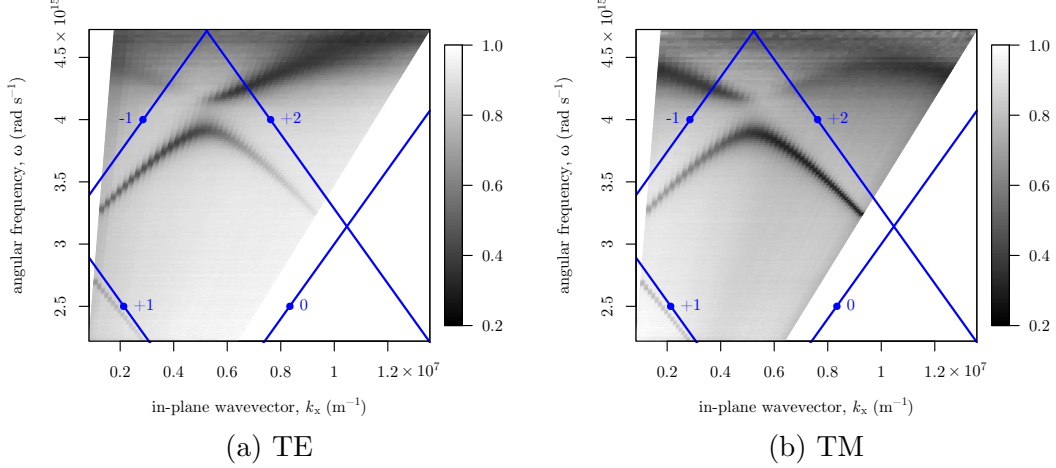


Figure 8.9: The dispersion of the SPP modes mapped as a function of (a) TE and (b) TM reflectivity on an asymmetric zigzag grating. The blue lines are the calculated positions of the diffracted light lines. The colour scale indicates the absolute reflectivity.

outlined in chapter 4, with the polar angle range of $7^\circ < \theta < 60^\circ$ in steps of 0.5° , and a wavelength range of $400 \text{ nm} < \lambda_0 < 850 \text{ nm}$ in steps of 2 nm .

The SPPs associated with $\pm 1\mathbf{k}_{gx}$ and $+2\mathbf{k}_{gx}$ diffraction are clearly coupled to in each case. In the TE case in figure 8.9(a), the $\pm 1\mathbf{k}_{gx}$ SPPs are coupled strongly, and the $+2\mathbf{k}_{gx}$ scattered SPP is coupled, albeit weaker than the $\pm 1\mathbf{k}_{gx}$ case. Under TM polarised illumination, the dispersion shown in figure 8.9(b) shows the opposite response, with the stronger coupled mode having scattered by $+2\mathbf{k}_{gx}$, and the weaker, yet still coupled mode, having scattered by $\pm 1\mathbf{k}_{gx}$. This is consistent with the predicted magnitude of the Fourier components for each polarisation case, shown in figure 8.7, and may be considered a perturbation of the symmetric zigzag case detailed in chapter 7, with the polarisation response of the surface still partially governed by the same zigzag considerations, but with additional, smaller Fourier components destroying the symmetry which led to the perfect separation of TE and TM coupled SPPs. The additional Fourier components in the surface profile have provided direct scattering routes for the excitation of the $+2\mathbf{k}_{gx}$ scattered SPPs observed for both polarisation cases in figure 8.9.

For unpolarised light, the dispersion is mapped in figure 8.10. The coupling to the SPP dispersion is now found to be reasonably symmetric around the first BZ boundary (at $\approx 5.5 \times 10^7 \text{ m}^{-1}$), as the SPP eigenmodes of the surface are coupled to by either the TE or TM components of the unpolarised light. The level of absorption is $\approx 40\%$ with this non-optimised sample. It is possible that a sample that is optimised for the

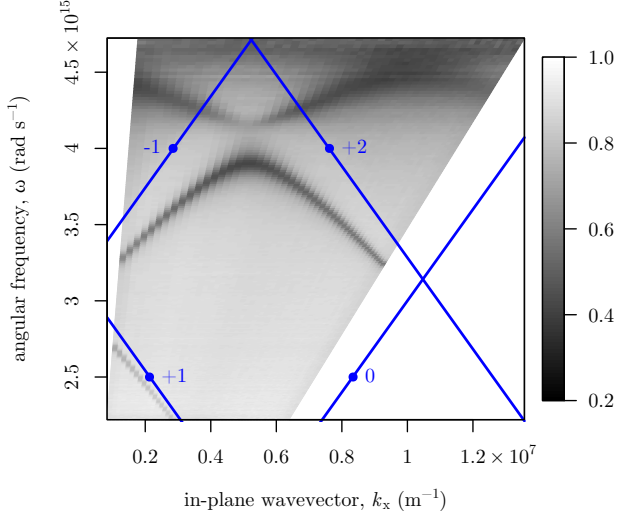


Figure 8.10: The dispersion of the SPP modes mapped as a function of unpolarised light reflectivity on an asymmetric zigzag grating. The blue lines are the calculated positions of the diffracted light lines. The colour scale indicates the absolute reflectivity.

coupling of light to the surface modes could provide 100% absorption of polarised light and excitation of the SPP bands. This would be a highly efficient mechanism by which to excite the same SPP mode along a surface, since on ordinary diffraction gratings, 50% of un-polarised incident light will not couple at $\phi = 0^\circ$. Plasmonic devices such as SPP enhanced fibre Bragg gratings [145, 146] could benefit from such an optimised structure as conversion of TE incident light in to a SPP surface wave with TM character could improve the coupling into TM fibre optic modes. SPP enhanced photo-detectors [147] could also benefit from these relaxed polarisation constraints.

8.4 Band Structure of SPPs on an Asymmetric Zigzag Grating

In chapter 7, we saw how a zigzag grating which possesses mirror symmetry has strict constraints on the possible band structure of SPPs travelling along such a grating. It was shown that the interaction of the $-1\mathbf{k}_{gx}$ and $+1\mathbf{k}_{gx}$ scattered SPPs is very weak and, most strikingly, that the formation of a band-gap at the first BZ (the interaction between the $-1\mathbf{k}_{gx}$ and $+2\mathbf{k}_{gx}$ scattered SPPs) was forbidden by the symmetry of the charge distributions.

In the case of an asymmetric zigzag grating, both these conditions on the SPP band structure are no longer true. Band-gaps are experimentally observed at both the high-

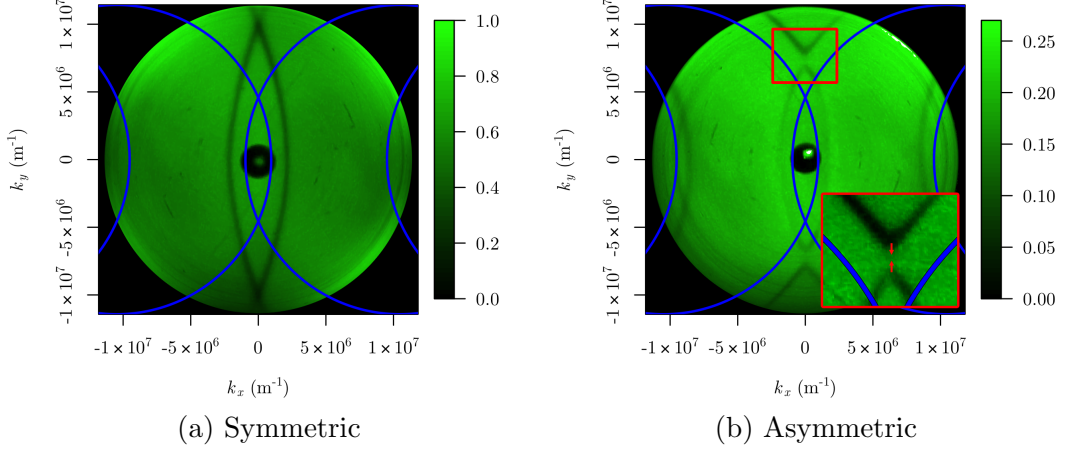


Figure 8.11: The iso-frequency contours at $\lambda_0 = 550$ nm measured on: (a) a symmetric zigzag from chapter 7; (b) An asymmetric zigzag grating. Along $k_x = 0$ two SPP bands cross in both cases, one scattered from $-\mathbf{k}_{gx}$, and one from $+\mathbf{k}_{gx}$. The red square inset in (b) shows the magnified region of the band gap, with the red arrows showing that the direction of the group velocity contains no k_x component.

symmetry points: at $k_x = 0$ and at the first BZ boundary, $k_x = \pi/\lambda_{gx}$. The following section outlines the experimental observations of these band-gaps on an asymmetric zigzag grating, and offers a discussion on the origin of these SPP energy gaps. Further to these results, evidence is found that the combination of highly anisotropic dispersion of SPPs and the allowed formation of band-gaps may forbid the propagation of SPPs in all directions for a range of frequencies, forming a full plasmonic band-gap.

8.4.1 Band Gaps at $k_x = 0$

The interaction of the $\pm\mathbf{k}_{gx}$ SPP modes at $k_x = 0$ requires a sufficiently large Bragg scattering amplitude of the SPPs so that they might interfere strongly and form a standing wave. The two possible SPP standing waves, which lay along the zigzag surface and not over the grooves, will possess energetically different arrangements of charge density. These standing waves have different frequencies, and between these two frequencies SPP propagation is forbidden; a plasmonic band gap exists. This second point is also true of symmetric zigzags, covered in chapter 7, but SPPs on these symmetric gratings are only weakly Bragg scattered, as the surface functions contains no significant even components to couple the SPP modes together. In the asymmetric zigzag case, however, the surface function of the asymmetric zigzag pattern introduces higher harmonics to the grating surface profile, both odd and even. These harmonics provide a direct coupling mechanism of $2\mathbf{k}_{gx}$ for the $\pm\mathbf{k}_{gx}$ SPP modes meeting at $k_x = 0$,

and consequently a plasmonic band gap may form.

This is observed for an asymmetric silver zigzag grating fabricated as outlined in section 8.2, using imaging scatterometry to obtain the iso-frequency contours of the SPP modes. For the case of an illuminating wavelength of $\lambda_0 = 550\text{ nm}$, the obtained contour is shown in figure 8.11(b). For comparison, the scattergram of the symmetric zigzag grating from chapter 7 is also included in figure 8.11(a). Both experimental maps use the polarisation which gives the greatest contrast of the contours over the entire momentum range. Due to SPPs being excited with either polarisation in a asymmetric case, the iso-frequency contour in figure 8.11(b) is recorded using unpolarised light, while the symmetric zigzag is recorded using plane polarisers. These experimental results show that at the intersection of the two scattered SPP contours at $k_x = 0$, the SPP contours are split in to two distinct bands for the asymmetric case. The group velocity of the SPP modes is $\mathbf{v}_g = \nabla\omega(\mathbf{k})$, and so the local group velocity direction is determined on these diagrams as orthogonal to the local contour. At $k_x = 0$, there is no component of \mathbf{v}_g in the x direction, since in this direction standing waves have formed. Compare this to the result shown in figure 8.11(a), for the zigzag grating from chapter 7. These SPP bands pass through each other unperturbed, having only weak multiple-scattering processes available to them by which to couple.

The surface of our sample provides the strong scattering and so stronger interaction of these scattered SPP modes by a combination of a larger zigzag amplitude and the asymmetry introduced by offsetting an apex by $\delta = 150\text{ nm}$.

8.4.2 Band Gaps at the 1st BZ Boundary

The lack of a band-gap at the first BZ for SPPs on symmetric zigzag gratings detailed in chapter 7 is a result of the two possible standing wave solutions being degenerate in energy. This is because the two possible arrangements for a standing wave of charge density on a zigzag surface lie in identical electromagnetic environments. Since there is no difference in energy between the two states, no band gap is observed.

In the experimentally mapped dispersion of the asymmetric zigzag grating, shown in figure 8.10, a clear band-gap has now opened at the first BZ, where the $-1\mathbf{k}_{gx}$ and $+2\mathbf{k}_{gx}$ scattered SPPs cross. In this angular frequency range of $3.9 \times 10^{15}\text{ rad s}^{-1}$ to $4.2 \times 10^{15}\text{ rad s}^{-1}$, there is no coupling of light to either SPP, meaning no SPP propagation occurs within this frequency gap for this orientation of the grating. The gradient of the SPP contours falls to zero at the BZ, meaning that the SPPs on the upper and lower frequency band edges have zero group velocity, and are standing waves.

This band gap is a consequence of the broken mirror symmetry of the diffraction grating, and may be demonstrated using a FEM model. In figure 8.12 we show the

8. Optical Response of Asymmetric Zigzag Bigratings

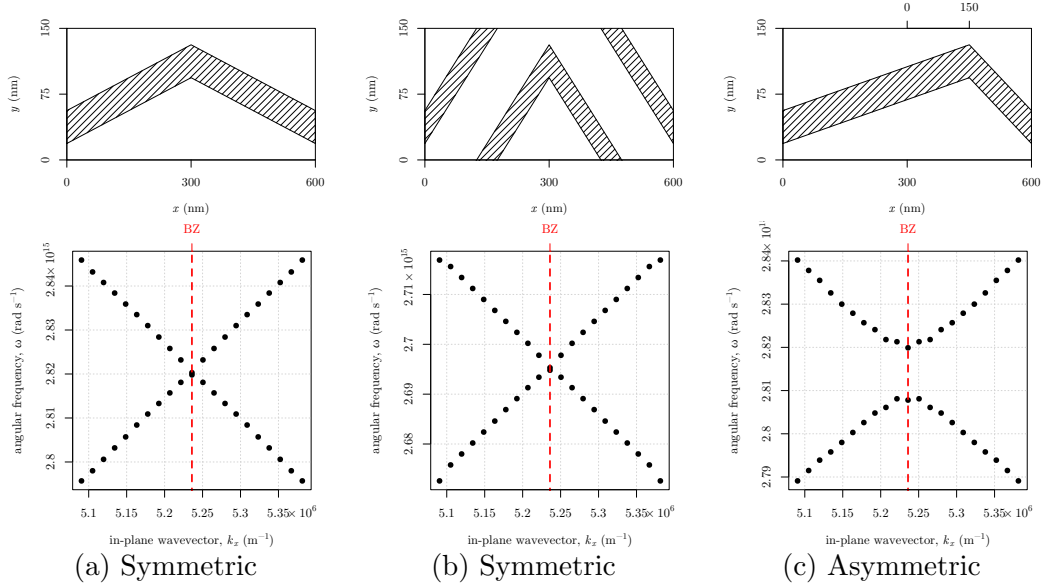


Figure 8.12: The calculated eigenmodes for the crossing of the $-1\mathbf{k}_{gx}$ and $+2\mathbf{k}_{gx}$ scattered SPPs at the first BZ for the cases of: (a) a symmetric zigzag; (b) a symmetric, high-amplitude zigzag and; (c) an asymmetric zigzag. The unit cell for each is shown above the modelled dispersion plots.

modelled dispersion for the $-1\mathbf{k}_{gx}$ and $+2\mathbf{k}_{gx}$ SPP crossing at the first BZ. The model used is an eigenmode calculation using the FEM modelling techniques described earlier. Three dispersions are shown, each for a different zigzag grating.

Figure 8.12(a) shows the dispersion at the BZ boundary for a typical symmetric zigzag grating. As detailed in chapter 7, band-gaps are forbidden to form at this BZ boundary by the symmetry considerations of the allowed charge distributions. As such, the SPP dispersion is unperturbed, and the $-1\mathbf{k}_{gx}$ and $+2\mathbf{k}_{gx}$ scattered SPPs pass through each other without interacting. This is also the case in figure 8.12(b), where the symmetric zigzag amplitude has been increased by 150 nm. This unit cell maintains the mirror symmetry of the zigzag grating and so, once again, formation of a band gap is forbidden. However, by offsetting the zigzag grating, as modelled in figure 8.12(c), the formation of a band gap is immediately achieved in the modelled SPP dispersion. The group velocity (the gradient of the SPP dispersion curves) falls to zero at the BZ boundary, and a region of forbidden SPP propagation opens up.

The formation of a band gap at the first BZ boundary is a consequence of the SPP standing waves differing in energy. Figure 8.13 shows the modelled magnitude of electric field plotted in the xz plane for the low and high energy standing wave solutions.

These two standing wave solutions have three ‘hot-spots’ of electromagnetic field

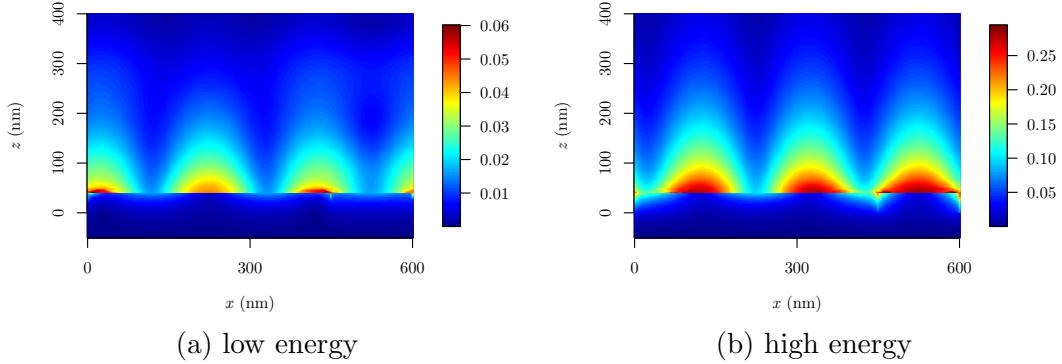


Figure 8.13: Field plots of $|\mathbf{E}|$ (colourplot) a for the (a) low energy and (b) high energy standing waves at the first BZ. The cross section is taken at $y = 75$ nm.

per unit cell, equating to a wave with a wavevector $3\mathbf{k}_{gx}/2$, as you would expect for a SPP standing wave at the first BZ formed between the $-1\mathbf{k}_{gx}$ and $+2\mathbf{k}_{gx}$ scattered SPPs . The difference in energy between the two modes is easily identifiable by the decay lengths of the electric fields. In the low energy case, the SPP dispersion is pushed down in energy, away from the light line. Consequently, the electric field profile is more ‘plasmon-like’, confined closer to the surface than the high energy solution, which is more ‘photon-like’, having been pushed up in frequency, towards the diffracted light line.

The origin of this difference in energy between the two standing wave states is due to the different arrangements of surface charge along the zigzag. This is demonstrated in the modelled magnitude of electric field plotted in a plane just above the zigzag, displayed in figure 8.14.

In this figure, the two standing wave solutions are shifted spatially by a quarter phase lag along the grating. This positions the nodes and anti-nodes of the standing wave as shown in the figure, with the low energy solution placing the field extrema close to the apexes of the zigzag, and placing the high field points for the high energy solution along the edges of the zigzag. Without any mirror symmetry of the zigzag grating, these two arrangements for the standing wave surface charge are different, and so an energy difference exists between them. As a consequence, an SPP band gap now opens at the first BZ boundary.

8.4.2.1 Coupling of Light to the Band Edges

Figure 8.15 shows the experimentally mapped band gap at the first BZ boundary for the three polarisation cases; TE, TM and average polarised light. It is seen that in

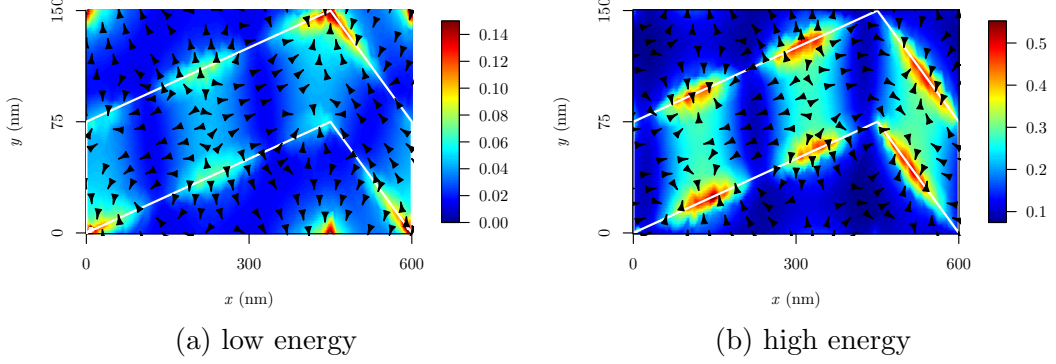


Figure 8.14: Field plots of $|\mathbf{E}|$ (colourplot) and $\hat{\mathbf{E}}$ (arrows) for: (a) the low energy and; (b) high energy standing waves at the first BZ. The cross sectional height is 1 nm above the grooves at 41 nm.

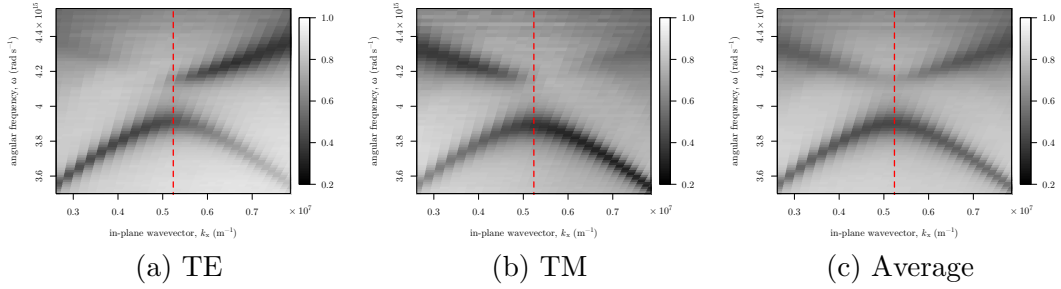


Figure 8.15: Experimental reflectivity colour plots mapping the dispersion of the band gap around the 1st BZ, for incident (a) TE polarised light, (b) TM polarised light and (c) average polarisation. The red dotted line indicates the position of the BZ boundary.

all three cases, the lower energy band edge is coupled to by both TE and TM light relatively strongly with a dark band of $\approx 20\%$ reflectivity, while the higher-frequency band edge is never coupled to as strongly, with a reflectivity of $\approx 90\%$, absorbing only $\approx 10\%$ of the incident light.

To determine why light will preferentially couple to the lower frequency mode, we may consider the overlap integral of the fields for both cases. The overlap integral gives a quantitative measure of how much a driving electric field will match that of the resonance, and hence allow us to determine relative coupling strength between the two modes. The overlap integral is defined in a plane as [148],

$$\zeta = \frac{|\int E_1 E_2 dA|^2}{\int |E_1|^2 dA \int |E_2|^2 dA} \quad (8.8)$$

8. Optical Response of Asymmetric Zigzag Bigratings

E_1 and E_2 are the two electric fields to consider, in our case the SPP eigenmode and the incident plane wave. A plane of area A integrated over an area equal to the plane of incidence, in this case ($\phi = 0$), the xz plane. We shall use field profiles for the resonant standing waves from the calculated FEM model and make several simplifications to the overlap expression for ζ . Firstly, we note that the z dependence for the electric field of a SPP has the same functional form in each case, an exponential in the z direction. Immediately then, we can simplify the integral to a one-dimensional line integral in x , as the normalized contributions from the E_z of the SPP and the light field overlap will be equal in both cases. Secondly, we take the sum of the E_x field along y to account for the whole unit cell. Since this is now a numerical calculation, the expression for the simplified overlap, ζ^* is,

$$\zeta^* = \frac{|\sum_{x=0}^{\lambda} E_{x,SPP} E_x^0|^2}{\sum_{x=0}^{\lambda} |E_{x,SPP}|^2 \sum_{x=0}^{\lambda} |E_x^0|^2} \quad (8.9)$$

The data for $E_{x,SPP}(x)$ are extracted from the numerical simulation shown in figure 8.14, for a region in the grooves at $z = 20$ nm. At the first BZ boundary, the incident light, $E_x^0(x)$ has an in-plane wavevector equal to $k_x = k_{gx}/2$, and so the expression used for E_x^0 is,

$$E_x^0 = \sin\left(\frac{k_{gx}x}{2} + \psi\right) \quad (8.10)$$

with ψ equal to the phase of the wave at the surface. Since the band-gap under consideration is not for normal incidence, the incident electric field propagates in the x direction, which we can represent as a change in ψ . At certain values of ψ , optimal coupling will occur and at 90° in phase to this, no coupling will occur. When considering the overlap integral for each standing wave case, we optimise the value of ψ to give the largest value of ζ^* , corresponding to a phase at which the light is optimally matched to the standing-wave fields. The functional forms for both E_x^0 and $E_{x,SPP}$, for both band edge solutions are shown in figure 8.16. It is found that for the low energy solution, $\zeta_-^* = 0.0212(4d.p.)$, while for the high energy solution $\zeta_+^* = 0.0000(4d.p.)$. The overlap of the impinging E_x is far greater for the lower energy solution by comparison with the high energy solution, which to a fair approximation is zero. Returning to figure 8.16, the physical reason for this preferred coupling is now clear. In the low energy case, E_x^- is compressed (and so enhanced) in region 2 ($450 \text{ nm} < x < 600 \text{ nm}$). This region correspond to E_x originating from just right of the zig-zag apex crossing the grooves to the lower apex edge at $x = 600$ nm, whereas for E_x^+ , the field is reasonably uniformly distributed across the zigzag. The asymmetrically enhanced field in the E_x^- case adds a $k_{gx}/2$ component to the SPP field, allowing it to couple strongly to the light, which

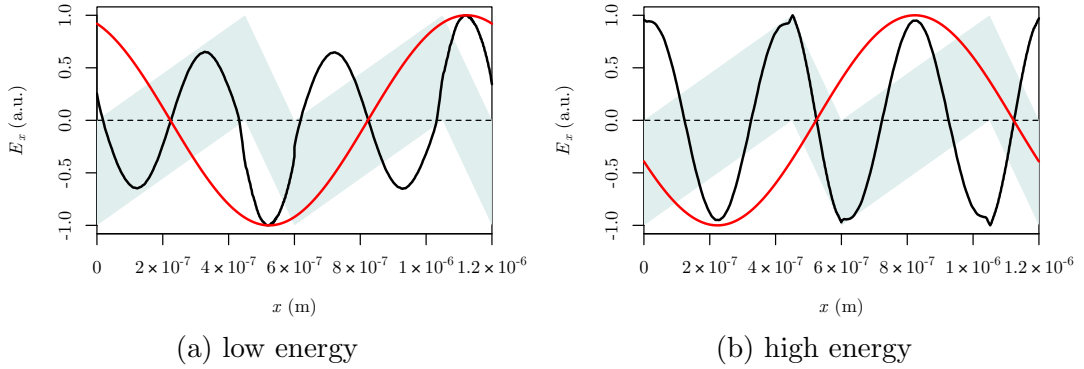


Figure 8.16: The (a) low energy and (b) high energy x -component of the SPP standing wave electric field (black, E_{SPP}) and incident field (red, E_x) varying across two unit cells of the asymmetric zigzag grating (light grey shapes indicate the zigzag in the xy plane).

itself has a $k_{gx}/2$ component at the BZ boundary. Similar explanations exist for the coupling for band edges on surface relief blazed gratings [85, 114] explained in chapter 4.

8.4.2.2 A Full Surface Plasmon Band Gap

SPP propagation on a zigzag grating is naturally anisotropic with respect to propagation direction, due to the large band gaps which can form when the SPPs run over the grooves, and the relatively small (or forbidden) band gaps that form when the SPPs run along the zigzags. In chapter 7, it was shown that this anisotropy can be so large that a zigzag grating may form the basis of a SPP collimating device, with the group velocity of SPP modes solely in one direction. The asymmetric zigzag also shows this increasing anisotropy with frequency, as shown in figure 8.17. As the frequency of the light is increased, the SPP contours lie further from the zero-order circular SPP cones, and become more ellipsoidal. These contours also split due to band-gaps along the $k_x = 0$ symmetry plane.

The anisotropic propagation combined with the ability for SPPs to form band gaps at the 1st BZ boundary lead to a mechanism by which we may forbid the propagation of SPPs in all directions along the grating surface, forming a full plasmonic band gap.

When the dispersion of the SPPs has become sufficiently anisotropic so that the group velocity of the SPPs are in a single direction, the SPP contours intersect the first BZ at π/λ_{gx} with momentum only in the x direction. This was observed before in the symmetric zigzag case in chapter 7: figure 7.23, where the SPP contours pass

8. Optical Response of Asymmetric Zigzag Bigratings

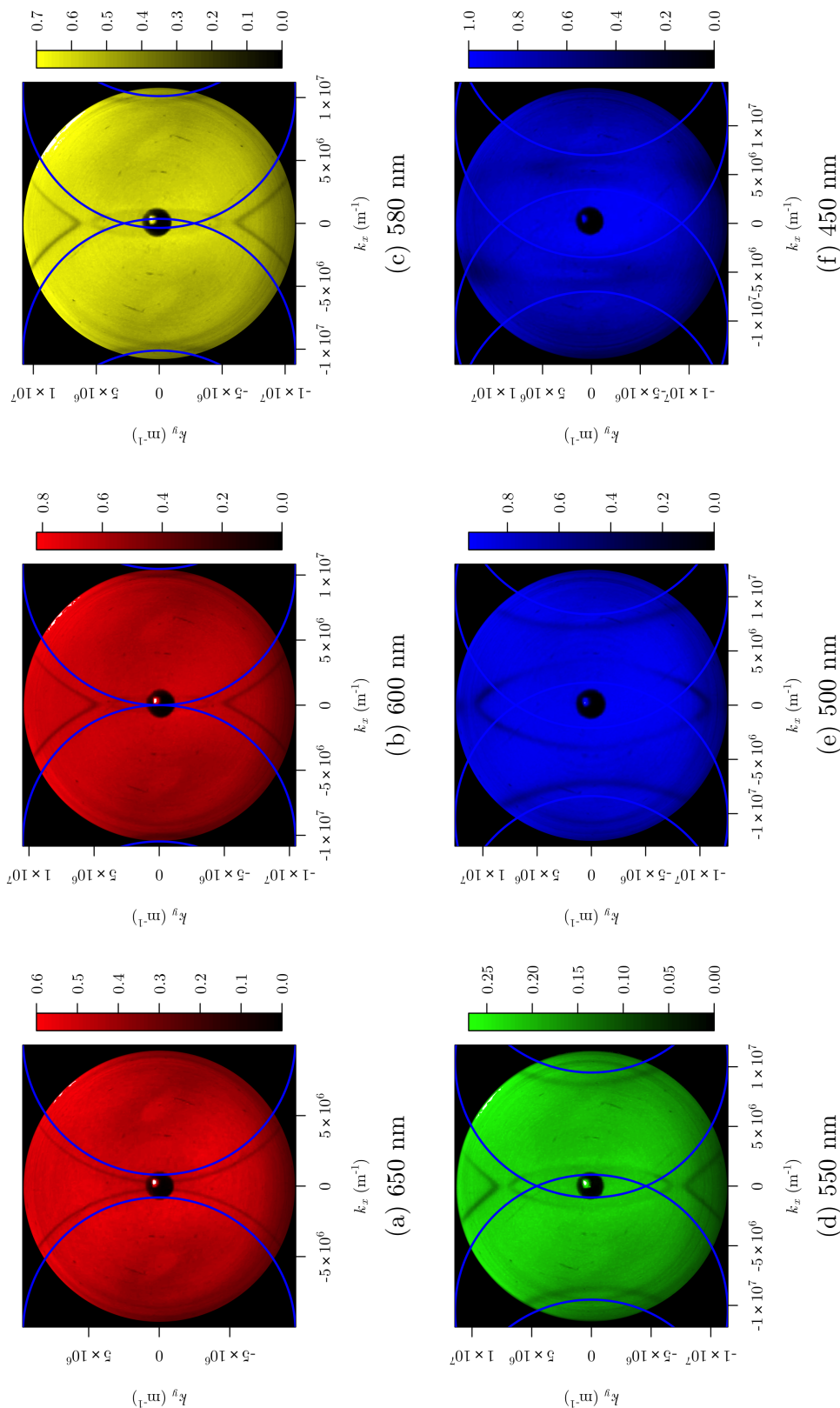


Figure 8.17: Iso-frequency contours of an asymmetric zigzag grating for a range of wavelengths, measured using the reflectivity of unpolarised light in the imaging scatterometer. The blue circles indicate calculated diffraction edges.

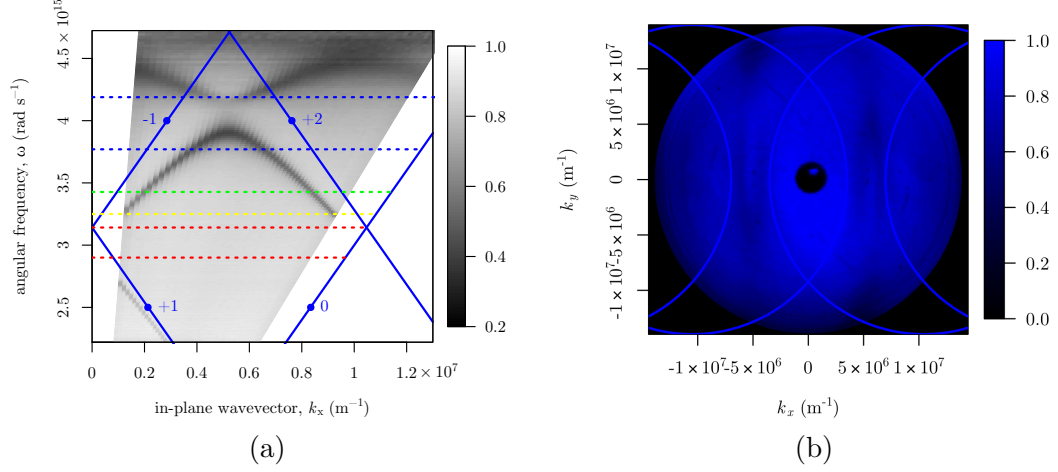


Figure 8.18: (a) The dispersion of the SPP modes on an asymmetric zigzag grating for $\phi = 0^\circ$ mapped using the reflectivity of unpolarised light. Included are the wavelength slices corresponding to the iso-frequency scattergrams in figure 8.17, ranging from low frequency (red, 650 nm) to high (blue, 450 nm), (b) The scattergram for $\lambda_0 = 450$ nm, corresponding to the highest frequency slice in (a).

through the BZ boundary with the contour parallel to the boundary. In the asymmetric zigzag grating case, the SPP iso-frequency contours still approach the BZ boundary approximately parallel, but now form a band gap at the boundary. This means that the SPP band gap at this boundary forms at all values of momentum simultaneously, and so a frequency band over which all SPP propagation is forbidden is opened. This is a full plasmonic band gap. Figure 8.18 shows an iso-frequency contour for $\lambda_0 = 450$ nm close to the forbidden frequency region, and shows minimal coupling for light to SPPs across the entire light cone. This iso-frequency contour is not at the exact frequency of the observed band gap, shown in the corresponding dispersion plot in figure 8.18, due to experimental limitations. The poorly coupled SPP contours in the scattergram also show stronger (yet still weak) coupling towards the edges of momentum-space, and it is clear that the contours are, in fact, slightly curved. This shows that the dispersion is not as anisotropic as would be necessary for the contour to intersect the BZ boundary simultaneously. However, these results demonstrate in principle the engineering of a full plasmonic band gap by using a sub-wavelength periodicity to introduce large anisotropy in SPP propagation and then the ability for such gratings to form band gaps at the BZ in all directions simultaneously. Optimising the sample and experimentally measuring the forbidden frequency band is left as future work.

8.5 Conclusions

We have demonstrated in this chapter that manipulation of the surface symmetry on a zigzag grating can lead to some novel optical effects.

The coupling of any polarisation to SPP modes on such gratings was explained and experimentally verified in section 8.3, with both TE and TM polarised light resonantly driving the same SPP modes. The coupling strength was still preferentially to TE or TM polarised light depending on the order of diffraction involved, but the optimisation of this coupling might be possible using a different broken symmetry geometry.

The formation of band gaps on these gratings has also been measured, for both planes of symmetry accessible to experiment for this sample. The energy difference between these standing waves arises from the energetically dissimilar arrangements of charge along the asymmetric zigzag. The coupling of light to these standing wave states is found to depend on the symmetry of the surface, analogous to how the phase of Fourier components determines the light coupling on surface-relief gratings. This is explained in depth in section 8.4.

Finally, the potential for this structure to provide a full surface plasmon band gap is explored, with the combination of the highly anisotropic SPP dispersion and the formation of band-gaps at the BZ boundary showing promise for the engineering of a full surface plasmon band-gap device.

Chapter 9

Conclusions

9.1 Summary of Thesis

This thesis details original experimental investigations on the excitation of SPPs along metallic diffraction grating surfaces. Broadly, these investigations can be divided into two main categories: the investigation of SPPs on traditional ‘crossed’ bigratings with novel symmetries, and the introduction of a new type of diffraction grating supporting SPPs, the ‘zigzag’ grating.

The work on the traditional ‘crossed gratings’ is presented in chapters 5 & 6, exploring gratings with symmetries that have previously received little attention in the literature. Chapter 5 experimentally explores the dispersion and coupling of SPPs on a rectangular bigrating. The groove profiles of such bigratings are described as a Fourier expansion of the constituent gratings, and this is used to explain the experimentally observed scattering and interaction of the supported SPP modes. Surface plasmon band-gaps are seen to occur at the boundaries of the rectangular BZ and are recorded using the novel technique of imaging scatterometry. This measurement technique for acquiring the iso-frequency contours of SPPs in k -space is original to this thesis, and detailed in chapter 4. The measured SPP contours at the BZ boundary are reproduced using FEM modelling, showing good agreement with experiment.

Chapter 5 also shows that by increasing the depth of a constituent grating, the SPP travelling in the orthogonal direction can be slowed in group velocity. Experimental results also show that the SPP iso-frequency contour can be shaped by changing the available grating harmonics and hence the strength of scattering amplitudes. This is demonstrated experimentally as a mechanism by which to design anisotropic SPP propagation, which could be useful for the development of SPP surface optics.

Chapter 6 investigates SPPs on gratings with the lowest symmetry of all the 2D Bravais lattices, oblique bigratings. SPP mediated polarisation conversion is observed

on these gratings due to the broken mirror symmetry of the surface. Measurements of the dispersion also show evidence that SPPs may undergo self-coupling. This is the mechanism of a propagating SPP mode being able to resonantly drive another, different, SPP mode. This is a possibility providing the two modes do not travel orthogonally to one another.

The iso-frequency contours of these SPPs are mapped experimentally using imaging scatterometry, and it is found that band-gaps do not necessarily occur at the conventional definition of the BZ boundary. A discussion of the symmetry considerations on such a grating is used to explain why this is the case, concluding that since the BZ boundary is itself not a contour of high-symmetry for an oblique lattice, there is no condition for the band-gaps to form at this arbitrary boundary. There are, however, isolated high-symmetry points along the BZ boundary, and when the plane of incidence intersects these unique points, it is experimentally observed that SPP band-gaps do still occur.

The final two experimental chapters introduce a new type of diffraction grating: the zigzag grating. These are gratings where a diffractive periodicity has been introduced by ‘zigzagging’ a set of sub-wavelength (non-diffracting) grooves in a metal surface. The electric field of plane polarised light incident on such a zigzag grating will intersect the surface regardless of the polarisation angle, inducing surface charge. This results in SPP excitation on these gratings with either TE or TM polarised light.

Chapter 7 details such a zigzag grating that possesses a single mirror plane. The symmetry of this zigzag structure leads to the observation that TE polarised light excites SPPs scattered by odd-order grating vectors, while TM polarised light excites SPPs scattered by even-orders. This separation of SPP diffracted orders by polarisation selectivity is explained using a simple theoretical treatment, and is observed experimentally.

A second consequence of this symmetric zigzag grating is that the standing surface wave states at the first BZ boundary are found to be degenerate in energy. By modelling the system using the FEM, it is found that the two possible SPP standing waves inhabit identical electromagnetic environments, and so no energy difference exists between them and no bad-gap may form. Experimental observations confirm this lack of SPP band-gap at the first BZ boundary.

The final results of chapter 7 show that SPP band-gaps associated with the short sub-wavelength pitch cause the observed SPP iso-frequency contours to deform. So large is this perturbation that at high frequencies the SPP contours are flat, and the SPP’s group velocity is constrained to be parallel to the long-pitch direction, irrespective of incident angle of the coupling light. This, combined with the forbidden band-gaps, makes these zigzag gratings excellent candidates for surface wave collimation devices.

The final experimental results of this thesis are shown chapter 8 and pertain to the

SPPs excited along a zigzag grating which possesses no mirror symmetry. This leads to the experimental observation that either TE or TM polarised light may excite the same SPP modes. Band-gaps may now form, as the asymmetric zigzag surface leads to different energetic arrangements of surface charge for the different standing wave states. The anisotropic propagation of SPPs on such a surface observed in chapter 7 is also observed for these asymmetric zigzag gratings, which, when combined with the large SPP band-gaps, leads to the formation of a full SPP band-gap, for which SPP propagation is forbidden in all directions.

9.2 Future Work

Throughout this thesis we have demonstrated some novel optical effects related to SPPs on metal gratings, and this provides a wealth of possible future work.

The manipulation of SPP band structures presented using rectangular bigratings in chapters 5, 7 and 8 may provide useful tools in the design of SPP surface optics, including lenses, collimators and perhaps even negative index devices. Smoothly varying the depths along such gratings would change the effective mode index along the surface, and be used to guide or direct SPPs.

The use of sub-wavelength grooves shaped along their length to provide diffractive coupling to SPPs has a large potential for many interesting future studies. The use of the grating in chapter 7 as a collimating device for surface waves would be an excellent avenue for investigation. A schematic of a possible experimental arrangement is shown in figure 9.1. In this figure, a SPP point source (red dot) excites and couples to SPPs on a planar metal surface. The use of a near-field optical microscopy (SNOM) tip or a small point scatterer illuminated with a laser could provide near-field coupling into a SPP wave which, in the absence of the grating, will propagate outwards radially. With the addition of a grating similar to the one presented in chapter 7, the allowed momentum states of the SPP are constrained to propagate in a single direction only, causing collimation of the surface wave. The distance between the grating and the point source would control the final (presumably Gaussian) SPP beam width. This collimation could then be observed by measuring the electric field across the surface using SNOM, or by using leaky radiation microscopy [61] to image the beam.

The potential exists, by altering the zigzag period, the sub-wavelength period or the depth of the sub-wavelength grooves, to allow for the onset of flat SPP contours at a lower frequency than that found in chapter 7, possibly providing a device which can collimate SPP waves over a broad range of frequencies.

Another potential device that could incorporate a zigzag diffraction grating is an SPP mediated light source. Metal-Insulator-Metal (MIM) devices with the top metal

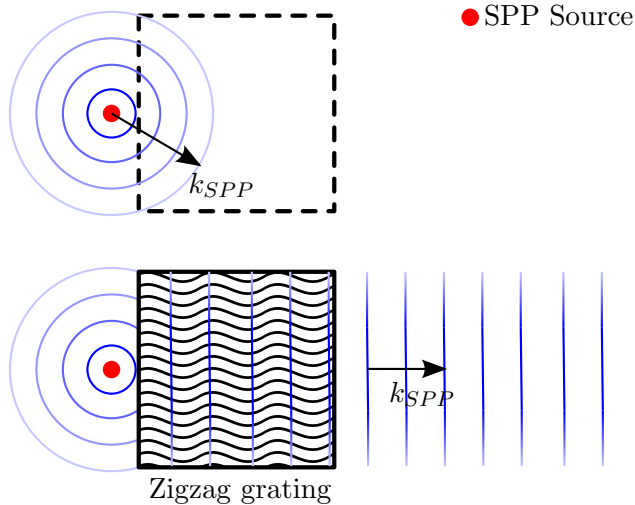


Figure 9.1: A possible experimental arrangement for the observation of collimated surface waves using zigzag gratings.

surface corrugated to form a diffraction grating have been shown to emit light when driven with a suitable voltage [149]. This process is mediated by the excitation of SPPs by electrons followed by the out-coupling of these SPPs to light by the diffraction grating. Replacing the top surface diffraction grating with the symmetric zigzag grating described in chapter 7 would result in the emission of TE polarised light into the $\pm 1, \pm 3, \pm 5, \dots$ diffracted orders and also the emission of TM polarised light into the $\pm 2, \pm 4, \dots$ orders. The device would be a polarisation directing/separating light source. The use of an asymmetric zigzag as detailed in chapter 8 would result in the emission of unpolarised light into the diffracted orders.

The asymmetric zigzag in chapter 8 also provides some exciting possibilities for other future work. Investigation into the effect of different asymmetric patterns would most likely lead to effects analogous to changing the phase of a $2k_g$ component on a traditional surface-relief grating. If a device could be constructed where the unpolarised light could couple to the SPP standing wave states (and so a region of high density of SPP states) in the upper band edge (as opposed to the preferential coupling to the lower band edge observed in chapter 8), one could envisage a device with great potential in SPP enhanced lasers or SPP enhanced solar cells. In such devices, it is desirable to couple the SPP into a gain medium coating the surface, which favours the upper-band edge of SPP band-gaps since these fields are more ‘photon-like’ extending further into the surround gain medium than the ‘plasmon-like’ lower-band edge. The advantage of using an optimised asymmetric zigzag is that the same SPP modes can be coupled to with any incident polarisation, possibly improving efficiency. The polarisation insensitivity

9. Conclusions

to the generation of the locally TM polarised SPP waves could also prove useful for the efficient coupling of light into optical fibres.

Publications

Journal Articles in Print

Surface Plasmons on Zig-Zag Gratings, T. J. Constant, T. Taphouse, H. J. Rance, S. C. Kitson, A. P. Hibbins, and J. R. Sambles. Opt. Express **20**, 23921–23926 (2012).

Surface Waves at Microwave Frequencies Excited on a Zigzag Metasurface, H. J. Rance, T. J. Constant, A. P. Hibbins, and J. R. Sambles. Phys. Rev. B **86**, 125144 (2012).

Journal Articles in Preparation

Mapping Surface Plasmon Iso-Frequency Contours Using Imaging Scatterometry, T. J. Constant, A. P. Hibbins, A. P. Lethbridge, E. K. Stone, J. R. Sambles and P. Vukusic. (2013).

Poster Presentations

Direct Imaging of Surface Plasmon Band-gaps on zig-zag gratings, T. J. Constant, A. P. Hibbins and J. R. Sambles. 4th International Topical Meeting on Nanophotonics and Metamaterials, Seefeld, Tirol, Austria. (January 2013)

Zig-Zag Gratings, T. J. Constant, A. P. Hibbins and J. R. Sambles. 3rd International Topical Meeting on Nanophotonics and Metamaterials, Seefeld, Tirol, Austria. (January 2011)

Surface Plasmons on Rectangular Bi-Gratings, T. J. Constant, A. P. Hibbins and J. R. Sambles. The Institute of Physics: Plasmonics UK Meeting, Institute of Physics, London, United Kingdom. (May 2010)

Surface Plasmons on Rectangular Bi-Gratings, T. J. Constant, A. P. Hibbins and J. R. Sambles. The Royal Society, Theo Murphy International Scientific Meeting on Metallic Metamaterials and Plasmonics, Chicheley Hall, United Kingdom. (June 2010)

Future Publications

Other publications arising from this thesis and intended for submission in the near future include: a paper on the self-collimation characteristics of zigzag gratings presented in chapter 7, and a paper on the excitation of SPPs on the asymmetric zigzag grating geometry in chapter 8.

References

- [1] BARNES, W., DEREUX, A., AND EBBESEN, T.W. Surface plasmon subwavelength optics. *Nature*, **424**, 824 (2003). [1](#)
- [2] EDITORIAL. Surface plasmon resurrection. *Nat. Photonics*, **6**, 707 (2012). [1](#)
- [3] RITTENHAUSE, D. An optical problem proposed by F. Hopkinson and solved. *J. Am. Phil. Soc.*, **201**, 202 (1786). [1](#), [16](#)
- [4] LOEWEN, E.G. AND POPOV, E. Diffraction gratings and applications (optical engineering, 58) (1997). [1](#)
- [5] WOOD, R.W. On a remarkable case of uneven distribution of light in a diffraction grating spectrum. *Proc. Phys. Soc. London*, **18**, 269 (1902). [1](#), [20](#), [33](#)
- [6] STRONG, J. The Johns Hopkins University and Diffraction Gratings. *J. Opt. Soc. Am.*, **50**, 1148 (1960). [1](#)
- [7] RAYLEIGH, L. On the dynamical theory of gratings. *Proc. Phys. Soc. London, Sect. A*, **79**, 399 (1907). [2](#), [20](#), [33](#)
- [8] STRONG, J. Effect of evaporated films on energy distribution in grating spectra. *Phys. Rev.*, **49**, 291 (1936). [2](#)
- [9] FANO, U. Some theoretical considerations on anomalous diffraction gratings. *Phys. Rev.*, **50**, 573 (1936). [2](#)
- [10] FANO, U. The Theory of Anomalous Diffraction Gratings and of Quasi-Stationary Waves on Metallic Surfaces (Sommerfelds Waves). *J. Opt. Soc. Am.*, **31**, 213 (1941). [8](#)
- [11] FANO, U. On the anomalous diffraction gratings. II. *Phys. Rev.*, **51**, 288 (1937). [2](#)

- [12] ZENNECK, J. Über die Fortpflanzung ebener elektromagnetischer Wellen längs einer ebenen Leiterfläche und ihre Beziehung zur drahtlosen Telegraphie. *Ann. Phys.*, **328**, 846 (1907). [2](#)
- [13] SOMMERFELD, A. The broadening of the waves and the wireless telegraph. *Ann. Phys.*, **28**, 665 (1909). [2](#)
- [14] RITCHIE, R. Plasma losses by fast electrons in thin films. *Phys. Rev.*, **106**, 874 (1957). [2](#)
- [15] FERRELL, R. Predicted radiation of plasma oscillations in metal films. *Phys. Rev.*, **111**, 1214 (1958). [2](#)
- [16] STEINMANN, W. Experimental Verification of Radiation of Plasma Oscillations in Thin Silver Films. *Phys. Rev. Lett.*, **5**, 470 (1960). [2](#)
- [17] ABAJO, D., KOCIAK, M., XI, P.S., AND ORSAY, F. Probing the Photonic Local Density of States with Electron Energy Loss Spectroscopy. *Phys. Rev. Lett.*, **100**, 106804 (2008). [2](#)
- [18] OTTO, A. Excitation of nonradiative surface plasma waves in silver by the method of frustrated total reflection. *Z. Angew. Phys.*, **216**, 398 (1968). [2](#)
- [19] KRETSCHMANN, E. AND RAETHER, H. Radiative decay of nonradiative surface plasmons excited by light. *Z. Naturforsch., A: Phys. sci.*, **23**, 2135 (1968). [2](#)
- [20] TURBADAR, T. Complete absorption of light by thin metal films. *Proc. Phys. Soc. London*, **73**, 40 (1959). [2](#)
- [21] MONZO, D. Optical method to differentiate tequilas based on angular modulation surface plasmon resonance. *Opt. Lasers Eng.*, **49**, 675 (2011). [3](#)
- [22] MITSUSHIO, M. AND HIGO, M. Properties of a gold-deposited surface plasmon resonance-based glass rod sensor with various light-emitting diodes and its application to a refractometer. *Opt. Commun.*, **285**, 3714 (2012). [3](#)
- [23] STEWART, J.E. AND GALLAWAY, W.S. Diffraction Anomalies in Grating Spectrophotometers. *Appl. Opt.*, **1**, 421 (1962). [3](#)
- [24] HÄGGLUND, J. AND SELLBERG, F. Reflection, Absorption, and Emission of Light by Opaque Optical Gratings. *J. Opt. Soc. Am.*, **56**, 1031 (1966).
- [25] RITCHIE, R.H., ARAKAWA, E.T., COWAN, J.J., AND HAMM, R.N. Surface-plasmon resonance effect in grating diffraction. *Phys. Rev. Lett.*, **21**, 1530 (1968). [3](#)

REFERENCES

- [26] INAGAKI, T., GOUDONNET, J.P., AND ARAKAWA, E.T. Plasma resonance absorption in conical diffraction: effects of groove depth. *J. Opt. Soc. Am. B*, **3**, 992 (1986). [3](#), [31](#)
- [27] GLASS, N., MARADUDIN, A., AND CELLI, V. Surface plasmons on a large-amplitude doubly periodically corrugated surface. *Phys. Rev. B*, **26**, 5357 (1982).
- [28] LAKS, B., MILLS, D., AND MARADUDIN, A. Surface polaritons on large-amplitude gratings. *Phys. Rev. B*, **23** (1981).
- [29] GLASS, N. AND MARADUDIN, A.A.A. Surface plasmons on a large-amplitude grating. *Phys. Rev. B*, **24**, 595 (1981). [3](#)
- [30] COWAN, J. AND ARAKAWA, E. Dispersion of surface plasmons in dielectric-metal coatings on concave diffraction gratings. *Z. Physik*, **109**, 97 (1970). [3](#)
- [31] CHANDEZON, J., DUPUIS, M.T., CORNET, G., AND MAYSTRE, D. Multicoated gratings: a differential formalism applicable in the entire optical region. *J. Opt. Soc. Am.*, **72**, 839 (1982). [3](#), [34](#)
- [32] PALMER, C. AND LOEWEN, E. *Diffraction grating handbook*. Newport Optics, New York, 6th edition (2005). [3](#), [16](#), [92](#)
- [33] WATTS, R.A., HIBBINS, A.P., AND SAMBLES, J.R. The influence of grating profile on surface plasmon polariton resonances recorded in different diffracted orders. *J. Mod. Op.*, **46**, 2157 (1999). [3](#), [35](#)
- [34] BRYAN-BROWN, G.P., SAMBLES, J.R., AND HUTLEY, M.C. Polarisation Conversion through the Excitation of Surface Plasmons on a Metallic Grating. *J. Mod. Op.*, **37**, 1227 (1990). [3](#), [31](#), [32](#), [55](#), [82](#)
- [35] BARNES, W.L., PREIST, T.W., KITSON, S.C., SAMBLES, J.R., COTTER, N.P.K., AND NASH, D.J. Photonic gaps in the dispersion of surface plasmons on gratings. *Phys. Rev. B*, **51**, 11164 (1995). [3](#), [26](#), [107](#)
- [36] BAO, G., COWSAR, L., AND MASTERS, W. (editors). *Mathematical Modeling in Optical Science*. Society for Industrial and Applied Mathematics (1987). ISBN 978-0898714753. [3](#), [33](#), [35](#)
- [37] HOMOLA, J., YEE, S., AND GAUGLITZ, G. Surface plasmon resonance sensors: review. *Sens. Actuators, B*, **54**, 3 (1999). [3](#)

REFERENCES

- [38] BOG, U., HUSKA, K., MAERKLE, F., NESTEROV-MUELLER, A., LEMMER, U., AND MAPPES, T. Design of plasmonic grating structures towards optimum signal discrimination for biosensing applications. *Opt. Express*, **20**, 24881 (2012).
- [39] SINGH, B.K. AND HILLIER, A.C. Surface plasmon resonance imaging of biomolecular interactions on a grating-based sensor array. *Anal. Chem.*, **78**, 2009 (2006). [3](#)
- [40] JANSSENS, T.V.W., CLAUSEN, B.S., FALSIG, H., AND CHRISTENSEN, C.H. Catalytic activity of Au nanoparticles Au is usually viewed as an inert metal , but surprisingly it has been found. *Nano Today*, **2**, 14 (2007). [3](#)
- [41] LINDFORS, K., KALKBRENNER, T., STOLLER, P., AND SANDOGHDAR, V. Detection and Spectroscopy of Gold Nanoparticles Using Supercontinuum White Light Confocal Microscopy. *Phys. Rev. Lett.*, **93**, 3 (2004). [3](#)
- [42] WATTS, R.A., SAMBLES, J.R., AND HUTLEY, M.C. Optical characterization of a complex grating profile. *J. Mod. Op.*, **45**, 639 (1998). [3, 35](#)
- [43] T. HALLAM, J. R. SAMBLES, B. A non-contact technique for determining the depth of zero-order gratings. *J. Mod. Op.*, **47**, 1475 (2000). [3, 35](#)
- [44] WATTS, R.A., HARRIS, J., HIBBINS, A., PREIST, T., AND SAMBLES, J.R. Optical excitation of surface plasmon polaritons on 90 and 60 bi-gratings. *J. Mod. Op.*, **43**, 1351 (1996). [3, 24, 35, 122](#)
- [45] BUTUN, S., CINEL, N.A., AND OZBAY, E. Nanoantenna coupled UV subwavelength photodetectors based on GaN. *Opt. Express*, **20**, 2649 (2012). [3](#)
- [46] OULTON, R.F., SORGER, V.J., ZENTGRAF, T., MA, R.M., GLADDEN, C., DAI, L., BARTAL, G., AND ZHANG, X. Plasmon lasers at deep subwavelength scale. *Nature*, **461**, 629 (2009). [3](#)
- [47] H'DHILI, F., OKAMOTO, T., SIMONEN, J., AND KAWATA, S. Improving the emission efficiency of periodic plasmonic structures for lasing applications. *Opt. Commun.*, **284**, 561 (2011). [123](#)
- [48] OKAMOTO, T., SIMONEN, J., AND KAWATA, S. Plasmonic band gaps of structured metallic thin films evaluated for a surface plasmon laser using the coupled-wave approach. *Phys. Rev. B*, **77**, 115425 (2008).
- [49] BERINI, P. AND DE LEON, I. Surface plasmonpolariton amplifiers and lasers. *Nat. Photonics*, **6**, 16 (2011). [3, 123](#)

- [50] POLMAN, A. AND ATWATER, H.A. Photonic design principles for ultrahigh-efficiency photovoltaics. *Nat. Mater.*, **11**, 174 (2012). [3](#)
- [51] FERRY, V.E., VERSCHUUREN, M.A., LARE, M.C.V., SCHROPP, R.E.I., ATWATER, H.A., AND POLMAN, A. Optimized Spatial Correlations for Broadband Light Trapping. *Nano. Lett.*, pages 4239–4245 (2011).
- [52] VAN DE GROEP, J., SPINELLI, P., AND POLMAN, A. Transparent conducting silver nanowire networks. *Nano. Lett.*, **12**, 3138 (2012). [24](#)
- [53] VAN LARE, M., LENZMANN, F., VERSCHUUREN, M.A., POLMAN, A., AND LARE, M.V. Mode coupling by plasmonic surface scatterers in thin-film silicon solar cells. *Appl. Phys. Lett.*, **101**, 221110 (2012). [24](#)
- [54] SHA, W.E.I., CHOY, W.C.H., CHEW, W.C., AND CHO CHEW, W. The roles of metallic rectangular-grating and planar anodes in the photocarrier generation and transport of organic solar cells. *Appl. Phys. Lett.*, **101**, 223302 (2012). [3](#)
- [55] ZAYATS, A.V.A., SMOLYANINOV, I.I.I., AND MARADUDIN, A.A.A. Nano-optics of surface plasmon polaritons. *Phys. Rep.*, **408**, 131 (2005). [3, 115](#)
- [56] WELSH, G.H., HUNT, N.T., AND WYNNE, K. Terahertz-pulse emission through laser excitation of surface plasmons in a metal grating. *Phys. Rev. Lett.*, **98**, 3 (2007). [3](#)
- [57] SHUBINA, T., GIPPIUS, N., SHALYGIN, V., ANDRIANOV, A., AND IVANOV, S. Terahertz radiation due to random grating coupled surface plasmon polaritons. *Phys. Rev. B*, **83**, 1 (2011). [3](#)
- [58] CHEONG, B.H., PRUDNIKOV, O.N., CHO, E., KIM, H.S., YU, J., CHO, Y.S., CHOI, H.Y., AND SHIN, S.T. High angular tolerant color filter using subwavelength grating. *Appl. Phys. Lett.*, **94**, 213104 (2009). [3, 24](#)
- [59] WATTS, R.A. AND SAMBLES, J.R. Reflection gratings as polarization converters. *Opt. Commun.*, **140**, 179 (1997). [3, 32](#)
- [60] YU, N., WANG, Q.J., KATS, M.A., FAN, J.A., KHANNA, S.P., LI, L., DAVIES, A.G., LINFIELD, E.H., AND CAPASSO, F. Designer spoof surface plasmon structures collimate terahertz laser beams. *Nat. Mater.*, **9**, 730 (2010). [3](#)
- [61] STEIN, B., DEVAUX, E., GENET, C., AND EBBESEN, T. Self-collimation of surface plasmon beams. *Opt. Lett.*, **37**, 1916 (2012). [3, 116, 119, 147](#)

REFERENCES

- [62] EBBESEN, T.W., LEZEC, H.J., GHAEMI, H.F., THIO, T., AND WOLFF, P.A. Extraordinary optical transmission through sub-wavelength hole arrays. *Letters to Nature*, **391**, 667 (1998). [3](#), [58](#)
- [63] LEZEC, H.J., DEGIRON, A., DEVAUX, E., LINKE, R.A., MARTIN-MORENO, L., GARCIA-VIDAL, F.J., AND EBBESEN, T.W. Beaming light from a subwavelength aperture. *Science*, **297**, 820 (2002).
- [64] MAHBOUB, O., PALACIOS, S.C., GENET, C., RODRIGO, S.G., EBBESEN, T.W., GARCIA-VIDAL, F.J., AND MARTIN-MORENO, L. Optimization of bull's eye structures for transmission enhancement. *Opt. Express*, **18**, 161 (2010).
- [65] GARCIA-VIDAL, F.J., MARTÍN-MORENO, L., AND PENDRY, J.B. Surfaces with holes in them: new plasmonic metamaterials. *J. Opt. A: Pure Appl. Opt.*, **7**, S97 (2005). [3](#)
- [66] BELOTELOV, V., DOSKOLOVICH, L., AND ZVEZDIN, A. Extraordinary Magneto-Optical Effects and Transmission through Metal-Dielectric Plasmonic Systems. *Phys. Rev. Lett.*, **98**, 077401 (2007). [3](#)
- [67] CHEN, J., BADIOLI, M., ALONSO-GONZÁLEZ, P., THONGRATTANASIRI, S., HUTH, F., OSMOND, J., SPASENOVIĆ, M., CENTENO, A., PESQUERA, A., GODIGNON, P., ELORZA, A.Z., CAMARA, N., GARCÍA DE ABAJO, F.J., HILLENBRAND, R., AND KOPPENS, F.H.L. Optical nano-imaging of gate-tunable graphene plasmons. *Nature*, **487**, 77 (2012). [3](#)
- [68] BARBER, D.J. AND FREESTONE, I.C. An investigation of the origin of the colour of the Lycurgus cup by analytical transmission electron microscopy. *Archaeometry*, **32**, 33 (1990). [7](#)
- [69] HUANG, K. On the Interaction between the Radiation Field and Ionic Crystals. *Proc. Phys. Soc. London, Sect. A*, **208**, 352 (1951). [8](#)
- [70] LAGOIS, J. AND FISCHER, B. Calculation of Surface Exciton polariton spectra and comparison with experiments. *Solid State Communications*, **18**, 1519 (1976). [8](#)
- [71] ELMZUGHI, F., CONSTANTINOU, N., AND TILLEY, D. Theory of electromagnetic modes of a magnetic superlattice in a transverse magnetic field: an effective medium approach. *Phys. Rev. B*, **51**, 515 (1995). [8](#)
- [72] PENDRY, J.B., MARTÍN-MORENO, L., AND GARCIA-VIDAL, F.J. Mimicking surface plasmons with structured surfaces. *Science*, **305**, 847 (2004). [8](#), [74](#)

REFERENCES

- [73] HIBBINS, A.P., EVANS, B.R., AND SAMBLES, J.R. Experimental verification of designer surface plasmons. *Science*, **308**, 670 (2005). [8](#), [74](#)
- [74] RAETHER, H. *Surface plasmons on smooth and rough surfaces and on gratings*. Springer-Verlag, Berlin (1988). [8](#)
- [75] KITTEL, C. AND MC EUEN, P. *Introduction to solid state physics*, volume 7. Wiley New York (1996). [12](#), [24](#), [28](#), [88](#)
- [76] KRETSCHMANN, M. AND MARADUDIN, A. Band structures of two-dimensional surface-plasmon polaritonic crystals. *Phys. Rev. B*, **66**, 1 (2002). [24](#)
- [77] POPOV, E., MAYSTRE, D., MCPHEDRAN, R.C., NEVIÈRE, M., HUTLEY, M.C., AND DERRICK, G.H. Total absorption of unpolarized light by crossed gratings. *Opt. Express*, **16**, 6146 (2008). [58](#), [122](#)
- [78] POPOV, E., BONOD, N., AND ENOCH, S. Comparison of plasmon surface waves on shallow and deep metallic 1D and 2D gratings. *Opt. Express*, **15**, 4224 (2007). [24](#)
- [79] TETZ, K., LOMAKIN, V., PANG, L., NEZHAD, M.P., AND FAINMAN, Y. Polarization weighting of Fano-type transmission through bidimensional metallic gratings. *J. Opt. Soc. Am. A*, **27**, 911 (2010). [24](#), [58](#)
- [80] LIU, Z. AND JIN, G. Phase effects in the enhanced transmission through compound subwavelength rectangular hole arrays. *J. Appl. Phys.*, **106**, 063122 (2009).
- [81] CONSTANT, T.J., TAPHOUSE, T., RANCE, H.J., KITSON, S.C., HIBBINS, A.P., AND SAMBLES, J.R. Surface plasmons on zig-zag gratings. *Opt. Express*, **20**, 23921 (2012). [24](#)
- [82] REGAN, C.J., GRAVE DE PERALTA, L., AND BERNUSSI, A.A. Equifrequency curve dispersion in dielectric-loaded plasmonic crystals. *J. Appl. Phys.*, **111**, 073105 (2012). [24](#)
- [83] ZHOU, W., GAO, H., AND ODOM, T. Toward broadband plasmonics: tuning dispersion in rhombic plasmonic crystals. *ACS Nano*, **4**, 1241 (2010). [24](#)
- [84] NASH, D.J. AND SAMBLES, J.R. Surface plasmon-polariton study of the optical dielectric function of silver. *J. Mod. Op.*, **43**, 81 (1996). [25](#), [81](#), [101](#), [104](#), [109](#), [111](#), [113](#)

REFERENCES

- [85] Barnes, W.L., Preist, T.W., Kitson, S.C., and Sambles, J.R. Physical origin of photonic energy gaps in the propagation of surface plasmons on gratings. *Phys. Rev. B*, **54**, 6227 (1996). [26](#), [107](#), [112](#), [141](#)
- [86] Yablonovitch, E. Photonic band-gap crystals. *J. Phys.: Condens. Matter*, **5**, 2443 (1993). [28](#)
- [87] Chandezon, J., Maystre, D., and Raoult, G. A new theoretical method for diffraction gratings and its numerical application. *J. Opt. (Paris)*, **11**, 235 (1980). [29](#), [33](#), [34](#)
- [88] Li, L., Chandezon, J., Granet, G., and Plume, J.P. Rigorous and Efficient Grating-Analysis Method Made Easy for Optical Engineers. *Appl. Opt.*, **38**, 304 (1999). [29](#)
- [89] Depine, R.A. and Lester, M. Internal symmetries in conical diffraction from metallic gratings. *J. Mod. Op.*, **48**, 1405 (2001). [31](#)
- [90] Elston, S.J., Bryan-Brown, G.P., and Sambles, J.R. Polarization conversion from diffraction gratings. *Phys. Rev. B*, **44**, 6393 (1991). [31](#)
- [91] Cotter, N.P.K., Preist, T.W., and Sambles, J.R. Scattering-matrix approach to multilayer diffraction. *J. Opt. Soc. Am. A*, **12**, 1097 (1995). [34](#)
- [92] Preist, T., Sambles, J.R., and Cotter, N. Periodic multilayer gratings of arbitrary shape. *J. Opt. Soc. Am. A*, **12**, 1740 (1995). [34](#)
- [93] Harris, J.B., Preist, T.W., Sambles, J.R., Thorpe, R.N., and Watts, R.A. Optical response of bigratings. *J. Opt. Soc. Am. A*, **13**, 2041 (1996). [34](#), [58](#)
- [94] Chandezon, J. and Plume, J.P. Application to trapezoidal gratings. *J. Opt. Soc. Am. A*, **18**, 2102 (2001). [35](#)
- [95] Bai, B., Meng, X., Laukkonen, J., Sfez, T., Yu, L., Nakagawa, W., Herzig, H., Li, L., and Turunen, J. Asymmetrical excitation of surface plasmon polaritons on blazed gratings at normal incidence. *Phys. Rev. B*, **80**, 1 (2009). [35](#), [92](#)
- [96] Humphries, S. *Finite-element Methods for Electromagnetics*. John Wiley, New York (1990). ISBN 0-8493-1668-5. [35](#)
- [97] ANSYS. ANSYS HFSS (2012). [35](#)

REFERENCES

- [98] KOPP, M. *An Introduction to HFSS : Fundamental Principles , Concepts and Use.* ANSYS Inc, Pittsburgh, PA (2009). [36](#)
- [99] CHEM, M. NANO PMMA and Copolymer (2012). [43](#)
- [100] NANOBEST. Nanobeam nB4 (2013). [43](#)
- [101] BERNSTEIN, G. AND HILL, D. On the attainment of optimum developer paramters for PMMA resist. *Superlattices and microstructures*, **7**, 237 (1992). [44](#)
- [102] NAGPAL, P., LINDQUIST, N.C., OH, S.H., AND NORRIS, D.J. Ultrasmooth patterned metals for plasmonics and metamaterials. *Science*, **325**, 594 (2009). [45](#)
- [103] NAGPAL, P., LINDQUIST, N.C., OH, S.H., AND NORRIS, D.J. Ultrasmooth patterned metals for plasmonics and metamaterials. (Supporting Online Suppliment). *Science*, **325**, 594 (2009). [45](#)
- [104] SHI, L., YIN, H., ZHU, X., LIU, X., AND ZI, J. Direct observation of iso-frequency contour of surface modes in defective photonic crystals in real space. *Appl. Phys. Lett.*, **97**, 251111 (2010). [51](#)
- [105] REGAN, C.J., KRISHNAN, A., LOPEZ-BOADA, R., GRAVE DE PERALTA, L., AND BERNUSSI, A.A. Direct observation of photonic Fermi surfaces by plasmon tomography. *Appl. Phys. Lett.*, **98**, 151113 (2011). [51](#)
- [106] GIANNATTASIO, A. AND BARNES, W. Direct observation of surface plasmon-polariton dispersion. *Opt. Express*, **13**, 428 (2005). [51](#)
- [107] TETZ, K.A., ROKITSKI, R., NEZHAD, M., AND FAINMAN, Y. Excitation and direct imaging of surface plasmon polariton modes in a two-dimensional grating. *Appl. Phys. Lett.*, **86**, 111110 (2005). [51](#)
- [108] KITSON, S.C.S.C., BARNES, W.L.W., BRADBERRY, G.W., SAMBLES, J.R., AND BRADBERRY, G.W. Surface profile dependence of surface plasmon band gaps on metallic gratings. *J. Appl. Phys.*, **79**, 7383 (1996).
- [109] SWALEN, J., GORDON, J., II, M., PHILPOTT, A., AND POCKRAND, I. Plasmon surface polariton dispersion by direct optical observation. *Am. J. Phys*, **48**, 669 (1980). [51](#)
- [110] STAVENGA, D.G., WILTS, B.D., LEERTOUWER, H.L., AND HARIYAMA, T. Polarized iridescence of the multilayered elytra of the Japanese jewel beetle, Chrysochroa fulgidissima. *Philosophical transactions of the Royal Society of London. Series B, Biological sciences*, **366**, 709 (2011). [52](#)

REFERENCES

- [111] STAVENGA, D.G., LEERTOUWER, H.L., PIRIH, P., AND WEHLING, M.F. Imaging scatterometry of butterfly wing scales. *Opt. Express*, **17**, 193 (2009). [52](#), [55](#)
- [112] BD, W., MICHELSSEN, K., H, D.R., AND DG, S. Hemispherical Brillouin zone imaging of a diamond-type biological photonic crystal. *J. R. Soc. Interface*, **9**, 1609 (2012). [52](#)
- [113] BARNES, W., MURRAY, W., DINTINGER, J., DEVAUX, E., AND EBBESEN, T. Surface Plasmon Polaritons and Their Role in the Enhanced Transmission of Light through Periodic Arrays of Subwavelength Holes in a Metal Film. *Phys. Rev. Lett.*, **92**, 1 (2004). [58](#)
- [114] KITSON, S.C., BARNES, W.L., AND SAMBLES, J.R. Full photonic band gap for surface modes in the visible. *Phys. Rev. Lett.*, **77**, 2670 (1996). [58](#), [123](#), [141](#)
- [115] TEPERIK, T.V., GARCÍA DE ABAJO, F.J., BORISOV, A.G., ABDELSALAM, M., BARTLETT, P.N., SUGAWARA, Y., AND BAUMBERG, J.J. Omnidirectional absorption in nanostructured metal surfaces. *Nat. Photonics*, **2**, 299 (2008). [58](#)
- [116] GOODMAN, J.W. *Introduction to Fourier Optics*. Roberts & Company Publishers, third edition (2005). ISBN 0-9747077-2-4. [60](#), [130](#)
- [117] SÁNCHEZ-LÓPEZ, M.D.M., MORENO, I., AND MARTÍNEZ-GARCÍA, A. Teaching diffraction gratings by means of a phasor analysis - OSA Technical Digest Series (CD). In *Education and Training in Optics and Photonics*, page EMA1. Optical Society of America (2009). [60](#)
- [118] PALIK, E.D. *Handbook of Optical Constants of Solids*. Academic Press (1985). [67](#)
- [119] SABAT, R., ROCHON, N., AND ROCHON, P. Dependence of surface plasmon polarization conversion on the grating pitch. *J. Opt. Soc. Am. A*, **27**, 518 (2010). [69](#)
- [120] RADAELLI, P.G. Lecture 4 Symmetry in the solid state - Part IV : Brillouin zones and the symmetry of the band (2012). [86](#)
- [121] NEWNHAM, R.E. *Properties of materials : anisotropy, symmetry, structure*. Oxford Univ. Press, Oxford (2005). [89](#)
- [122] KLEEMANN, B.H., RUOFF, J., AND ARNOLD, R. Area-coded effective medium structures, a new type of grating design. *Opt. Lett.*, **30**, 1617 (2005). [92](#)

REFERENCES

- [123] RIBOT, C., LALANNE, P., LEE, M.S.L., LOISEAUX, B., AND HUIGNARD, J.P. Analysis of blazed diffractive optical elements formed with artificial dielectrics. *J. Opt. Soc. Am. A*, **24**, 3819 (2007). [92](#)
- [124] ZHELUDEV, N.I. Applied physics. The road ahead for metamaterials. *Science*, **328**, 582 (2010). [93](#)
- [125] CHEN, Y., SCHWANECKE, A.S., FEDOTOV, V., KHARDIKOV, V., MLADYONOV, P., PROSVIRNIN, S., A.V. ROGACHEVA, ZHELUDEV, N.I., AND HUQ, E. Electron beam lithography for high density meta fish scale operational at optical frequency. *Microelectronic Engineering*, **86**, 1081 (2009). [93](#)
- [126] SCHWANECKE, A.S., FEDOTOV, V.A., KHARDIKOV, V.V., PROSVIRNIN, S.L., CHEN, Y., AND ZHELUDEV, N.I. Optical magnetic mirrors. *J. Opt. A: Pure Appl. Opt.*, **9**, L1 (2007). [93](#)
- [127] KIM, H., TAGGART, D.K.D., XIANG, C., PENNER, R.R.M., AND POTMA, E.O. Spatial control of coherent anti-stokes emission with height-modulated gold zig-zag nanowires. *Nano. Lett.*, **8**, 2373 (2008). [93](#)
- [128] WATTS, R.A., PREIST, T.W., AND SAMBLES, J.R. Sharp surface-plasmon resonances on deep diffraction gratings. *Phys. Rev. Lett.*, **79**, 3978 (1997). [94](#)
- [129] KOVACS, G.J. Sulphide formation on evaporated Ag films. *Surf. Sci.*, **78**, L245 (1978). [100](#)
- [130] HERMINGHAUS, S., KLOPFLEISCH, M., AND SCHMIDT, H.J. Attenuated total reflectance as a quantum interference phenomenon. *Opt. Lett.*, **19**, 293 (1994). [101](#)
- [131] OZBAY, E. Plasmonics: merging photonics and electronics at nanoscale dimensions. *Science*, **311**, 189 (2006). [115, 123](#)
- [132] OGAWA, Y., OMURA, Y., MEMBER, S., AND IIDA, Y. Study on Self-Collimated Light-Focusing Device Using the 2-D Photonic Crystal With a Parallelogram Lattice. *J. Lightwave Technol.*, **23**, 4374 (2005). [116](#)
- [133] KOSAKA, H., KAWASHIMA, T., TOMITA, A., NOTOMI, M., TAMAMURA, T., SATO, T., AND KAWAKAMI, S. Self-collimating phenomena in photonic crystals. *Appl. Phys. Lett.*, **74**, 1212 (1999). [116](#)
- [134] KIM, S.H., KIM, T.T., OH, S., KIM, J.E., PARK, H., AND KEE, C.S. Experimental demonstration of self-collimation of spoof surface plasmons. *Phys. Rev. B*, **83**, 165109 (2011). [116](#)

REFERENCES

- [135] LUO, C., JOHNSON, S., JOANNOPOULOS, J., AND PENDRY, J. All-angle negative refraction without negative effective index. *Phys. Rev. B*, **65**, 201104 (2002). [116](#)
- [136] RUAN, Z. AND QIU, M. Negative refraction and sub-wavelength imaging through surface waves on structured perfect conductor surfaces Abstract :. *Opt. Express*, **14**, 6172 (2006). [116](#)
- [137] PLUM, E. *Chirality and Metamaterials*. Ph.D. thesis, University of Southampton (2010). [122](#)
- [138] GENET, C., LALUET, J.Y., AND EBBESEN, W. Optical chirality without optical activity : How surface plasmons give a twist to light. *Opt. Express*, **16**, 5418 (2008).
- [139] SCHWANECKE, A., FEDOTOV, V., KHARDIKOV, V., PROSVIRNIN, S., CHEN, Y., AND ZHELUDOV, N.I. Nanostructured metal film with asymmetric optical transmission. *Nano. Lett.*, **8**, 2940 (2008).
- [140] KAO, T.S., HUANG, F.M., CHEN, Y., ROGERS, E.T.F., AND ZHELUDOV, N.I. Metamaterial as a controllable template for nanoscale field localization. *Appl. Phys. Lett.*, **96**, 041103 (2010).
- [141] FEDOTOV, V. AND SCHWANECKE, A. Asymmetric transmission of light and enantiomerically sensitive plasmon resonance in planar chiral nanostructures. *Nano. Lett.*, **7**, 1996 (2007). [122](#)
- [142] HIBBINS, A.P., SAMBLES, J.R., AND LAWRENCE, C.R. Azimuth-angle-dependent reflectivity data from metallic gratings. *J. Mod. Op.*, **45**, 1019 (1998). [122](#)
- [143] BONOD, N., TAYEB, G., MAYSTRE, D., ENOCH, S., AND POPOV, E. Total absorption of light by lamellar metallic gratings. *Opt. Express*, **16**, 15431 (2008). [123](#)
- [144] OKAMOTO, T., HDHILI, F., KAWATA, S., AND DHILI, F.H. Towards plasmonic band gap laser. *Appl. Phys. Lett.*, **85**, 3968 (2004). [123](#)
- [145] EPSTEIN, I., DOLEV, I., BAR-LEV, D., AND ARIE, A. Plasmon-enhanced Bragg diffraction. *Phys. Rev. B*, **86**, 205122 (2012). [134](#)
- [146] BOLTASSEVA, A., BOZHEVOLNYI, S., NIKOLAJSEN, T., AND LEOSSON, K. Compact Bragg gratings for long-range surface plasmon polaritons. *J. Lightwave Technol.*, **24**, 912 (2006). [134](#)

REFERENCES

- [147] JESTL, M., KOCK, A., BEINSTINGL, W., AND GORNIK, E. Polarization- and wavelength-selective photodetectors. *J. Opt. Soc. Am. A*, **5**, 1581 (1988). [134](#)
- [148] DAMASK, J. *Polarization Optics in Telecommunications*. Springer, 2005th edition (2004). ISBN 0387224939. [139](#)
- [149] THEIS, T., KIRTLLEY, J., DiMARIA, D., DONG, D., AND KIRTLLEY, R. Light Emission from Electron-Injector Structures. *Phys. Rev. Lett.*, pages 750–754 (1983). [148](#)